Department of Mechanical and Aerospace Engineering

University of Strathclyde

Enhancing the Methodology for Rain Erosion Testing

PhD Thesis

James Nash

Project Supervisors: Professor Margaret M. Stack, Professor Bill Leithead

September 23, 2024

Declaration of Authenticity and Author's Rights

This thesis is the result of the author's original research. It has been composed by the author and has not been previously submitted for examination which has led to the award of a degree.

Signed: James William Kazimierz Nash

Date: 21/02/2023

Acknowledgements

I would like to thank my academic supervisor, Margaret Stack and the Tribos group research associate, Iasonas Zekos. Margaret has provided support to me throughout my PhD, enabling me to follow my hypothesises. Without her support and guidance, I wouldn't have been able to design, build and test a complex machine, such as the whirling arm rain erosion test rig. Iasonas has been a great friend and colleague, supporting me academically on research papers and being helpful with any task as and when needed.

I would like to thank Kieran Pugh for help and support as a colleague and a friend. The Research group excursions wouldn't have been the same without him.

I would like to thank all of my friends from home (Connor, Matt, Kieran, Nick, Joel, Harrison, Dilan, Olivia, Alex W and Alex G) who have helped me to keep going throughout this challenging process, providing some much needed rest and relaxation.

I would like to thank all of my Glasgow friends (Philipp, Alessio, Miguel, Georgie, Alessia, Sarah, Jack, Iain, Emad and John) and colleagues for all of their support throughout my studies and for making this experience as great as it has been, before, during and after the pandemic.

I would like to thank Grant Leischman for his friendship and technical guidance during my PhD. His valued guidance provided help and insight throughout my studies.

I would like to thank the SPIRE2 project and the Interreg fund for enabling me to conduct my research and to transition into the wind sector from my previous background in biomedical engineering.

I would like to thank Drew Irvine for his support and time in building the rain erosion

test rig and for providing me with technical and practical guidance during this complex build. Without his support, probably never would have been built.

I would like to thank Lee Stewart for his friendship and support during the test rig build. His welding expertise was a primary component of the workshop team that helped with the build and it couldn't have been done without him.

I would like to thank Chris Cameron, Alistair Kerr, Fiona Sillars and the rest of the workshop team for their time, friendly attitude and all of their help along the way. They made a southerner feel very welcome.

I would like to thank Ghulam Rasool for his guidance during the early part of my studies and for his friendly smile. He was always a great personality to have around and very knowledgeable too.

I would like to thank Richard Munro and Phil Hicks for their technical help with installing and commissioning the rain erosion test rig. Their expert knowledge of electronic drives was a key component of the test rig build and without their help and support, it would not have been possible.

I would like to thank Paul Moore (MET Eirann) and the UK Met Office team for their help and guidance throughout my rain erosion modelling work.

I would like to thank Maria Lodeiro and the NPL for the non-destructive testing they carried out on my behalf.

I would like to thank Drew Smith for recommending me for this PhD opportunity and Bill Leithead and the rest of the CDT for their support throughout my studies.

I would like to thank Applied Polymer Developments for the supply of rain erosion testing samples.

I would like to thank my father Peter, mother Joan and brother Paul, my mum's carer Edith and my Cat Bobby for their unwavering support of me. They have always believed in me and supported me where possible.

Last but definitely not least, I would like to thank my best friend Sarah Louise Kelly for her undying support. She has been there for me and supported me throughout this entire process and enduring me when times have been tough. I couldn't have completed my PhD without her.

Abstract

Leading-edge erosion has been identified as one of the key challenges in the wind turbine sector. This phenomenon damages the surface of a wind turbine blade leading to energy production losses as well as potential structural issues. There has been much research over the past 100 years on the topic, however, there are still challenges that need to be addressed. This thesis focuses on identifying the current deficiencies in rain erosion testing practice and providing insight on how to improve them as well as providing a framework for the development of rain erosion testing facilities with the ability to address some of these deficiencies directly. Here, clear guidance on how best to characterise the mechanical performance of materials, with specific mechanical and topological properties that influence rain erosion testing results is identified. Key insights into realistic weather conditions encountered by wind turbines in the field are identified through stochastic rain texture modelling using real data from weather stations operating in the Republic of Ireland. Rain chemistry data for the island of Ireland is analysed to identify relevant pollutants that may corrode wind turbine blades. Non-destructive testing (NDT) methods are used to analyse a coated composite panel containing defects, with the results qualitatively discussed. The design, manufacture and testing of a rain erosion testing facility are outlined and discussed in some detail. The testing of this rig involved a component failure incident, which is discussed in detail, identifying possible design flaws that led to its failure. Following the incident, components were redesigned and manufactured correcting the identified flaws. Finally, the research here is discussed with its limitations outlined and avenues for future work and development on the rain erosion topic are outlined.

List of Publications

Pugh, K. ; Nash, J.W.K. ; Stack, M.M. et al. **Review of analytical techniques for assessing rain drop erosion resistance of materials.** Paper presented at 14th Conference on Sustainable Development of Energy, Water and Environment Systems, Dubrovnik, Croatia.24 p.

Pugh, K. ; Nash, J. ; Reaburn, G. et al. **On analytical tools for assessing the raindrop erosion of wind turbine blades.** In: Renewable and Sustainable Energy Reviews . 2021 ; Vol. 137.

Nash, James W. K. ; Zekos, Iasonas ; Stack, Margaret M. **Mapping of meteorological observations over the island of Ireland to enhance the understanding and prediction of rain erosion in wind turbine blades.** In: Energies. 2021 ; Vol. 14, No. 15.

Contents

List of Figures

List of Tables

List of Symbols and Acronyms

Acronyms

Acronym	Description
A	Athenry
A	Subscript for Annual
AEP	Annual Energy Production
Al	Aluminium
AR	Subscript for Annual at Rated speed
BA	Ballyhaise
BE	Belmullet
C	Casement
C	Rain chemistry station
C	Subscript for Coating
C	Subscript for Rayleigh Wave
CA	Cork Airport
Ca^{2+}	Calcium
CAD	Computer Assisted Design
CF	Carbon Fibre

CFD	Computational Fluid Dynamics
CFRP	Carbon Fibre Reinforces Polymer
CL	Claremorris
Cl^-	Chloride
CSC	Continuous Spar Cap
CT	Computer Tomography
D	Dunsany
DA	Dublin Airport
DMA	Dynamic Mechanical Analysis
EMEP	European Monitoring and Evaluation Programme
EP	End Piece
ESM	Erosion Safe Mode
F	Finner
FE	Final Erosion
G	Gurteen
GF	Glass Fibre
GFRP	Glass Fibre Reinforces Polymer
GHG	Greenhouse Gas
HAWT	Horizontal Axis Wind Turbines
HAWT	Horizontal Axis Wind Turbine
IP	Epoxy
IP	Incubation Period
IP	Unsaturated Polyester
IPCC	Intergovernmental Panel on Climate Change

IR	Infrared
J	Johnstownii
K^-	Potassium
KA	Knock Airport
L	Subscript for Liquid
LC	Subscript for Liquid-Coating interface
LCOE	Levelised Cost of Energy
LE	Leading Edge
LEE	Leading Edge Erosion
LEP	Leading Edge Protection
MA	Mace Head
MD	Mt Dillon
Mg^{2+}	Magnesium
MH	Malin Head
MP	Moore Park
MU	Mullingar
MWh	MegaWatt hour
N	Newport
Na^+	Sodium
NDT	Non-Destructive Testing
NI	Northern Ireland
NPL	National Physics Laboratory
NREL	National Renewable Energy Laboratory
OEM	Original Equipment Manufacturer

OP	Oak Park
PT	Pulse Thermography
PU	Polyurethane
R	Rated speed over a specified time period
R	Roches Point
RET	Rain Erosion Test
ROI	Republic of Ireland
S	Subscript for Substrate
SA	Shannon Airport
SAM	Scanning Acoustic Microscope
SC	Subscript for Substrate-Coating interface
SEM	Scanning Electron Microscope
SENT	Single Edge Notch Tensile
SH	Sample Holder
SI	Sherkin Island
SNL	Sandia National Laboratories
$SO_2^{\ 4-}$	Sulphate
SS	Stainless Steel
SSC	Split Spar Cap
SSE	Steady State Erosion
TE	Trailing Edge
UKEAP	UK Eutrophying & Acidifying Network
US	Ultrasound
V	Valentia

VAWT	Vertical Axis Wind Turbines
VAWT	Vertical Axis Wind Turbine
VT	Vibrothermography
W	Weather station
w	Subscript for Water

Symbols

Symbol	Description	Units
γ	Variable relating to the stress wave reflections	
λ	Expected rain droplet density at a given rain intensity	Droplets m^{-3}
λ_w	Wave length	m
ν	Poisson's ratio	
ω	Revolutions per hour	h^{-1}
ω_s	angular speed	$rads^{-1}$
ψ	Acoustic impedance difference	Pa s m^{-1}
ρ	Density	kgm^{-3}
σ_U	Ultimate tensile strength	N/mm^2
A	Frontal Area	m^2
b	The slope of the Wolher curve, a term related to the knee in the fatigue curve, the ultimate tensile strength and the endurance limit of the coating	
C	Acoustic velocity	ms^{-1}
d_w	Droplet diameter	m
d_{10}	10th percentile droplet diameter	m
d_{95}	95th percentile droplet diameter	m

E_K	Kinetic Energy	J
f	Frequency	Hz
H	Mean Humidity at rated speed	%
I	Rain Intensity	mmhr^{-1}
J	Mass moment of inertia	kgm^2
k	Variable relating to the stress wave reflections	
K_{IC}	Mode 1 fracture toughness	$MPam^{1/2}$
m	mass	ms^{-1}
n	Lifetime estimation of a material/ number of impacts	
P, σ^o	Impact pressure	Pa
RH	Relative Humidity	%
S	Material's strength	N/mm^2
T	Mean Temperature at rated speed	°C
V	Impact velocity	ms^{-1}
v	Swept Volume	m^3
V_{DT}	Damage Threshold Velocity	ms^{-1}
X	Longitude	(°E)
Y	Latitude	(°N)
Z	Acoustic impedance	Pa s m^{-1}
Z	Altitude	m
D	Diameter	m
R^2	Coefficient of determination	
RMSE	Root Mean Square Error	
RPM	Revolutions Per Minute	min^{-1}

Chapter 1

Introduction

Over the past two decades, sustainability and climate change have become more prominent in the public eye. Political and social pressure has driven a shift away from traditional sources of energy. The use of fossil fuels has become undesirable politically and now even economically. This has led to large shifts in global investment.

Climate change has become a mainstream issue in the public eye, with projections by the Intergovernmental Panel on Climate Change (IPCC) that global warming will cause irrecoverable damage to the planet if we do not reduce global carbon emissions to neutral by 2050 and negative following on. This has led countries to form internationally binding commitments to reducing carbon emissions with annual pledges at the Coalition Of Parties conference. The damage of the increasing global temperatures has been particularly visible, with the world's first climate refugee announced in 2005 [23]. Not only is climate change expected to increase global sea levels, but also extreme weather events are expected to become much more common. Recent flooding in the UK or the dramatic drop in temperatures in Texas to give two examples [24, 25].

1.1 Wind Energy

To combat climate change, one particularly key area to decarbonise is the power sector, especially with the governmental push to electrify both transport and heating. This key reason has been the driver behind renewable energy investment.

Whilst there are many forms of renewable energy, wind energy has become the centrepiece for the UK's transition to carbon neutrality. Wind is important particularly as it is currently seen as the lowest carbon method of energy production. This coupled with one of the lowest Levelised Cost of Energy (LCOE) of any energy production form [26] for onshore wind and the relaxation of planning restrictions has poised the industry to become an even larger contributor to the UK power generation capacity [27].

However desirable wind energy is as a form of power generation, the sector has a number of challenges that must be addressed in order for it to become a truly sustainable energy form. The ecological impact, decommissioning, component recycling and degradation are key challenges the sector faces which must be addressed.

During its operational lifetime, a wind turbine is exposed to widely varying weather conditions and loads. Whilst wind turbines are designed and built to last 20-30 years, they inevitably fail, with some much earlier than expected. Component failures are common and can happen for numerous reasons [28].

With the development of offshore wind with both fixed and floating foundations, servicing wind farms is becoming more challenging. There is also a drive to increase blade size and rotational speed, which allows energy capture to be more efficient and gearbox sizes to reduce, respectively [29]. These two factors lead to significant cost reductions per turbine and to the LCOE. These driving factors enhance the importance of leading-edge erosion as a problem for the sector.

1.2 Aims and Objectives

As will be discussed throughout this thesis, rain erosion is one of the key industry challenges for wind turbines and understanding this problem is key to reducing maintenance costs and thus the LCOE for wind turbines. One of the main problems with the current testing standards is the lack of consistency and clear framework to understand the problem and the interrelation between various parameters. This thesis aims to improve and standardise the methodology used for rain erosion testing, through the following aims;

- To standardise materials characterisation, so that the reporting of rain erosion testing becomes more consistent, allowing for better cross-comparison between rain erosion test rigs and materials property investigations.
- To investigate surface and sub-surface defect characterisation methodologies, improving available options for future research to investigate the role defects play in the damage evolution.
- To identify realistic onsite conditions that occur during rain erosion that may promote damage evolution.
- To design, build and test a rain erosion test rig, with the ability to manipulate test conditions based on the previous three investigations and to provide a framework for doing so.

1.3 Thesis Outline

The outline of this thesis is as follows:

1. Coating Property Characterisation - The influence of material and physical properties is key to understanding the rain erosion process. New materials must be developed to overcome this issue and understanding which material properties are desirable is key to any new development. This objective will focus on identifying the key coating characteristics that are likely to influence the rain erosion process. It will aim to address specific issues around testing viscoelastic materials and outline more appropriate testing methods.
2. Non-Destructive Testing and Subsurface Defects Characterisation - Although the desire is to understand the fundamental properties or conditions that lead to failure, the manufacturing processes of materials or coatings can lead to early failure, through manufacturing defects. Currently, there is a lack of understanding of how subsurface defects lead to early coating failure in the rain erosion process. Further to this there, there is little research on what methods are available to

characterise the defects that lead to failure. A qualitative comparative analysis will be conducted on three non-destructive testing methods with the aim of identifying suitable methods for characterising subsurface defects in coatings used to protect wind turbine blades. This will help in characterising: how defect tolerant materials and coatings are, the relative distribution of defects within coated composites and how the number and type of defects is affected by manufacturing conditions and/or material/coating combinations.

3. Meteorological Data Modelling - Modelling approaches would be used to understand the physical conditions that occur in the field and whether synergistic effects might be present. The results from this modelling would then be used to enhance rain erosion testing practices, through more realistic testing conditions as well as allowing the testing of specific parameters to investigate their effect on the rain erosion process. The following parameters would be investigated: accumulated impact numbers, rain kinetic energy, droplet size, humidity, temperature and precipitation chemistry.

4. Rain Erosion Test Rig Development - A new rain erosion test rig would be designed, built and tested, for the purpose of researching the rain erosion phenomenon at the University of Strathclyde. This new test rig would be designed in order to allow the control of parameters not typically possible in industry-standard machines. Through this, it would allow fundamental research to take place and the in-house design, use of off-the-shelf components and modularity would allow flexibility.

The activities outlined here should help to achieve the main goal of this these: to improve current rain erosion testing standards. It should also improve the current understanding of rain erosion more generally.

Chapter 2

Literature Review

2.1 Climate Change

Currently man-made pollution has led to weather patterns changing. This is primarily due to Greenhouse Gas (GHG) emissions, historically these have mostly been from developed nations, although more recently developing nations are now the largest emitters.

GHG emissions are largely as a result of burning fossil fuels, with CO2 being one of main pollutants. Weather patterns because of this are projected to have enhanced hydrological activity in northern latitudes. Analysis of environmental data within the island of Ireland displays trends of increasing extreme weather events, including precipitation since 1975 [30]. With similar results well documented elsewhere.

Global temperatures are expected to rise, melting Arctic and Antarctic ice, resulting in sea levels rising. With a large part of global population centres situated near the sea on low lying land, climate refugees are expected to become common place.

To combat the effects of climate change there is a global push towards net zero; globally the human race producing equal amounts of GHGs as is sequestered. The first step to achieving this will be the electricity sector, through building renewable power plants to generate zero or low carbon electricity. The next step will be for large sectors such as transport and heating to be electrified. As a result, the electricity generation sector will have to expand and so there is a global shift towards the development and

integration of renewable energy, primarily solar panels and wind turbines.

2.2 History of Wind Energy

Historically, humans have been harnessing the power of the wind since neolithic times, through sails used on ships. Around the 9th century, wind mills were developed to power devices such as pumps and later for grinding grain. However, wind electricity generation took around 1 millennium longer when in 1887 James Blyth (Professor at Glasgow and West of Scotland Technical College, later becoming University of Strathclyde) utilised wind power to produce electricity for the first time, with a type of .

Unfortunately, at the time these designs were considered uneconomical. It wasn't until 1951 that the first utility-scale grid-connected turbine was constructed in the Orkney Islands, UK. Even with this development, wind power took until the early 1990s to really develop.

2.3 Wind Turbine

There are 2 main categories of wind turbines, VAWTs and . Technical challenges limited the proliferation of VAWTs and so, HAWT implementation took off. HAWTs typically consist of a foundation, tower, nacelle, nose cone and three blades (Figure 2.1). The foundation of an onshore wind turbine is generally made from concrete, with the tower manufactured from steel. On top of the tower sits the nacelle, which houses the drive train. The drivetrain is typically either a permanent magnet direct drive or alternatively contains a gearbox connected to a generator. Most wind turbines these days have pitch and yaw mechanisms, to change the blade's angle of attack, regulating power output and keep the wind turbine facing the oncoming wind, respectively.

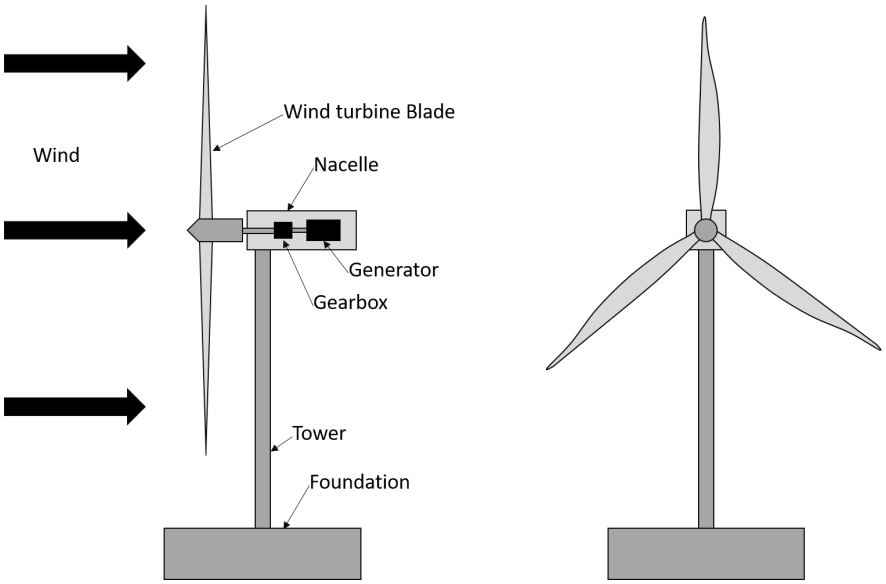

Figure 2.1: A Horizontal Axis Wind Turbine (HAWT) schematic.

2.4 Wind Turbine Blades

The primary focus of wind turbine design is to capture energy from the environment. Secondly, they are designed to last a long time; however, more recently as designs have improved, longevity has become a more pressing issue. The current motivation is to improve wind turbine lifetime, reducing maintenance requirements and therefore cost. Wind turbine blades are the most expensive component on a wind turbine [1]. In order to fulfil the desire of reducing costs and improving reliability, wind turbine blades must be understood in great depth. Blade materials and architecture, manufacturing methods, damage sources and types, loading conditions and the effect of temperature must be understood in order to properly understand why damage develops and how to predict it.

2.4.1 Blade Structure & Materials

2.4.1.1 Structure

Structurally, the blade consists of 3 main parts, the spar and shear web, the aerodynamic shell and the root joint [31].

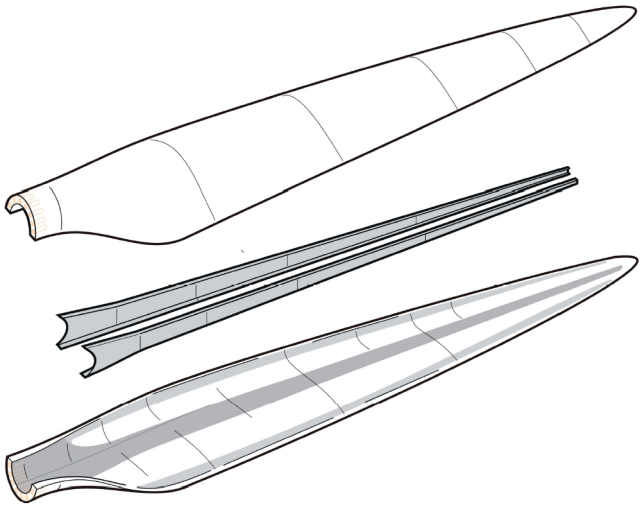

Figure 2.2: The assembly of a 2 shear web wind turbine blade (grey colour indicates the primary load-carrying composites) [1].

Typically, there is at least 1 shear web, although more commonly there are two. In designs where there is more than one shear web, the distance between them decreases towards the tip of the blade (Figure 2.2) [2]. An increased distance between shear webs reduces the moment about the shear webs, which should result in lower deflection. The spar and shear webs typically form a rectangular box section beam comprised of the upper and lower spar caps and by 2 vertical shear webs which provide bending stiffness and torsional rigidity [1, 31, 32] (Figure 2.3). This structure usually takes approximately 80% of the loading during operation.

The aerodynamic shape is given by 2 aerofoil shells which are joined together and to the spars at both sides. The 2 shells are bonded together with high toughness adhesive at the Leading-Edge (LE) and Trailing-Edge (TE), as are the shear webs and the spar caps. The exterior of the blade is typically coated with a gelcoat, providing UV protection and preventing moisture ingress. Typically, in larger blades, the spar caps are formed from a thick laminate of Glass Fibre Reinforced Polymer or Glass Fibre (GF)/ Carbon Fibre (CF) hybrids, while the shells and the shear webs are sandwich panels composed of GFRP skins and a thick foam or balsa wood core [32]. The shell is responsible for creating the pressure distribution that generates lift. For this reason

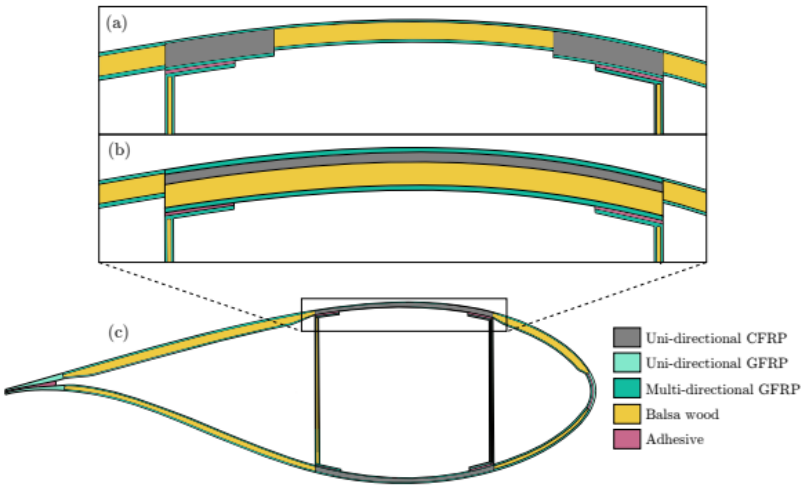

Figure 2.3: Various spar cap topologies explored by Rosemeier and M Batge [2]. (a) Split Spar Cap (SSC) concept, (b) Continuous Spar Cap (CSC) concept, and (c) baseline.

the aerofoil shape and chord length changes with the position along the blade length, twisting in order to maintain an optimal angle of attack during operation. The shell takes approximately 20% of the total load [31]. The root joint is the only metallic part of the blade, which connects the blade to the hub using screws. This metallic joint is covered by composite laminates internally and externally [31]. The most common root attachment method for current state of the art wind turbine designs is a circular bolted root connection, with bolts pretensioned [33].

2.4.1.2 Composite architecture

As can be seen in figure 2.3, the wind turbine blade is made from carbon fibre or glass composite structures that differ depending on their location. Typically, blades are made from unidirectional, biaxial and triaxial fabrics [31]. This is important as fibre orientation is tailored to meet the performance requirements of each area of the blade structure. Most of, if not all fibres that follow the length of the blade begin at the root and run along the blade, dropping off towards the tip. Transitions between different thicknesses throughout the blade are gradual as fibre drop off creates stress concentration [1, 33]. Unidirectional fibres are typically used at the leading-edge, the

trailing edge and at the spar cap, there are unidirectional fibres, with CFRP being common in the spar cap for larger multi megawatt turbines [2]. The spar and shear web also contain biaxial fibres [31]. The aerodynamic shell is made from either biaxial or triaxial fibres. Multiaxial fibres used for wind turbine blades are stitched, not woven. This selection is due to the fatigue properties of woven fabrics. Out of plane curvature of woven fabrics cause stress concentrations to occur which can dramatically reduce fatigue performance [31]. As wind turbine blades are relatively thin structures with high loads, they are particularly sensitive to buckling and so sandwich structures are used. This helps to provide stability, prevent buckling and improve strength to weight ratios [2, 32].

2.4.1.3 Materials

As mentioned above, wind turbine blades are mainly composed of fibre reinforced polymers, often in a sandwich configuration with some sort of core material. These composites are more commonly glass fibre, although carbon fibre composites are becoming more common. Core materials are usually either balsa wood alternatively a polymer foam [1, 2, 31–33]. The blade is connected to the rotor using bolted connections, however this will not be discussed. Composite materials are inherently variable and so, partial reduction factors are applied during certification to account for this and other variances [33].

2.4.1.4 Fibres

Composite stiffness is determined by the fibre stiffness and fibre fraction. E-glass fibres are the most common. Fibre volume content is typically quite high for unidirectional composites, however above 65%, resin dry areas become more common, which reduce the fatigue strength of the composite. GFRP composites for wind turbine blades are typically up to 75% glass by weight. Whilst there are other types of glass fibre that have better properties than E-glass, these are significantly more expensive and so their use is less common. Carbon fibres are a promising alternative to glass, with a higher stiffness and lower density, allowing thinner, stiffer and lighter blades. However, they

have lower damage tolerance, compressive strength and ultimate strain and are much more expensive than glass. They are more sensitive to misalignment and waviness, with even slight misalignments leading to significant reductions in compressive and fatigue strengths. Carbon Fibre Reinforced Polymer (CFRP) are commonly used by Vestas and Siemens Gamesa in structural components such as the spar caps of larger blades. Aramid and basalt fibres are being investigated, but as far as the author is aware have not seen wide scale implementation. Hybrid composites are a promising alternative, providing mass reduction potential, with only a limited increase in cost. Currently, LM Wind Power (Owned by GE) have implemented hybrid composites in their blades. Hybrids offer the potential to improve the impact and tensile failure strain properties of CFRPs [1].

2.4.1.5 Matrix

Most composites use thermoset resins (80%). They typically allow room temperature cure (if desired) and have low viscosity making infusion easier. Initially polyester resins were used, however with the development of larger blades epoxy resins were favoured due to their improved performance. More recently, polyester resins have improved and are now gaining traction again. The wind turbine sector is seeking to improve its environmental credentials and create a circular economy. This is driving research and development of recyclable thermoplastic resins, which have improved fracture toughness. These resins would also allow the possibility of automation, however fatigue performance is a concern [1]. The new 81m Siemens Gamesa RecyclableBlades are currently undergoing testing which exemplify this development [34].

Nanoengineered matrices are a potential avenue for further matrix development and research has proved fruitful with these materials showing increased fracture toughness and tensile, shear and compressive strength. However, this is currently mostly research and to the author's knowledge has not seen wide scale implementation [1].

2.4.1.6 Sizing

During manufacture, fibres are typically coated providing protection and improving resin wetting during manufacture, acting as an intermediary between the fibre and the matrix. As they are inorganic, glass fibres require sizing, however carbon fibres don't have the same compatibility. Carbon fibres still often receive a surface treatment and a sizing, as do natural fibres [1].

2.4.1.7 Coatings

In order to protect wind turbine blades, they are often coated with polymer coating. This is mostly in the form of an in-mould gel coat applied over the whole blade. Alternatively, coatings can be applied after manufacture and are usually for leading-edge erosion. Coatings protect the blade from moisture ingress, UV, chemical attack as well as damage during transit and impacts and from various other hazards. In mould gelcoats can take a variety of different forms, but the most common are polyester, epoxy, acrylate or polyurethane [35, 36].

2.4.2 Blade Damage

2.4.2.1 Damage by Source (Blade Specific)

All wind turbine blade structures are susceptible to damage as they're continuously in operation under cycle loads in harsh environments. Performance or structural issues can occur from a number of sources. The most common are listed below:

- Cleaning: Dust/ dirt, insect accretion, tree sap [4, 5, 37–39]
- Corrosion: galvanic corrosion at the blade root, possible corrosion of leading-edge protection coating [12, 33].
- Fatigue loads: As wind turbines are typically in constant operation during their lifetimes (20 years), the blades are under constant cyclic loading, which will eventually cause fatigue and lead to blade failure [1, 32].
- Environmental degradation: Humidity, temperature, UV, cycling

- Extreme loading scenarios: Blades are occasionally subjected to high loads, close to or potentially higher than those designed for which can damage in the form of cracks, delamination, gelcoat or skin debonding, etc. This type of scenario can even lead to the blade striking the tower [1].

- Icing: Ices can accumulate on the surface of the blade during colder months or in colder climates. This accumulation causes several problems including; completely stopping the wind turbine from rotating, disrupting the aerodynamics of the blade, increasing fatigue due to loading imbalances, increasing crack propagation due to the additional loading and damage cause from water ingress and later freeze thaw [1, 32].

- Leading-edge erosion: damage formed from the impact of airborne projectiles impacting and eroding the surface of the leading-edge. This typically propagates from the very tip of the blade at the leading-edge. The erosion modifies the aerodynamic shape of the blade reducing the lift and increasing drag, which in turn reduces power production. Hail, sand, rain, graupel, sleet are all possible sources. Initially, only the surface is damaged, however, if left unchecked the damage can become structural which is more challenging to repair [1, 4, 5, 12, 32, 39].

- Lightning: Blades are the most vulnerable components of the wind turbine blade to lightning damage. Lightning strikes are expected during a wind turbines life and each turbine is fitted with a lightning protection system, to reduce damage as much as possible. However, it is common to see scorching and cracking around the lightning attraction point, with spar rupture separation and surface tearing in more extreme cases [1, 4, 5, 32, 39–41].

- Manufacturing defects: Voids, wrinkles [1, 5]

- Other impacts: Bird/ bat strikes

- Transport/ logistical damage [4]

2.4.2.2 Damage by type

Failure of various adhesive layers, laminate delamination, debonding between the gelcoat and skin, splitting along fibres, in-plane compressive failure and cracks in the gelcoat are all common in static and cycling loading tests. Damages in the primary load carrying laminates are of major concern (main spar and laminates in the leading and trailing edges), however composites are inherently damage tolerant. One of the challenges with complex structures like wind turbine blades is many of these damage modes are difficult to detect, since they are not superficial and so not visible. For instance, in thick composite parts, wrinkles may lead to the formation of compression failure and delamination. Cracks and delamination also start from processing details such as ply-drops that locally cause stress concentrations. Cracks at trailing edge bond lines can be seen visually, but it is more difficult to assess how far they extend into the composite structure [1]. Composite damage types can be broadly broken down into the following [32] (Figure 2.4):

- Type 1: damage formation and growth in the adhesive layer joining skin and main spar flanges (skin/adhesive debonding and/or main spar/adhesive layer debonding)
- Type 2: damage formation and growth in the adhesive layer joining the up and downwind skins along leading and/or trailing edges (adhesive joint failure between skins)
- Type 3: damage formation and growth between face and core in sandwich panels in skins and main spar web (sandwich panel face/core debonding)
- Type 4: internal damage formation and growth in laminates in skin and/or main spar flanges, under tensile or compression load (delamination driven by tensional or buckling load)
- Type 5: splitting and fracture of separate fibres in laminates of the skin and main spar (fibre failure in tension; laminate failure in compression)

- Type 6: buckling of the skin due to damage formation and growth in the bond between skin and main spar under compressive load (skin/adhesive debonding induced by buckling, a specific type 1 case)
- Type 7: formation and growth of cracks in the gelcoat; debonding of the gelcoat from the skin (gelcoat cracking and gelcoat/skin debonding)

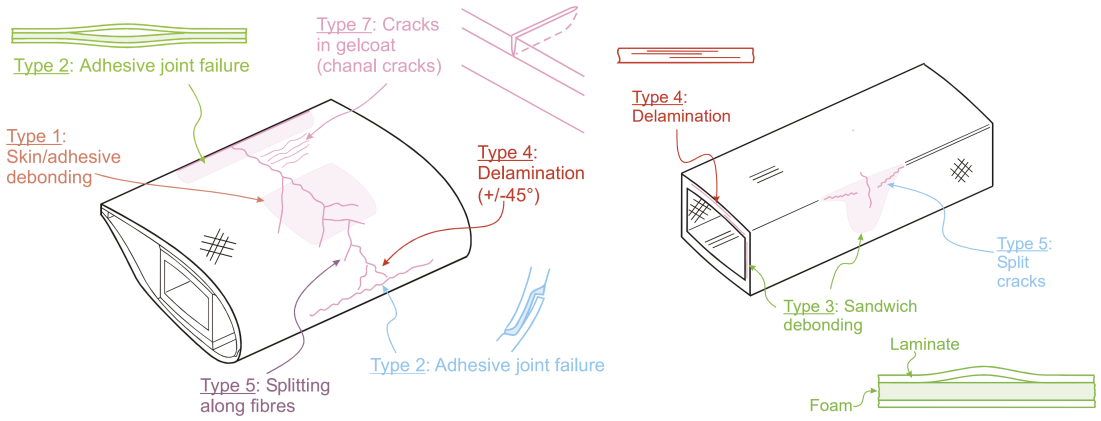

(a) (b)

Figure 2.4: 2.4a shows damage types 1,2,4,5 and 7, 2.4a show damage types 3, 4 and 5. Damage type 6 is not shown, but is a subclass of damage type 1 (reprinted from [3]).

2.4.2.3 Damage occurrence

Currently, damage reporting is largely a grey area. Whilst blade damage is widely seen, proprietary agreements have lead to a lack of understanding in the wind energy community of the scale of the blade damage problem. Here we will discuss the material available on the subject. The National Renewable Energy Laboratory blade testing campaigns are one source of damage reporting. The most common failures observed here are either laminate defects or bond line issues in the shear web and leading or trailing edges, with failures more significantly more common in fatigue testing than static tests [4]. However, these defects occur during well-defined testing procedures, of which the natural operating conditions of a wind turbine is not. Individual static and fatigue tests are useful, but blade loading will occur in varying directions and extreme

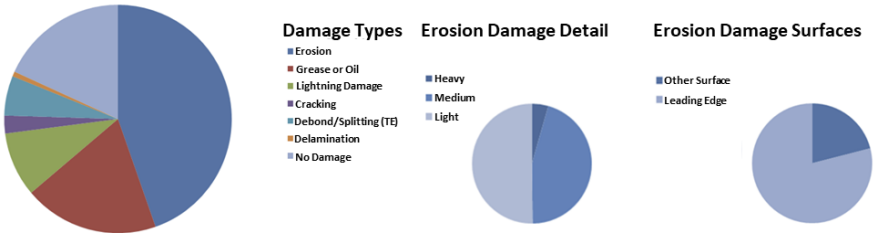

Figure 2.5: Reported damage types from the SNL survey with erosion severity and location included in more detail, adapted from [4].

loading scenarios will happen after the blade has undergone fatigue loading essentially creating combined loading conditions. However, whilst useful due to the nature of the tests they are inherently biased. As they test for specific failure types in controlled environments. Sandia National Laboratories (SNL) also report that transport, logistical and installation damage is common [4]. However, aside from this, there have been a few surveys looking more generally at blade damage as well as specific problems [4, 5, 12, 39–41]. Inspection reports are subjective and qualitative, rather than quantitative, limiting the usefulness of these surveys. The reports provide a low-level understanding, but if we take the SNL survey [4](Figure 2.5) as an example individuals report lightning damage, cracking, debonding/splitting at the TE and delamination, all of which could be as a result of and therefore classified as lightning damage. If this were the case, these damage types would also be close to the tip and so, would be significantly different in severity compared to cracking at the root, which could lead to blade and maybe even turbine failure.

According to the research, leading-edge erosion is one of, if not the most common damage type that wind turbines experience. Leading-edge erosion degrades the profile of the wind turbine blade, leading to reduced annual energy output. In their survey, Law and Koutsos found this to be as high as 4.9% in as little as 2 years, with higher rates of damage found at sites in the UK close to the sea and quarries [12]. Leading-edge erosion can significantly reduce profitability, however it is less likely to cause structural damage and blades are typically repaired before they get to that stage. Globally lightning damage is a big problem for wind turbines and with turbines becoming bigger, the problem is only expected to increase. In India, research suggests lightning damage is

the main cause of wind turbine downtime, one of the main types of damages observed (Figure 2.6) and is a frequent cause of emergency callouts [5]. Over the period 1992-1997, in Germany and Denmark for 3000 turbines surveyed there were around 6% damaged from lightning annually, even considering the average hub height was 30m [40]. In Texas, a 2008 report suggests that over a 3-year period approximately 5% of wind turbines surveyed reported some lightning damage [41]. Lightning is one of the main causes of fires too. Interestingly, EDP Renewables didn't include lightning damage in their survey, although this could be that they've categorised it as other types [39]. Dirt and grease are common in some of the surveys [4, 39], but not mentioned by Boopathi et al. [5]. This could be as they weren't considered a damage type, that they were included in surface damage or that it wasn't considered relevant to the survey. Cracking in wind turbine blades is relatively common, however information on the type and location isn't well documented in the surveys. Boopathi et al. note that surface damage at the blade root was the second most common reason for downtime, but there is no elaboration on the exact meaning of this. Surface damage here is likely to either be corrosion or cracking as this is the location of the highest bending moment and the area with metallic screws. Impacts and lightning strikes are unlikely here due to the location. In their surveys, structural cracks are common in both Europe and India [5]. According to both the SNL and the EDP Renewables surveys cracking and debonding/splitting represent a significant proportion of damage types observed on wind turbine blades [4, 39].

Icing damage is not reported in any of the surveys. This could be due to the locations of most of the wind parks. European blade inspection normally takes place in the summer, where weather conditions are generally better and there are generally lower wind speeds meaning energy outputs, and therefore profits are lower. Therefore understanding the influence of icing on blade and quantifying icing damage is more challenging.

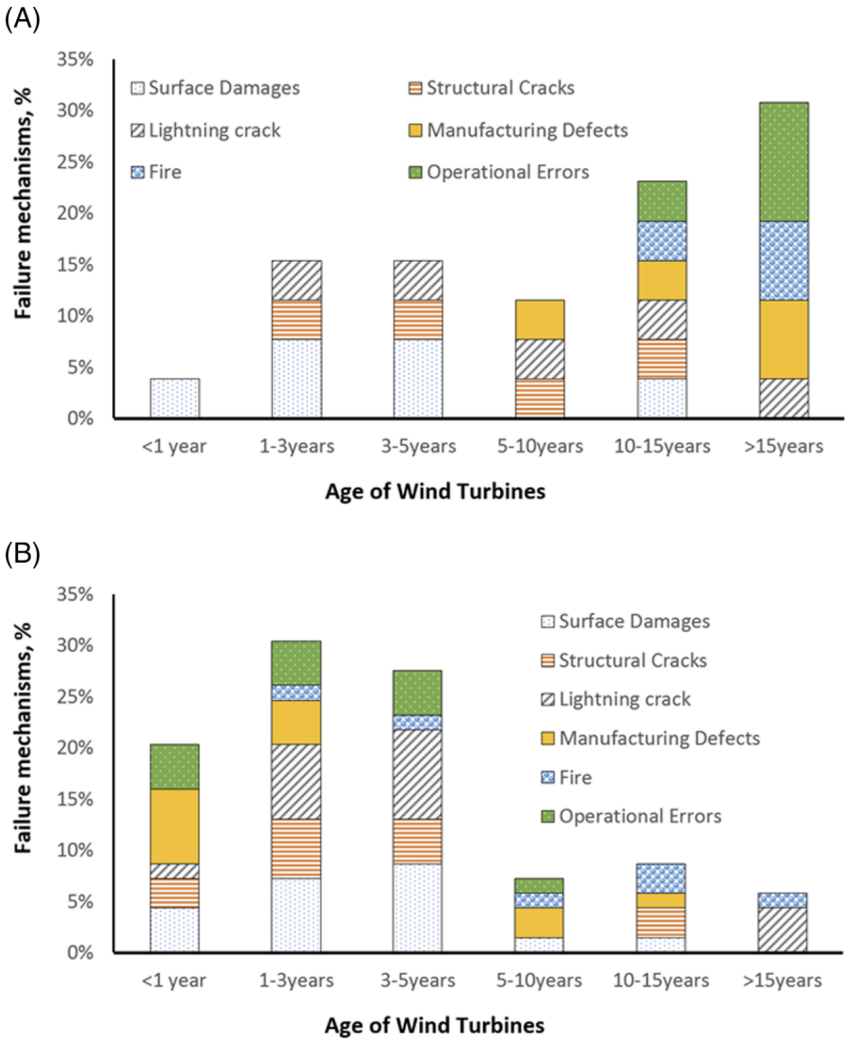

Figure 2.6: Figures 2.6a and 2.6b showing the reasons blade failure rates in Europe and India against the age of the respective wind turbine, respectively [5].

2.4.3 Defects

During manufacture, defects within components are formed. For homogeneous materials, defects in the form of voids, inclusions, cracks and surface deformations appear and affect their material properties. When you consider composite or multilayered structures, the number of possible defects increases and characterising the shape, size and types of these defects becomes more challenging, as does their effect on the mechanical properties of a given structure.

In composite structures, defects appear numerous different forms, including but not limited to porosity, delamination, inclusions, fibre misalignment, fibre waviness, resin-rich areas, uncured resin, resin-starved areas, poorly wetted fibres, broken fibres, etc. [42–45].

In coatings and coated composites defects can take the form of debonding, porosity, surface waviness, uncured resin, sagging, fish eyes, cracking, blistering, wrinkles [43, 46, 47]

These defects often lead to the premature failure of structures and in particular for wind energy can be very costly if not caught early [5]. What's more in the above surveys although the types of failures are listed, there is no detailed root cause analysis and it's likely that in most cases the cause of premature failure, if not environmental or operator driven is the result of manufacturing defects.

There are in fact detailed root cause analyses of failed blades, however they are often only limited to individual failures and would not provide a representative understanding of how and why wind turbines fail during their lifetime [48].

Defects are commonly found during manufacture but also during repair even with experienced technicians carrying out repair work [49]. Therefore there is a need to ensure damage tolerance is incorporated into the design.

2.4.4 Maintenance and Repairs

As mentioned above, defects and damages are commonly found during the inspection of wind turbine blades. The design and manufacture of wind turbine blades are typically proprietary and so access to legacy or equivalent material is not usually possible. Further to this point, the wind turbine repair sector isn't well regulated, meaning results vary significantly [49, 50].

The costs of repair are comprised of transport, equipment, material and labour. If unscheduled, then this should also include the cost of downtime for the required period [49]. Repair work is also subject to the availability of repair teams and materials, which may limit selection. However, as Mishnaevsky et al. note there is much room for improvement.

Many damage types are defect-driven and so optimising application is key to ensuring longevity [43, 49].

2.5 Rain Erosion

Currently in the wind turbine sector, Leading-edge Erosion (LEE) of wind turbine blades is considered one of the most pressing issues. Investigations showing potential losses ranging from 2% up to approximately 25% in annual energy output [51, 52], building the case for tackling this problem. To understand this issue in more depth, industry and academia have sought to investigate the rain erosion phenomenon using laboratory testing methods. Testing the rain erosion resistance of coatings and materials through various methods has concluded that the use of a whirling arm type rig is optimal, with other methods producing incomparable results or are simply too expensive [11, 53].

Rain erosion is the individual or repeated impact of rain droplets onto a material, composite or multilayered material system. During this process, damage either happens immediately or after a period of time. The rain erosion process, for most materials and provided that the impacts don't cause immediate failure, can be divided into three sections. Firstly, there is an incubation period during which there is no apparent damage. Secondly, Initial damage then becomes measurable and progresses linearly with time in a steady state manner. Finally, there is the final erosion state, where the processes become more complex. See figure 2.7 Most research has typically focused on the incubation period and understanding damage initiation [11, 35].

2.5.1 The Impact Event

When a droplet impacts the surface, the initial contact area of the droplet is compressed, generating a shockwave in the droplet 2.8. As the impact event unfolds, the contact edge expands faster than the shockwave. Eventually, the contact edge slows and the

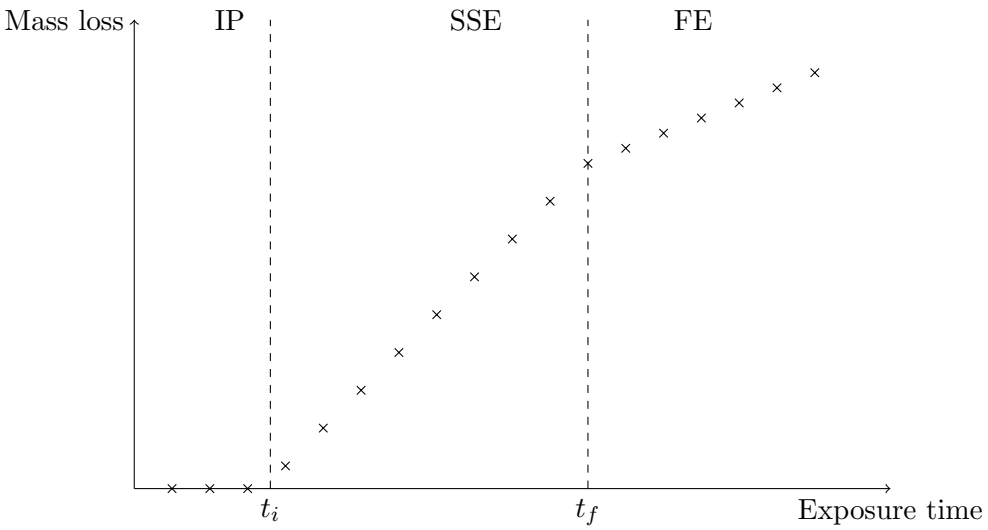

Figure 2.7: Data points from a standard rain erosion test comparing mass loss with exposure time. IP, SSE and FE meaning incubation period, steady-state erosion and final erosion, respectively

shockwave overtakes it. At this point, lateral jetting occurs (2-5 times the initial impact velocity) [6].

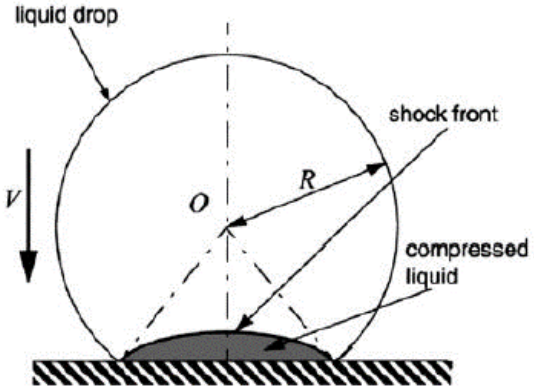

Figure 2.8: The impact scenario of a droplet of radius R, impacting the surface of a material at velocity v (taken from [6]).

The initial impact generates a compression wave followed by a shear and then a Rayleigh wave inside the material. The Rayleigh wave contains most of the energy (2/3), followed by the shear wave and then the compression wave [54]. The Rayleigh wave is therefore considered to be an important damage source [7, 55].

Damage, therefore, occurs from one of the following four sources:

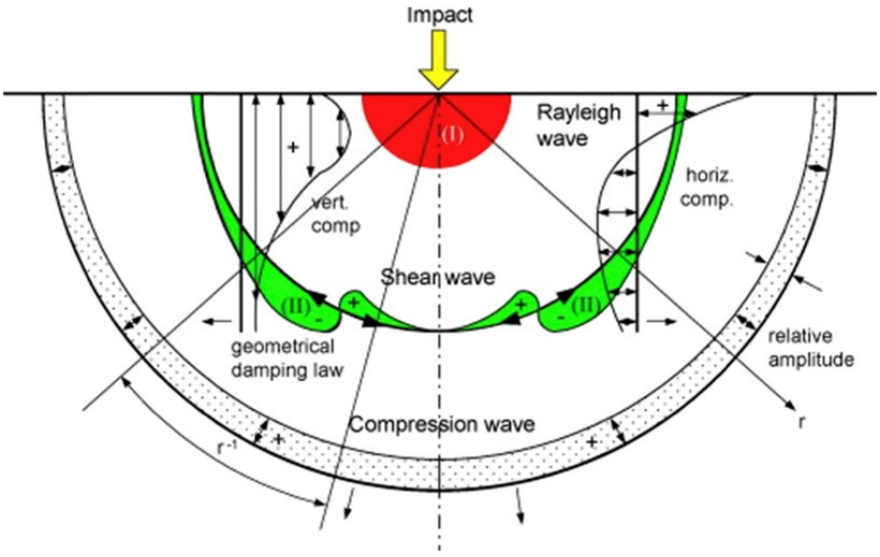

Figure 2.9: Acoustic waves generated inside the material during an impact from a droplet (taken from [7]).

- Initial contact pressure, which can be close to or higher than the tensile strength of the material [56]
- Lateral jetting which can interact with uneven and irregular parts of the surface [57, 58]
- Rayleigh waves are generated in the material surface which can cause large strains and strain rates which lead to fatigue and therefore microcracks and tears [7]
- Stress wave reflections in the material, as a result of differences in acoustic impedance arising from defects or interfaces [11]

Wind turbines have an expected life of 20-25 years, therefore considering the risk that rain erosion poses to wind turbine blades and the likelihood of its occurrence, investigating how and why it happens is of paramount importance. As is developing tools and strategies to mitigate this hazard.

2.6 Energy Efficiency

As rain erosion progresses down the length of the blade from tip to root, the roughness of the leading-edge of the blade increases and the geometry of the wind turbine blade changes, modifying its aerodynamic performance. The modification to the surface geometry can lead to the generation of eddies and an early transition from laminar to turbulent flow, which in turn can lead to a thickening of the boundary layer making the boundary layer more susceptible to early separation, i.e stall. Stall then leads to a reduction in the lift produced. These geometry changes also increase drag forces acting on the blade. These changes to the stability of the boundary layer reduces the range of angles of attack available to the wind turbine for generating lift without stalling. As erosion progresses, the geometry of the damage expands, in terms of surface area and depth. As this occurs, the performance of the wind turbine progressively decreases, due to changes in the lift and drag forces acting on the wind turbine blade and modify the control strategy of the turbine reducing power output for a given set of flow conditions, changing the loading patterns and generating acoustic noise. Moreover, most literature involving the assessment of the effect of leading-edge erosion has focused on 2D CFD, which is not able to capture 3D effects. Additionally, there is a lack of research involving higher Reynolds numbers, such as those experienced by larger, modern winder turbines [59–64].

2.7 Erosion Mitigation Strategies

There are 4 possible mitigation strategies for leading-edge erosion [60]:

1. Control - Reducing turbine speed during specific conditions (Such as Erosion Safe Mode, ESM [65, 66])
2. Material Selection - Materials with sufficient erosion strength [11, 67, 68]
3. Droplet Breakup - Methods that breakup droplets before impact [11, 67]
4. Droplet Diversion - Methods that move droplets away from the surface [11, 69, 70]

In general, the most commonly implemented method has been the use of erosion-resistant materials. This has been the focus for reducing the impact of rain erosion in helicopter blades, missile and radar radomes, planes and steam turbines with a reasonable amount of success. However, due to the operational requirements of wind turbine blades, new challenges have arisen. The complex operational environment, challenges with repair and maintenance and the life expectancy of 20-30 years mean that erosion-proof materials have been harder to develop. Additionally, the avoidance of conductive materials due to their lightning risk and the required flexibility due to the blade deflection mean metals and ceramics are unfavourable candidates for the task [11, 67, 68].

ESM, The idea of modifying the control strategy of wind turbines, has been recently popularised by Danish Technical University. However, this relies on erosion being caused by a small number of relatively short duration, high rain intensity events. Whilst these events are likely damaging, data on their relative frequency is unknown. Furthermore, more research is required to understand whether a small number of events are the drivers behind the rain erosion process [65, 66].

Droplet breakup is unlikely to be a credible option to mitigate rain erosion, as this would likely require modification to the aerodynamic properties of the wind turbine or the generation of a shockwave. As wind turbines operate well below the acoustic velocity of air and energy capture is desirable, neither is a favourable approach [11, 67].

Although naturally, very small droplets and ice particles are naturally diverted from the leading-edge of a moving aerofoil, to the author's knowledge there are no practical methods to cause this diversion that wouldn't influence or impede the operation of the wind turbine [11, 69, 70].

2.8 Rain Erosion Testing Standards

Four current standards specifically relate to rain erosion on wind turbine blades:

- ASTM G73 - 10: Standard Test Method for Liquid Impingement Erosion Using Rotating Apparatus [71]

- DNVGL-RP-0171: Testing of rotor blade erosion protection systems [72]
- DNVGL-CP-0424: Coatings for protection of FRP structures with heavy rain erosion loads [73]
- DNVGL-RP-0573: Evaluation of erosion and delamination for leading edge protection systems of rotor blades [74]

ASTM G73 discusses liquid impingement erosion more generally and is not specifically dedicated to rain erosion on wind turbine blades, instead referring to all machines that experience it. Rain erosion damage progression differs in polymers than in typical elastic materials. There are several reasons for this which require additional characterisation and testing, including but not limited to temperature, moisture ingress, UV, chemical attack and viscoelasticity, which will be discussed later in chapter 3. This viscoelasticity specifically means that in practice damage evolution may not follow the same trends that elastic materials would. In the standard, it does suggest the recording of ambient, test chamber, liquid and target temperature, if considered appropriate, however in the case of polymers and elastomers, it should be a requirement due to their temperature sensitivities. Additionally, there is mention that the performance of elastomeric coatings can vary by 10-15% due from exposure to environmental conditions, however this is quite vague. Thus, they cannot be treated in the same way and require additional characterisation and test condition monitoring which is largely not covered. It contains 2 metrics for characterising the severity of the testing programme.

Firstly, the use of impingement, H_0, referring to the cumulative volume of water impinging upon the exposed surface per unit area Secondly, the use of specific impacts, N_0, which can either relate to the number of impacts that occur at any point on the exposed surface or in the case of distributed impacts, this is rationalised. The impacts are assumed to be uniformly distributed over the exposed surface and is equal:

$$N_0 = N_{tot} * A_{imp}/S_{tot} \tag{2.1}$$

Where N_{tot} is the total number of impacts the surface receives, A_{imp} is the area of influence for each impact and S_{tot} is the total exposed surface area. A_{imp} is defined as

the projected area of the impacting body.

DNVGL have developed a series of standards that relate specifically to offshore wind turbines and coated fibre-reinforced polymers. The standard set is more detailed and rigorous in their specification of parameters, testing methods and requirements for testing. They have made significant progress in outlining relevant parameters to the rain erosion process in the CP-0424 and RP-0171, tailoring the characterisation of the material and testing environment to polymers specifically. Additionally, the RP-0171 sought to standardise Rain Erosion Testing (RET) practise by providing minimum specifications for the test machine. The RP-0573 provided functional approaches for estimating the lifetime of Leading-Edge Protection (LEP) systems. Their lifetime estimation approach as stated in the RP-0573 builds on Springer's model, but instead of characterising the erosion strength of an LEP using bulk material properties, it instead uses RET data and acoustic properties to estimate erosion strength, which in practise simplifies the data acquisition process for characterisation.

As highlighted in the IEA Wind Task 46 report [75], the DNVGL standards supersede the ASTM standard, however the two differ in their measure of erosion. DNVGL favour the use of specific impacts and not impingement, likely as it is a more granular parameter and provides less detail than specific impacts. For instance, the use of impingement would equate one impact from a larger droplet to several smaller droplets. Currently, as will be discussed throughout this thesis, the influence of droplet diameter is not known. Additionally, a criticism of the earlier DNVGL-RP-0171 was that the term for specific impacts did not incorporate the rationalisation for area of influence as it had been within the ASTM-G73-10 [76]. However, this has been addressed by instead incorporated into the DNVGL-RP-0573 practise for the calculation of the erosion strength parameters.

Both standards use the commonly accepted performance metric 'incubation period for assessing leading edge erosion performance. Both testing standards recommend the use of calibration samples and calibration testing. ASTM highlight the challenges in identifying relevant material properties to rain erosion and also states that there are challenges in related results from different facilities, which can be overcome by assigning

severity factors to different RET facilities. This differs from the DNVGL series, which seeks to standardise the testing regime and practise instead.

2.9 Summary

Wind turbine blades contain many different components and are vastly complex structures. As they have to weather the environment, building in damage redundancies is key to their longevity. As has been shown, their cost effectiveness has allowed market penetration, however there is a drive to increase blade size and therefore tip speed which increases the likelihood of damage developing and propagating. Leading-edge erosion and lightning strikes are the most common damage types and can do significant damage. Defects are commonly found and increase the likelihood of premature failure. The challenge of in-field repair work mean that defects are even more likely, and even with an experienced technician in lab conditions can be common, acting as failure initiation sites. Repair work can mitigate the need for discarding whole blades and limit damage progression, however require further improvement. Leading-edge erosion has been introduced as a concept, providing a basis for the following chapters to build upon.

Chapter 3

Coating Property Characterisation

The following chapter is a modified version of that printed in the journal Renewable and Sustainable Energy Reviews in the article "On analytical tools for assessing the raindrop erosion of wind turbine blades" by K.Pugh, J.W.Nash, G.Reaburn and M.M. Stack [77], Namely the section Introduction and Materials Characterisation sections.

3.1 Introduction

The importance of this topic provides the necessity for clear, concise methods to characterise the materials and coatings prior to rain erosion testing. Rain erosion resistance is contingent on thorough documentation of material parameters. Poor documentation may also lead to incorrect or spurious conclusions by authors when trying to compare different studies.

The surface of a material and its characteristics are known to play a significant role in the damage evolution of wind turbine blade coatings and therefore, characterising the surface is key to understanding its influence on rain erosion performance. If this is fully understood it can prove extremely beneficial when predicting the lifetime of the blades in order to schedule maintenance, repair and replacement at the optimum time in order to maximise energy production and generate the most income.

Subsurface damage or defects are thought to be initiation points or enhance damage propagation in coating layers. Erosion damage can form below the surface prior to damage on the surface, as noted by industrial standards agency DNVGL [72]. This is an area that has received little attention from the wider scientific community and to the author's knowledge, no methods have been used in any published material to investigate this phenomenon. This chapter will aim to provide insights into the possible methods available to researchers and industry.

DNVGL highlight the lack of standardised methods to post-process samples and compare results [72]. Therefore, this chapter provides an overview of appropriate materials characterisation methods and surface analysis techniques for rain erosion coatings. By standardising the methods in which we analyse these features, researchers and industry can progress in tackling this complex issue.

3.2 Materials characterisation

The issue of rain erosion is a complex one. Most current work makes reference to the work by Springer, in his widely regarded "Erosion by Liquid Impact" [11]. Presented here is one of the few mathematical models that has gained wider acceptance, seeking to provide a relationship between the lifetime estimation of a material, (n), the material's strength, (S) and the pressure from a droplet impact, (P or σ^o). Although recent work from Eisenberg et al. [78] appears to show success in the application of this model to wind turbine blades in the field, the model itself has inherent flaws recognised by both Springer himself [11] and Adler in Treatise on Materials Science And Technologies Vol. 16 [79, 80], which will be discussed throughout this section. Another model presented by Slot et al. [7, 81], provides an alternative method for lifetime estimation, but as of yet is incomplete. In light of the associated limits and to begin the process of standardising characterisation regimes, the Springer model will be used here as a basis. Therefore, the initial failure is assumed to be due to material fatigue.

Rain erosion applies to many materials and material/coating combinations, with the area of interest here being wind turbines. Wind turbine blades materials are primarily

coated composites, but also composites and polymeric materials to a lesser extent. It is important understand that when considering coated materials, the model assumes that the coating fails before either the coating/substrate interface or the substrate itself. According to Springer [11], the model also has broad applicability to materials that follow ductile behaviour, with agreement for brittle materials too. Issues arise when applying the model to elastomers, as using traditional characterisation methods do not capture the material behaviour or response correctly under loading conditions. Therefore, a separate approach should be taken with these material types, either by adapting the model or the development of a new one. However, it should be highlighted that recent work from ORE Catapult do show that these viscoelastic polymers fail in an elastic and brittle and brittle manner depending on the impact conditions, thus highlighting the relevance of previous work on both elastic and brittle materials [75].

The Springer model equations are outlined below for reference (equations 3.1, 3.2, 3.3),

where n_{iC} is the number of impacts required to initiate damage at a specific location and is proportional to the ratio of the coating strength, S_{eC}, to the average stress, σ^o, at the point of impact at the surface; σ_U is the ultimate tensile strength of the coating; the term b is the slope of the Wolher curve, a term related to the knee in the fatigue curve, the ultimate tensile strength and the endurance limit of the coating; ν is the Poisson ratio of the coating; the terms k, ψ and γ are terms related to the stress wave reflections caused by acoustic impedance mismatches; ρ is the density; C is the acoustic velocity and V is the impact velocity. The subscripts S, C and L refer to substrate, coating and liquid respectively. The subscripts LC and SC refer to the liquid-coating and substrate-coating interfaces respectively. A thorough explanation of the model itself is beyond the scope of this chapter and so for further reading, the authors would recommend referring to the original text.

$$n_{iC} = 7 \times 10^{-6}(\frac{S_{eC}}{\sigma_o})^{5.7}) \tag{3.1}$$

$$S_{eC} = \frac{4\sigma_{uC}(b_C - 1)}{(1 - 2\nu_C)(1 + k|\psi_{SC}|)} \tag{3.2}$$

$$S_{eC} = \frac{\rho_L C_L V}{1 + \rho_L C_L / \rho_C C_C}[1 - \psi_{SC}\frac{1 + \psi_{LC}}{1 + \psi_{SC}}\frac{1 - \exp\gamma}{\gamma}] \tag{3.3}$$

Although equation 3.1 only provides a value for the incubation period, the basis for springer's model of mass loss rate of the steady state erosion stage is reliant on the same strength and pressure parameters. The equations stated here also apply to pure materials without coatings, with the equations modified slightly. Importantly, Springer assumes that the mass loss rate is still reliant on the same material parameters and so the results follow the same trends in material parameters.

As stated by Adler [80], there are four main damage modes associated with the material removal process. This is determined by the materials response to the droplet impact itself. As Adler states, although the interaction is complex it is likely that the dominant damage mode is through hydrostatic pressure, which would occur as a result of inconsistencies in the surface of the material/coating during the impact itself or during lateral jetting. This hypothesis on material removal is also supported by Field et al. [67]. Field at al. state that during the impact any water trapped inside a crack or pit would lead to a strong hydrodynamic effect increasing the level of damage.

Although the research by Field et al. focussed on brittle materials, their discussion on the process of surface damage exacerbation appears to have a broader implication. Another significant damage mode mentioned by Adler is the passage of stress waves throughout the surface and inside the material. If a surface stress wave is emitting from the impact location, it may pass through a crack. If it is of sufficient magnitude and duration, it will cause the stress intensity factor to reach its critical value, and so the crack will grow in length. This process is dependent on the material fracture toughness, the elastic wave velocity and the size distribution of the pre-existing surface flaws, as well as the water drops size and velocity. It would seem reasonable to attempt to apply the same condition to other material types with defects present on the surface, between coating layers and other subsurface defects. These two factors would suggest that the

mass removal process is governed by a different set of equations, which is beyond the scope of this chapter.

Equation 3.2 provides a value for the coating strength in terms of rain erosion resistance. As stated previously, the Springer model was developed for ductile materials, not elastomers, and so the use of terms as the ultimate tensile strength or endurance limit are not appropriate descriptors. At the present time, the authors do not have a replacement for this equation and instead just note the difficulties with applying the analysis to this problem. If materials such as brittle or ductile gelcoats, such as epoxy or polyester, are being investigated the equations should apply as intended.

The combination of materials and coatings with different acoustic velocities and densities (usually combined into the term acoustic impedance, Z) can have synergistic effects, with the coating potentially becoming an amplifier for the stress wave in magnitude [11, 82]. If the thickness of a coating is chosen incorrectly, it can lead to further problems in that it generates stress wave reflections, accelerating fatigue failure [11, 67, 83].

P is typically approximated using a modified form of the water hammer equation [7, 10, 11]. The acoustic velocity is dependent on the stiffness properties of a material, whose definition can be found in Springer [11]. A different equation is presented here for the variable (equation 3.3). This equation is an enhanced form of the modified water hammer equation and is used in order to account for stress wave reflections, if present. In the absence of reflections, for example in materials with no coatings, the equations simplify to equations 3.4, 3.5, 3.6.

$$n_i = 7x10^{-6}(\frac{S}{P})^{5.7} \tag{3.4}$$

$$S = \frac{4\sigma_{uS}(b_S - 1)}{(1 - 2\nu_S)} \tag{3.5}$$

$$P = \frac{\rho_L C_L V}{1 + \rho_L C_L / \rho_S C_S} \tag{3.6}$$

Equation 3.4 provides a reasonable approximation for most materials but begins to

diverge from this equation for materials with particularly low stiffness properties upon which it underestimates the impact pressure [11]. Elastomers such as polyurethane are an example of such materials and so the stiffness properties of a material or coating must be considered, as should their densities. It is important to note that the impact pressure cannot be accurately determined using this equation.

Whilst the model provides a good basis for rain erosion resistance, the influence of a number of parameters has not been mathematically deduced. These parameters include hardness, toughness, surface roughness, interfacial strength, with the addition of appropriate elastic and viscoelastic properties of polymeric and elastomeric coatings. Some of these materials also have a noted temperature sensitivity around their operational range, with thermal aging also having the potential to influence their behaviour [84–86]. Field et al. also discusses the possibility of frictional heating of the testing sample during rain erosion testing [67]. The studies discussed are conducted at much higher velocities than those concerned here, but still do show this to be a consideration. The application of the Springer model to a material and coating combination should either be linked to an appropriate temperature, with the respective material properties stated at that temperature or mathematical models of those material properties should be calculated and incorporated into the model.

To produce the model, Springer made several assumptions relating to material properties. The model is comprised of experimental results from studies that have insufficient data sets for the model itself. Springer therefore seeks to make assumptions for the values of several material properties, and as Adler [80] highlights, specifically the material property b, determined by the fatigue performance of the material. Springer simply assumes that b = 20 for all materials, except for magnesium and copper where b = 17.6. It is likely that Springer did not have values for b for the majority of the materials tested in their respective studies, as the values do not appear in literature, and that these studies did not conduct fatigue testing due to expense and complexity of testing for material fatigue. This insufficient documentation of material properties presents some difficulties in linking material parameters to performance [57, 81, 82, 87]. The requirement, therefore, for systematically documenting material properties that are

thought to influence rain erosion performance is vital. Currently, there are standardised documentation for testing of various properties of rain erosion coatings, although limited [73, 88]. These documents describe some minimum performance characteristics using standardised testing regimes that coatings should have. These documents define a number of tests some of which are listed in 3.1 and some of which have more applicable testing methods that are available.

Table 3.1: Outlining the preferred testing methods to obtain parameters thought/known to be relevant to rain erosion.

Preferred Test Name /Equipment	**Property**	**Test Standard**	**Source**
Pull Off Test	Adhesive/ Cohesive Strength	ISO 4624	[53, 73, 82, 87, 89]
Peel Test	Adhesive/ Cohesive Strength		[82]
	Coating Layer Thickness	ISO 2808-2007	[73]
Tensile Test (Non-Viscoelastic Materials)	Stiffness		[84, 86]
DMA (Viscoelastic Materials)	Storage Modulus		[84, 86]
	Loss Modulus		[84, 86]
	Glass Transition Temperature (s)		[84, 86]
Nanoindentation	Hardness		[8, 82]
Tensile Test	Ultimate Tensile Strength	ISO 527-3 (specimen type 2)	[53, 73, 84, 86]
	Failure Strain		[53, 73, 84, 86]
	Max Strain Rate		[73]
	Poisson's ratio		[73]
Tensile-Tensile Cyclic Loading	Fatigue Performance		[86]
TBD	Fracture Toughness		
	Density	BS EN ISO 1183-1:2012 (Method A)	
Optical Profilometer	Surface roughness		[90]

3.2.1 Coating adhesion strength

A key indicator of coating performance is its ability to adhere to the substrate material. The 'Pull Off' test is the most widely used standardised method to test for coating adhesion [57, 73, 82, 87, 89], with its ease of use and proven applicability makes it the preferred choice of method for many analyses. The typical target value for an LEP system is $>= 5MPa$. This type of test can help to identify likely failure modes of the coating [75].

The peel test is another method but is used to a lesser extent. It cannot be used for all material coatings, as the material must be flexible and so works better for tape-type coatings [75, 82]. There are reports of both the material flaking or delaminating in large pieces during rain erosion testing and also a concern of tape type coatings peeling away from the material, hence limiting their application.

Research has shown poor adhesion between the coating and its substrate are a common failure mode and lead to premature failure and should be avoided [57, 73, 75, 82, 87, 89].

3.2.2 Coating layer thickness

The coating layer thickness is significantly important too, with the performance inextricably linked to its performance. Defects such as "sagging" or coating delamination can be caused due to incorrect coating thicknesses [47]. Therefore, it is not only important to apply the correct coating layer thickness, but also as discussed above the thickness should be selected in order to optimise the performance of the coating itself [11, 83].

3.2.3 Acoustic Velocity

Springer defines the acoustic properties of the substrate and coating as of high importance, stating that a mismatch between the acoustic impedances can lead to stress wave reflections and instigate early failure. The acoustic velocity can be multiplied by the density of the material to calculate the acoustic impedance. There is broad consensus supporting Springer's theory that acoustics play an important role in the damage evo-

lution. To measure the acoustic velocity, a small test coupon of known thickness can be manufactured and easily tested either using a transmission or reflection technique [74, 75, 82, 91].

3.2.4 Stiffness, Storage Modulus and Loss Modulus

In order to produce approximations for the impact pressure and evaluate the strength of a coating and subsequent substrate material combination (equations 3.2 and 3.3), the acoustic impedance is necessary and can be calculated using the material's elastic modulus [11]. For materials with limited viscoelasticity, simple methods like tensile testing as outlined in Ref. [73] provide values for the elastic modulus. However, for strongly viscoelastic materials, stiffness properties are more complex and dependent on temperature, frequency and loading regime. Therefore, the storage modulus can be used [82]. The stiffness of viscoelastic materials can be described by three properties; the storage modulus, the amount of elastic energy stored by the material, the loss modulus, the amount of energy dissipated through heating and viscous losses, and the tan delta value, the ratio of loss modulus to storage modulus.

The importance of these parameters, with respect to their rain erosion performance has been investigated by O'Carroll et al. [8] using nanoindentation. Nanoindentation is the process of pressing a specifically designed tip into a material, whilst recording the depth of the indentation tip and the applied load. Care must be taken to ensure that defects are not present at the indentation site and that it is far enough away from a material interface or free edge, due to the influence this may have on the results. This indentation process provides information on how the material responds to deformation. Additionally, following the indentation, the site can be monitored to characterize the short and long-term recovery characteristics of the material. These investigations established a negative correlation between storage modulus and rain erosion performance but failed to do the same with loss modulus. This, therefore, contradicts the work of Heymann [6, 68, 92], in which increasing the stiffness of a material improved its rain erosion performance. However, this may be explained by the nature of the materials tested by Heymann and the materials tested by O'Carroll, Elastic vs. Viscoelastic and

the relative strength of the materials, which is discussed further in the next section 3.2.5. Impact rate and material recovery have also been noted to play a part in the erosion process, with RET tests containing multi-day gaps displaying different failure characteristics compared to tests without exposure gaps [75].

Nanoindentation typically only measures these stiffness properties at one frequency and temperature. As noted by O'Carroll et al., it may have been preferable to capture this information using Dynamic Mechanical Thermal Analysis (DMTA). DMTA can capture the dynamic material properties of a material over a wide range of temperatures and frequencies, including important material characteristics such as glass transition temperatures or ageing of the material. Temperature and strain rate are particularly important to how viscoelastic materials respond to loading and change the mechanical properties significantly [75]. As mentioned above, several coatings of interest have temperature sensitivities around their operational range. DMTA could therefore calculate these mechanical properties through a range of frequencies and temperatures [84, 86].

3.2.5 Hardness

Rain erosion testing studies on various materials have provided different conclusions regarding the relationship between rain erosion resistance and hardness. Different authors have claimed increasing hardness either improves or degrades rain erosion performance with conflicting evidence. In metals, Heymann presented evidence to suggest that rain erosion resistance improves with increasing hardness [68], conversely others such as O'Carroll et al. 3.1 presented evidence to suggest the opposite trend with respect to polymers [8, 57]. This is likely to be related, at least in part, to the way in which a material responds to an indentation test. One possible reason is explained by Shaw and DeSalvo [93]. They state that solids should be divided into two different classes when considering hardness, one for metals and one for glasses and polymers. This is based on their stiffness to uniaxial compression flow stress ratio. Metals typically have much higher stiffness to flow stress ratios than glasses and polymers. Hence, during indentation from a blunt indenter, glasses and polymers tend to distribute stresses in a more uniform manner over the indentation area, but metals typically produce Hertzian

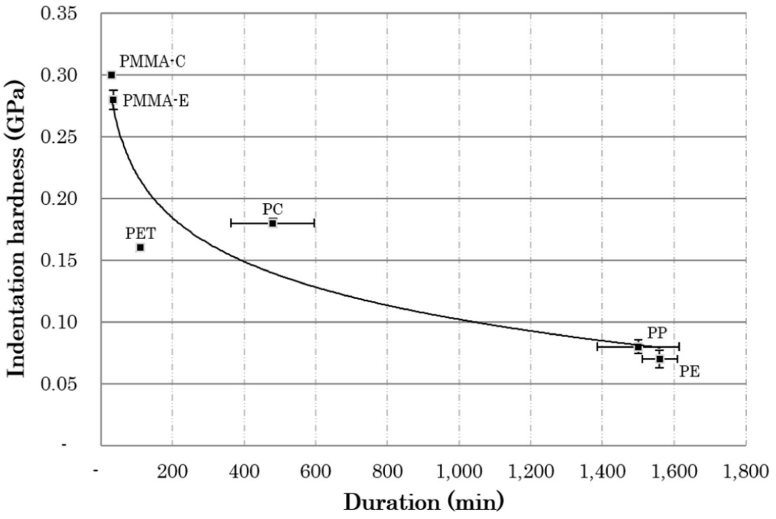

Figure 3.1: Hardness Vs. Duration of incubation period for various polymers tested in whirling arm type rig. Figure from O'Carroll et al. [8] with permission from Elsevier.

distributions. Indentation testing is also somewhat analogous to the impacts themselves, but at a slower rate and so it would be fair to assume a direct relationship. For high velocity impact erosion occurs at higher strain rates than at lower velocities and therefore conventional hardness measurements would be likely to not be applicable at such strain rates. One should note that indentation results are particularly dependent on the surface roughness, meaning that if performed on a rough surface anomalous results may be obtained.

The DIN EN 59 hardness test for coatings stated in the DNVGL standards documentation [73] for testing rain erosion protection coatings is designed for use with thicker coatings (0.5 mm). Coatings used on wind turbine blades are known to be thinner than this minimum thickness and thin films often display different properties to that of the bulk material as the close proximity to the interface can influence the result, so more appropriate testing regimes have been sought after [82]. Recent studies have shown the potential of nanoindentation testing, with favourable applicability to thin samples (0.5mm), like those used in the multi-layer LEP systems for wind turbine blades [8, 55, 82].

3.2.6 Tensile Properties

The Tensile properties as stated above can be found using the standard tensile test outlined in ISO 527-3, using specimen type 2 for flexible materials. As the strength model outlined by Springer [11] is intended for ductile materials, it is important to investigate other properties aside from those outlined in the model. Elastomeric materials typically fail through fatigue, when exceeding a strain rate higher than the material can withstand or an elongation higher than the material can accept [7, 57, 75, 84, 86]. More appropriate parameters may therefore be used to describe the material strength, S. Tensile-tensile cyclic loading testing can also be used to produce the Wohler curve as is necessary for the Springer model [86].

3.2.7 Damage Resistance

For materials to be resistant to rain erosion, their ability to resist damage initiation and limit crack propagation should be important factors. The importance of fracture toughness as outlined in the literature reviews of Keegan et al. [10] and Gohardani [54] is the relation of fracture toughness to the damage evolution in the rain erosion phenomenon. Springer [11] speculated that fracture toughness would influence rain erosion performance, which has been supported by Busch et al. [94] with their investigation into the notch sensitivity of various polymers and rain erosion. Previous work by Evans et al., sought to relate the erosion of brittle materials from solid projectiles to their fracture toughness with good agreement (equation 3.7) [9]. Keegan [10] used this equation to show the significant effect this could have on epoxy coatings with different fracture toughness values (Figure 3.2). Zhang et al. [57] investigated the impact resistance of various coatings and their rain erosion performance; however, the experimental work in this regard was limited and a fracture toughness value was not produced. The results showed that the coating with a poor rain erosion performance also failed during the impact test by detaching from the surface, compared with the two samples that performed significantly better in both. Another damage resistance characteristic investigated by Zhang et al. was abrasion resistance. Zhang et al. conducted Taber abrasion resistance testing with coatings lasting longer in the abrasion rig, also lasting longer in

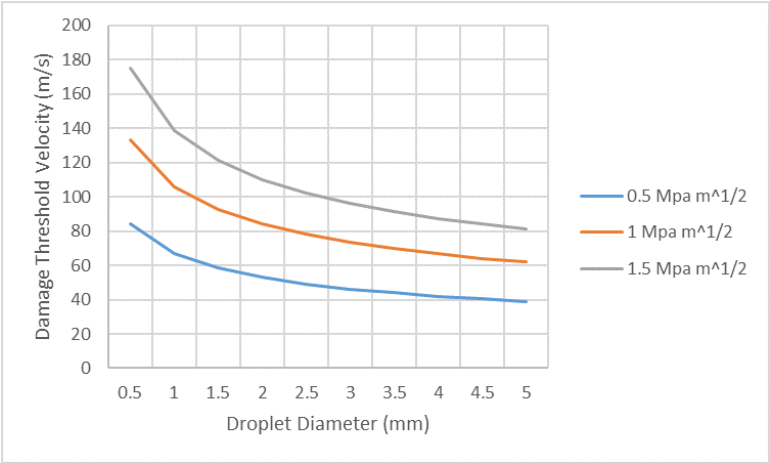

Figure 3.2: Damage Threshold Velocity (V_{DT} Vs. droplet diameter using equation 3.7 from Ref. [9] for epoxy coatings with different fracture toughness values. Figure adapted from [10]. C_R, = 942m/s, ρ_w, = $1000kg/m^3$, C_w, = 1490 m/s.

the whirling arm test rig. This indicates that the abrasion and erosion processes may be governed by at least some of the same materials characteristics.

$$V_{DT} \approx 1.41(\frac{{K_{Ic}}^2 C_R}{\rho_w^2 c_w^2 d_w})^{1/3} \tag{3.7}$$

where V_{DT} is the damage threshold velocity, above which the material damage will occur. The definition of this damage is not stated. K_{IC} is the fracture toughness, C_R is the Rayleigh wave velocity, ρ_w is the density of water, c_w is the speed of sound in water and d_w is the droplet diameter.

As noted by Field [67], most rain erosion literature appears to suggest that, provided there are enough impacts, a material can fail at any velocity. This would infer that a damage threshold velocity does not exist for any material per se as there are many other parameters which affect the erosion process. Hence, if one was to assume the rain erosion process is a fatigue process, it may instead be likely that there is an effective damage threshold velocity where the number of impacts to initiate a failure exceeds the life of a wind turbine. Therefore, the use of such a term is justified. The link between damage resistance characteristics and rain erosion is not clear with the limited data available, and so the selection of an appropriate toughness parameter is not possible. Furthermore, an in-depth discussion and selection of appropriate fracture toughness

testing methods and model is complex and is far beyond the scope of this chapter. Instead, presented here are some thoughts on how one should approach the selection of an appropriate test configuration. During rain erosion, a material or coating is continuously degraded. Damage can be initiated through direct failure, surface fatigue or through the presence of a defect. In the majority of situations, failure develops from the exposed side of the coating or material. Fracture toughness analysis should therefore use single edge notch tensile (SENT) testing [75, 84]. Currently the most appropriate methodology reverts to the use of bulk materials testing regimes. Rain erosion in itself is not a steady state or quasi-static situation; it involves repeated impulses from droplet impacts. Therefore, a cyclic or transient testing format would be most applicable.

3.3 Surface quality

Surface quality and surface roughness influence the rain erosion process [58]. Experiments using spray nozzles have shown that the incubation period decreases with increasing relative roughness and groove depth. Experimental jet impingement results from Zhang [95] have shown microcracks linking preexisting surface pin holes following exposure to rain erosion testing. As has been well documented, lateral jetting interacts with surface discontinuities resulting in damage development. It is likely that surface roughness plays a significant role in damage development post-incubation period too. Interestingly, O'Carroll's [91] experiments showed that material mass loss rate from a sample subjected to RET experiments is related to the rate at which it is roughened. This evidence presents the case for surface roughness as an important characteristic, not only influencing the onset of erosion but also monitoring the process itself. Surface roughness therefore may be one metric for monitoring the erosion process.

Not only is Surface degradation important in this aspect, but it also strongly influences the performance of wind turbine blades. Even newly manufactured blades may have surfaces rough enough leading to lower Annual Energy Production (AEP) than designed for [96]. Research has indicated that surface roughness is the range of 0-1mm

in depth can begin to influence the AEP of a wind turbine blade. AEP loss is generally considered to be in the single digits, however authors have reported values as high as 25% [97]. According to BVG Associates [98] one single wind turbine at Whitelee wind farm (The UK's largest onshore wind farm) each turbine (of the 215 turbine fleet) produces 11.5MWh, per day which is enough energy for $\sim$ 1,100 homes. If we take severe erosion to be 5% of this total works out to be 55 homes or 0.575MWh per day. And we then take the strike price to be £83/MWh (estimated in 2011, 2 years after Whitelee had been commissioned and so likely lower than agreed) [99], that would equate to a loss per turbine of £47.7 per day. For all 215 turbines this would equate to £10,300 per day or £3.7 million per year.

Because of these two aspects, characterising the surface roughness is particularly important. The surface of a wind turbine blade materials can be characterised using a microscope, Scanning Electron Microscope (SEM), a contact profilometer (stylus) or an optical profilometer (for example using a confocal laser) [90, 100–108]. Each method will give you slightly different information, SEM and optical microscopy will give you mechanistic information, whereas a profilometer will characterise the surface and allow the estimation of surface roughness. Moreover, the use of an SEM can be combined with energy dispersive X-ray spectroscopy to provide surface chemistry information. Unfortunately though, when using and SEM, samples typically need to be gold coated which limits the techniques usefulness.

3.4 Conclusion

Understanding the rain erosion process on wind turbine blade materials is critical in maintaining AEP and mitigating potential structural issues that may entail. The correct testing and characterisation of materials and aspects that relate to rain erosion are paramount for developing accurate material models. Standardising these methods is therefore necessary. In this chapter, the main known aspects that influence the rain erosion process have been discussed and the preferred methods of characterisation have been established.

Chapter 4

Non-Destructive Testing and Subsurface Defects Characterisation

Part of the following chapter is a modified version of that printed in the journal Renewable and Sustainable Energy Reviews in the article "On analytical tools for assessing the raindrop erosion of wind turbine blades" by K.Pugh, J.W.Nash, G.Reaburn and M.M. Stack [77], Namely the section discussing subsurface analysis in that paper forms part of the Introduction and Non-Destructive Testing Methods sections outlined in this chapter.

4.1 Introduction

When considering rain erosion, comparatively little attention has been given to the presence of subsurface features or damage initiation inside the coating layers. The presence of defects in composites, such as voids or porosity, has been well documented [89, 109–111]. When coatings and multi-layer coating systems are then introduced into blade manufacture, this presents further possible sites for defects to exist [47]. Given the size of wind turbine blades, manufacturing structures such as these without the

presence of defects is not possible. When also considering the cost of discarding blades with defects or coating defects, especially as coatings are non-structural, subsurface defects are likely to be fairly common blades.

During the rain erosion testing of samples with good quality, smooth surfaces have generated inconsistent results, one possible reason for this is the presence of subsurface defects [35, 53, 56, 112–116]. Two reasons why defects are of concern are, firstly, their effect on material/coating performance and secondly, their ability to cause stress wave reflections. The defect size of interest, that is likely to lead to interfacial failure includes those that are of comparable size to the coating layer thickness and larger [46]. With respect to stress wave reflections, any defect, whereby there is air or a material inclusion with significant differences in acoustic properties inside the protective coating will cause stress wave reflections upon impact from a droplet. Reflections lead to early material fatigue and therefore the detection of defective coatings could prove useful for preventing premature failure. The defect size of interest is dependent on the wavelength of stress waves emitted during impact. Acoustic waves only interact with objects of a similar size to their wavelength and larger. More specifically in ultrasound (US) Non-Destructive Testing (NDT), defects should be at least about half of the wavelength of the frequency used [117]. Although it is currently not possible to measure the wavelength of the waves emitted through the coating during droplet impacts, the time period of the waves generated will relate to the impact velocity. Higher velocity impacts should cause higher coating particle velocity during impact, leading to the generation of higher frequency waves inside the material. This would lead to smaller wavelengths and so will interact with smaller defects. The penetration of acoustic waves reduces with increased frequency. Therefore, smaller defects will likely only influence damage propagation caused by reflections if they are close to the surface, but as distance increases only larger defects will likely be of importance.

Currently this topic is yet to be properly investigated, so the true influence is unknown. The ability of different methods to detect various defect types will be discussed,

with comments on the considerations for designing a test setup and some other considerations will be addressed. A coated composite panel will then be inspected and the results discussed. The aim is to conduct a qualitative study into possible detection methods for detecting defects within coated composite samples. Applicable methods fall into four main categories; ultrasound, radiology, microwave NDT and thermography. X-ray imaging will be discussed, however it will not be used for inspection.

4.2 Non-Destructive Testing Methods

4.2.1 Ultrasound

US is one of the most common NDT methods, with its application widespread. It works on the basis of generating mechanical vibrations within a material, typically propagated in compressive or shear waveform through the material. When these waves are introduced to interfaces between materials of differing acoustic impedances, liquids or gases, they are reflected back, and the signal is received and processed. There are two possible configurations; the first is a combined transmitter and receiver probe, called transceiver and the second is a separate transmitter and receiver probe. The data is typically generated into B- and C-scan forms, which give you cross-sectional views of the specimen and plan views, respectively. With modern developments of phased array probes, robotic scanning arms or Gantry systems and computers 3D scans of samples can be generated. Due to inherent limitations with the near-field effect in contact probes, they cannot be used for thin samples like those used in rain erosion testing. It could be possible to use an immersion probe, which would require submerging the whole or part of uneroded and eroded components into water. Any investigator should consider whether this is feasible to do and whether or not submerging components inside water for periods of time may affect the material properties through absorption. An alternative method would be to use a laser US generation method. This method has been shown to work and achieve reasonable results in carbon fibre composites, but no such studies investigating glass fibre composites were found by the authors [118, 119]. This method would enable eroded specimens to be analysed without immersion inside

a tank, but importantly the laser impulse on the surface could affect the material properties of any particular temperature sensitive materials, such as those discussed previously. To achieve a high resolution, it will be necessary to use high frequency ultrasound. It is likely that a scanning rig would need to be set up to automate the inspection of the specimens and produce a 3D model of the subsurface. The exact form of data that will be collected will still need to be determined. Both pulse echo and time of flight diffraction have their individual merits and it appears possible to collect both and use them in a complimentary fashion. The frequency selected will be dependent on the materials tested (See Figure 4.1). The main benefit of using ultrasound would be that the price would be significantly less than X-ray [117, 120]. One of the main concerns surrounding Ultrasound and its use in testing composite components is due to the high attenuation, caused by scattering from the fibres [20]. It can also be difficult distinguishing between the initial impulse and reflections caused by defects in thin samples [118].

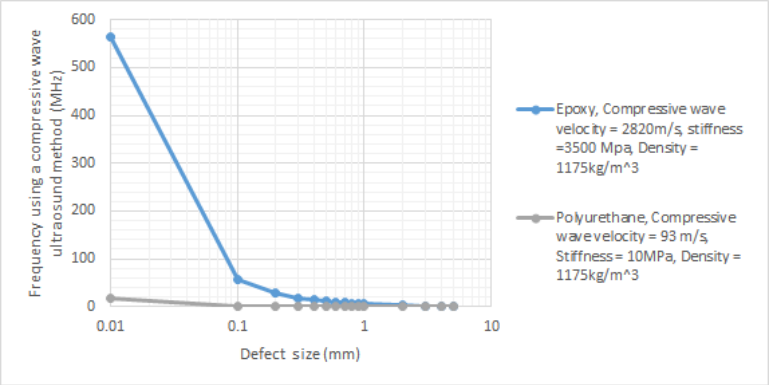

Figure 4.1: Displayed here is a graph showing defect size vs. approximate frequency required to detect it. Materials data was sourced from Slot et al. [7]. Wave speed was calculated using the equation provided by Springer [11]. Frequency was calculated using the standard wave equation $C = \lambda_w f$, where C is the speed of sound, f is the frequency and λ is the wavelength.

4.2.2 Radiology

Radiographic methods are desirable with their significantly higher resolving power, they can provide a much higher level of detail (individual fibres) then other techniques.

There are a few different methods for radiology: gamma radiology, x-ray radiology and neutron radiology (although this is different in operational principle). Gamma radiology and x-ray radiology follow the same principles, but their difference is the source of photon energy and how it is generated. They operate on the principle of irradiating a sample, with different materials and defects having different absorption properties. The transmitted radiation is then detected, more commonly these days, using a detector. The result is a 2D image of the specimen and so the orientation of the component can be key in detecting defects. The absorption of a material is dependent on the density of the specimen and its thickness [120, 121]. This presents a problem for polymeric materials, due to their low density, which gives a poor contrast [20]. With the development of computers, computed tomography has become available allowing a series of 2D X-ray images to be compiled into 3D scans which can help to reduce problems with orienting the specimen properly. Although this is desirable in most cases, X-ray and gamma-ray imaging become very costly and x-ray imaging is also a slow process. Typically, with this in mind, its ability to detect very fine defects such as pores, voids or cracks can make it more favourable compared with other NDT methods. The possibility of using X-ray opaque coatings could provide a possibility for investigating the effect of defects [20, 110, 120, 121].

4.2.3 Microwave Imaging

Microwave imaging relies on passing microwaves through a specimen using a transducer and receiving the signal either in the sample probe or using a separate probe. Microwaves are reflected at interfaces between materials with different dielectric properties. It therefore has significant potential in the testing for defects in polymer coated composites. It has advantages over traditional inspection techniques such as x-ray, being that it is significantly cheaper and safer, and Ultrasound, in that it can detect stacked defects within samples. It is well suited to the testing of high porosity composites (2%) and less attenuation occurs whilst scanning GFRP composites, which typically makes Ultrasound methods challenging. Currently, defects of approximately 1.5 mm in diameter and a thickness of 0.5 mm can be detected with reasonable visi-

bility. The technology is relatively immature, largely being developed at the National Physics Laboratory. The main application is the investigation of butt welds in HDPE pipes and as well as some composite components [122–124]. It should be noted that microwave NDT cannot be used to image carbon fibre or graphite composites, due to the carbon fibre's high conductivity which attenuates most of the microwave signal. Air-gaps of 0.25 mm are also possible to image (ideally larger at 0.4 mm), which essentially constitute delamination. To mimic delamination, laboratory testing of thin slithers of Teflon sandwiched between rubber has been tested with good levels of accuracy (see Table 4.1). Disbonds of 0.03 mm can be imaged. Microwave NDT can also provide information on the state of cure as well as moisture ingress [20].

Table 4.1: Thin sandwich structures of Teflon and rubber have been imaged, alternating in material to mimic delamination. The layers of Teflon were estimated using microwave imaging techniques respectively. Adapted from [20].

Layer	Relative Complex Permittivity	Thickness (mm)	Estimated Thickness (mm)
Rubber	4.80-e0.17	3.175	
Teflon	2.00-j6E-4	0.381	0.385
Rubber	5.31-e0.22	6.35	
Teflon	2.00-j6E-4	0.508	0.518
Rubber	4.80-e0.17	3.175	

4.2.4 Thermography

There are two main types of active thermography; optical thermography, thermal energy is transmitted to the specimen from an external heat source or vibrothermography (VT), where the test specimen is subjected to mechanical vibrations. Optical thermography uses a device to apply heat and a thermal sensor to image the specimen. Infrared radiation excites the surface and then penetrates the specimen. As thermal energy penetrates the specimen, it excites various parts differently, thermal conductivity changes lead to thermal wave reflections which are received by the sensor. VT applies heating differently by vibrating the surface of a specimen which causes internal features to heat up.

Infrared (IR) thermography has seen application in the wind turbine sector for some time now, although mainly during manufacture and assembly. Some studies have

looked at detecting defects inside coated composites with success, however the size resolution of which is not reported [113, 116]. Adhesive bonds in particular can be inspected and when defects are found, it is possible to repair them prior to service, saving the structure, time and money in the longer term. The primary benefit of thermography is the ability to detect defects on larger sections quickly and efficiently, with the potential for in situ application. The main type of thermography that will be considered here is transient pulse thermography (PT). PT in particular is sensitive to a number of characteristics that can make inspection difficult; surface reflections, surface roughness, optical arrangement, quality of light source, etc. Data acquisition is complex too and typically requires extensive analysis. VT provides interesting possibilities, as this can be coupled with ultrasound or with PT, however these are beyond the scope here [125].

4.2.5 Summary

Whilst there has been some research in using X-ray CT imaging to characterise and quantify defects in coatings, more cost-effective, versatile and easy-to-use methods are necessary to understand the prevalence of defects in real wind turbine blades. In light of this, the non-destructive testing of coated composite panels with defects inside was undertaken, providing a comparative analysis of various methods available. This study will therefore focus on the use of US, Thermography and microwave NDT and therefore, X-ray CT will not be used here.

More specifically, the focus here was the presence of voids. Other defects present in the coated composite panel tested will also be discussed. The aim of the following study was to find an effective, low cost and easy-to-use method that would allow defect detection either; inside the lab, to find more defect tolerant materials; for blades to be tested after manufacture, to find defects early and repair them before the blades left the factory or for repair work carried out in the field to be quality controlled and problems to be picked up early.

4.3 Methodology

A composite panel was manufactured from biaxial weave glass fibre and Greenpoxy resin. The resin was mixed with a mass ratio of 100:27 (resin: hardener). 8 sheets of glass fibre were used for this panel and upon cure a total thickness of 2mm was achieved. A cork dam was placed around the edge of the molding area, providing the resin with a dam. This cork dam also allowed each sheet of glass fibre and the cowling plate to be located correctly. The mold was then painted with release agent. Following this, the mold was first painted with resin. The resin was spread using an applicator tool. This was then followed by laying a sheet of glass fibre and a roller was used to ensure the resin impregnated the sheet. These three steps were repeated until all 8 sheets were placed into the mold and impregnated. The composite was then covered with release film, followed by the cowling plate. Bleeder fabric was placed on top and the whole mold was placed inside a vacuum bag, sealed with tacky tape. The cowling plate was then weighted down with 4x1kg weights and The vacuum pump was then turned on. The composite panel was then left to cure for 24 hrs.

The composite panel was then polished with 120-grit sandpaper, providing a mechanical key for the subsequent coating application. TopClear, a transparent EP/PU blend, was selected as the coating for the composite panel, making defect visualisation and quantification possible using an optical microscope. Resin and hardener were then mixed with a mass ratio of 3:2. Thinner was not added, as it would have reduced the viscosity of the coating, making it easier for air bubbles to escape. The resin was then vigorously stirred introducing air into the mixture and poured in a thick $\sim 0.5mm$ layer onto the composite panel (Figure 4.2). It was then cured inside a fume cupboard for 4 days. The panel was then inspected to confirm the presence of defects using a microscope and after, sent to the National Physics Laboratory (NPL).

A 100mm x 100mm area of the composite panel was selected. The specification for each system used is outlined below:

- Sonix UHR2000 Scanning Acoustic Microscope (SAM) with a 15MHz focussed

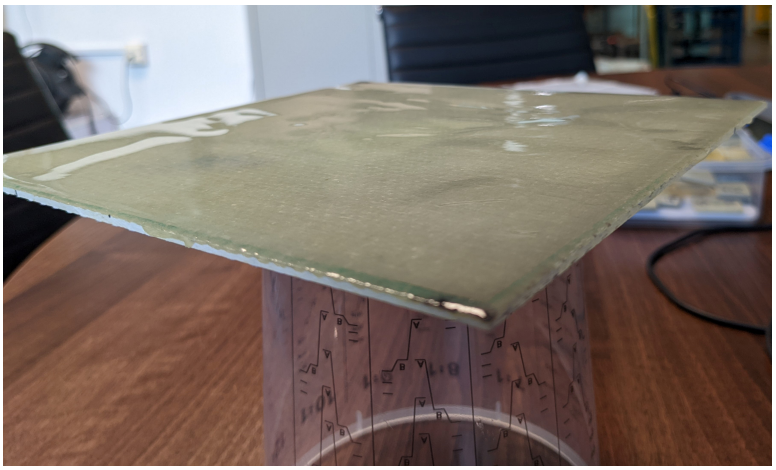

Figure 4.2: Cured GFRP panel coated with TopClear.

probe. 100 µm spatial sampling intervals.

- Thermal Wave Imaging ThermoScope flash thermography system, with a 3-5 µm MWIR. 320 x 256 infrared pixel camera.

- Evisive microwave scanning system, with a 24GHz probe. 1 mm spatial sampling intervals.

After a visual inspection of the results from each NTD method investigated, it was possible to extract information on void size, to investigate the spatial resolution of the SAM, however it was not possible to obtain depth resolution. The edges of the scans top and left-hand sides were removed to remove the free surfaces of the sample. Canny edge detection was then applied to the ultrasound C-scans of the coating surface and subsurface to extract the voids from the coating [126]. As is noted by other authors [116, 126, 127] and will be discussed later 6.9.3.3, Canny edge detection is a widely used algorithm for robustly detecting the edges of objects in images in the presence of noise. Any coating defects detected in the surface were also subsequently subtracted from the subsurface result. This was not possible for the composite surface due to the complexity of its topography.

4.4 Results

4.4.1 Microscope

As discussed above, the panel was initially inspected to confirm the presence of voids inside the coating at the University of Strathclyde using an optical microscope (Figure 4.3a). After the panel was received by the NPL, the panel was subsequently inspected to look for defects in the selected inspection region (Figure 4.3b).

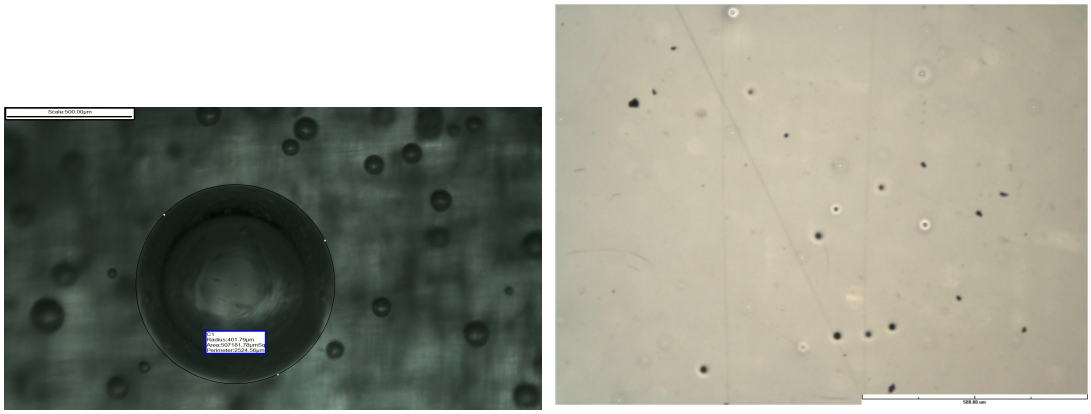

(a) (b)

Figure 4.3: Figures 4.3a and 4.3b show images taken using optical microscopes at the university and NPL. Figure 4.3a shows one of the larger subsurface voids observed inside the coating, with a radius of approx 0.4mm.

During the microscope inspection, Surface and subsurface voids ranged between 0.01-0.5mm in approximate diameter, with the majority of defects smaller than 0.1mm.

4.4.2 Ultrasound

4.4.2.1 Coating thickness

US provided results for the coating layer thickness. More specifically, if the acoustic velocity is known, accurate measurements of this can be taken. From the scans, sharp changes in coating layer thickness were clearly visible (Figure 4.4b). One can see peaks and troughs in the coating using the colour map (Figure 4.4a), with bluer areas showing thinner areas of coating and red areas showing thicker areas.

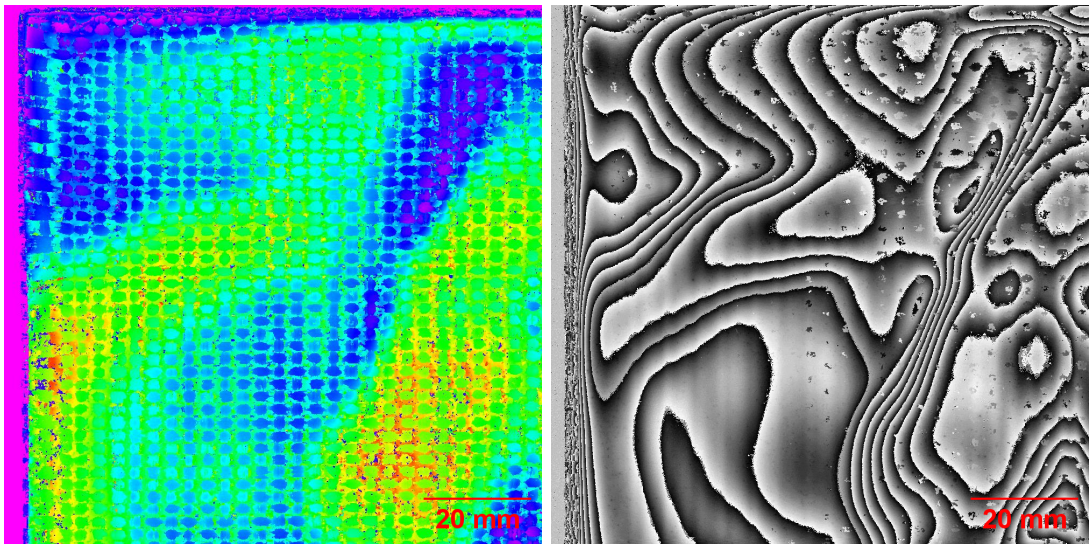

(a) (b)

Figure 4.4: The underlying composite panel surface, visible through the coating using US.

By segmenting the thicker and thinner areas, visualising these differences was easier (Figure 4.5).

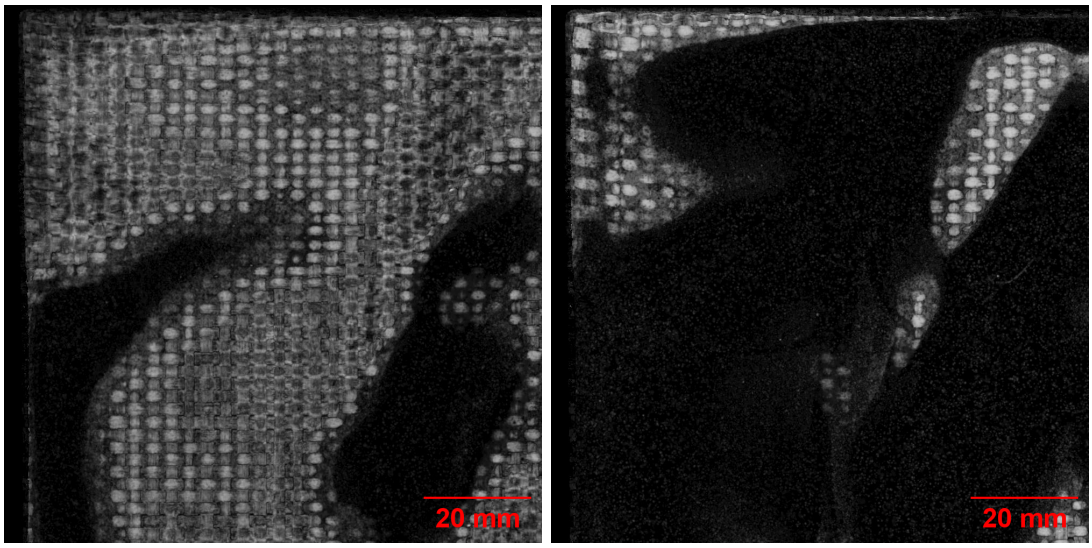

(a) (b)

Figure 4.5: The underlying composite panel surface, visible through the coating using US.

Using B scans (Figure 4.6) of different regions of the sample, it was possible to see

the surfaces of both the coating and the underlying composite, however looking deeper into the composite was more challenging due to signal attenuation.

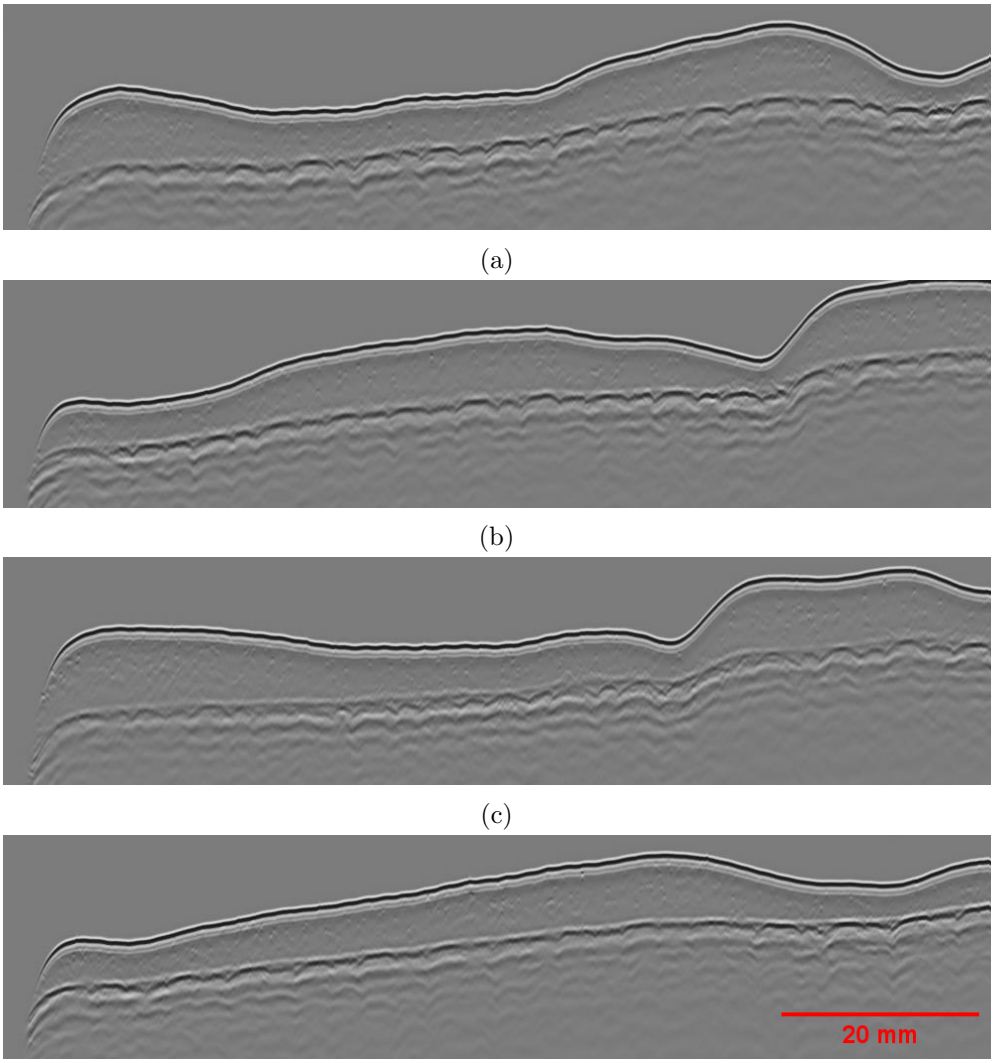

(a)

(b)

(c)

(d)

Figure 4.6: The underlying composite panel surface, visible through the coating using US.

4.4.2.2 Defects

As is shown in Figure 4.7a, using US it was possible to detect and display the surface topography of the sample. Voids were present at the surface, inside the coating and on the surface of the composite 4.11. As can be seen in Figures 4.11, 4.7b and 4.7a, the

artefact from the wavy surface was present.

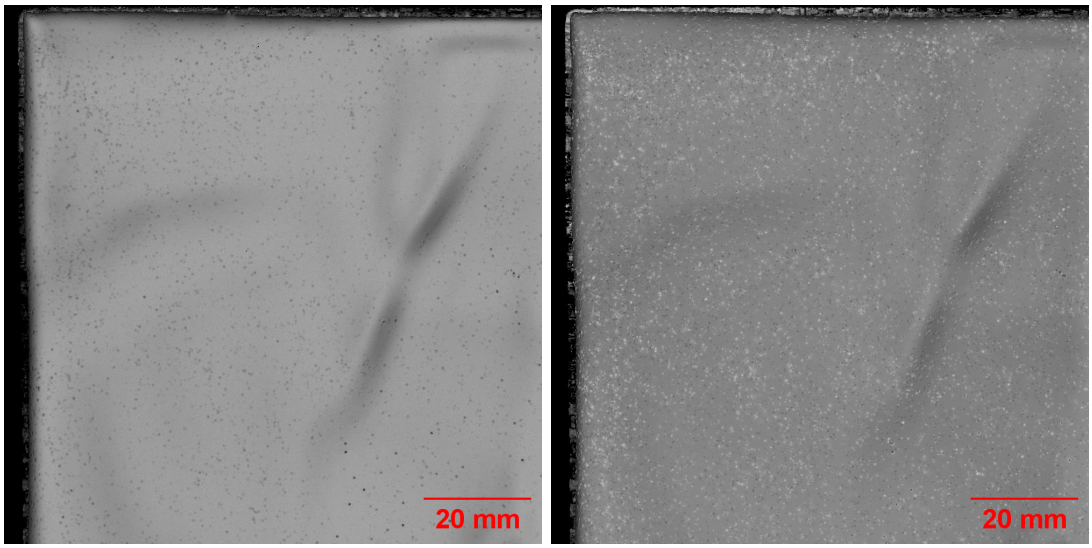

(a) (b)

Figure 4.7: Defects on the surface of the coating 4.7a and inside the coating 4.7b, visible through the coating using US

6,943 and 12,479 instances were detected in the surface and subsurface, respectively. The results from the edge detection can be seen below in figure 4.8.

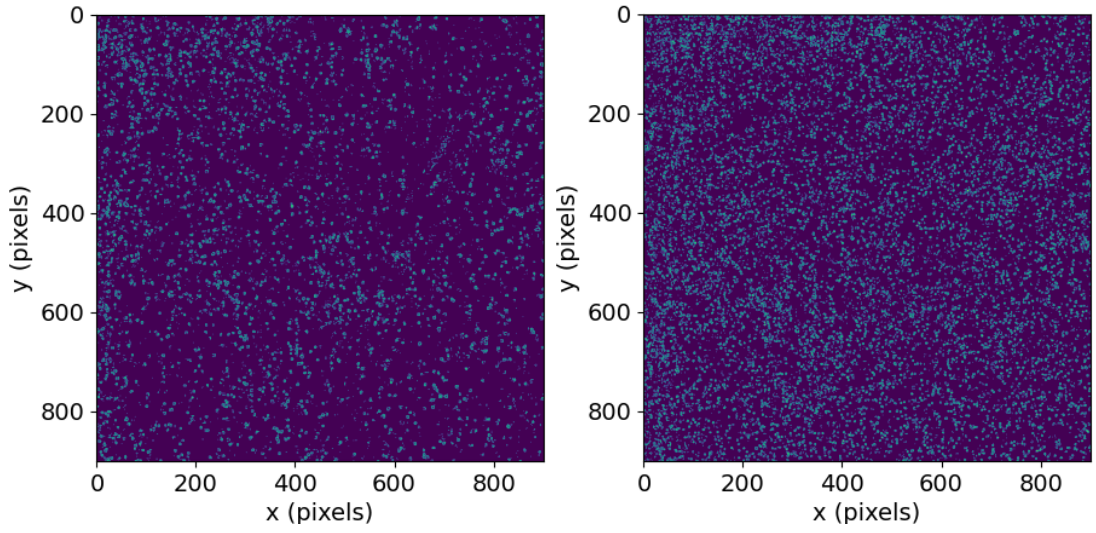

(a) (b)

Figure 4.8: Canny edge detection of the voids on the surface 4.8a and inside the coating 4.8b, respectively.

There were approximately double the number of instances detected within the surface than on the surface, likely due to the increased available space that could be occupied by a void. Equivalent void diameters can be seen in figures 4.9 and 4.10.

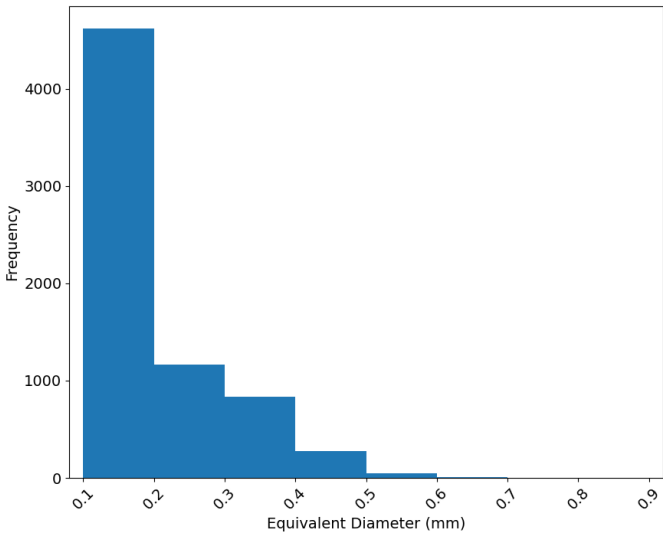

Figure 4.9: Histogram of equivalent void diameter as detected by the Canny edge detection on the surface.

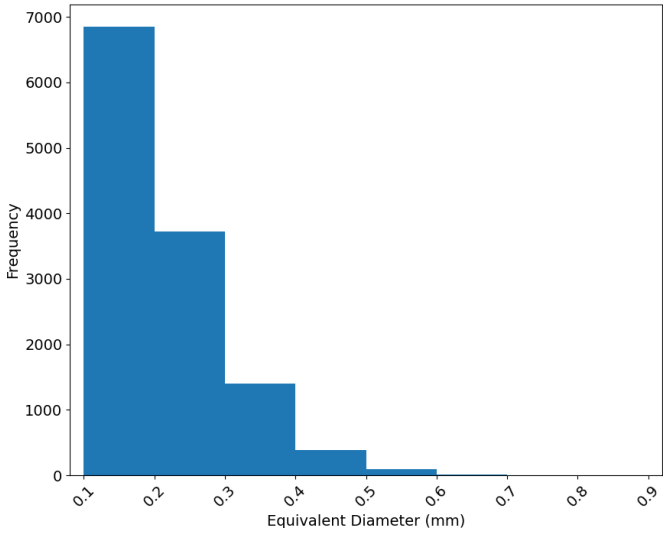

Figure 4.10: Histogram of equivalent void diameter as detected by the Canny edge detection inside the coating.

The majority of detected instances from the C-scan on the surface and inside the coating were determined at a size of 1 pixel x 1 pixel, with a pixel spacing of

0.1mm/pixel, giving a modal void diameter of 0.1mm.

Figure 4.11 displays the underlying composite panel surface. As mentioned above, the attenuation of the signal is significant, making the detection of defects inside the composite panel difficult. Small defects on or close to the surface of the GFRP were visible, however seeing anything deeper was not possible.

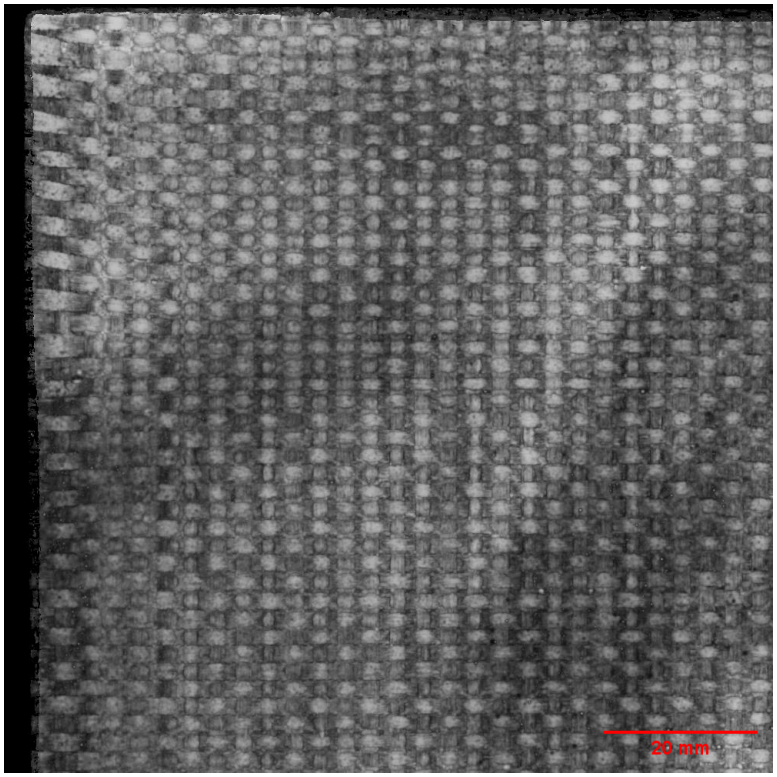

Figure 4.11: The underlying composite panel surface, visible through the coating using US.

4.4.3 Thermography

Using thermography, it was possible to visualise the surface waviness of the composite panel (Figure 4.12). However detecting finely detailed surface structures such as residual discontinuities from expelled air was not possible.

Thermography failed to detect the very fine voids seen in the US scans, however it was possible to see larger features present in the composite panel. The brighter regions visible in figure 4.13 show areas of higher thermal conductivity, with darker regions

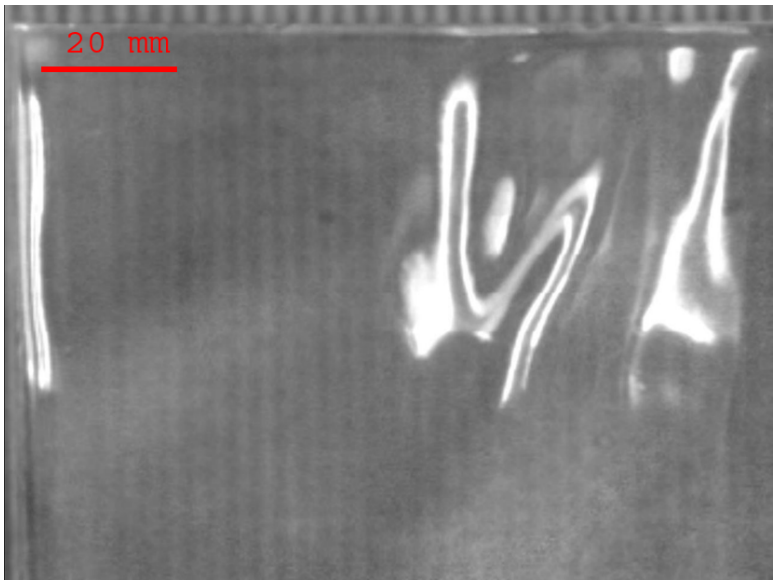

Figure 4.12: Surface Undulations of the composite sample (2nd time derivative), visible using thermography.

representing areas of lower conductivity.

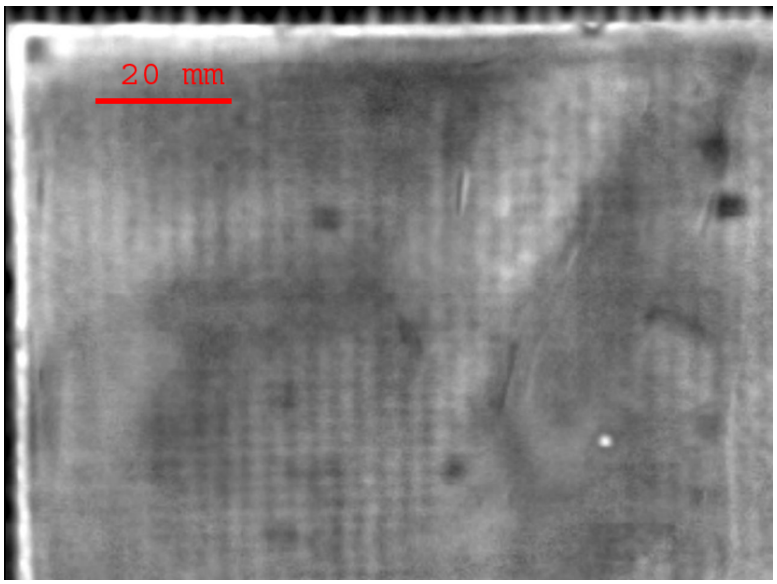

Figure 4.13: Sub-surface defects of the composite panel, visible using thermography.

The bright spot is likely to either be a metallic inclusion (due to its increased thermal conductivity), the composite edge (where there is more exposed surface to the heat lamp) or alternatively a region where there is less material (i.e a void, or a thinning

of the coating). However, there was not a significantly large void in the coating in that region in the US scans which indicates that it's likely to be inside the GFRP itself. The concentrated darker patches indicate differences in the material properties. This could be due to a poor cure of the composite, or resin rich areas.

4.4.4 Microwave

Similarly to thermography, microwave imaging failed to capture the fine detail of the voids present inside the coating 4.14. However, it was not possible to detect information about the surface quality of the composite panel. Coating layer thickness variations were detectable as well as some of the darker regions which were also present in the thermography scans, which are likely defects inside the composite panel itself rather than the coating.

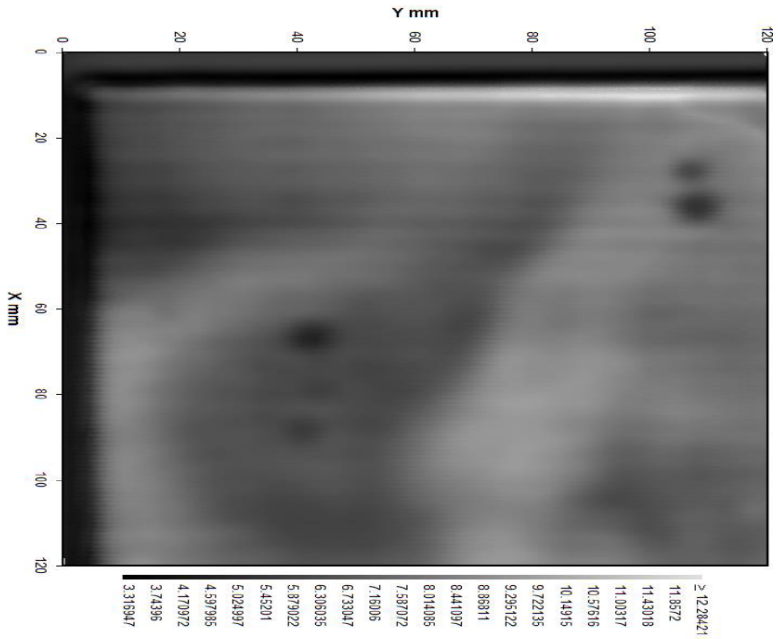

Figure 4.14: Sub-surface defects of the composite panel, visible using microwave.

4.5 Discussion

The objective of this study was to provide a qualitative analysis of three different NDT methods that could be used to detect and monitor defects inside a rain erosion test sample. US had the highest resolution of all NDT methods tested, followed by thermography and microwave NDT, However quantification of this was not possible. Surface waviness was detected in US and thermography, however not using microwave NDT. Thickness variations were detected in all three NDT methods. US was the only method able to detect the small voids present within the coating itself clearly as well as surface discontinuities too. However, the US signal deteriorated quickly with the presence of material interfaces of different acoustic impedance. More specifically, the fibres and the coating/composite interface. Interestingly, US was able to detect the composite surface reasonably well even considering the surface waviness and the number of defects inside the coating, which suggests it may be possible to monitor erosion progress for coatings containing surface, subsurface defects and even interfacial defects. Thermography and microwave NDT detected defects within the composite panel itself, but not in the coating. This is likely due to the reduced resolution of these techniques at this present time, with microwave NDT having a lower resolution than thermography. Some, but not all of the features present in the thermography were present in the microwave image. In this present study, the composite panel was manufactured from GFRP. Thermography becomes more challenging in materials and composites that have higher thermal conductivity, for example CFRP, with studies reporting higher values than that of GFRP [128–131]. Therefore authors looking to apply the results here to alternative FRPs should proceed with caution. Further to this microwave NDT has challenges with CFRP due to its high electrical conductivity [132].

The results produced here have wider ramifications. Currently to the author's knowledge, there are no studies that have used ultrasound to monitor or record defects in coated composite samples such as those used for rain erosion testing. Further to this, ultrasound is not widely used to inspect the quality of LEP application or leading-edge

repair work and to the author's knowledge, there have been no other studies carried out on such an application. In addition, Ultrasound could be used for gathering real data on the real-world application process to understand the relative occurrence of defects within coating systems or repair work and due to its relative low cost, technological maturity and practicality, it would be achievable to implement on a larger scale than other methods such as x-ray NDT.

The coated composite sample contained defects that are known to be present and common within coatings used as LEPs. In particular, voids are one of the most common defects to have been studied [46, 47, 75, 114, 115, 133]. Ultrasound was the only NDT method able to detect the small surface and subsurface voids that appeared on the coating, further highlighting its value as a tool for investigating defect-driven leading edge erosion. This highlights the applicability of the results produced here to RET and present a good opportunity for investigating coatings with inconsistent failure rates.

The spatial resolution of the SAM was limited to 100 microns, meaning that this was the effective resolution of the instrument. Without knowing the processing pipeline and the speed of sound of the coating, it is not possible to determine with certainty whether defects smaller than this were captured, however, the results from the microscopy (Figure 4.3b) indicate that a reasonable proportion of defects smaller than 100 microns are likely to have been counted as the single pixel voids and as has been discussed in section 4.2 due to the low acoustic velocity of LEP materials, the wide range of available probe frequencies commercially available and the reasonably high penetration found here, smaller defects could be visualised with a tailored system.

However it must be stressed, ultrasound is only applicable where contact is possible or in instances where there is a transmission medium present and where a constant stand-off distance can be maintained or a changing one can be accounted for. The leading edge of a wind turbine blade is a complex convex shape, differing from the composite panel scanned in this study, which was flat. This makes the scanning of a wind turbine blade surface challenging and care must be taken when approaching this complex task.

Moreover, preliminary results displayed here must be taken with caution. The

results here are only stated for one coating and composite combination. Further work must be done on other coating and composite combinations and it is possible that other coating/composite combinations do not work as well, for example, if there are inclusions inside the coating (carbon nanotubes) or if its internal structure attenuates the ultrasound signal.

The results here are also stated for a single-layer coating and not a multi-layer coating system and so the attenuation observed is likely to be larger. Although, in reality, this is similar to the process of stress wave transmission throughout the wind turbine blade surface and may help to understand the depth, in terms of layer and distance, at which defects are important for rain erosion. When inspecting leading edge repair work, there is often complex geometry consisting of multiple interfaces (likely more than the original LEP), which will likely increase the noise observed in the scans making defect detection more challenging.

In contrast to other studies such as those by Nash [114] or Mishnaevsky [115], here a low-cost versatile method has been shown, able to capture very small voids such as those found inside of coated composite panels. Further work must be done however to validate this technique against X-ray CT methods. Further to this, detecting defects is an important first step in the process of understanding their influence, however any future work should also be combined with RET similarly to research by Jensen et al. [113, 116]. It may be the case that defects of this size are not relevant to the rain erosion process and that defects detected by infrared of the size that influence RET are more important.

Further to the points discussed, there are other types of defects that may influence the rain erosion process and here only a select few have been characterised. Specifically, Further work must be carried out on coating debonding or delamination, another common failure mechanism [46, 47, 133]. The work here investigating voids shows the ability of ultrasound for detecting small defects which are inclusions of differing acoustic properties such as air. This indicates that ultrasound in theory should be able to detect delamination, however this will be highly dependent on the thickness of the delamination and so may only be possible in certain circumstances.

In addition to the points raised above, in terms of cost, for high resolution thermography equipment is comparable in price to a scanning acoustic microscopy. However, during this experimental campaign it was not possible to visualise voids with thermography, which would make it hard to justify the expense for an inferior technique. With no commercially available system for microwave NDT, a comparison is not possible that here.

Whilst data acquisition is far simpler for thermography than for SAM or microwave NDT, data processing and interpretation is more challenging and as has been apparent here, the exact interpretation and characterisation of damage is more challenging for thermography. This is similar too for microwave NDT, with the added challenges associated with data acquisition, as discussed in 4.2. Despite using an ultrasound probe requires some training, the results are more intuitive for the user to understand, making it overall easier to use. Additionally, if a SAM is used, training and use is simpler.

4.6 Conclusion

The study outlined here shows an initial investigation into the use of NDT on coated composite samples. Here a comparative analysis of the different types of NDT possible on polymer coated samples has been outlined and qualitative observations have been discussed. To the author's knowledge, this is the first comparative analysis study on the use of all three NDT methods on polymer coated GFRP panels.

The use of ultrasound for rain erosion testing is a promising opportunity for the monitoring of subsurface defect driven failure and provides a more cost-effective and practical, alternative to the use of x-ray imaging. Further to this, the minimum detectable size of a defect is far smaller than any of the other NDT methods tested and in the author's opinion ultrasound is likely to be the most effective option for detecting voids in RET samples out of the methods tested, with thermography and microwave NDT not able to detect the subsurface voids present in the sample. Whilst the use of thermography provides a non-contact alternative to ultrasound, the exact relationship

between defect size and damage initiation is still unclear. It Provides users with a faster, simpler and safer tool that can be applied to much larger areas. Further work would be required, however, to apply this technique to the profiled samples used in RET.

Chapter 5

Meteorological Data Modelling

A modified form of the following chapter was published in the Energies special issue on rain erosion: "Advancements in Leading-edge Erosion Science of Wind Turbine Blades" in the article "Mapping of Meteorological Observations over the Island of Ireland to Enhance the Understanding and Prediction of Rain Erosion in Wind Turbine Blades" by James W. K. Nash, Iasonas Zekos and Margaret M. Stack [134].

5.1 Introduction

To combat the effects of climate change, there is a global shift towards the development and integration of renewable energy, primarily solar panels and wind turbines. Wind park operators aim for their turbines to meet their expected lifetime (20+ years) with minimal repair work. However, this is highly dependent on the environmental conditions in which they are placed. One of the most prevalent factors is the presence of rain and the subsequent rain erosion of the leading-edge of wind turbine blades (Figure 5.1). Damage caused by impacts from other projectiles, including hail [135–137], sand [35, 138–140], insects [141, 142] and birds, also contributes to the degradation. However, they are less understood and particularly site-specific, with early research on hail erosion displaying little erosion damage [137], insects preferring warm humid air for flight [142], sand being mainly present in dry, arid areas or certain coastal sites [35] and turbine siting and development aiming to minimise bat or bird strikes. Extreme

weather and rainfall have increased over recent years in northern latitudes [30]. With the increasing size of turbines and therefore tip speed, one can assume that rain erosion is set to become a dominating issue for the sector, highlighting the need to find a solution. In some cases, severe erosion (Figure 5.1b) can occur in as little as 2 years [143].

(a) (b)

Figure 5.1: Minor (**a**) and major (**b**) erosion damage on the leading-edge of wind turbine blades (reprinted from [12]).

Typically, the leading-edge of a wind turbine blade is protected using some form of LEP, typically a polymeric coating or tape. LEPs are susceptible to environmental conditions during erosion. Temperature sensitivities are particularly common in polyurethane (PU) coatings, with their low glass transition temperatures. In recent solid particle erosion tests, PU coatings have exhibited varying erosion behaviours at a range of temperatures (−30 °C – 100 °C) [139, 144]. This performance is largely dependent on coating composition and, although some of the temperatures used were outside of typical operational values during rain events, these results exemplify their temperature sensitivities. Thermal cycling and ageing can also affect mechanical properties, further highlighting the need to understand the impact conditions [36, 77, 142, 145–148].

During rain events, the relative humidity is often high. This atmospheric moisture can interact with polymers to a varying degree. Degradation from humidity fluctuations through water ingress and hydrolysis can temporarily or permanently change mechanical properties [36, 77, 145, 146, 149–151]. Hydrothermal ageing is well documented too within pure composites [152, 153]. However, to the authors' knowledge, there have been investigations of the influence of humidity or hydrothermal ageing.

Furthermore, as wind turbine blade surfaces contain two or more different polymers (at least one LEP layer and the composite), even if the top layer is not affected by humidity, another LEP layer or the composite beneath may potentially absorb water, leading to swelling, which could delaminate or fatigue the interface between layers.

Impurities in rain can also lead to chemical reactions and, with the prevalence of acid rain in northern Europe and sea salt aerosols in coastal and offshore sites, this contribution to the erosion process requires further investigation. In northern Europe, sulphuric and nitric acids are the most common, typically from burning fossil fuels or agricultural sources, respectively. Sea salt aerosols are predominantly composed of chloride (Cl^-), sodium (Na^+), sulphate ($SO_2{}^{4-}$), magnesium (Mg^{2+}), calcium (Ca^{2+}), and potassium (K^-). Salt concentrations are typically much higher than acidic pollutants and are of interest in situations where materials (including polymers) are prone to corrosion [146, 147, 153]. Recent evidence [12, 154–156] suggests enhanced degradation due to the presence of sea salt, acidity or at sites in close proximity to quarries. The influence of salt will be more pronounced at sites near the coast or offshore. Exposure to other pollutant concentrations, such as particulate matter and air pollution, is irregular, site-specific and changes over time in relation to the pollution from factories, vehicles and other sources. Without the appropriate data, addressing these other pollutant influences becomes difficult.

The recent DNVGL-RP-0171 recommended practice [72] for RET sought to standardise the reporting of these environmental conditions and other aspects. It recommends documenting chamber pressure and temperature, sample temperature and water temperature and quality, as well as the accelerated ageing parameters extreme temperatures, UV exposure, humidity and salt spray. However, exposure to these conditions occurs simultaneously and during rain erosion, creating synergistic effects that are yet to be properly documented. The resultant effects could be severe and further enhance degradation mechanisms [12, 36, 146, 147, 154, 157–161].

This chapter will focus on Ireland, where rain is predominantly orographic or stratiform. As noted by other authors [30, 159, 162], orography strongly influences rainfall in Ireland (compare Figures 5.2a and 5.2b).

Wind from the west, south-west and south typically brings in wet Atlantic weather, with annual rainfall on the west and east coasts in the range of 1000 mm–1400 mm and ∼700 mm, respectively. Rainfall is highly seasonal with winter monthly precipitation on the west coast reducing from 150 mm to 50 mm in the summer. Conversely, monthly precipitation on the east coast remains ∼60 mm throughout the year [30, 159]. Rain is typically characterised using rain intensity and exposure time, with size distributions (e.g., the Best distribution [163]) for droplet diameters at a given intensity. Rain intensity can be determined using empirical methods, such as rain gauges, at discrete locations. However, this is not feasible for determining rain intensity accurately over the island of Ireland with reasonable temporal resolution.

Weather radars are much more appropriate. However, they suffer from artefacts produced by physical objects, such as buildings or wind turbines. One feature can also be obscured by another between it and the radar station and their accuracy degrades with distance from the station itself, requiring the creation of mosaics from multiple radar stations. Signal processing can reduce spurious data outputs and significantly clean the data and calibration using data from the few rain gauges available is effective and helps to remove artefacts [164, 165]. The use of radar composites is therefore beneficial and at this present time the simplest, widely available method to generate rain intensity maps for large areas. Site-specific rain intensity histograms can be generated from these data, and when coupled with wind data can provide an effective tool for rain erosion lifetime estimation (either by estimating the impact kinetic energy or by modelling material fatigue from impact numbers) [17] or instead can be used to implement methods such as the Erosion Safe Mode (ESM) [66]. However, further calibration work for the radar network in Ireland is required and, currently, the data available are insufficient.

Numerical Weather prediction models provide a further opportunity for erosion modelling, with the added benefit that they don't suffer from artefacts generated from wind turbine parks or large objects. However the complexity of running these simulations requires sophisticated computational power and they generate a wealth of data, not necessarily relevant. They therefore require the use of supercomputers, such as

JASMIN (UK Met Office), just to extract the relevant data in a reasonable time frame. More specifically, if we consider the Unified Model developed by the UK Met Office [166], the time resolution is restricted to every three hours, with hourly predictions for up to 36 hours ahead of time. The spatial resolution of this model is restricted to 2km square grided locations over the UK and Ireland, however as technological advancements take place these resolutions are expected to be further refined.

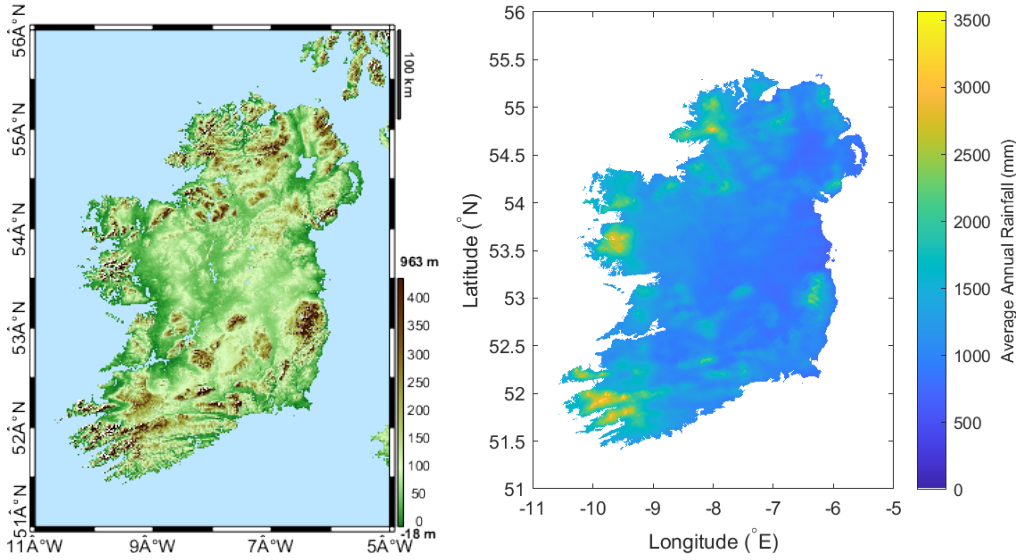

(a) (b)

Figure 5.2: Topographical data (**a**) obtained from NASA and average annual rainfall data for the 30-year period 1981–2010 (**b**) obtained from Met Éireann[13] were mapped using the READHGT function [14] and MATLAB's [15] imagesc function, respectively.

This chapter seeks to address knowledge gaps in the rain erosion process, particularly the approximate magnitude of impact numbers and annual impact kinetic energy, droplet size, temperature, humidity, ion concentrations (sodium and sulphate) and pH, as well as how these parameters vary geographically across the Island of Ireland and annually. Areas which are more prone to damage from rain erosion will be highlighted and site-specific conditions can be characterised. Furthermore, seasonal variations in weather patterns may help to identify periods of enhanced or reduced erosion, as well as other degradation mechanisms. Results from this work will also seek to inform RET protocols. This will pave the way for future work to fully understand the influence of

these conditions on the rain erosion phenomenon.

5.2 Methodology

5.2.1 Rain Erosion Modelling

Currently, there are two approaches for evaluating the rain erosion damage process: firstly considering the transfer of kinetic energy [17, 167, 168], E_K, or secondly, the Springer/water-hammer/fatigue model [11].

The kinetic energy model popularised in the field of soil erosion is used to assess the damage severity of rain events [167, 168]. It assumes during a droplet impact, all of the kinetic energy is transferred (eq. 5.1) to the target, which in this case is the soil.

$$E_K = 1/2mV^2 = \pi/6(d_w^3)\rho_w V^2 \tag{5.1}$$

where E_K is the kinetic energy of the impact, m is the mass of the droplet, V is the impact speed, d_w is the diameter of the droplet and ρ_w is the density of water.

As discussed by Johansen [76], is only valid for a plastic impact where no mass is lost and the droplet merges with the target. In the case of higher-speed rain erosion on moving targets, lateral jetting occurs and during the impact process, as does droplet fragmentation, leading to a loss of energy. Thus kinetic energy is not fully transferred and so the damage process cannot be considered as such. It has some limited application, however currently there are no analytical equations for describing the energy transfer process or attributing what proportion is absorbed by the material. Thus, it is not possible to use this equation for lifetime estimation. It can however be used for indicative purposes for assessing erosion environments, as it benefits from the simplicity of considering droplet diameter, without considering shape changes due to aerodynamic forces, impact physics or material characteristics.

The Springer model [11] is the most common analytical model, with authors such as Eisenberg [78] reporting a good fit with reality. It posits that rain erosion is a fatigue process with repeated impacts or cycles that are below the tensile strength of

a material. The damage from these cycles accumulates and eventually leads to failure. However, the model was developed for brittle and elastic materials, and fails to consider the influence of droplet diameter directly on the impact pressure or material strength for uncoated materials. Additionally, assessing the performance of a material requires mechanical testing, which is cumbersome.

The Springer model states that impact pressure is given by the modified water hammer equation:

$$P = \frac{\rho_L C_L v}{1 + \frac{\rho_L C_L}{\rho_S C_S}} \tag{5.2}$$

where the variables ρ, C and V are the density, speed of sound and velocity, with the subscripts L and S referring to liquid and solid, respectively. The impact pressure is linked to the acoustic impedance, Z:

$$Z = \rho_S C_S \tag{5.3}$$

which is in turn linked to a material's stiffness. If the environmental conditions are known and one accepts the Springer model [11], as in Pugh et al.'s work [77], the lifetime of a specified turbine at a location can be estimated. However, validating the model requires rain erosion to be assumed a fatigue problem, with the endurance limit determined through a whirling arm RET program over a range of velocities, similarly to DNVGL-RP-0573 [74]. This maps the number of cycles to failure, N for a given impact pressure, P, generating an S-N curve. n will be used in this chapter instead of N, accompanied by the following subscripts: A, meaning annually at a specified speed range; AR, meaning annually at rated speed; and R, meaning at rated speed over a specified time period.

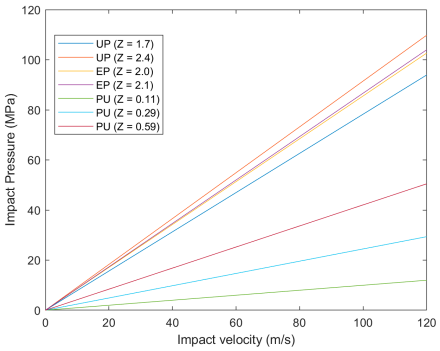

Figure 5.3: Using Equation (5.2) and data obtained from Slot et al. [7], the impact velocity for droplets is plotted against the impact pressure for LEP coating materials (UP, unsaturated polyester; EP, epoxy and PU, polyurethane). Different plots of each polymer represent slight variations in composition, which lead to different acoustic impedances (given by Equation (5.3)).

According to Springer's model, stiff materials, such as gelcoat materials (epoxy or polyester, tensile strength = ∼97 MPa [169] and ∼123 MPa [170], respectively), are more prone to damage, particularly if cracks or defects are present, with impact pressures often close or even higher than their tensile strengths (Figure 5.3). Softer, viscoelastic materials (e.g. PU) are preferred for their significantly reduced impact pressures. However as discussed in some detail by Johansen [76], the model was not developed for this type of material and impact scenario which presents challenges in using it for this purpose. In order to develop and validate models, further work must be carried out to compare inspection reports and failure rates with results computed using impact conditions and environmental data. The variation of impact pressure with impact velocity for a range of materials can be seen in figure 5.3.

In light of the associated challenges here in applying either the kinetic energy model or Springer model to the rain erosion process, neither here will be selected for the lifetime estimation and instead number of impacts for different wind speeds and total annual accumulated energy for the tip of a wind turbine will be used for indicative purposes.

In order to understand the influence and variation of droplet diameter, a size distribution must be used. The most common, termed the 'Best distribution', is generally accepted [163]; however, recent investigations [171, 172] question its accuracy and ap-

plicability. As discussed by Herring et al. [171], Best's work is the collation of data from two different manual methods. Both are subject to human error and had small data collection time periods, as consecutive droplets can interfere with one another, producing inaccuracies. These techniques also have a limited size resolution of 0.5 mm, reducing their applicability to low rain rates (< 1 mmhr^{-1}), where most droplets are between 0 mm and 2 mm. In spite of these disadvantages, the Best distribution is widely accepted and is relatively simple to implement, making it a good basis to build upon. RET programs commonly use worst-case scenario conditions of $\sim$25 mmhr^{-1}, with a droplet size of $\sim$2 mm, as this is the respective mean size [11, 72]. However, further work characterising the influence of droplet diameter on the erosion process is required as well as understanding the range of realistic droplet densities, λ, that appear in nature. A more detailed discussion of this is beyond the scope of this chapter though. The recent development of a rain texture model now enables the prediction of the number of impacts, n, and therefore the lifetime of the leading-edge [173].

Traditionally, interpolation methods such as kriging, have been used to create geospatial rainfall maps for large areas (Figure 5.2b). Weather processes are complex and these methods rely on relationships that are not fully understood. So, producing accurate, detailed maps for rain intensity using kriging with a high temporal resolution is not possible. However, reasonable annual and monthly rainfall maps can be produced. Although lacking the histographic rain intensity information, they do indicate areas that are more prone to rain erosion.

The probability of an extreme weather event is identified using return period rainfalls, indicating the maximum rainfall experienced at a site within a specified return or time period. Developed by Fitzgerald [16] and currently used by the Irish Meteorological Office (Met Éireann), the model covers the island of Ireland. It not only determines the maxima, but acts to scale what is considered an extreme event for a location. Sites with higher values experience higher intensity rain more often, as confirmed by comparing Figures 5.2 and 5.4. Fitzgerald [16] confirms this, noting the distinct correlation between average annual rainfall (Figure 5.2b) and median yearly maximum 24 hr rainfall (Figure 5.4b).

As higher intensities produce higher densities, they cause more damage, regardless of whether the damage process is dictated by impact force or kinetic energy. As will be discussed later, if the damage process is controlled by kinetic energy, larger droplets would also cause more damage from a single impact and the compounded effect of both more droplets and larger droplets would accelerate deterioration further.

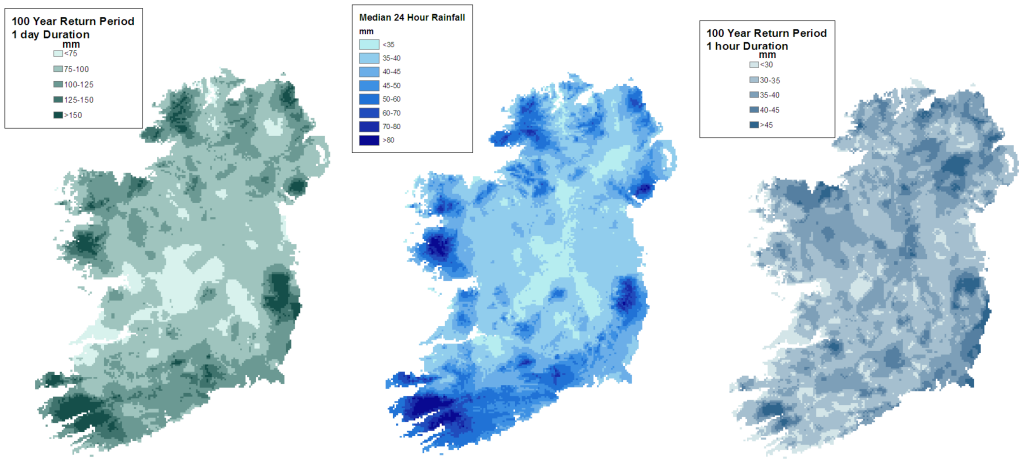

(a) (b) (c)

Figure 5.4: Rainfall return period mapped for (**a**) 100 year return, 1 day duration; (**b**) 1 year return, 1 day duration; (**c**) 100 year return, 1 h duration. Mapped by Fitzgerald for Met Éireann for the island of Ireland. Reprinted from [16].

5.2.1.1 Rain Texture Model

The rain texture model proposed by Amirzadeh et al. [173] will be used here. The model uses the relationship first proposed by Best (Figure 5.5) [163]. As stated by Best, droplet diameters, d, are considered to be accurate above the 10th percentile, d_{10}, and below the 95th percentile, d_{95}. So, $d < d_{10}$ and $d > d_{95}$ were truncated.

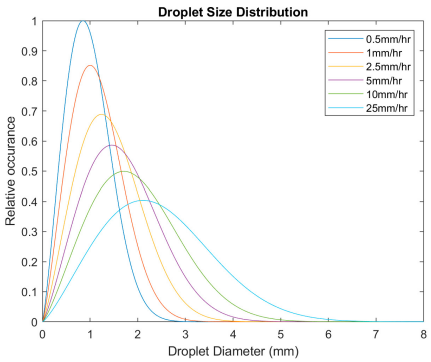

Figure 5.5: Droplet size distribution for different rainfall intensities, produced using the Best distribution.

Amirzadeh states the droplet density (droplets m^{-3}) has a Poisson distribution about the equation:

$$\lambda = 48.88I^{0.15} \tag{5.4}$$

As Equation (1) is exponential, initial increases in rain intensity lead to proportionally higher densities than at higher intensities. Figure 5.4c highlights that intensities of >30 $mmhr^{-1}$ are improbable during the lifetime of a wind turbine for more than 1 h, and that even intensities >10 $mmhr^{-1}$ only occur at most for 25 h a year in few locations [165]. Using Equation (5.4), realistic densities would be in the range of 35 droplets m^{-3} (0.1 $mmhr^{-1}$)–69 droplets m^{-3} (10 $mmhr^{-1}$). As in Amirzadeh et al.'s work, a stochastic spatial droplet distribution is assumed. The result of the model is a 3D distribution of rain droplets.

5.2.2 Weather Station Data Analysis

Hourly station data obtained from 23 of Met Éireann's synoptic weather stations located around the island of Ireland will be discussed (Table 5.1 and Figure 5.6) [13]. All measurements were recorded at ground level, except for wind speed, which was measured using a 10 m wind mast.

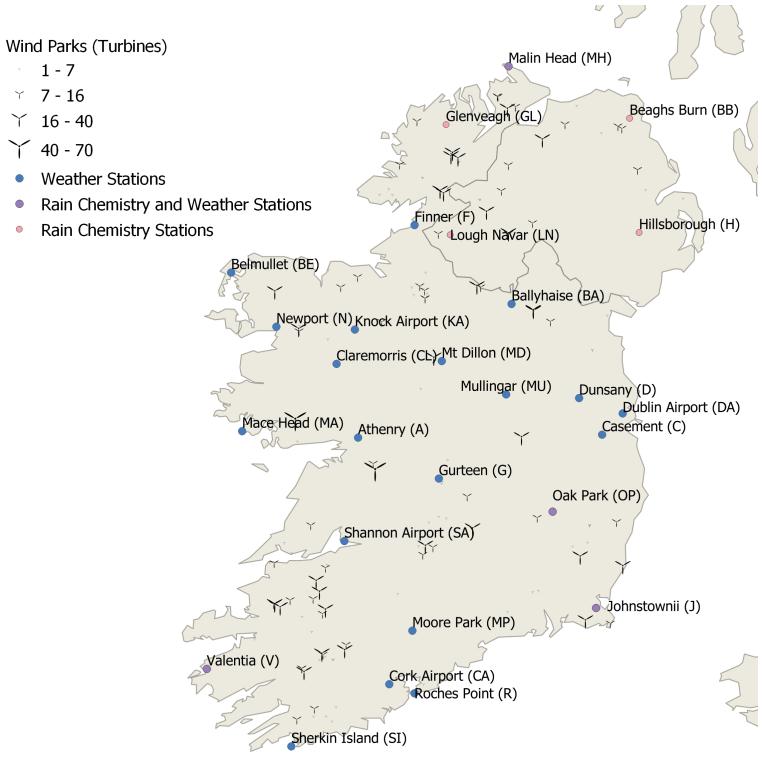

Figure 5.6: A map of Ireland with all known wind turbine parks in both the Republic of Ireland (ROI) and Northern Ireland (NI), marked. The 23 weather stations and the 8 rain chemistry stations used in this chapter are also marked.

For simplicity, each of the weather stations will be assumed as though they were a 100 m diameter wind turbine, with the recorded measurements at hub height and the Revolutions per Minute (RPM) curve taken from Letson et al. (Figure 5.7) [17]. It was assumed the tip of the wind turbine blade is a 10 cm $\times$ 10 cm flat plate [174], with all impacts occurring perpendicularly when the blade is horizontal. The influence of wind on the droplet, falling velocity and, due to a lack of data, impact efficiency will all be ignored.

Table 5.1: List of stations, country, station type (W—weather, C—rain chemistry), latitude (°N), longitude (°E), sample collection height (10m a.g.l. for wind data, Z) and time period.

Location	Country	Type	°N	°E	Z (m)	Start/End Dates	Years
Athenry (A)	ROI	W	53.29	−8.79	40	05/08/2010–01/08/2020	10
Ballyhaise (BA)	ROI	W	54.05	−7.31	78	01/01/2004–01/09/2019	15.7
Belmullet (BE)	ROI	W	54.23	−10.01	9	01/01/1989–01/09/2019	30.7
Casement (C)	ROI	W	53.31	−6.44	91	01/01/1990–01/08/2020	30.6
Claremorris (CL)	ROI	W	53.71	−8.99	68	01/01/1990–01/08/2020	30.6
Cork Airport (CA)	ROI	W	51.85	−8.49	155	01/01/1990–01/08/2020	30.6
Dublin Airport (DA)	ROI	W	53.43	−6.24	71	01/01/1990–01/08/2020	30.6
Dunsany (D)	ROI	W	53.52	−6.66	83	31/12/2006–01/08/2020	13.6
Finner (F)	ROI	W	54.49	−8.24	33	29/05/1997–01/08/2020	23.2
Gurteen (G)	ROI	W	53.05	−8.01	75	31/12/2007–01/10/2019	11.8
Glenveagh (GL)	ROI	C	55.05	−7.94	44	01/2010–12/2012	3
Johnstownii (J)	ROI	W	52.30	−6.50	62	01/01/2004–01/09/2019	15.7
		C				01/2010–12/2018	9
Knock Airport (KA)	ROI	W	53.91	−8.82	201	31/07/1996–01/08/2020	24
Mace Head (MA)	ROI	W	53.33	−9.90	21	01/08/2004–01/08/2020	16
Malin Head (MH)	ROI	W	55.37	−7.34	20	01/01/1989–01/09/2019	30.7
		C				01/2014–12/2018	5
Moore Park (MP)	ROI	W	52.16	−8.26	46	01/08/2003–01/08/2020	17
Mt Dillon (MD)	ROI	W	53.73	−7.98	39	08/12/2006–01/08/2020	13.6
Mullingar (MU)	ROI	W	53.54	−7.36	101	01/01/1990–01/08/2020	30.6
Newport (N)	ROI	W	53.92	−9.57	22	31/12/2004–01/08/2020	15.6
Oak Park (OP)	ROI	W	52.86	−6.92	62	01/08/2003–01/08/2020	17
		C				01/2010–12/2011	7
						01/2014–12/2018	
Roches Point (R)	ROI	W	51.79	−8.24	40	01/01/1990–01/08/2020	30.6
Shannon Airport (SA)	ROI	W	52.69	−8.92	15	01/01/1990–01/08/2020	30.6
Sherkin Island (SI)	ROI	W	51.48	−9.43	21	30/04/2004–01/08/2020	16.3
Valentia (V)	ROI	W	51.94	−10.24	24	01/01/1989–01/09/2019	30.7
		C				01/2010–12/2018	9
Beaghs Burn (BB)	NI	C	55.09	−6.17	252	01/2010–12/2018	9
Hillsborough (H)	NI	C	54.45	−6.08	120	01/2010–12/2018	9
Lough Navar (LN)	NI	C	54.44	−7.90	130	01/2010–12/2018	9

It is possible that the wake of upwind turbines influence droplet impact pathways, as well as some level of deflection caused by the boundary layer surrounding the wind turbine blade, which may lead to droplet break up or other effects not considered here [11, 67]. Furthermore, the threshold diameter below which droplet deflection due to inertia begins is ∼0.2 mm and the lowest droplet diameter projected is 0.2 mm due to the selected size resolution [78]. The actual influence of blade curvature on impact kinematics is generally considered to be low and it is only significant for larger droplets and in smaller wind turbine blades [175]. This may, however, present a bigger issue for the highly curved samples used in RET. The rain gauges used here were only able to measure precipitation and not, type (hail, snow, etc.) and so for the sake of simplicity, all precipitation will be assumed to be rain. Certain stations did note different weather events; however, detail was limited and so this was not considered.

The weather station data were filtered to remove any data points with missing sensor outputs for either temperature, humidity, wind speed or rain. All data, where the wind speed was 0 ms^{-1}, above the cutoff speed or where there was no rain, were then removed.

To generate the tip speed, the wind speed was taken and, using the relationship below (Figure 5.7), an RPM was calculated. The tip speed was then given by:

$$V = \frac{\omega}{60}\pi D \tag{5.5}$$

where ω is the RPM and D is the wind turbine diameter in meters. A 3D droplet distribution was generated using the rain texture model for each hourly rain data point. Using ω, the number of revolutions per hour was then generated and combined with the swept volume, v, of the blade tip per revolution:

$$v = A\pi D \tag{5.6}$$

where A is the frontal area of the wind turbine blade tip. This gives the swept volume per hour. This volume was then combined with the 3D distributions to produce a distribution of droplets impacted over that hour, with their respective impact speeds.

The weather station data were then either compiled over the time duration for each station and normalized giving annual results or compiled monthly across all stations and averaged, giving an average month at an average station. Due to the limited resolution of the wind speed measurement apparatus (nearest ms^{-1}), the bin size for impact velocity was much larger than desired.

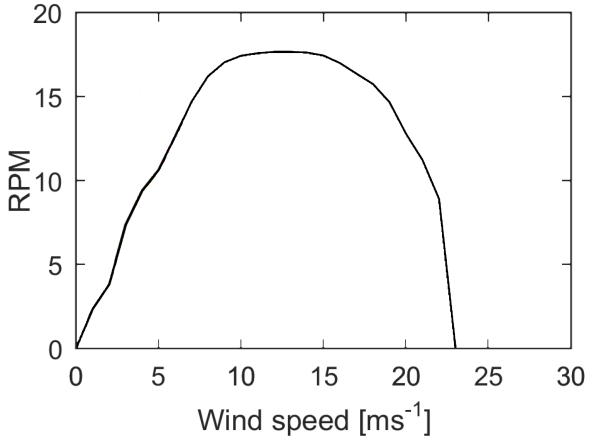

Figure 5.7: Wind turbine RPM curve adapted from [17]. The turbine rotates at an approximately rated speed over the wind speed range of 9 ms^{-1}–16 ms^{-1}.

As other authors have reported that the wet weather primarily comes from the Atlantic and that the wind direction is predominantly westerly, southwesterly and southerly, a series of least squares linear regression models were developed as a basis to investigate the relationship between geographical parameters (longitude, X, latitude, Y, and altitude, Z) and rainfall characteristics (impacts at each speed bin, n_A, total annual kinetic energy, $E_{K,A}$, mean temperature, T, and mean humidity, H) with and without MATLAB's 'Robust' option [15]. In each case, coefficients of determination were then calculated. The resulting models were then mapped over the island of Ireland geospatially.

Due to the wealth of data generated, data from three stations will also be presented—A, MA and N. They were selected as they surround the Galway Wind Farm. It is the largest onshore wind farm in Ireland and is on the west coast of Ireland and so, is subjected to higher winds and rain, and therefore erosion. This will be followed by a brief profile of the park using the regression models.

5.2.3 Rainwater Composition

During the period 2010–2018, there were eight stations sampling precipitation chemistry in Ireland—three sites in Northern Ireland (NI) and five in the Republic of Ireland (ROI) (Figure 5.6). The NI sites were sampled on a multi-day basis, ranging from 6 days to 29 days. The ROI sites were sampled daily. All sites contribute data to the cooperative programme for monitoring and evaluation of the long-range transmission of air pollutants in Europe (EMEP) [176], except Hillsborough and Beaghs Burn. All three sites in NI contribute to the UK Eutrophying & Acidifying Network (UKEAP) and the five sites in ROI additionally contribute to Ireland's Atmospheric Composition and Climate Change Network [177]. Data for the respective sites were available from EBAS (provided by EPA (Ireland) [178], Met Éireann [13]) and UK-AIR [179]. The NI sites are operated by Ricardo Energy & Environment on behalf of the UK Department for Environment, Food and Rural Affairs. The sites within ROI are all operated by the EPA, except Valentia which is operated by Met Éireann. The pH of rainwater collected from these sites, as well as sodium and sulphate ions (representing sea salts) present within the samples will be analysed. Acidity and ion content were initially investigated month by month. With no apparent variation in acidity month by month, annual results are instead reported. Due to the limited number of stations, understanding a clear geographical pattern proved too difficult and was unreliable.

5.3 Results

In the following sections, temperature and humidity results for the model that included rain intensity as well as median droplet sizes, temperatures and humidities were not included. Droplet size resolution was too low, and therefore median results were considered unsuitable. For temperature, there was no appreciable difference for the model that included rain intensity as opposed to just rain events. Median temperatures were in good agreement with mean values. There were, however, some differences between mean and median RH values, but not enough to have significant consequences. The differences were more pronounced for monthly humidity standard deviations, with stan-

dard deviations being smaller for the model when considering rain intensity, However, these were not considered significant enough to be included here as they mostly affected spring and summer months at non-rated tip speeds.

5.3.1 Wind

Geographical Variation All locations received between 10^6 and 10^8 rated speed impacts, annually (Figure 5.8). MH had the highest n_{AR} of any station, with 99 million impacts. Most stations displayed an increasing n_A with tip speed. Across all stations, the lowest speed bin had the lowest n_A.

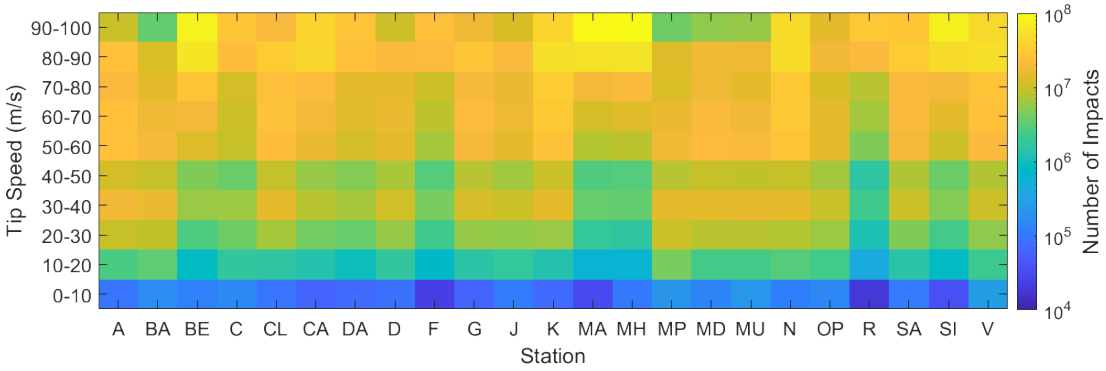

Figure 5.8: n_A at each site for each impact speed bin, as calculated.

Even stations, such as BA and MP, with relatively few hours at rated speed, still managed to receive $\sim 10^6$ impacts (Figures 5.8 and 5.9). N had the most rain hours of all stations with 2375 h. However, surprisingly MH had the highest $E_{K,A}$ ($\sim$670 kJ) with only 1768 h.

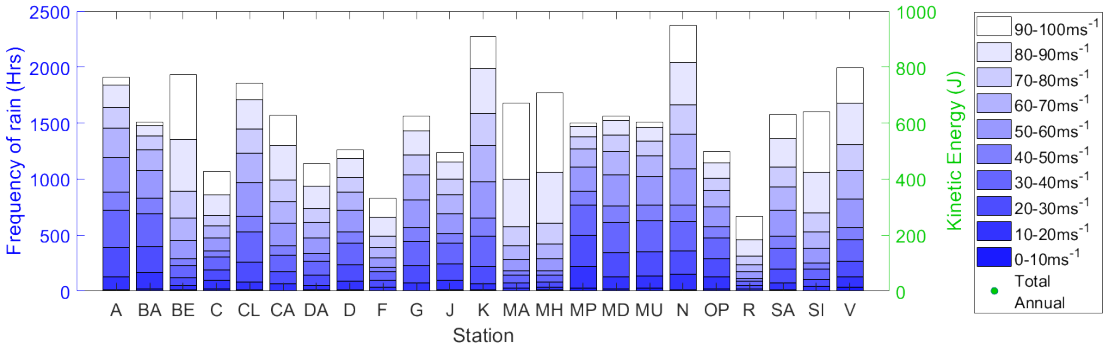

Figure 5.9: Number of rain hours and $E_{K,A}$ for each impact speed bin, at each station

The highest R^2 (0.48) for both $E_{K,A}$ and n_A regression models was for two predictor variables, X and Y. There was little correlation (<=0.30) between n_{AR} and other geographical parameters. In this case, the Root Mean Square Error (RMSE) was particularly high (∼132 kJ), equal to ∼20% of $E_{K,MH}$. Interestingly, the largest R^2 (0.57) was for $n_{A,70-80}$ and all three predictor variables.

Using the regression estimates, $E_{K,A}$ is given by:

$$E_K = 612,080 - 115,910X + 491.34Z \tag{5.7}$$

Using the model, Galway wind park would have an $E_{K,A}$ of ∼585 kJ. By extrapolating the models, the three wind parks with the highest $E_{K,A}$ would be Clydaghroe (∼673 kJ), Kilgarven (∼662 kJ) and Coomacheo (∼658 kJ).

Maximum droplet diameters for most stations across all velocities were in the range of 3 mm–4 mm, (Figure 5.10a–c, with the exception of a few stations with larger droplet sizes in the lower velocity ranges such as N. Generally, intensities greater than 6 mmhr^{-1} were uncommon, occurring for < 1 h, across all speed bins and stations (Figure 5.10d–f). Most events were concentrated around the lowest intensity bin (0 mmhr^{-1}–0.5 mmhr^{-1}). Of the three stations selected, N had the highest droplet diameter with 5 mm (Figure 5.10c).

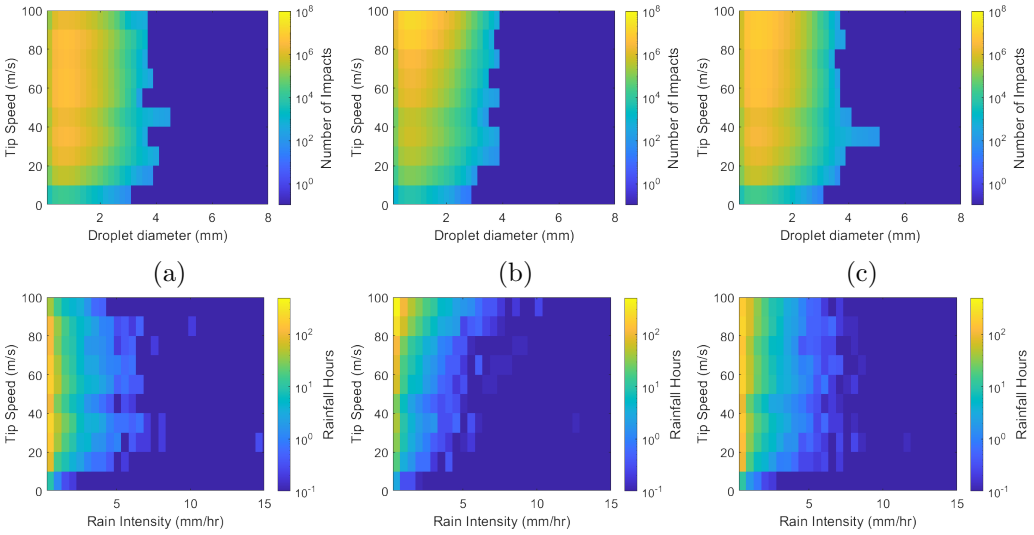

Figure 5.10: Annual impact distributions for the sites: A (**a**), MA (**b**) and N (**c**) for each given speed bin. Total annual number of rainfall hours at a given rain intensity, for a given speed bin for A (**d**), MA (**e**) and N (**f**).

Across all stations, the mean and standard deviation of droplet size increased with velocity (Figure 5.11). In the rated bin, all stations displayed a mean droplet size in the range of 0.95 mm–1 mm, with a large standard deviation in the range of 0.8 mm–0.9 mm.

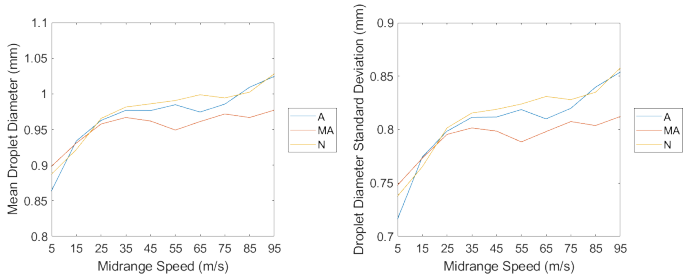

Figure 5.11: The variation of mean seen in (**a**) and standard deviation in (**b**) for droplet diameter with the midrange tip speed of each bin for stations A, MA and N, as calculated by the model.

Annual Variation Throughout the year, there was a pronounced cyclical pattern in the high-velocity impacts. n_R was highest during January and December, with $\sim 10^7$

impacts, and lowest during July with $\sim 10^6$ impacts (Figure 5.12).

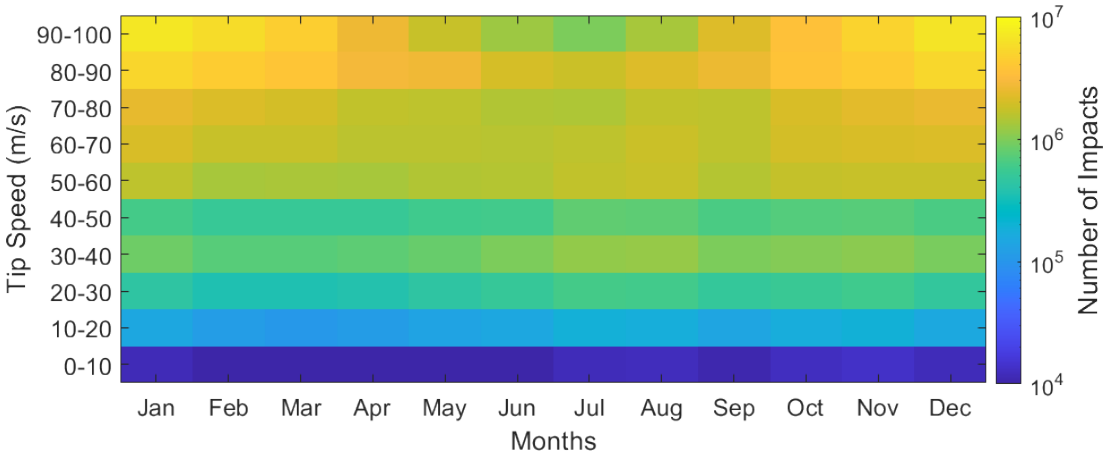

Figure 5.12: n_A for each month, for each speed bin, as calculated.

Rated wind speeds during rainfall occurred ~10 times more often in winter than in summer (Figure 5.13), with more rain events during winter months (October–March) than summer months (April–September), particularly at higher speeds. This results in considerably more E_K in winter months. December averaged the highest E_K of any month (~63 kJ), compared to July, which had the lowest (~22 kJ). Interestingly, the fewest hours occurred during June and not July, with 99 h. On average annually, there was 1552 h of rainfall.

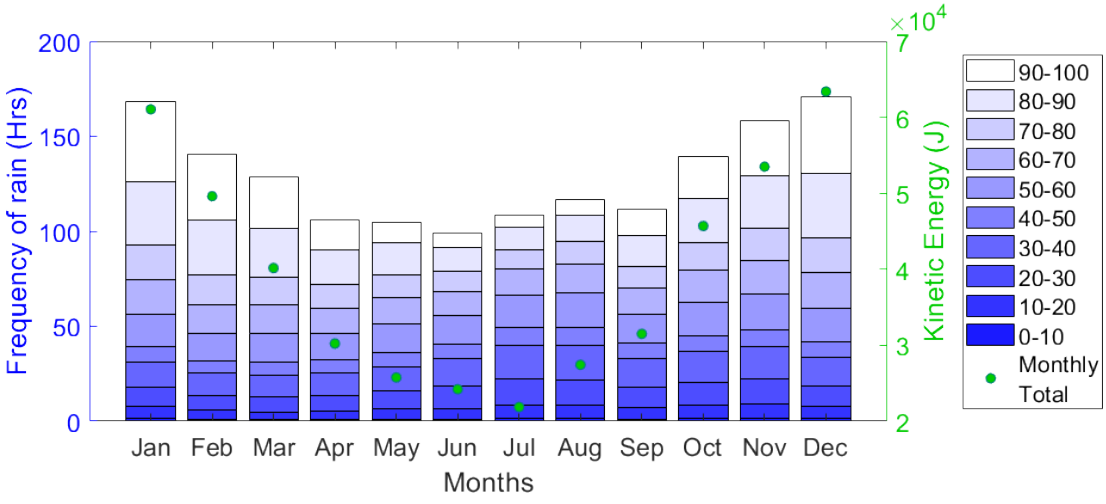

Figure 5.13: The number of rain hours and E_K for each impact speed bin for each month.

Droplet size distributions varied significantly between the summer and winter months. There were more events at high speeds during winter and higher intensity events at lower speeds during summer. During winter, rated speed events on average had higher intensities, increasing the average droplet diameter. The increased high intensity events during summer at lower speeds increased the maximum droplet diameter observed. Summer also had fewer rated speed rain events, resulting in much fewer impacts (Figure 5.14).

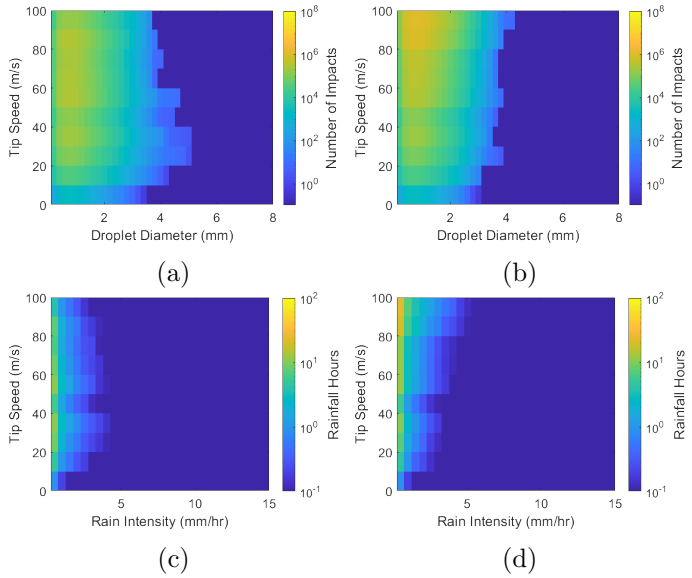

Figure 5.14: The average impact distributions during the months July (**a**) and December (**b**), respectively, for each given speed bin. (**c**,**d**) show the total number of rain hours for a given speed bin during the same periods.

The highest rain intensity was recorded in July, with an intensity of ∼41 mmhr^{-1}. The event occurred when the tip speed was between 20 ms^{-1} and 30 ms^{-1}. In fact, the highest intensity event at rated speed across all data analysed was ∼21 mmhr^{-1}, during September, which, when normalised and averaged, occurred for 0.002 h. Most high intensity events occurred during summer months when turbine speed was sub-optimum. This is illustrated by the elongation of the size distribution at speeds below 60 ms^{-1} in Figure 5.14a. Diameters > 4.5 mm were infrequent at rated speed (< 1000 per year) (Figure 5.14a,b). As in Section 5.3.1, rain intensities much higher than 6mmhr^{-1} rarely occurred, with most rain events concentrated around the lowest rainfall intensity

bin.

As in Section 5.3.1, in all months the mean and standard deviation of droplet size showed an increase with velocity (Figure 5.15). For all months at rated speed, mean droplet size was between 0.95 mm and 1.05 mm, with a smaller standard deviation range of 0.8 mm–0.88 mm. Interestingly, mean and standard deviation curves were steeper for winter months, whereas summer month curves were flatter.

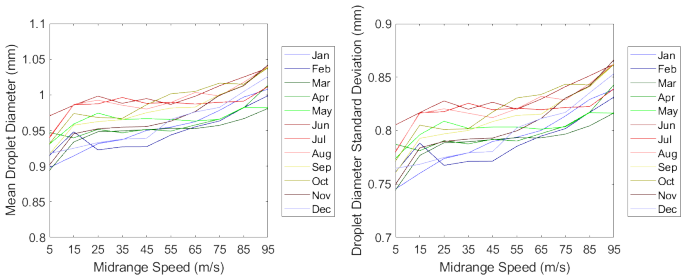

(a) (b)

Figure 5.15: The variation of mean (**a**) and standard deviation (**b**) for droplet diameter with the midrange tip speed of each bin for each month, as calculated by the model.

5.3.2 Temperature

Geographical Variation At low rain intensities, temperatures during rain events were well distributed. Common temperatures ($\geq$1 h) at the lowest rain intensity bin ranging between 5 °C and 15 °C (Figure 5.16). Mean temperatures started at just below 10 °C and, in contrast to standard deviation, as rain intensity increases, it skewed upwards (Figure 5.17). Precipitation events with temperatures below zero or exceeding 20 °C occurred very rarely (Figure 5.16).

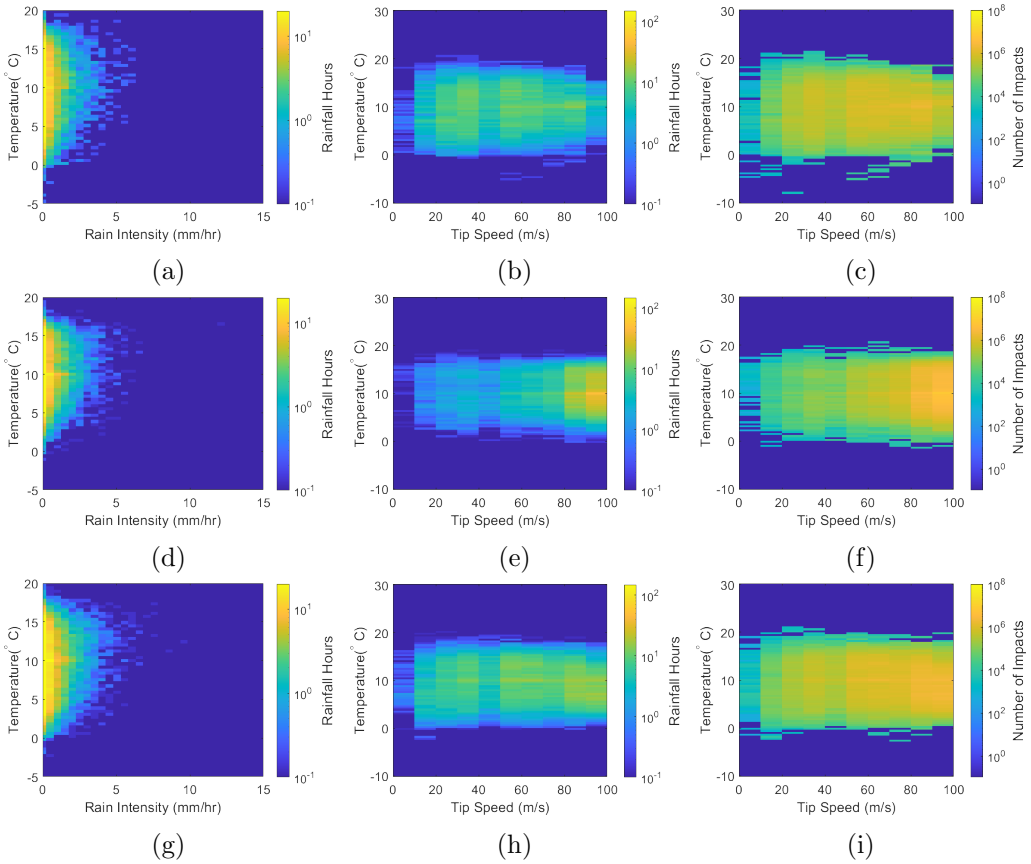

Figure 5.16: Average annual temperature/rainfall (**a**–**c**), temperature/rainfall/tip speed (**d**–**f**) and temperature/n_A/tip speed (**g**–**i**) distributions for stations A, MA and N, respectively.

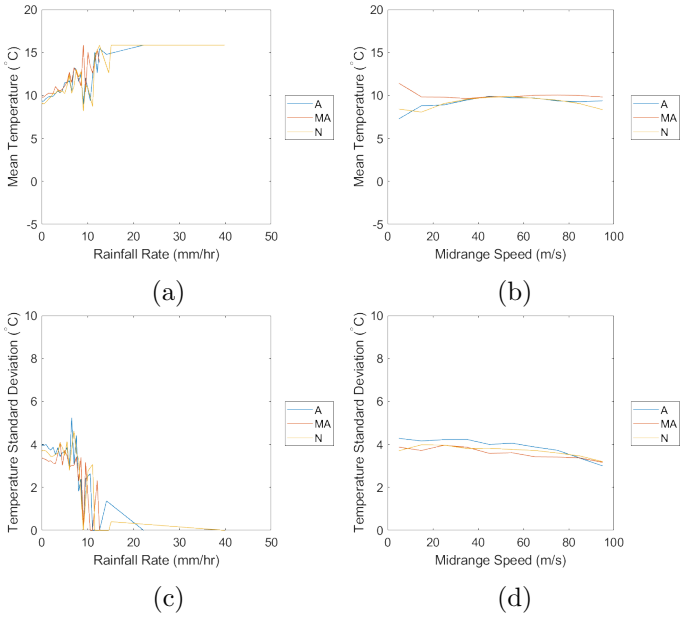

Figure 5.17: Mean (**a**,**b**) and standard deviations (**c**,**d**) of data presented in Figure 5.16 against the midrange tip speed of each bin, for the respective stations.

Temperatures between 5 °C and 15 °C were relatively common across all velocities (Figure 5.16). There was little temperature variation with tip speed; however, standard deviation had a decreasing trend (Figure 5.17). K had the lowest mean temperature across many of the speed bins, whereas SI and V mostly had the highest. Even temperatures as low as ∼1 °C–3 °C had relatively frequent impacts ∼ 10^5–10^6 at some stations. In total, 77% of stations had mean and median temperatures within 8 °C–10 °C across all speeds. This tightened when reducing the scope to just rate speed values (Table 5.2).

Table 5.2: Distributions of mean and median temperatures for rainfall hours and n_A across all stations.

Temperature vs. Tip Speed	**Statistical Variable**	**Range (°C) (All Speeds)**	**Range (°C) (Rated Speed)**	**% Values between 8 °C and 10 °C (All Speeds)**	**% Values between 8 °C and 10 °C (Rated Speed)**
Rainfall Hours	mean	7.3–14.5	7.7–10.2	77	91
	median	6.6 –12.2	7.4 –9.8	82	83
n_A	mean	6.9 –11.6	7.7 –10.2	76	92
	median	7.0 –12.2	7.4 –9.8	81	83

Using the mean temperature at a given speed and its respective n_A, the model with the highest R^2 value was found to be for the predictor variables, Y and Z, and the response variable, T, at rated speed, at 0.73. T is given by:

$$T = 36.2419 + -0.5052Y + -0.0071Z \tag{5.8}$$

Using the model (Equation (5.8)) to estimate T for Galway wind park would give ∼7.6 °C, with the same wind parks described in Section 5.3.1 with T = 6.7 °C, 7.2 °C and 6.9 °C, respectively.

Annual Variation In contrast to Section 5.3.2, at low rain intensities, the temperature distribution is much narrower (Figure 5.18). In July, common temperatures at the lowest rain intensity bin range between 13 °C and 16 °C. However, in December, this range is between 5 °C and 10 °C. Mean temperatures during each month are much flatter with rain intensity (Figure 5.19). During July and December, the distribution profiles still skew during higher intensity events downward and upward, respectively (Figure 5.18). However, temperatures during summer events displayed an increasing mean with intensity (Figure 5.19). The standard deviation does reduce too, with increasing rain intensity (Figure 5.19).

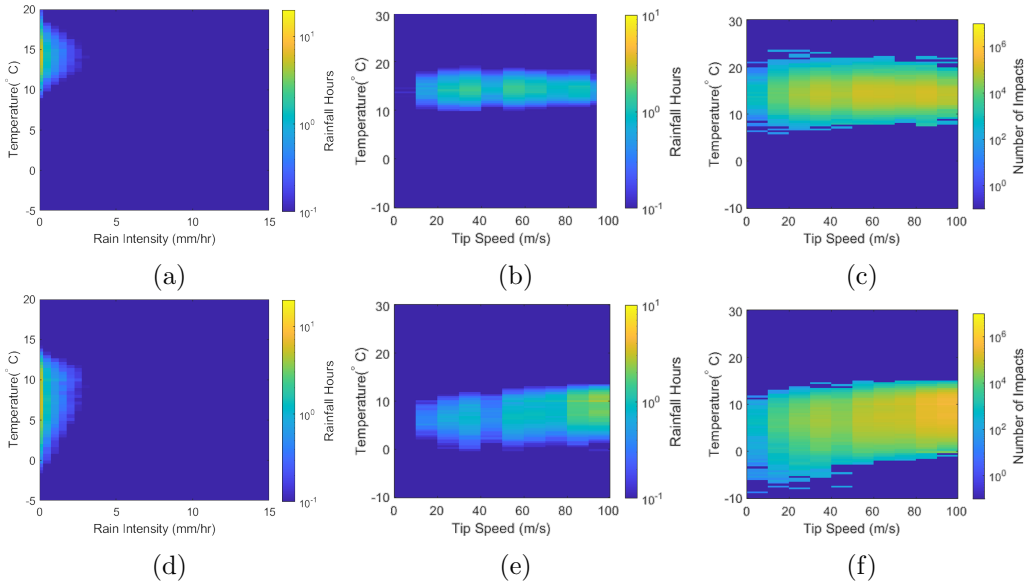

Figure 5.18: Average annual temperature/rainfall (**a**,**d**), temperature/rainfall/tip speed (**b**,**e**) and temperature/n_A/tip speed (**c**,**f**) distributions for July and December, respectively.

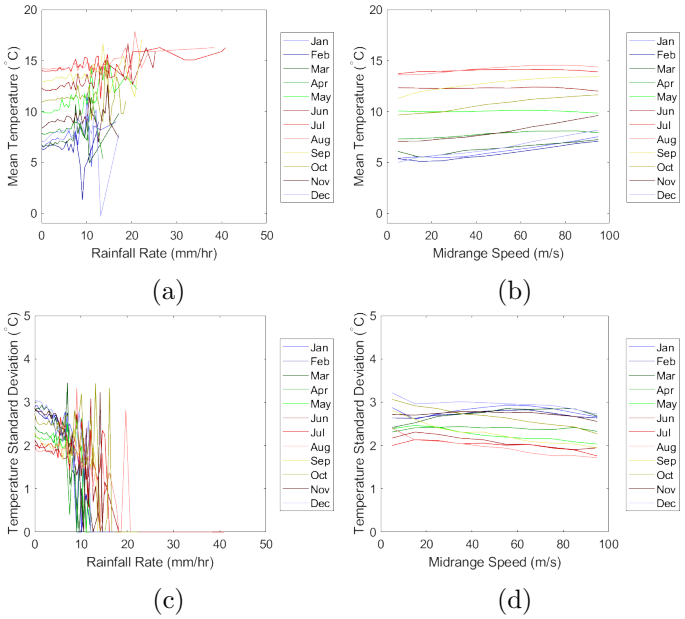

Figure 5.19: Mean (**a**,**b**) and standard deviations (**c**,**d**) of data presented in Figure 5.18 against the midrange tip speed of each bin for the respective months.

During summer months, rain events were reasonably distributed across all of the speed bins, with temperatures between 10 °C and 15 °C (Figure 5.18). However, during

winter, most rain events occurred close to or at rated speed (>80 ms^{-1}), with cooler temperatures ranging between 5 °C and 11 °C. Subzero temperatures were infrequent (< 1 h) for all speed bins. In summer months, rated speed impacts (> 10^5) were common at the narrow temperature range of 12 °C–15 °C and rarely exceeded 20 °C (< 1 h). However, during winter, rated speed impacts (> 10^5) occurred over a much broader range of 2 °C–12 °C.

As one would expect, average temperatures during summer rain events were higher than winter. Interestingly, mean temperatures increased with turbine speed during winter months. Standard deviations across all speed bins were lower in summer months than winter.

5.3.3 Humidity

Geographical Variation During rain events, the relative humidity was predominantly >90% at all stations (Figure 5.20). This is highlighted for rain intensities of >5 $mmhr^{-1}$. Relative Humidity (RH) was particularly skewed towards a value of around 95–96%. Generally, mean RH increased with rain intensity; however, the standard deviation (Figure 5.21) and minimum/maximum range (Figure 5.20) decreased. As discussed earlier, some of these decreases in standard deviation will be due to the reduced number of events.

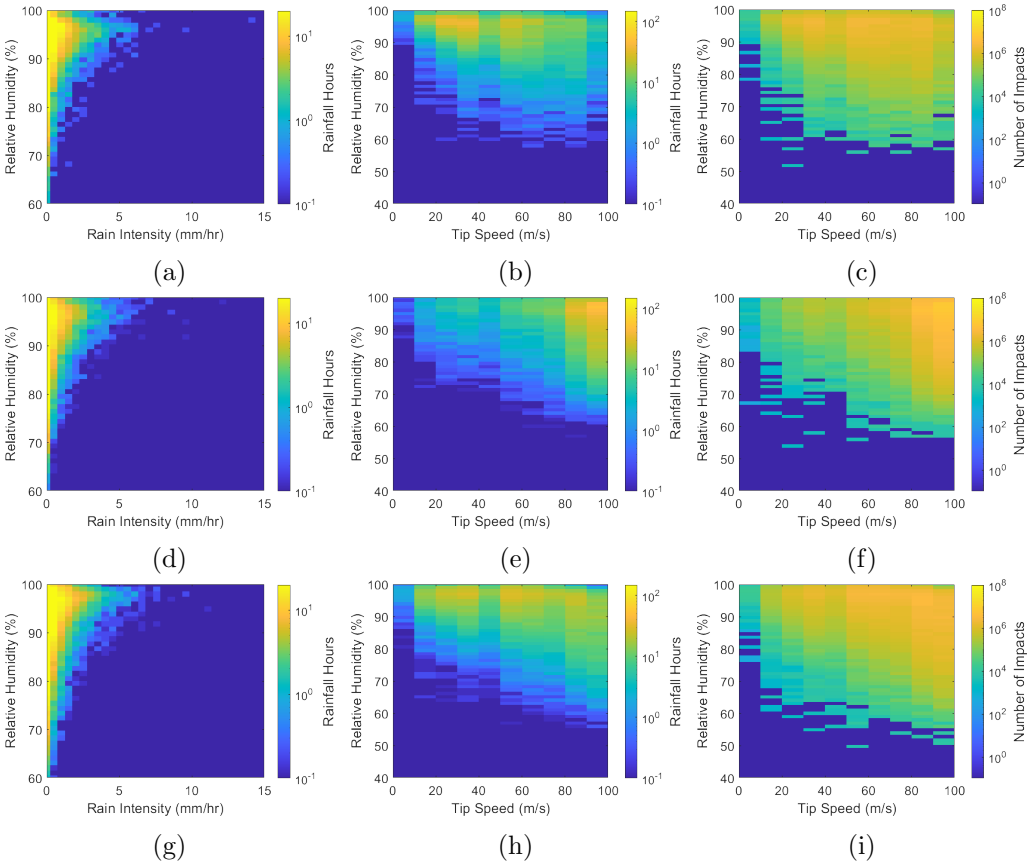

Figure 5.20: Average annual humidity/rainfall (**a**–**c**), humidity/rainfall/tip speed (**d**–**f**) and humidity/n_A/tip speed (**g**–**i**) distributions for the stations A, MA and N, respectively.

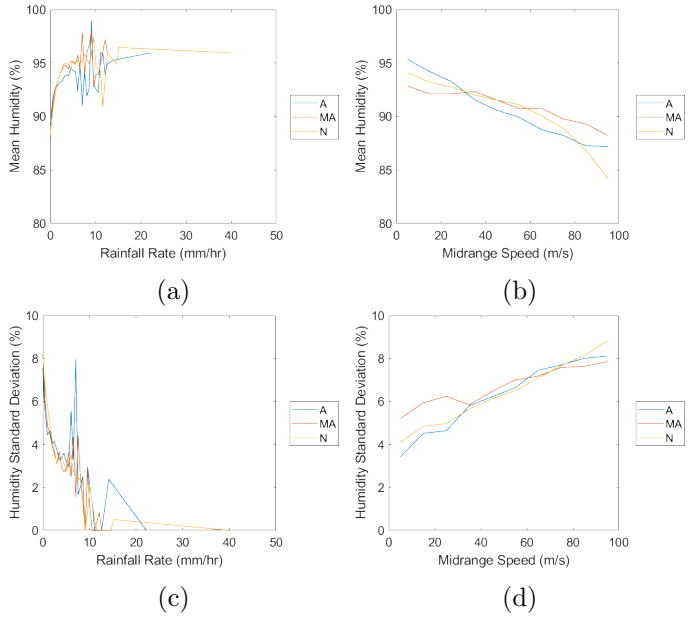

Figure 5.21: Means (**a**,**b**) and standard deviations (**c**,**d**) of data presented in Figure 5.20 against the midrange tip speed of each bin, for the respective stations.

At most stations, the RH minimum/maximum range increased with tip speed (Figure 5.20), largely because of a decreasing minimum RH value. Most stations reported RH values as low as ∼75% for at least 1 h. Across all speeds, stations mostly reported mean values above 90% (Figure 5.21). However, in contrast to rain intensity, with increasing tip speed mean RH decreased whereas standard deviation increased (Figure 5.21). This meant most rated speed mean values were less than 90% (Table 5.3).

Using mean RH values for rain events and for n_A, the model with the highest R^2 value was found to be for the predictor variables, Y and Z, and the response variable, H, at rated speed, at 0.52. H was given by:

$$H = 146.9518 + -1.1419Y + -0.0347Z \tag{5.9}$$

Using the above model, Galway wind park would have an $H = \sim 94\%$, with the wind parks mentioned in Section 5.3.1 having a mean RH of 103, 101 and 102%, respectively.

Table 5.3: mean and median RH distributions for rainfall hours and n_A across all 23 stations.

RH vs. Tip Speed	**Statistical Variable**	**Range (%) (All Speeds)**	**Range (%) (Rated Speed)**	**% Values between 85 and 90% (All Speeds)**	**% Values between 85 and 90% (Rated Speed)**
Rainfall Hours	mean	83–97	83–94	35	70
	median	84–98	84–96	26	74
n_A	mean	84–97	84–94	33	78
	median	84–98	84–96	25	70

Annual Variation Rain intensity varied with RH in the same manner as in Section 5.3.3. There was no discernible seasonal pattern and most characteristic trends were the same. The main difference was the increased number of events during winter compared to summer months (Figure 5.22).

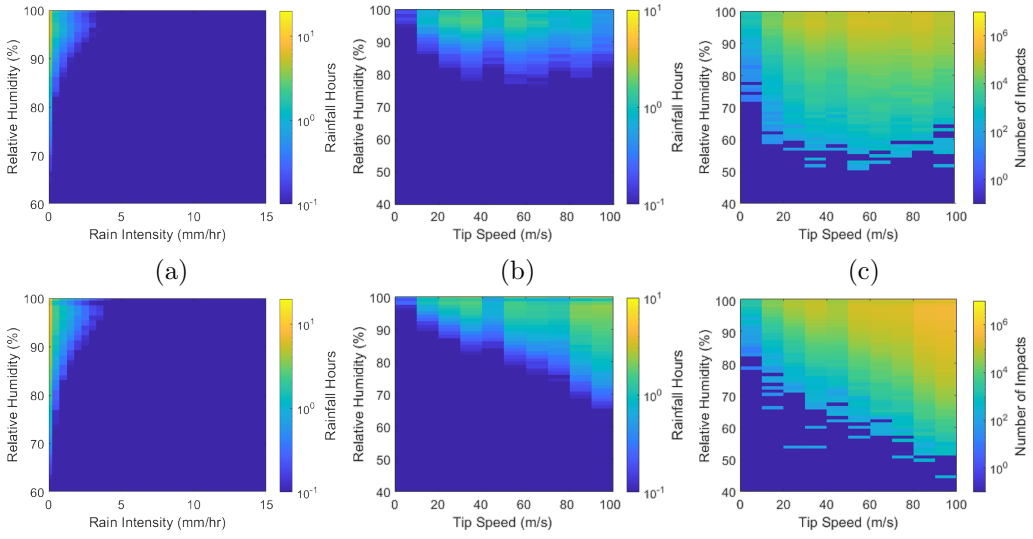

Figure 5.22: Average annual humidity/rainfall (**a**,**d**), humidity/rainfall/tip speed (**b**,**e**) and humidity/n_A/tip speed (**c**,**f**) distributions for July and December, respectively.

There was, however, a seasonal variation in RH with tip speed (Figure 5.22). During summer months, there were fewer events at higher tip speeds. RH values were typically higher in upper speed bins and the range covered was significantly reduced. Mean RH values had a more gentle gradient compared to winter months (Figure 5.23). Interestingly, spring months had lower mean and median values at nearly all speeds, with higher standard deviations in April and May in most speed bins. During winter months, as in Section 5.3.3, the RH range increased with tip speed, with this mainly being due to a decreasing minimum RH value (Figure 5.22). The mean RH gradient is the steepest for winter months, interestingly having the highest mean RH in the lowest speed bin and almost the lowest mean RH in the highest speed bin (Figure 5.23). The standard deviation during summer months has a gentler slope in contrast to the rest of the months. In contrast to Sections 5.3.1 and 5.3.2, the influence of including rain intensity is more pronounced. This increased the mean RH in almost all cases (118/120). The highest increase was in April in the highest speed bin with an RH of 0.7%. All cases except one (119/120) had higher standard deviations when excluding rain intensity. The highest increases were in April (30 ms^{-1}–40 ms^{-1}) and July (40 ms^{-1}–50 ms^{-1}) at 1.6% in both cases.

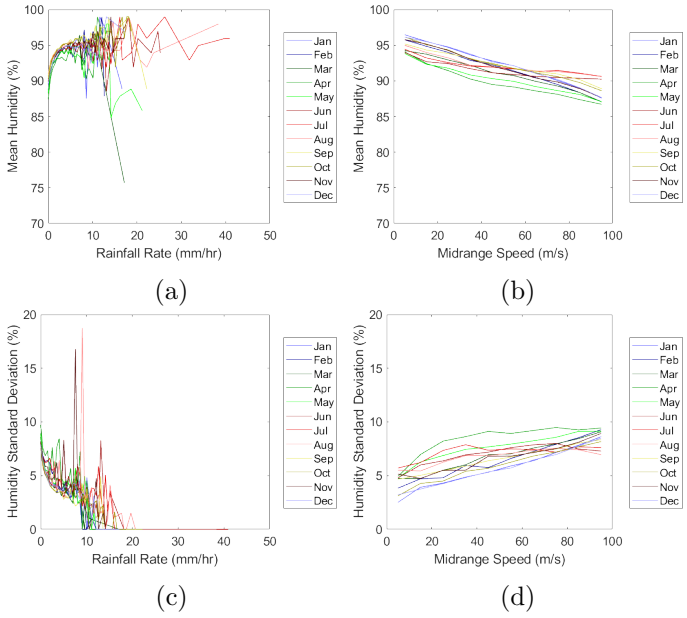

Figure 5.23: Mean (**a**,**b**) and standard deviations (**c**,**d**) of data presented in Figure 5.22 against the midrange tip speed of each bin for the respective stations.

5.3.4 Composition

Acidity Overall, stations mostly displayed an increase in annual mean pH when comparing 2018 with 2010 (Table 5.4). However the increase was slight in four out of five ROI stations (1.5–8.1%) and there was a decrease in one out of five (−3.2%). All NI stations displayed an increasing trend, with typically larger increases (6.9–18.1%). The range of values in annual mean pH in NI was also higher (5.5–6.5) than ROI (5–6), indicating that NI is less acidic than ROI.

Table 5.4: Mean pH values at year station across the selected years 2010–2018. Empty cells in the table are due to unavailable data.

Station	Year								
	2010	**2011**	**2012**	**2013**	**2014**	**2015**	**2016**	**2017**	**2018**
J	5.32	5.40	5.70	5.68	5.64	5.69	5.70	5.88	5.75
GL	5.44	5.39	5.59						
MH					5.42	5.49	5.64	5.69	5.77
OP	5.96	6.21			5.96	6.05	6.01	5.89	6.05
V	5.60	5.42	5.37	5.45	5.4	5.37	5.40	5.48	5.42
H	5.96	5.92	5.93	5.88	5.94	6.05	5.98	6.36	6.47
BB	5.76	5.63	5.57	5.61	5.55	5.65	5.71	5.79	6.16
LN	5.51	5.77	5.66	5.57	5.44	5.80	5.83	5.97	6.51

All stations had a reasonably low standard deviation of approximately 0.5 across all years. The median values also tracked the mean values very closely, with the minimum value across all stations for all years reported as ∼3.73 (J, 2014). No seasonal variation or correlation with precipitation volume was found.

Salinity The ratio of mean sodium to sulphate concentrations was ∼10 (Figure 5.24), indicating that sea salts dominate rainwater chemistry. The mean sulphate concentration trends generally follow that of sodium concentration, with peaks at the start of the year, decreasing through summer, then rising back up towards the end. The standard deviations are very high (larger than some of the mean values) at ROI stations for some months in both sodium and sulphate. The sites closest to the west coast (MH and V) have particularly high sea salt concentrations. All stations in the ROI had larger maximum concentrations for both ions than stations from NI (Figure 5.25).

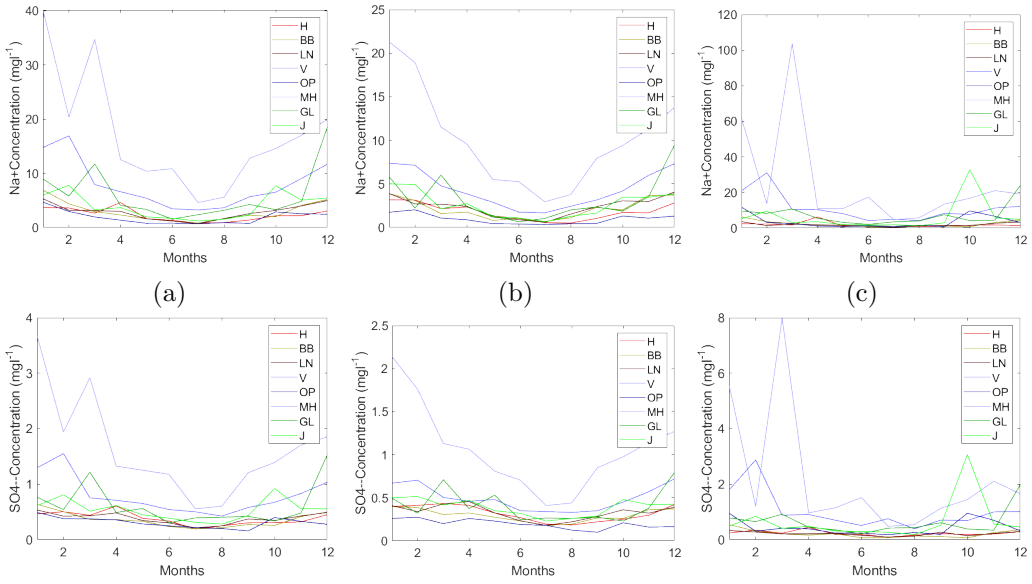

Figure 5.24: Annual variations in the mean (**a**,**d**), median (**b**,**e**) and standard deviation (**c**,**f**) of sodium and sulphate ion concentrations, respectively, in rainwater collected at each site.

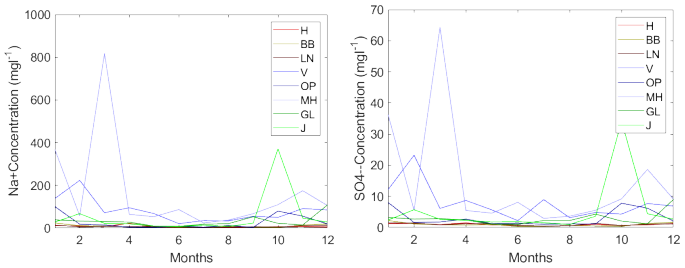

Figure 5.25: Maximum values reported by the stations of sodium (**a**) and sulphate (**b**) ion concentrations in rainwater collected at each site.

5.4 Discussion

5.4.1 Wind

The data presented here broadly support the consensus that rainfall across the west coast is considerably higher. Most rain events had low intensities, with most stations (13/23) reporting a trend of increasing rainfall hours with tip speed. In all instances,

the lowest speed bin (0 ms^{-1}–10 ms^{-1}) had the lowest number of rainfall hours. The rated speed bin usually had either close to or the highest n_A across all stations, with the same increasing trend as rainfall hours. These are likely due to two reasons: firstly, the 90 ms^{-1}–100 ms^{-1} tip speed bin covers a larger wind speed range than any other and, secondly, during rated speed operation, the RPM is higher, meaning more impacts per minute. Other authors have noted the synergistic nature of rain and wind [180, 181]. The exact reason that some stations did not display the trend of increasing rainfall hours with tip speed is unknown as they did not display reduced rainfall nor mean wind speeds [182].

The influence of rated speed rainfall hours on kinetic energy is quite apparent (Figure 5.9) when comparing stations such as MP, MD, and MU with SA. All four stations had similar rainfall hours, yet SA experienced significantly more hours in the 80 ms^{-1}–90 ms^{-1} and 90 ms^{-1}–100 ms^{-1} bins, leading to an increase in kinetic energy of 44–59%. Overall, the equation and data (Figure 5.26) support evidence reported by others that westerly winds carry much of the wet weather and that orographic enhancement plays a significant role, in increasing rain kinetic energy. However, the inclusion of latitude into the equation reduced R^2, conflicting with the hypothesis that there is a significant southerly component. This indicates that the mountains on the west coast and areas exposed to the wet Atlantic weather are more affected by rain erosion [30, 181]. An R^2 value of 0.48 shows that the regression model poorly reflects reality. It is likely that relationships between the geographical parameters and kinetic energy are nonlinear, with other factors such as micro-climates influencing localised weather patterns. The limited number of weather stations investigated here will also have some influence. Furthermore, it is problematic in applying this model to mountainous regions where significant variation is expected and data are limited [159, 162, 165] or in extrapolating it above kinetic energies reported here.

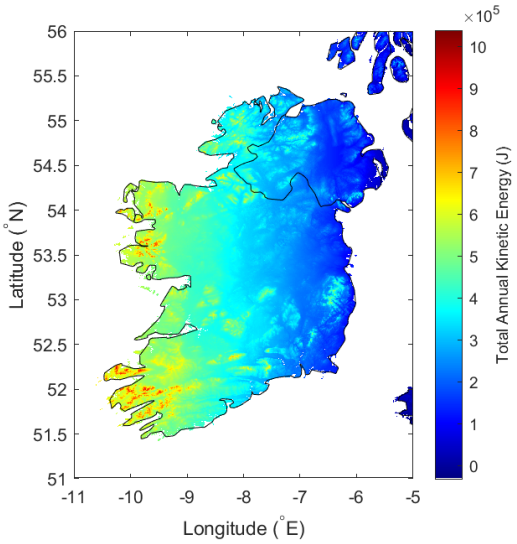

Figure 5.26: A total annual kinetic energy map of the island of Ireland, generated using Equation (5.7), using topographical data obtained from NASA and processed with the READHGT function [14].

When comparing the total annual kinetic energy of sites in Ireland and that produced by Letson et al. [17], the results here display significantly more energy in rain, compared to the sites investigated in the USA, 10^7 Jm^{-2}–10^8 Jm^{-2} vs. 10^1 Jm^{-2}–10^2 Jm^{-2}, respectively. One reason for this will be the temporal resolution of the data. One should consider two separate cases, a 10 min interval (10 mmhr^{-1}) and two 5 min consecutive intervals (20 mmhr^{-1} and 0 mmhr^{-1}). Calculated droplet concentrations, using Equation (5.4), differ significantly and average out to be ∼69 droplets m^{-3} and ∼38 droplets m^{-3}, respectively. Just in this one instance, the same volume of water would have accumulated, but the second case had an average droplet concentration and therefore n equal to 55% of the first case. If a turbine with the same specifications as outlined here, but with $\omega = 15$, the $E_K m^{-2}$ from the first and second cases would be 769 Jm^{-2} and 699 Jm^{-2}, respectively. Therefore, the reduced temporal resolution of the data here will likely lead to an overestimation of the total kinetic energy at each site as well as the n.

The wind speed data are also limited to hourly resolution and so are the average wind speeds throughout that hour and as ω is capped to rated speed, the total kinetic

energy inside the rated speed bin will be overestimated. This is justified as there will be periods during that hour where ω is suboptimal, meaning that the impact speeds will be lower, also reducing n_A. There was no attempt made here to convert to the wind speed at hub height. Hub height wind speed is highly dependent on site-specific characteristics (i.e., local topology, obstructions, wind direction, etc.), and so mapping erosion potential with this conversion would have added considerable complexity [183].

Upon reviewing wind speed data from Letson et al. [17], the selected wind turbine rarely reaches rated speed, although there were sites here with suboptimal wind conditions, such as BA, where rated speed occurred for just 1.6% during rainfall. The total annual impact energy per m^2 is still approximately 20,000 KJm^{-2}. Assuming for 1 h $\omega = 15$, A = 0.01 m^2, D = 100 m and the rain intensity is such that $\lambda = 50$ ($\sim$1 $mmhr^{-1}$), with all droplets having a uniform diameter of 1mm. This would give a kinetic energy concentration of 22,800 Jm^{-2}, far higher than reported by Letson et al. (0.3 Jm^{-2}–50 Jm^{-2}).

The wind turbine RPM curve and blade diameter used should also be considered. Most RPM curves are quite similar in shape but have different rated speed ranges/profiles. The RPM curve taken from Letson et al. may also be for a smaller turbine and, as kinetic energy per impact is proportional to D^2, this would substantially reduce the tip speed, and therefore impact speed, as well as the kinetic energy compared to that reported here [56]. Their model of impact speed (noted as closing velocity), which includes droplet velocity and blade position, could account for some of the difference too, although it would likely lead to an increase in kinetic energy. However, in spite of the limitations of the model produced here, the ability to compare and contrast each site using the rain kinetic energy provides a useful tool in analyzing the relative erosivity.

The data presented here demonstrate no discernible geographical variation in mean or standard deviation of rain droplet diameter. A clear pattern, however, emerged between mean droplet diameter and tip speed. As the lowest mean diameter occurs during the lowest turbine speed (< 10 ms^{-1}), it implies that very low intensity rain is often accompanied by mild wind and that its presence decreases with wind speed. Two

potential reasons for the increase in standard deviation of droplet diameter (Figure 5.11b) could be a broader range of common intensities at higher tip speeds and that the tails of the distributions become shorter. Mean droplet sizes (∼1mm, across all velocities) reported here are 50% lower than those typically used in RET or droplet impact simulations (∼2 mm). During RET, samples are subjected to 25 mmhr^{-1}, high intensity rain, which in nature has a mean droplet diameter of ∼2 mm (as given by the Best distribution). As given by the data, if we accept a mean droplet diameter of ∼1mm with a standard deviation of ∼0.8 mm, then this would cover ∼68% of the total data. This would imply most RET is conducted under unrealistic conditions, especially when considering rain intensities beyond 10 mmhr^{-1} very rarely occur at rated speed.

There is strong annual variation in weather characteristics. Winters are characterized by stronger more consistent winds coupled with significantly more rain. Summers tend to be calmer and, on average, dryer. Interestingly, the majority of high intensity events (> 10 mmhr^{-1}) occur during summer months (Figure 5.27), a phenomenon noted by others [180, 184]. As the model specifically looks at tip speed, rather than wind speed, it makes it difficult to understand whether these high intensity events occur during high (greater than max rated wind speed, ∼16 ms^{-1}) or low winds (less than min rated wind speed, ∼9 ms^{-1}). On further inspection of the raw data, it can be seen that the majority occurred during low wind (0.75 h), fewer during rated speed wind (0.15 h) and a small fraction occurring during high wind (0.01 h).

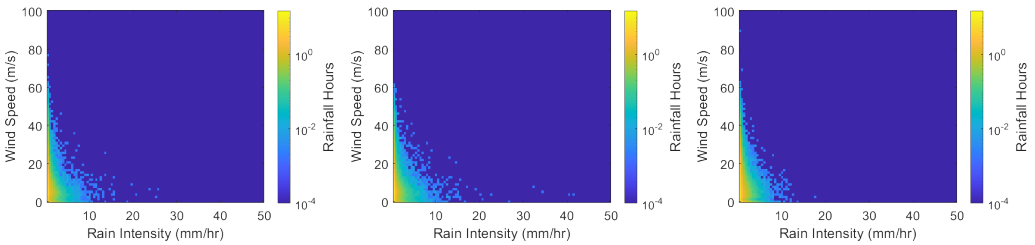

Figure 5.27: Frequency distribution of wind vs. rain data for the months of June (**a**), July (**b**) and December (**c**).

The differences in n_R and kinetic energy between summer and winter months can be explained by the following three reasons: the rated speed bin covers a broader range of

wind speeds, the wind speeds are more consistently reaching rated wind speeds during rainfall events and there is significantly more rain. This is supported by other authors, reporting strong annual variations in wind speed and capacity factor [185, 186], coupled with the change in rainfall [180, 184, 187]. Upon investigating the frequency of each droplet diameter during December and July, the comparison revealed the influence that winter months have on the droplet size distribution, skewing it upwards. During rated speed events, mean droplet diameters across all months were $\sim$1 mm. The pattern observed in mean droplet diameter implies that, during summer months, rainfall is somewhat similar across all speeds, whereas, during winter, rainfall intensity becomes heavier on average with increased tip speed. The exact reasoning for this is unclear; however, it is likely in part due to a change in the hydrological cycle. Furthermore, it can be seen that the majority of the larger droplet sizes ($>$ 3.5 mm, Figure 5.14) that exist are unlikely to occur during high-speed operation. This is particularly important for modelling droplet impacts, in order to understand the upper limit of what is commonly observed in reality. Overall, the data presented here indicate that the kinetic energy of rain is much higher in winter than in summer and that high intensity events are unlikely to contribute significantly to the rain erosion process.

Erosion mitigation strategies, such as ESM, assume that rain erosion is predominantly caused by a limited number of rated speed, high intensity events [65, 183, 188]. By comparing the results here and the results of Bech et al. [65], the $\sim$9 min a year of high intensity rain ($>$ 10 mmhr^{-1}) forecasted would be insufficient for the onset of coating loss at rated speed (79 h at 10 mmhr^{-1}, stated by Bech). Most rain erosion tests typically last longer than an hour at intensities of 25 mmhr^{-1} before the incubation period is completed. However, the time resolution of data used here is very limited and erosion is site specific. As stated by Bech et al., the rain intensity of a 1 h period can vary as much as 10 times for convective rainfall, which although infrequent in and around the British Isles, provides some context. Work on rain radars carried out by Fairman et al. [164, 165] for the British Isles would also suggest that high intensity rainfall rates are more common than observed here (as much as 25 h per year in some locations). So, it is reasonable to assume that higher intensities occur, but are

effectively averaged out. Further work must be carried out to investigate site-specific rainfall rates using higher time resolution methods such as radar, the results of which should be compared to field data.

Not considered here is the influence of the wind itself on the terminal velocity of the droplet and the direction/impact angle of the droplet onto the blade. Wind acting on a droplet would increase droplet velocity, possibly with horizontal components as high as vertical and impact angles relative to the ground of up to 45° [11, 189]. This effect is likely to be of some importance, considering a droplet velocity of up to ∼10 ms^{-1}, which could increase rated speed impacts by up to ∼10% and the kinetic energy by up to ∼23%.

The model and results here are primarily focused on Ireland; however, the concept of generating mathematical models to characterise erosion could be applied to other countries/geographical regions. It is likely that regions with less exposure to marine environments or large water bodies would produce simpler, more accurate linear regression models. Consequently, with reduced exposure to water, there would likely be less rain erosion.

5.4.2 Temperature

Mean and median temperatures during rainfall events across most stations displayed a general trend to increase with rainfall intensity. As explained above, higher intensity events typically occur during summer when temperatures are consistently higher. This caused a skew in the overall distribution of the data and the increasing mean/median temperature with rainfall intensity. High intensity weather events usually occur due to an increased air temperature, increasing the amount of water vapour it can contain. This means high intensity events occur due to more specific conditions, which do not usually occur during winter. The standard deviation reduces as these high intensity events require a more selective set of conditions that are atypical for the Irish climate. However, this is beyond the scope of this chapter.

The mean and median impact/rainfall temperatures remained relatively constant across all speeds at all stations, although with a slight decreasing gradient as tip speed

increased. This is to be expected, as most summer events occurred at lower tip speeds and the converse is true during winter, as discussed above. As expected, there was a reduced temperature at rated tip speed and a higher temperature at lower tip speeds, which can be seen when viewing the differences in minimum and maximum values in the mean. Excluding tip speeds of 0 ms^{-1}–10 ms^{-1}, the minimum/maximum differences range from 0.4 °C–1.9 °C and 0.4°C–2.0 °C, for n and Hrs, respectively.

Stations at higher latitudes and altitudes experienced colder events, leading to a lower mean, as displayed by Equation 5.8 and Figure 5.28. However, mean rainfall temperatures ranged between 7.9 °C and 11.9 °C for rainfall events between 0 mmhr $^{-1}$C and 5 mmhr $^{-1}$C, which is mostly due to Ireland's location, size and orography ($<$ 1040 m). As sites closer to the west coast, with higher altitudes and which are more southerly, experienced more rainfall events, their distributions were more populated. Temperature variations were moderated by proximity to the marine environment, with few regions far from the sea [190], and the linear equation here fails to capture this.

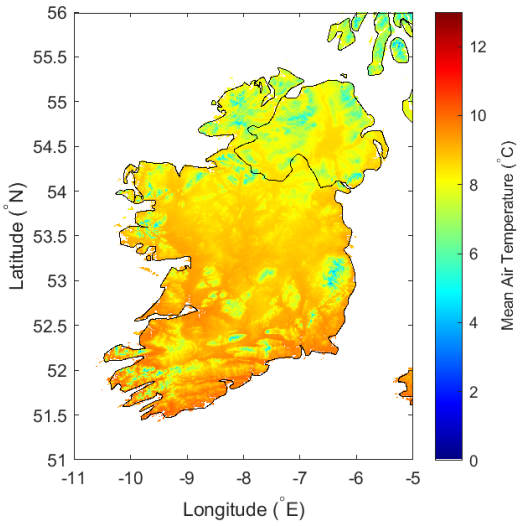

Figure 5.28: A mean air temperature map of the island of Ireland, generated using Equation (5.8), using topographical data obtained from NASA and processed with the READHGT function [14].

The seasonal variation in temperature during rainfall events was to be expected. However, during winter, the trend of a slight increase with rainfall intensity is likely due

to the capacity of the air, when warmer, to hold more moisture. This, in turn, leads to heavier rainfall events occurring during warmer temperature periods [191, 192].

During autumn and winter, the trend of increasing temperature with tip speed is due to warmer (relatively) sea temperatures, which cause westerly, southwesterly and southerly winds travelling over the Atlantic to heat up [181]. Higher temperature gradients, occurring during winter, lead to stronger winds. This can be seen in Figure 5.27, with wind speed data skewed upwards, meaning that rated speed observations are more common, explaining the increase in temperature with wind speed. Typically, in summer, wind speeds are lower because of reduced temperature gradients [190]. This would also explain the increase in standard deviation for winter months, as wind speeds higher than rated speed are more frequent, especially in the decreasing gradient portion of the RPM curve. This in turn means air temperatures are more likely to have more distributed data points in winter than in summer.

Temperature strongly influences the mechanical properties of temperature sensitive polymers [77, 148]. Impacts generating localized heating and fluctuations in air temperature during rainfall may well lead to accelerating the ageing process. As discussed by Pugh et al. [77], Polymeric materials typically used as coatings may have glass transition temperatures in the range of 0 °C–30 °C. In practice, this means the behaviour of coatings will change over the operational range of a wind turbine.

Temperature stated here is the air temperature and as previously discussed, all precipitation is assumed to be rain. There are a limited number of events in the data, where the temperature falls below 0 °C and, as noted by others, snowfall is a small proportion of overall precipitation in Ireland [180]. This assumption, therefore, did not skew the results.

5.4.3 Humidity

Higher intensity rainfall events tend to occur when atmospheric humidity is increased, as is shown by the data. This is in part because higher intensity events require increased levels of water vapour in the air, but also partly because when rain falls, evaporation begins, increasing ground level humidity. The data presented show a strong latitude

and altitude influence (Figure 5.29) and, as above, humidity is strongly influenced by proximity to the coast. These factors mean that the linear regression model (Equation (5.9)) failed to capture the nonlinear geospatial variance of humidity, which explains the low coefficient of determination (0.52). This failure is highlighted by mountainous regions finding poor representation, leading to humidities of above 100%.

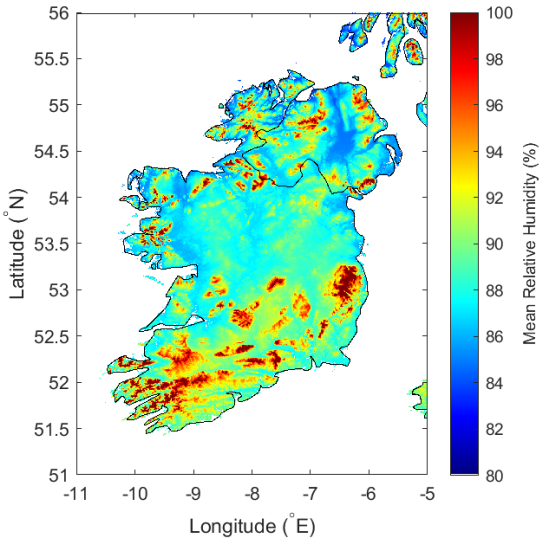

Figure 5.29: A mean relative humidity map of the island of Ireland, generated using Equation (5.9), using topographical data obtained from NASA and processed with the READHGT function [14].

It was expected that RH data reported at stations would decrease with tip speed, partially due to rainfall seasonality, with summers having higher rain intensities at lower wind or tip speeds. These high intensity events would also explain the increased standard deviation in summer months at lower speeds compared to winter. The trends observed in Figure 5.23 of a decreasing mean humidity with tip speed conflict with the results of Figure 5.15 as they indicate that mean rain intensity decreases with tip speed. According to the Penman evaporation potential theory, evaporation rates are dependent on humidity, wind speed and air temperature [193]. Summers are characterised by increased temperatures, reduced RH and lower wind speeds, whereas winters are characterised by reduced temperatures, higher RH and higher wind speeds, with more rain

events at the rated speed [194]. It is possible that this complex process of evaporation may account for the variations experienced here; however, investigating this is beyond the scope of this chapter.

During impacts from projectiles, heat is generated in the target material. Humidity can enhance the heat transfer from materials into the surrounding air, influencing the erosion process, particularly with high impact rates [195]. Humidity is a problem for polymers, causing degradation through hydrolysis and water ingress. This process can be catalysed by salts, reducing the mechanical properties of wind turbine blade materials and enhancing erosion damage [146, 147, 156].

5.4.4 Composition

Due to the limited number of stations available, no reliable geographical correlation was attainable for either pH or ion concentration. Ahern and Farrell [159] reported an increase in anthropogenic pollutants towards mainland Europe with mean pH values in the range 4.62–5.25, with a weighted mean of 4.98, for the 1994–1998 period. The values reported here are far higher and over the last 22 years, emission compositions across Europe have significantly changed, making their results incomparable. All stations here reported only slightly acidic pH levels, meaning any influence is likely to be limited. There was no apparent seasonal variation in pH levels nor was there a discernible year-on-year trend in ion concentration.

As most sodium within rainwater is of marine origin, and the ratio of sodium to sulphate ions is quite large, this indicates precipitation chemistry is dominated by marine ions. The stations are also all relatively close to the sea. This limits the applicability of the results to inland regions. However, it highlights the significance for onshore parks in coastal countries such as Ireland, the UK, Denmark, etc., as well as offshore parks. The saline content, across all stations, is much higher during the winter than summer when precipitation levels are much higher. Sea salt aerosol generation is controlled by the wind, which generates waves, splashing onto rocks and breaking. This forms bubbles and foam, which in turn generates aerosols. A more detailed explanation is available from Tryso et al. [160].

Malin Head and Valentia typically have higher sea salt concentrations, likely explained by their proximity to the west coast. During the winter months, the westerly Atlantic winds begin to pick up, driving sea salt production. All ROI stations had larger maximum values than NI stations, largely due to data collection methods. In NI, data are collected over multi-day periods compared to ROI, where data are collected on a daily basis. Therefore, the NI data average out any large peaks that would otherwise occur, which explains why the mean and median values are of the same magnitude.

As noted by Rasool et al. [156], data from RET experiments show enhanced degradation in both the presence of saline and acidic solutions. Pugh et al. [154, 155] support this, noting that the presence of salt within the working fluid appears to enhance rain erosion through the crystallisation of salts on the surface. The data presented by Law and Koutsos [12] support this with wind parks closer to the coast displaying more severe damage in a shorter period than those in remote regions. Law and Koutsos also investigated sites with nearby quarries, which displayed enhanced erosion. This could be due to the high particulate matter air pollution present in areas with operating quarries. Networks such as the EMEP are unsuitable for determining these relationships with their reduced station numbers, remotely located from strong pollution or particulate sources.

Research indicates that lower humidities lead to increased levels of pollen, PM2.5 and PM10 particulates in the air and that deposition is far higher during rainfall events. Therefore, the results here imply more chemical and particulate depositions occur during lower wind speed rainfall events [196–198].

With this observation network and the concerted effort over the past 50 years to reduce acid rain prevalence within Europe, rain pH is likely to remain constant or increase. Salt content, however, probably will not change and the influence and prevalence of particulates and other pollutants require further investigation.

Currently, there is a lack of understanding of synergistic effects between chemical components, temperature, humidity and other testing parameters. To the authors' knowledge, there have been no RET studies which have sought to monitor the combined influence of water composition, temperature and humidity on rain erosion, with only

a few studies investigating acid rain or artificial seawater. This highlights the lack of understanding of these synergistic effects. With the expansion into offshore in and around the UK as well as elsewhere, further work is required.

5.4.5 Galway Wind Park

Using the model data presented here, Galway wind park is placed in a moderate-highly erosive environment, with a total annual rain kinetic energy of ∼585 kJ and, during rated speed impacts (> 90 ms^{-1}), a mean humidity and temperature of ∼94% and ∼7.6 °C, respectively. Based on the results, this would also likely receive 10^6–10^8 impacts, but it was not possible to develop a model and give a prediction. Without field data, model validation is not possible. Further work on temperature and humidity effects is required to understand their relationship to erosion.

5.5 Conclusion

Presented here is the first attempt to geospatially map erosion environments and erosivity over the island of Ireland. The models developed here suggest that the western region of Ireland is a particularly erosive environment, especially in the mountainous regions west of Cork, i.e., Kerry and Galway, where kinetic energy was predicted to be the highest. Common impact numbers estimated using the rain texture model and RPM curve ranged between 10^6 and 10^8. The warmer southern regions are much less susceptible to cold weather events (0 °C–5 °C) compared to the northern and elevated regions, which will likely lead to differences in the erosion performance of some materials. The more humid, mountainous regions imply that chemical deposition may be less likely during rainfall events, but also indicate that material performance may be reduced. Coastal regions are much more susceptible to chemical attacks, with blade materials and coatings potentially undergoing enhanced hydrolysis. Acid rain is likely to be of limited influence due to the neutrality of pH values observed over Ireland. Overall, the results here indicate that mountainous regions are the most likely to experience severe erosion, especially in the west/southwest of Ireland. However, further

work is required in order to confirm this.

Importantly, the results of this chapter suggest that RET protocols, such as [71, 72], should be revisited. The influence of using unrealistic rain intensities and droplet diameters is unknown and, with the time dependent nature of viscoelastic materials, this could be key to further understanding rain erosion. The test chamber humidity should be recorded and further work investigating the influences of rain intensity, temperature, humidity, composition as well as droplet diameter should be undertaken. Complex architectures of viscoelastic materials layered in coating systems mean these factors should not be overlooked. Future RET studies should also focus on understanding the influence of synergistic effects of the environment on rain erosion.

Seasonal variations in both rain kinetic energy, temperature, humidity and chemical composition indicate that erosion occurs differently depending on the time of year. Rainfall amounts are significantly reduced in the summer and enhanced in the winter in terms of rain events. Rainfall intensities peak in the summer; however, this is usually with suboptimal wind speeds. The majority of rainfall intensities are low and, according to the analysed data, rated speed, high intensity events, at > 10 mmhr^{-1}, are unlikely to occur, especially in winter. At rated speed, temperatures and humidities are often much lower during winter than summer, which will influence material performance. Sea salt aerosols are much more prevalent during winter months, which, when combined with the decreased humidity at rated speeds, could lead to increased depositions and therefore enhance damage processes. The results here indicate that the erosion process is much more severe during winter.

The limitations of the study can be summarised as follows:

- Limited data time resolution likely led to overestimates in both rain kinetic energy and impact numbers, which in some cases could be 10 and 82% higher, respectively.

- The reduced number of stations reduced the accuracy of the models and monthly estimates. There was also a lack of weather station data from higher altitudes, which created bigger uncertainties for extrapolating the models.

- Data were measured at ground height or at 10m for wind speed. In future, it would be desirable to either use a conversion to estimate hub height parameters or to measure data at closer altitudes to hub height.

- The wind turbine RPM curve used was not necessarily applicable. As RPM curves are highly dependent on wind characteristics, this may cause more or less degradation than predicted here, producing uncertainty in the model.

- The limited number of chemical analysis stations meant that characterising the rain chemistry geographically and with time proved difficult. This meant generalisation of their results was not possible. This could be resolved through the use of more stations or a chemical deposition model.

- Linear regression was likely unsuitable for modelling these impact condition parameters geospatially. In future, using either nonlinear regression models, RADAR data or numerical weather prediction models to estimate site-specific erosion would provide a more accurate representation of the impact conditions and improve the reliability of rain erosion modelling.

The limitations highlighted above present the challenges in the current framework used to characterise the erosivity of a selected location and how this varies over time. However they do provide an insight into what conditions occur on the ground. Future work should seek to investigate the sensitivity of the framework to the time resolution of the data, as well as the use of methods to capture a finer spatial resolution. This would provide a greater insight into the reliability of the results produced here.

Due to the inherently complex nature of weather processes, the models here cannot be generalised, however, through the use of numerical weather prediction models or RADAR data, the framework for analysing rain erosion can be. Future work should focus on developing the approach for the use of geospatial weather data to allow for this.

The current droplet size distribution and rain texture model used is a key area for improvement additionally, as rain generation depends on far more than just a single

input parameter. This will likely require the use of meteorological field data and/or the use of more advanced droplet size distribution models. Additionally, making sure to adjust for hub height differences.

Understanding the geospatial variance of rain erosion will be key in understanding and optimising Operations and Maintenance campaigns for LEPs and understanding risk to the turbines.

More laboratory work aiming to characterise the influence of impact conditions on RET results will be critical and could explain the variation in lifetime seen in the field.

Finally, there must be a high level focus to combine these research topics with cost modelling approaches into a useful tool for determining and ultimately increasing the lifetimes of wind turbine blade materials, as well as optimising inspection and maintenance scheduling.

Chapter 6

Rain Erosion Test Rig Development

6.1 Introduction

The rain erosion problem was initially discovered in steam turbines (1920s) and aeroplanes (1940s), in the USA and UK [199]. High speed impacts during flight were particularly dangerous as droplets would damage wind screens or RADAR radomes, limiting a pilot's ability to safely operate planes. Extensive testing campaigns throughout the 20th century sought to almost eliminate the problem altogether, developing materials such as ceramics able to withstand repeated impacts [67].

The development and expansion of wind turbines over the last 40 years has led to a massive increase in turbine blade size. By 2014, blade tip speeds had reached as high as $\sim$ 110m/s [35], with speeds projected to further increase. This increase in size combined with the expected lifetime of a wind turbine blade (20-25 years) has led to the reemergence of rain erosion as an issue for composite wind turbine blades.

6.2 Rain Erosion Testing

Early rain erosion testing began with the "Wheel and Jet" rig in the 1920s. Testing later moved onto the whirling arm rain erosion rig, beginning in 1946 [67]. Later, in an

attempt to reduce costs and simplify testing, researchers attempted to develop alternative methods, one of the most prominent being the jet impingement rig. However, large performance discrepancies between them and whirling arm rigs, hindered their popularity. Researchers have since sought to investigate jet impingement devices further, improving upon previous designs and correcting these inconsistencies [57]. Numerous other methods have been developed over the years including rocket sleds, ballistics tests, etc[200, 201]. Rain erosion testing methods can broadly be broken down into two main categories; jet impingement or droplet impingement.

The main distinctions between these two types are in projectile shape and volume. Typically for droplet impingement devices, the sample impacts a static or slow moving liquid droplet, whereas for jet impingement, a high velocity water jet impacts a static or slow moving target. Jet impingement devices typically fire a body of water in the form of a continuous stream of liquid, a discreet unit (slug) and others have produced more chaotic flows of water that essentially form a mist of droplets, with some even intentionally using mists instead.

It should clearly be stated here that this is in no way an exhaustive review of all rain erosion testing methods, but instead was used to determine the most appropriate rain erosion testing method available.

6.2.1 Jet Impingement

6.2.1.1 Wheel and jet

As mentioned above, the wheel and jet rain erosion rig is the earliest known rain erosion test rig. It featured a continuous water jet which impacts the surface of a sample. Samples were attached to a wheel, which rotated at a fast speed creating a high velocity differential between the sample and jet, allowing for periodic exposure [57].

6.2.1.2 Single Impact Jet Apparatus (SIJA) and Multiple Impact Jet Apparatus (MIJA)

The Single Impact Jet Apparatus or SIJA system operates by firing a single coherent water jet at a static sample. The jet is formed by filling a small cavity with water, the cavity is backed by a neoprene diaphragm. During operation, the diaphragm is struck by a lead slug fired from a converted air rifle. Once struck, the water is ejected from the cavity via a nozzle, reaching speeds of up to 1000ms-1 [67].

The reduced complexity of using an excited jet of water and having a static sample, compared with droplets impacting by a moving object, such as a projectile or whirling arm is a significant advantage. The SIJA also mitigates the turbulence and boundary layers generated by large (relative to a droplet) objects moving through air, such as those from whirling arms, which can cause droplet distortion or breakup [11, 67], hindering the reliability of results. With jet impingement rigs, whereby the jet of water is the only object moving quickly, there is comparatively little air disturbance, making the impact process simpler in some respects to reproduce. Issues remain, however, in that impacts from spherical droplets vs. jets have significantly different contact profiles and, therefore, pressure distributions and that controlling the jet shape is challenging [76].

Additionally as discussed by Springer [11], fast-moving droplets tend to shatter, due to the aerodynamic forces being greater than the surface tension forces holding them together. For droplets in the size range of 0.5mm - 5mm, shattering velocities range from 10m/s - 40m/s. Although a droplet shape differs from a water jet, the physics still apply, especially when considering impingement velocity would be in the range of 80m/s - 150m/s. Thus during the jet production and flight, distortion of the jet shape and its leading edge would occur. Research by Doagou-Rad and Mishnaevsky Jr [202] suggests that droplet shape influences the pressure distribution too, suggesting significant geometric changes caused by the different initial shape of the jet or changes that occur during flight and prior to impact will affect the damage evolution.

The Multiple Impact Jet Apparatus or MIJA was an upgraded form of the SIJA, allowing for multiple or repeated impacts to be automated. It also provided a more

consistent jet velocity and contact profile, as well as more precise control of the impact location [67].

6.2.1.3 Discrete Jet

Discrete jets are essentially a continuous jet rig, however, they have a rotating disk with one or multiple holes in. The period of time between the jet encountering each hole gives the impact rate, which can be tailored to any rate within reason. The jet velocity is flexible and recent improvements have allowed multiple samples to be tested by attaching samples to a wheel (similarly to the wheel and jet rig). Problems have generally arisen in the difficulty of characterising and controlling the shape and volume of the slug of water impacting the samples surface leading to significant material performance differences between this and the whirling arm rig [57].

6.2.2 Droplet Impingement

This section will mostly discuss water droplet impingement, however devices that have also used solid projectiles instead such as the Single Point Impact Fatigue Tester (SPIFT) rig will also be mentioned here [76, 203, 204]. Although the setup of the SPIFT is much more similar to a jet impingement, the shape of the projectile more closely resembles a droplet.

6.2.2.1 Whirling arm

The whirling arm rain erosion test rig is a device that essentially comprises of a propeller like sample holder, typically with 1, 2 or 3 blades. This propeller has samples attached to it's blades either in the form of coupons or profiles. Normally, An artificial rain field is generated using hypodermic needles which produce droplets of a given size, although variations in the past have also used jets. The propeller rotates inside of this rain field, with repeated droplet impacts causing erosion.

Centrifugal forces are an issue present in rotating objects, more specifically in whirling arm rain erosion test rigs. During operation, wind turbine blades have large spars that bear most of the centrifugal loading and are so long that whilst the tangential

speed is the same, the centrifugal force is proportional to the square of rotational speed multiplied by the rotational radius (ωr, 6.1). Therefore the residual forces experienced by the tested materials tend to be lower than those observed in real wind turbines.

$$F = mv^2/r = m\omega^2 r \tag{6.1}$$

During experiments using the Dornier whirling arm rig (D=2.4m), centrifugal forces were observed to influence the results of ductile and brittle substances above 400ms-1 and 600ms-1, respectively [67]. Using equation 6.1, with the same tip speed one can see that as rig diameter increases forces decrease, as do smaller/lighter samples. The sample size for the Dornier rig is 16.8mm diameter. Larger samples on smaller rigs, would therefore be more susceptible to the effects of centrifugal force. However, for wind turbine blades maximum tip speeds are significantly lower than those tested (Max tip speed is 100-150ms^{-1}).

6.2.2.2 Ballistic range

Various different setups over the years have used a ballistic range. Typically, a projectile containing a sample is fired at very high speeds ranging from Mach 2 - 6kms^{-1}. Originally, a natural rain field was used, later changing to an artificial rain field, likely for control and consistency reasons. Tests operated over short distances and time periods and generally, this method was favoured with it's controlled conditions. However, it is likely that costs and challenges with data capture limited its use [67, 200, 201]. Similarly, another method firing a sabot at a suspended droplet, using for example a fine web of perspex in aniline gained some popularity. After hitting the target, the sample would decelerate using velocity reduction tube. The speed of the projectile generates a shock wave destroying the web. Concerns around droplet distortion led to the use of a falling droplet (80% water, 20% ethylene glycol) inside a very low pressure chamber, instead. Both methods discussed here were very costly.

6.2.2.3 Rocket sled

In the USA, a desire to test significant parts of the aerodynamic structure of components at very high speeds (much higher than whirling arm rigs) led to the development of the rocket sled method. The centrifugal forces generated in whirling arm type rigs limited their top speed, which the rocket sled rig overcame. Reduced test times and enormous costs restricted its wider use. The name is relatively self explanatory, however for the avoidance of doubt, the rig consists of an aerodynamic structure (the test sample) which is attached to a monorail sled. Attached to the sled are solid propellant rockets, which when fired causes the sled to accelerate passing through an artificially generated rain field which is typically at least several kilometers long [67].

6.2.2.4 Wind tunnel

Attempts have been made to create a rain erosion testing facility using a wind tunnel with water injected into it, creating droplets that then impact an aerofoil. During initial testing, a layer of water developed on the specimen, meaning that the injector had to be oscillated in horizontal and vertical plane, to mitigate this. The impact speed range was limited to between 200-275ms^{-1}, with test times restricted to around 100s. The number of droplet impacts was significantly higher than would normally appear in nature and controlling droplet diameter uniformity was not possible [67, 75].

6.2.2.5 Solid particle impacts and SPIFT

The impact mechanics of a solid particle impact are significantly different to a liquid droplet impact. In a liquid, the forces holding the droplet together are weaker than in a solid. What's more during the liquid impact process, the point at which the contact edge slows down and is overtaken by the shock wave generated inside the droplet lateral, jetting occurs. This generates large shear forces between the fluid and the surface of the target and is not present during solid particle impacts.

However, in spite of this, attempts have been made to simulate rain erosion using polymer spheres. The reasoning for using solid particle impacts over liquid particle impacts is the ability to control the process more easily. For example, it is far easier

to have a static target and fire a solid sphere, producing repeatable results than it is using a liquid projectile, which will likely distort and possibly breakup during the firing process. Further still, it is possible with this technique to monitor the rain erosion process in more depth, with the ability to capture key insights into, for example, the acoustic waves emissions during the impact process [67, 76, 203, 204].

6.2.3 Summary

Rain erosion testing is currently limited by both the inconsistency between testing facilities and the inability to test more appropriate and valid conditions. This then constricts the development of objective models and equations for the process. Furthermore, current testing facilities do not monitor enough of the process to clearly understand the reasons for disparities between facilities. The current testing facilities at Strathclyde were also insufficient for testing at the required speeds, with centrifugal forces and rotational speeds being increasingly high for the size of the current rig (0.6m diameter). Nor does the rig monitor or allow the control of many of the necessary test parameters. It is for these reasons it was deemed necessary to develop a new rain erosion testing facility.

Upon reviewing the available literature and reading further more in depth reviews on the subject [57, 67] the choices were narrowed down to either developing a jet impingement (likely in the format of MIJA) or whirling arm rig. It is hoped that these new facilities will allow for:

- enhanced testing capability at the university, allowing more extensive published research
- testing of conditions and testing regimes that are currently not investigated
- testing of different working fluids that are not currently investigated

Further to the above research, LM WindPower (Denmark) were consulted directly as well as testing standards for leading edge erosion [71, 72]. LM WindPower were responsible for developing the DNVGL testing standards for rain erosion testing [72].

6.3 Version 1

6.4 Design and Optimisation

6.4.1 Initial Design Conception

The focus of rain erosion research at Strathclyde was the wind turbine sector and more specifically, for the Tribos research group; understanding and characterising the rain erosion phenomenon. The proposal was to improve current testing facilities, which would allow more accurate testing of the materials and coatings of larger, newer wind turbine blade materials that would experience much higher tip speeds in operation. Specific objectives for the design of the new testing facilities were outlined as follows:

- Impact speed test range should significantly increase (currently $\leq 60ms^{-1}$)
- Increase the sample size and shape options (currently 25mm x 25mm, square coupon)
- Ensure safe operation and control
- Ensure modularity and that testing conditions can be easily monitored and modified
- Allow for use of different working fluids

As stated above 6.2, there have been a multitude of methods employed over the years to simulate liquid droplet erosion. After reviewing the available methods, the choices were whittled down to: a multiple impact jet impingement device and to a whirling arm rain erosion test rig. These two options will be discussed here further, with the respective advantages and disadvantages summarised.

For wind turbine blades, rain erosion is typically tested using a whirling arm rain erosion test rig. There has been motivation in the industry to consolidate and standardise erosion testing with ASTM and DNVGL developing technical standards and result reporting [71, 72]. They have sought to eliminate the wide variation in results

reported from test rigs of the same design, or different test rigs that have used the same testing parameters. However even after their development variation is still present [72].

The second most common method has been water jet impingement. However, as stated above complications in relating jet impingement results to whirling arm results have been troublesome. However, there is generally a drive to develop this testing methodology further as it would allow significant testing cost reductions over whirling arm type rigs. Whirling arm rig design complexity and stringent safety requirements presents a challenge for most and generally a specialised facility is required to house them. Mechanistically, jet impingement rigs produce damage differently and until this problem is resolved, results from this test regime lack credibility [67, 95]. Summarised below are the main advantages and disadvantages 6.1.

Table 6.1: The main advantages and disadvantages of both rig types here are considered and summarised.

Rig Type	Advantages	Disadvantages
Whirling Arm	• More accurate results/process more closely resembles the natural process, with results correlating with in-flight data from the aerospace sector	• Expensive • Requires safety equipment • Complex design
Jet Impingement	• Cheaper manufacture • Inherently safer • Flexible sample geometry • Simple Operation	• Poor correlation with results from whirling arm rigs • Different impact mechanics

Based on benefits, limitations and risks, a new whirling arm rain erosion test rig was decided upon over a jet impingement rig. The main deciding factor was the reliability of results produced that could be correlated with the real rain erosion process. This led to some early design concept drawings which formed version 1 of the rain erosion test rig (See Appendix A, Figure A.1).

6.4.2 Required Operational Capabilities (Design Table)

The design was developed by identifying the main design aspects and scoring them based on design value, D, cost, C and risk, R. Design value was defined as the benefit it would add to the overall design; for example in order to produce more system flexibility, Multi functionality and produce more reliable higher quality results. Cost was defined in terms of monetary value, increased workload and difficulty to implement. Risk was defined as risk to safety and risk of failure, in terms of either to the project or the specific task. These parameters were given a weighting, W, reflecting their relative importance. The total score, S, was calculated using equation 6.2.

$$S = W_{DV} * D - W_C * C + W_R * R \tag{6.2}$$

The total score of each of design aspect was then used to develop the design further. Any of the design specification requirements which were rated 10 in any category were primary requirements. These were identified as remaining within the project budget, ensuring personnel safety through a safe enclosure design and the use of an aerofoil sample shape. The first two are relatively self-explanatory and therefore do not require further discussion. However, the third needs further explanation. The use of an aerofoil profile is essential for high speed operation, allowing drag reduction and thus power requirements, compared to flat samples. The use of a symmetric shape ensures that there are no lift forces and so there are little-to-no vertical forces or moments that could cause early fatigue or failure. Additionally, there is evidence uneven aerodynamic forces around the sample holder can lead to changes in air circulation within a whirling arm rig, which may reduce the reliability of RET results [205]. The smooth aerodynamic profile reduces turbulence and therefore encourages more reliable results, reducing the chance of droplet distortion or breakup. As shown in Finnegan et al. [75], sample geometry is critical to the impact characteristics of the test rig and the use of flat plate profiles can also lead to premature droplet formation. Aspects like aesthetics, mass and user friendliness were deemed less important and so improvement in these areas would be a bi-product of other aspects. For example, for the mass design aspect; modularity

would mean that a high total mass would not be an issue because component mass would be low enough for transport; and the enclosure safety, multiple working fluids, turbulent airflow, vibrations and tip speed aspects would mean that the rig is sufficiently large, safe and would use materials like stainless steel in construction, resulting in a high overall mass.

Table 6.2: Binary Weighted Design Matrix. Values for Weightings, Design Value, Cost and Risk were between 1-10.

No.	Parameter	Desired Result	Design Value	Cost	Risk	Total Score
	Weights		6	7	8	
1	Distance from rotational centre to middle of sample	Large as possible to reduce centripetal forces	7	3	1	29
2	Gauge length	$\geq$ 0.2m	9	3	2	49
3	Exposure zone	$>$ gauge length	9	3	2	49
4	Minimum sample size (gauge length + extra)	$\geq$ exposure zone	8	3	2	43
5	System balance	Reduce fatigue caused by imbalances	3	3	8	61
6	Vibrations	User comfort & no resonant frequencies within op. range	2	2	8	62
7	Sample holder mass	Minimal mass to reduce kinetic energy from broken off projectiles during op.	1	1	9	71
8	Sample thickness	2mm	6	1	2	45
9	Rainfield dimensions	Raindrops fall onto exposure zone only	8	1	1	49
10	Sample shape	Aerofoil profile	10	3	1	47
11	Tip speed	Up to 150ms^{-1}	9	2	3	64
12	Sample number	2 or 3	9	1	1	55
13	Aesthetics	Looks professional	3	4	1	-2
14	User friendly	Easy to use	6	4	1	16
15	Budget	Remain within budget	1	1	10	79
16	Turbulent air flow	Low as possible	8	5	7	69
17	Size	Must fit inside available space	6	5	8	65
18	Modularity	Easy to modify and change parts	7	3	3	45
19	Mass	Heavy enough so won't move during op., but light enough so can be moved	1	1	1	7
20	Sensors/Environmental monitoring	Operator should know environmental conditions during op.	8	2	4	66
21	Enclosure safety	Must be safe to operate	1	3	10	65
22	Multiple working fluids	Use of multiple working fluids (salt water, acid rain, water, etc.)	7	1	1	43
23	Drainage	Sufficient drainage to reduce chances of sitting water	7	2	2	44
24	Droplet diameter variation	Allow for the use of different droplet sizes	6	1	1	37

6.4.3 Concept Design Development

In this next section, the design process will be discussed with the two higher complexity components analysed in detail as well as each main sub-assembly having its own individual section. The design process was an iterative design process, which in nature is generally recursive. The design section will be structured in the following order: firstly the design of the rotating components will be outlined; secondly, a section on the enclosure and structural frame; thirdly, the more hands-on approach of developing the drive train will be detailed, selecting of off-the-shelf components without CAD drawings; fourthly, the balancing system and vibrations were then discussed; finally, the design was completed with design of the artificial rain field, water network and any electrical components or systems that were included. The design was initially developed based on a selected operation location, however this location later changed. By this point construction had begun and so main parameters of the initial design were maintained. The manufacture of the test rig will not be discussed in detail as the majority of the work was either carried out by the Mechanical and Aerospace Engineering workshop team or by external engineering firms. The design process will be followed by a section discussing the testing of the test rig and the subsequent failure of a component during testing. This chapter will then be finished with a section regarding the respective redesign of the failed component, the subsequent manufacture of this component and will be summarised with a general discussion and some conclusions.

It is worth highlighting here that some of the simulation work required technical skills beyond the scope of the author and so these were outsourced to another researcher with specialist skills in complex simulations (Mr. Iain Buchanan). Two main aspects required this investigation: 3D flow simulations for the air inside the enclosure and impact safety simulations for the situation of a loose component impacting the outer enclosure, both simulated at peak operational speed. As they were not carried out by the author, they will not be featured here. The 3D Computational Fluid Dynamics (CFD) flow simulations focused on reducing the turbulence intensity of the air inside the rig during maximum speed (2100rpm or 150m/s at the middle of the sample) for a range of different enclosure sizes (Figure 6.1). The design of the enclosure and access

door will be discussed in more detail below.

Further to this, there was a second, flat sample holder designed for the testing of flat samples. This will not be discusses here either, nor will the testing of this sample holder in significant detail.

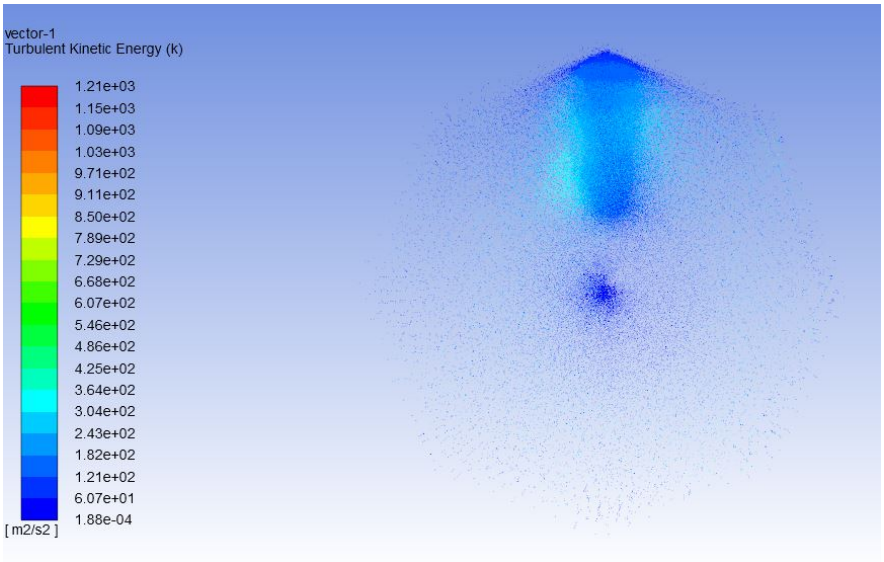

Figure 6.1: Top view of the rig showing Turbulence kinetic energy as calculated for 3D flow simulations during design optimisation using ANSYS for 2.6m diameter enclosure at rotational speed of 2100rpm.

6.5 Rotating Components

6.5.1 Introduction

This section mainly discusses the design process for the rotating components mounted on top of the main bearing. Minimising the generated turbulence, whilst also reducing the mass of any rotating components were of key concern here. Reducing turbulence generated inside the enclosure would lessen the chance of droplets being distorted or shattered during testing and would make it easier to characterise the environment inside the rig, therefore keeping results more controllable. It was decided for this reason that two sample holders would be used instead of three, which would also reduce the shadowing effect [72]. Reducing the mass of the sample holders and the disc would

reduce the centrifugal stresses experienced by the components, increasing component life expectancy. Lower component masses would reduce the kinetic energy and therefore danger of an impact from a loose or damaged component during testing.

6.5.2 Plate

6.5.2.1 Methodology: Design

The fixation of the sample holders to the drive train was identified as a key component. Following the DNVGL-RP-0171 [72], the radial position of the centre of the specimen needed to be as large as possible to reduce the centrifugal forces that would act on the sample. Initially, long sample holders were considered, but this was quickly discounted as it would add significant expense to the manufacture, without notable benefit. Similarly to some other whirling arm rigs, a central hub disc was instead selected for mounting the sample holders to, which was an easier to manufacture, more cost-effective alternative. It also made the design more modular, allowing for interchangeable sample holders. In addition, it distributed more mass over the rotating sub-assembly and providing a space for counter balancing weights, making it easier to balance. A disc shape also reduced the drag generated allowing a lower power electric motor to be selected.

6.5.2.2 Methodology: Shape and Assembly

There were several challenges that complicated the design of the plate. Reducing Costs through internal manufacturing was preferred, as it additionally allowed more design flexibility. However, there were dimensional restrictions. Reducing sample holder length was another consideration, however this increased the diameter of the disc. A diameter of 1.2m was selected with a thickness of 20mm. Different thicknesses and diameters of the disc were not considered. Three design concepts were initially considered: One large disc, 2 disc halves that would be fixed together or large arm sample holders (however this option was quickly discounted for the reasons stated above). Two additional design features were necessary; firstly, A method of balancing was necessary and secondly, a

method of housing the sensors mounted on the rig was required, both of which will be discussed in sections 6.8.2.2) and 6.9.2, respectively.

6.5.2.3 Methodology: Material

Material selection for the disc required some consideration:

- Mass, low enough for safety, ease of starting the machine and handling (including assembly/disassembly)
- Corrosion, frequent exposure to water and infrequent exposure to dilute acids and artificial seawater
- Strength and fatigue resistance, high cyclic loads during operation
- Costs and machineability

Two materials fit the material specification: high strength, aerospace grades of aluminium (Al) and high strength grades of stainless steel (SS).

Aluminium properties vary greatly from common 1000 series grades (99% Al) to the specialist 7000 series grades (typically the highest strength to weight ratio). This application required a high strength to weight ratio, therefore the 7000 series alloys were investigated. High tensile strength and good corrosion resistance were prioritised, with 7000 series tensile strengths ranging from $275MPA - 710MPA$, with densities of 2.7 and varying degrees of corrosion resistance. Operational conditions meant stress corrosion cracking and fatigue were also of concern [206].

Most common grades of stainless steel typically have ultimate tensile strengths of between $400-650MPA$ with densities of $8g/cm^3$, 2ith precipitation hardened grades of $1000MPA$. However, machineability is a challenge, in their hardened form. Machining typically occurs in the annealed form, followed by a heat treatment. Corrosion resistance in stainless steels is superior to aluminium in most cases too[207, 208]. Although initially considered a suitable material for the clamping plate, for both configurations the mass of the disc was deemed too high and increased complexities around heat treating led to Al7075-T7531 being selected as the material for the hub disc.

6.5.2.4 Methodology: Design Iterations

A feasibility study, using Finite Element Analysis (FEA), was conducted to investigate the design options available; the clamping plate design and solid plate design. The model was fixed using the inner bolt holes mimicking the bolted connection to the Mercedes van rear wheel hub. The solid plate was simulated initially (Figure 6.2). For the clamping plate configuration, A bonded connection was initially simulated which would conservatively estimate the stresses on the clamping plate, aiming to assess the feasibility of this design. The clamping plate was simulated as both Al-7075 and SS-316. The design with the clamping plate was then simulated with the pins located where the bolt holes pass through the clamping plate and the hub plate and with the no penetration bonding model. The material properties of the pins were defined as SS-304 bolts. The mesh for all simulations were set to fine. Settings for the simulation can be found in table 6.3.

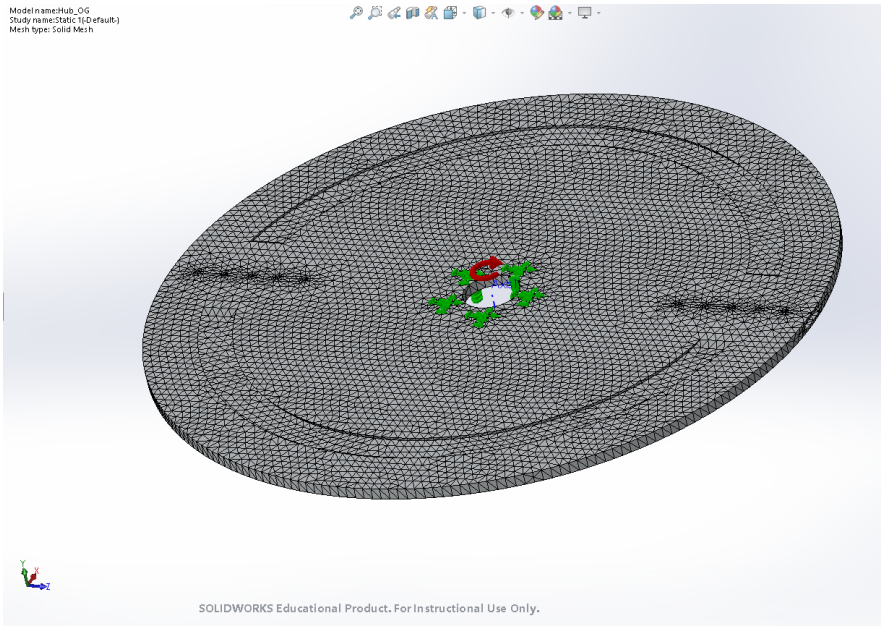

Figure 6.2: Setup of the solid plate FEA Model.

As tip speeds are increasing, it is appropriate to ensure that test speeds are high enough to cover the range experienced by rain erosion protection systems. A sample holder speed of 150m/s was selected for this reason and the required rotational speed

in rpm was calculated using equation 5.5, with the middle of the sample holder having a conservative approximate position of 0.7m (Figure 6.3) giving a rotational speed of 2100rpm.

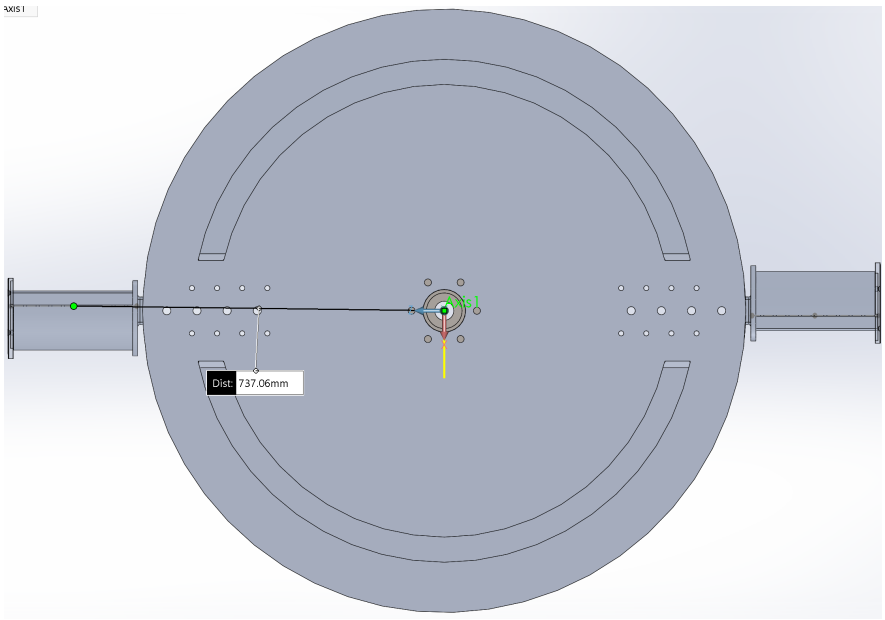

Figure 6.3: Radial position of the centre of the sample holder.

Table 6.3: Simulation setup for finite element analysis on machined plate component in the different design iterations.

Scenario	Solid Plate	2 Part Plate with Al Clamping Plate	2 Part Plate with SS Clamping Plate	2 Part Plate with Al Clamping Plate and pin connectors	2 Part Plate with SS Clamping Plate and pin connectors
Mesh Type	Standard Mesh				
Element size	15.851mm	17.888mm			
Mesh tolerance	0.793mm	0.894mm			
Fixtures	Central bolt holes were fixed on their cylindrical face				
Contact type	-	Bonded		No Penetration	
Loads	Centrifugal (2100rpm)				
Materials:					
Disc	Al 7075-T7351 (Yield = 505MPa, fatigue strength = 150MPa, 500 million cycles)				
Clamping Plate	-	Al 7075-T7351	Stainless Steel 316	Al 7075-T7351	Stainless Steel 316
Connectors	-	Stainless Steel 304			

Pin connectors are numbered in ascending order clockwise on the diagram with pin

connector 1 seen in figure 6.4.

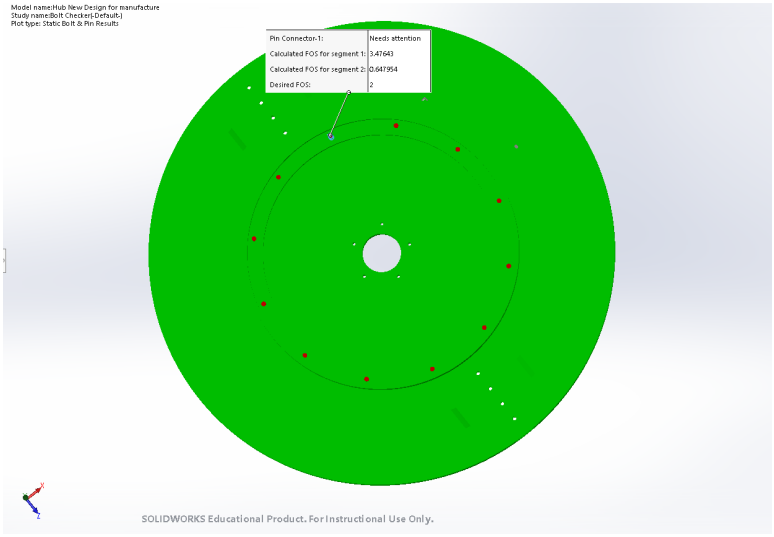

Figure 6.4: Pin connector configuration can be seen here, with pin connector 1 indicated. Remaining pins are numbered in ascending order in the clockwise direction.

6.5.2.5 Results

Below in table 6.4, the peak stresses for each of the different models are provided. As expected the peak stresses were significantly higher in the no penetration simulations, as all of the load is transmitted through the clamping plates. This is highlighted in figures 6.7c and 6.7d. Even if only considering the plate components themselves, the peaks stresses are significantly higher than the solid plate component.

Table 6.4: Peak stress results for each scenario, in MPa. Only the peak stresses here for the whole model are provided for the bonded simulations, whereas for the no penetration models, peak stresses in each of the constituent models are provided.

Component	Solid Plate	2 Part Plate with Al Clamping Plate	2 Part Plate with SS Clamping Plate	2 Part Plate with Al Clamping Plate and pin connectors	2 Part Plate with SS Clamping Plate and pin connectors
Plate	130	124	125	377	304
Clamp	-	-	-	211	275

For the simulations of the solid plate, peak stresses were observed in locations where stress concentrations were present (i.e Sharp changes in geometry) and around

bolt holes (Figure 6.5).

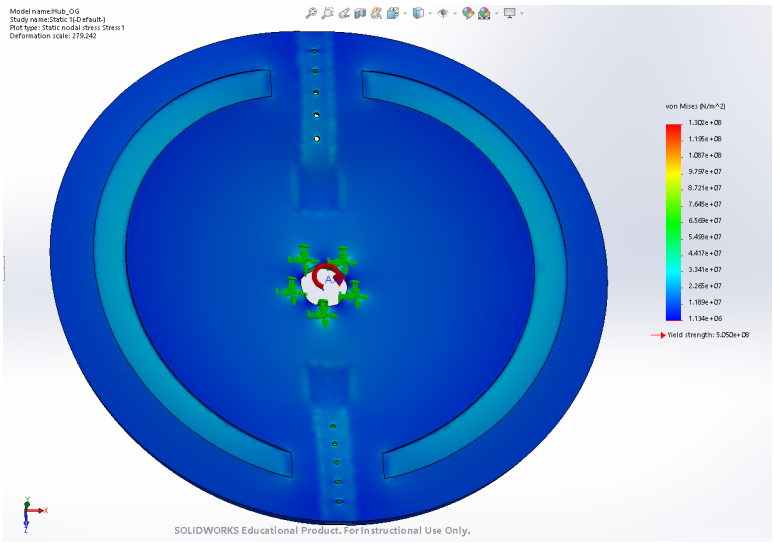

Figure 6.5: Solid plate configuration simulation results, showing stresses during max speed operation.

Similarly to the solid plate configuration, the bonded clamping plate simulation displayed similar stress distributions. Interestingly, although peak simulation stresses were similar in both bonded clamping plate simulations, the peak stresses observed in the stainless steel clamping plate were higher than those in the aluminium clamping plate (Figure 6.6).

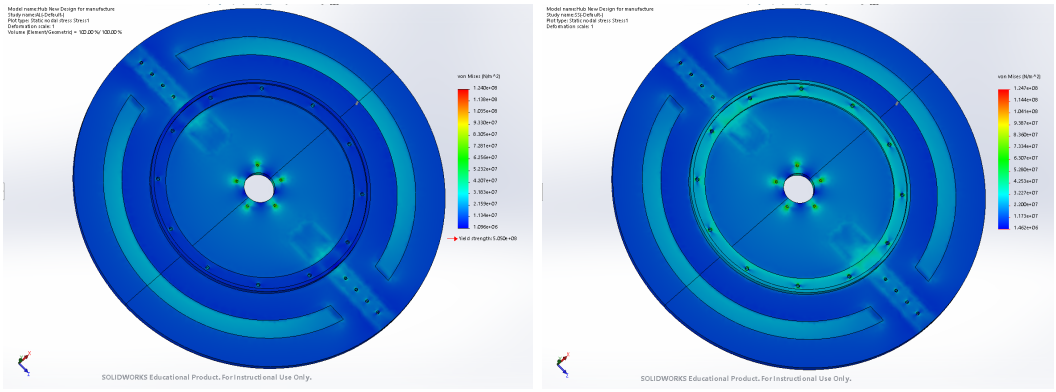

(a) (b)

Figure 6.6: Bonded clamping plate configuration simulation results, showing stresses during max speed operation. 6.6a showing the scenario where the material is Aluminium and 6.6b showing the scenario where the material is stainless steel.

For the unbonded clamping plate simulations, the average and peak stresses were significantly higher than the solid plate and the bonded clamping plate, more specifically stresses in the clamping plate were much higher (Figure 6.7).

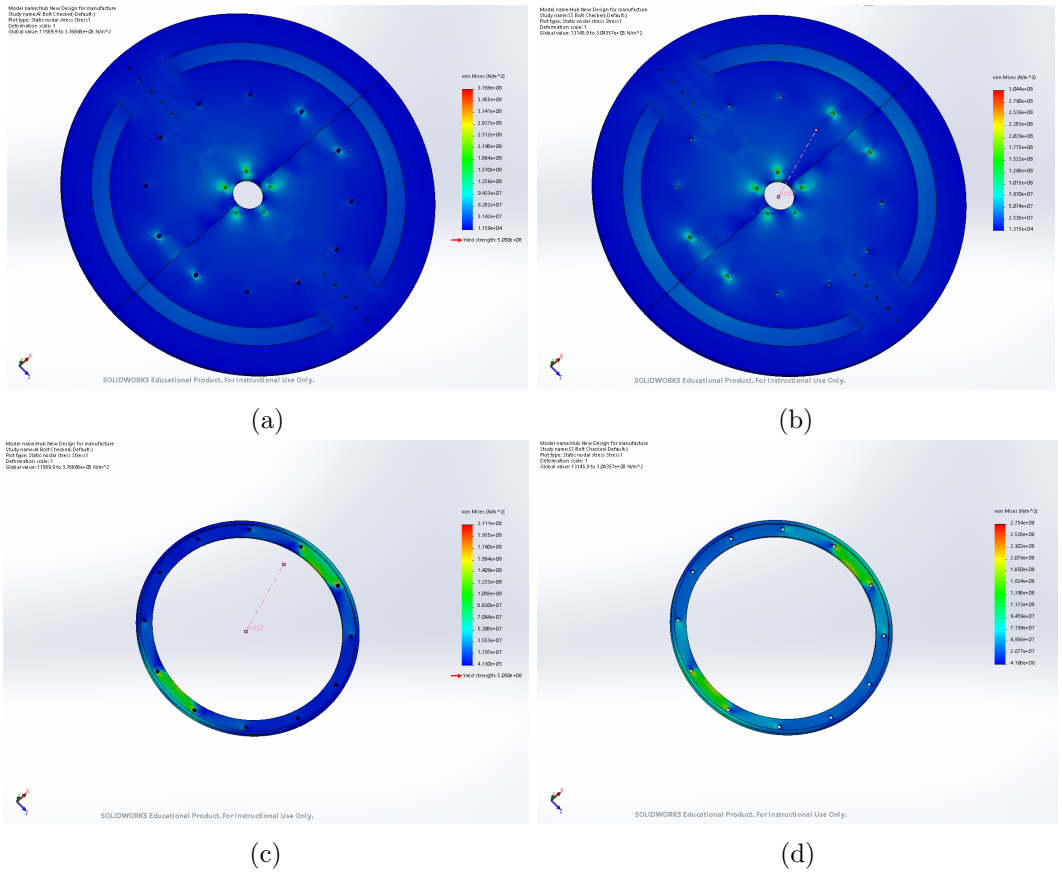

(a) (b)

(c) (d)

Figure 6.7: No penetration clamping plate configuration simulation results, showing stresses during max speed operation. Figures 6.7a and 6.7c showing the scenario where the material is aluminium. Figures 6.7b and 6.7d showing the scenario where the material is Stainless steel Figures 6.7a and 6.7b and Figures 6.7c and 6.7d show just the plate and just the clamp respectively.

Safety factors for the stainless steel clamping plate configuration were lower than those found in the Aluminium clamping plate configuration (Table 6.5). The safety factors in both cases were also significantly lower in bolts located farther from the dividing line between the plate halves, indicating that they are loaded much more.

Table 6.5: Bolt safety factors for plate designs with aluminium and stainless steel clamping plates.

Material	Pin Connectors												
	Segment	1	2	3	4	5	6	7	8	9	10	11	12
Al	1	3.5	1.4	0.2	0.3	1.2	3.9	3.9	1.4	0.2	0.2	1.3	3.5
	2	0.7	1.0	0.2	0.2	1.0	0.7	0.7	1.1	0.2	0.2	1.0	0.6
SS	1	1.8	0.9	0.2	0.2	0.8	2.8	2.8	0.9	0.2	0.2	0.9	2.5
	2	0.4	0.7	0.2	0.2	0.7	0.5	0.5	0.7	0.2	0.2	0.7	0.5

6.5.2.6 Discussion

The clamping plate configuration displayed significantly higher stresses than the solid plate configuration in the no-penetration scenarios. This can be explained by how the components transmit loads between each other. In the solid plate configuration, the component can transmit load throughout it during operation. For the clamping plate configuration, the two halves must transmit load firstly through the bolt holes and then secondly through the clamping plate itself. Stresses are also higher around the bolt holes, due to their stress concentrating nature. Furthermore, the added complexity from manufacturing multiple components as well as an increasing component count increases the likelihood of a failure (manufacturing defects, insecure fixation, etc.) raising reliability concerns.

The increased stresses in the stainless steel clamping plate configuration are likely due to combined effect of increased mass and stiffness of the clamping plates. As the bolts are simulated as pin connectors they have no preloaded tension and so are loaded in shear, which increases due to the centrifugal forces. The bolt stresses will also be higher as the clamping plate cannot deform as much, which reduces the ability of the two plate halves to support each other. During manufacture, tolerances are necessary for assembly, during operation, this could lead to one bolt being loaded significantly more. This design would require the use of high strength stainless steel bolts instead of those simulated here. It is also likely that larger bolts than those simulated would also be required as this would reduce the internal stresses placed on the bolts or instead loading the bolts in tension. However, increasing bolt size adds design complexity and modifications would be required elsewhere. For example, leaving the clamping plate

unmodified reduces the available material for load transmission between the two halves. Increasing the clamping plate size to account for this increases component mass, earlier identified (section 6.4.2) as undesirable. This in turn could also lead to some increases in stresses experienced. Moreover in this simulation, as the bolts are modelled as pins, the clamping stresses from the bolts are not present, which would increase the stresses observed inside the clamping plates for both materials.

In addition to increased stresses for the stainless steel clamping plate simulation, galvanic corrosion was another risk and so the use of a stainless steel clamping plate would need to provide significant benefit (i.e by greatly reducing stresses), which was not the case here.

The use of a thicker or larger diameter disc was not considered here due to the spatial limitations that were required at the time of this component's design and manufacture. However, a larger diameter disc would have allowed a lower rotational speed, generating lower centrifugal stresses. A thicker disc may also have reduced observed stresses, specifically around the electronics box and sample holder slots. However, both of these options would have presented manual handling challenges and the benefits and risks would need to be considered in more detail.

6.5.2.7 Design Selection and Detailed Analysis

From the above feasibility study, it was clear that the clamping plate configuration wasn't viable and therefore, the solid plate configuration was selected.

The design was further refined, by first selecting a rear wheel hub from a Mercedes Sprinter (Van) Rear wheel hub and taking detailed measurements. This was then developed into a CAD model was built (Appendix B). This meant that an additional hole was added to the inner bolt array. The bolt holes were also expanded to M14 bolt holes.

The sample holder pockets were not manufacturable in their present form and so pockets in the bottom face of the disc were added. This allowed the sample holders to be inserted deep enough to be attached securely. Pocket covers were added for manufacturability and to maintain load transmission from the sample holders to the

disc. This maintained the double shear bolted connection rather than a single shear bolted connection. Covers were secured using M10 button screws. The bolt holes for securing the sample holders increased in size to M16 bolt holes, but reduced in number from 5 to 4. This was then followed by a more detailed design analysis

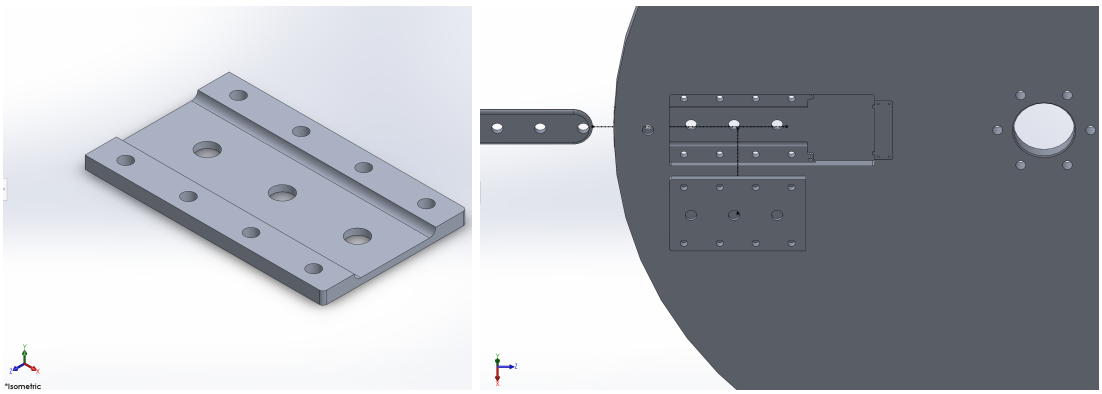

(a) (b)

Figure 6.8: Figure 6.8a shows the CAD model of the Plate Cover component. Figure 6.8b shows the assembly of the Plate Cover, Sample Holder and Plate.

6.5.2.8 Methodology

A further, more detailed FEA analysis was carried out for the central hub disc with the sample holder for the following scenarios:

1. The plate disc and plate covers with remote masses located for the attached sample holders
2. Same as 1., but instead including the attached sample holders, connected using pin connectors
3. Similar to 2., but instead the Mercedes hub was included and a bolted connection between the hub and the plate was used

Air resistance forces were calculated and applied to all three simulations. For the latter two cases, mesh refinements were made around the bolt holes and around the sharp geometry changes. The meshes and simulation setups for all three scenarios can be seen in figure 6.9.

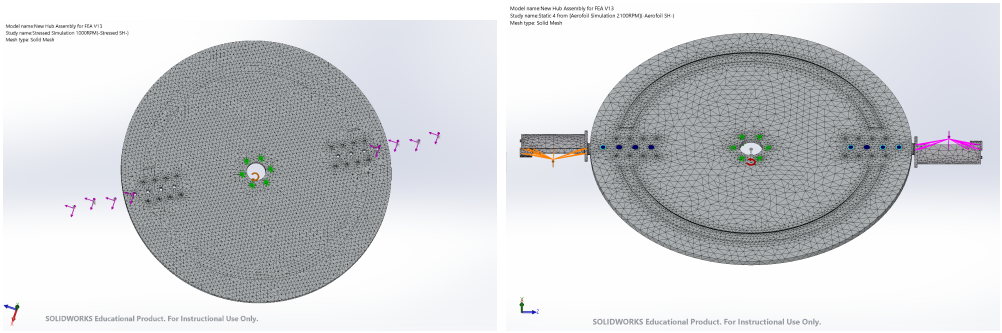

(a) (b)

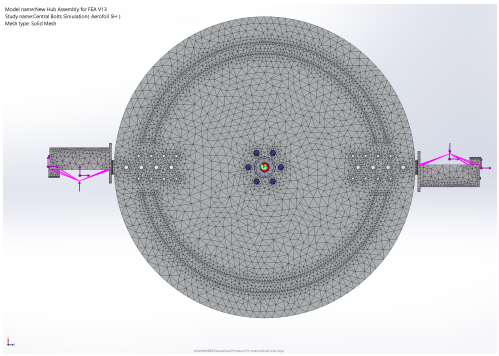

(c)

Figure 6.9: Figures 6.9a, 6.9b and 6.9c show the meshes and simulation setups for the Hub disc, the Hub disc with sample holders connected using pins and the Main bearing bolted connection simulations, respectively. For the Main bearing bolted connection simulation, the hub flange is attached to disc using bolted connection with no penetration contact between the two. Bonded connection was applied between the disc and sample holders.

The drag force used in the simulations was calculated using equation 6.3:

$$F_D = 1/2\rho V^2 C_D A \tag{6.3}$$

Where ρ is the density of air, v is the velocity, CD is the coefficient of drag and A is the frontal area. V was calculated using equation 6.4:

$$V = \omega r \tag{6.4}$$

Assumptions made for equations 6.3 and 6.4 are listed in table 6.7.

Table 6.6: Simulation setup for finite element analysis on hub disc and hub disc with sample holders.

Scenario	Hub disc	Hub disc with sample holders connected using pins	Main bearing bolted connection
Mesh Type	Standard Mesh	Curvature Based Mesh	
Maximum element size	15.984mm	33.519mm	
Mesh tolerance	0.799mm	-	
Minimum element size	-	6.704mm	
Fixtures	6 central bolt holes were fixed on their cylindrical face	6 central bolt holes were fixed on cylindrical faces. Pin connectors, connecting sample holders to main disc	Hub flange was fixed on cylindrical and bottom face. M14 bolt connectors between flange and disc. Torque = 210Nm.[a]
Contact type	Bonded	Bonded between plate cover and disc. No penetration between sample holders and plate cover disc	Bonded between sample holders and disc, no penetration between hub flange and disc
Loads	Centrifugal (2100rpm)		
	Sample holders, bolts and samples were modelled as remote masses acting through the connection holes across their cylindrical faces	Remote loads for the air resistance during operation were calculated using equation 1. These loads were located at the middle of the sample in on the surface, acting perpendicular to the sample.	Remote loads for the air resistance during operation were calculated using equation 1. These loads were located at the middle of the sample in on the surface, acting perpendicular to the sample.
	Remote loads for the air resistance during operation were calculated using equation 1. These loads were located at the middle of the sample in on the surface, acting perpendicular to the sample.		Remote loads were added for the end pieces and samples at their respective centre of masses, acting through the bolt holes modelled on the sample holder
Materials:			
Disc and plate cover	Al 7075-T7351 (Yield = 505MPa, fatigue strength = 150MPa, 500 million cycles)		
Sample Holders	Al 7050		
Samples	GFRP		
Connectors	N/A	A4-80	

[a]It is important to note here that using the bolted connection feature will lead to higher stresses reported in the model within the vicinity of 1 diameter of the bolt holes.

Table 6.7: Parameters used to calculate drag forces on sample holder. Velocity and radius values were taken for the tip of the sample holder. A conservative coefficient of drag was taken (0.045) [21].

Parameter	Aerofoil
$\boldsymbol{\rho(kgm^{-3})}$ at $\mathbf{20°C}$	1.225
R (m)	0.862
ω ($\boldsymbol{rads^{-1}}$ or RPM)	220 or 2100
V (m/s)	190
$\boldsymbol{C_D}$	0.045 (aerofoil)
A ($\boldsymbol{m^2}$)	0.25 * 0.028 = 0.007
$\boldsymbol{F_D}$ (N)	7

6.5.2.9 Results

The results of the Hub disc simulation can be seen in Figure 6.10.

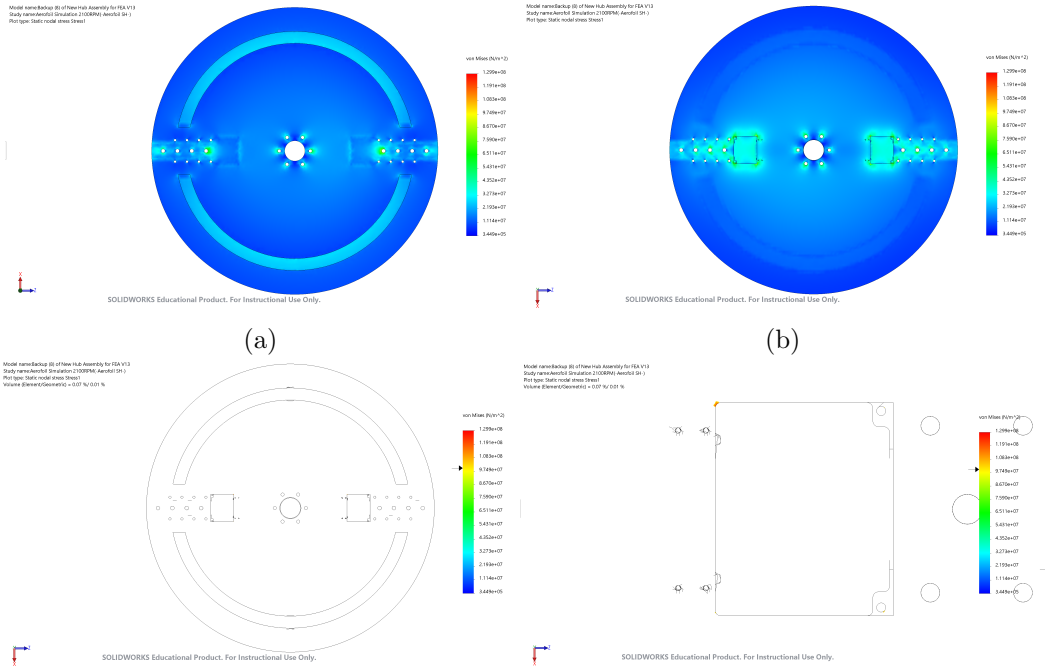

Figure 6.10: Figures 6.10a and 6.10b show stress maps of the top and bottom of the disc using the aerofoil sample holder whilst rotating at 2100 rpm, respectively. Figures 6.10c and 6.10d show the peak stresses (> 100MPa, fatigue safety factor < 1.5) identified on the radii of the electronics box slots whilst rotating at 2100 rpm.

Throughout the majority of the model stresses rarely exceeded 100MPa, except for the highlighted areas (Figures 6.10c and 6.10c). The peak stress in these locations was

found to be approximately $\sim$ 127MPa, which is below the fatigue limit. The results for the Hub disc with sample holders connected using pins simulation can be seen in Figure 6.11.

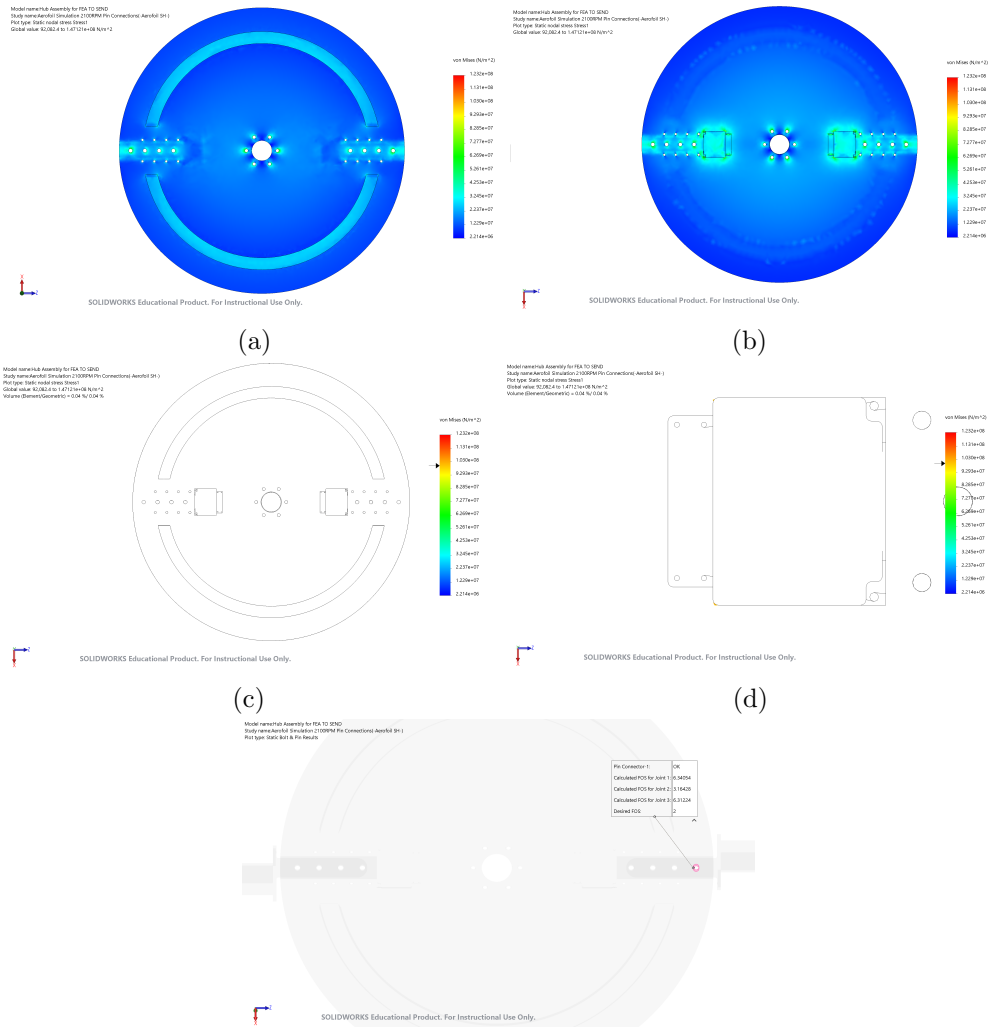

Figure 6.11: Figures 6.11a and 6.11b show stress maps of the top and bottom of the disc using the aerofoil sample holder whilst rotating at 2100 rpm, respectively. Components are connected using pin connectors. Figures 6.11c and 6.11d show peak stress hotspots on the disc ($>$ 100MPa). The simulation results mostly show the same stress distribution as in figure 6.10. As seen in figure 6.11e Pin connector safety factors with the lowest value was found to be the connection on the section of pin in contact with the sample holders, at 3.2.

Similarly to figure 6.10, the majority of the model stresses rarely exceeded 100MPa,

except for the highlighted areas (Figures 6.11c and 6.11d). The average stress during the simulation was found to be as low as 20MPa 6.8. Peak stresses in the highlighted areas were approximately $\sim$ 123MPa, which is still below the fatigue limit and is a similar order of magnitude to the previous simulation. Both simulations show the same overall stress distribution pattern, which generally showed stresses concentrated around stress concentrators.

The results for the Main Bearing Bolted Connection simulation can be seen in Figure 6.12. Similarly to figures 6.10 and 6.11, the majority of the model stresses rarely exceeded 100MPa, except for the highlighted areas (Figures 6.11c and 6.11d). However here, the stresses induced by the tightening of the bolts (torque = 210Nm) can be seen in figures 6.12c and 6.12e. A separate simulation, just of the bolts in-situ was conducted with no external forces present. The results from this simulation displayed the same distribution around the central bolt holes. The average stress during the simulation was found to be higher than those in the previous simulations at 24MPa (Table 6.8). Peak stresses in the areas around the electronics box slot were approximately the same with peak node values of $\sim$ 110MPa, which is still below the fatigue limit and is of a similar magnitude to previous simulations. However in this simulation, interestingly there are localised stress spikes near to the sample holder slot, with peak node values of 182-202MPa. All three simulations show the same overall stress distribution pattern, with concentrated around sharp geometry changes.

Table 6.8: Stress data and Minimum Safety factors found on either the plate or plate covers for each of the simulations. Values reported here are only for the plate and the plate cover components, not for any of the other components included in this simulation.

Simulation	Stress (MPa)			Failure Mode Safety Factor	
	Avg	Max	Min	Yield/ Failure	Fatigue
Hub Disc	17	130	3	3.9	1.2
Hub disc with sample holders connected using pins	20	123	2	4.1	1.2
Main Bearing Bolted Connection	24	299	3	1.7	-

During the Hub disc with sample holders connected using pins simulation all pin connectors were found to have significant safety factors, with the safety factors typically reducing radially from the axis of rotation 6.9. During the Main Bearing Bolted

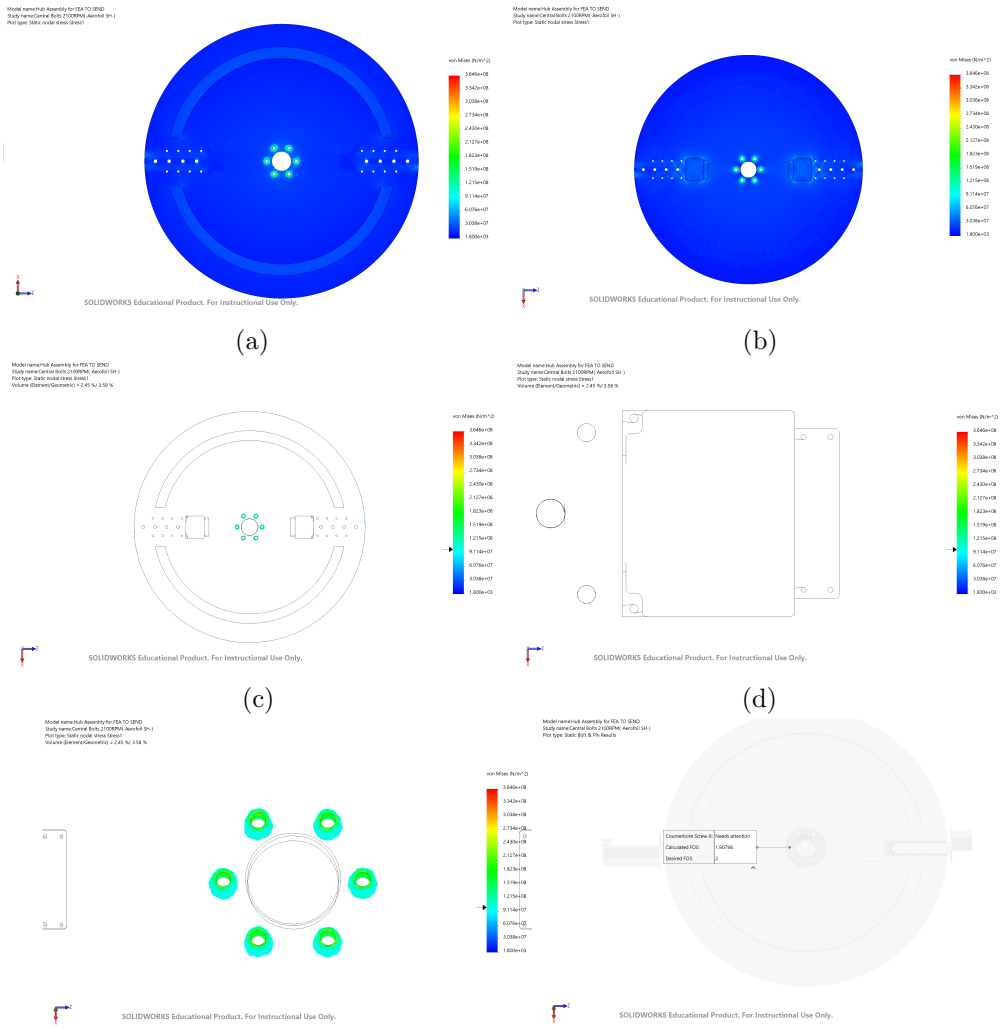

Figure 6.12: Figures 6.11a and 6.11b show stress maps of the top and bottom of the plate component with the hub connection bolted whilst rotating at 2100 rpm, respectively. Components are connected using pin connectors. Figures 6.11c and 6.11d show peak stress hotspots on the disc ($>$ 100MPa). The simulation results mostly show the same stress distribution as in figure 6.10. As seen in figure 6.11e Pin connector safety factors with the lowest value was found to be on the pin section in contact with the sample holders, at 3.2.

Connection simulation, no bolts failed and all bolts having approximately the same value 6.10.

Table 6.9: Safety factors for the connector pins for the section attached to the sample holders. Bolt 1 is the bolt furthest from the axis of rotation, with bolt numbers increasing as distance to the rotational axis decreases. All values were the same on each side, except for bolt 4 where safety factors were 12.3 and 12.4 and therefore the average is stated.

Bolt number	1	2	3	4
Safety factor	3.2	9.7	14.2	12.35

Table 6.10: Safety factors for the Bolts which attach the plate disc component to the Mercedes van hub.

Bolt number	1	2	3	4	5	6
Safety factor	1.9	1.8	1.8	1.9	1.8	1.8

6.5.2.10 Discussion

For the aerofoil sample holder scenario, failure of the Plate disc is unlikely due to the magnitude of the safety factors reported 6.8. Results displayed here show that low cycle fatigue of the component is unlikely, however knowing the exact values of stresses experienced inside the disc would be challenging. The stresses of the connectors (pins/bolts) between the plate and sample holders are mostly shear, with little to no axial forces expected. Pretensioning the bolts sufficiently transfers the loading from a shear load on the bolt to a tensile load in the support material [209]. Bolts holding the plate to the Mercedes van hub are fitted with spring washers to minimise slackening of the bolts. Even though these stresses are high, they therefore should remain constant, with bolt torques regularly checked. Therefore, the likelihood of fatigue in the hub disc as a failure mechanism is particularly unlikely. Disassembly of this component is also expected to be rare and so again, fatigue around the central bolts unlikely. As noted in the simulation software, stress results reported here within 1 diameter of both sets of bolt holes will be higher than the actual stresses.

Bolts securing the plate cover were not simulated. One reason was the use of Nyloc nuts, reducing the bolt torque required to maintain its position. During operation, forces in the vertical axis are not expected. Solely radial loading is expected and therefore this bolted joint connection should operate as though it were bonded. Similarly to

the central hub fixation bolts, fatigue is not expected as unfastening/refastening will not occur.

Even with the safety factors reported here generally being sufficient, efforts should be made to monitor the test rig for signs of fatigue or damage that could lead to early failure. All hot-spot areas identified from this analysis should be monitored during operation at least every 10 million cycles for signs of fatigue. Further improvements in the future should seek to investigate methods for reducing stresses caused by the use of bolts and if possible find alternatives for securing the hub disc and sample holder components.

6.5.3 Sample Holders and Samples

6.5.3.1 Design Specification

Using table 6.2 combined with the design of the plate (section 6.5.2), a design specification for the sample holders was developed. As centrifugal forces are of concern, reducing sample holder mass was a priority. Achieving this outcome would increase component life and reduce fatigue risk in both the sample holders and the disc. Many different configurations were considered and simulated. The DNVLG-RP-0171 document outlined further requirements. The sample holder requirements were combined into the list outlined below:

1. Modular
2. Simple mounting and integration of aerofoil profile samples
3. Safe
4. Corrosion resistant for artificial seawater and dilute acid
5. The samples should have a NACA 634-021 aerofoil profile with a chord thickness of 27.85mm
6. The middle of the sample should have a minimum rotational radius of 1m

7. The gauge length of the sample should be at least 0.2m, with the exposure zone being larger than this.

Following internal design discussions, increasing the diameter of the test rig was initially not possible such that the rotational radius of the middle of the sample would be 1m (design requirement 6). However, the rig diameter was maximised. This was largely due to the availability of space to house the test rig. Discussions with LM Windpower, confirmed that this was not detrimental to results produced. However achieving design requirement 7 would be necessary. LM Windpower stated that impacts close to the sample edge would lead to early failure, due to free-edge effects and so would not provide representative results [210, 211].

A hole and a passage between the sample holder and the disc was incorporated into the design allowing the placement of thermocouples onto the inside of the samples or any other sensors, such as accelerometers.

Care was taken to minimise sharp geometry transitions in the overall shape of the component due to their stress concentrating nature, whilst also ensuring aerodynamics maintained. Modularity was a key priority, whilst also maintaining secure fixation.

6.5.3.2 Methodology: Materials

The original intention was to mill the initial designs (V3) from a solid billet, however tooling limitations and costs heavily drove the early design optimisation process. 3D printing options were then investigated (V4-V8), however, available printing processes available and within budget were limited in component size. These versions required printing in two pieces and subsequent welding together. This process increased component material options, such as Titanium and 17-4PH stainless steel. Safety concerns were raised due to the welding requirement. Welding introduces residual stress into the component and the welding of 3D printed components had yet to be characterised. Further heat treatments may have improved overall quality, but would require a large enough furnace and complex design challenges to mitigate warping would have been necessary, all of which increasing cost and complexity. Further the fatigue properties of 3D printed components are not well characterised either. Later during the design

optimisation process (V9), increased commercial rapid CNC manufacturing options had recently developed (Hubs, Protolabs, etc.) with some grades of stainless steel and aluminium available at reasonable prices.

7000 series aluminium alloys are typically favoured for aerospace application with high strengths, more specifically very high specific strengths, as the density of aluminium is 1/3 that of steel. One widely available, high strength alloy with moderate corrosion resistance is Al 7075. Moreover it had very good machinability with a very good price and lead time through rapid CNC manufacture.

Commonly available stainless steel alloys have reasonable strength, but with a much higher density than aluminium, presenting a challenge for rotating machinery. This combined with galvanic corrosion potential in this case makes stainless steel an unfavourable candidate. Higher strength alternatives such as 17-4PH are one alternative, however for design optimisation, the sample holder would need significant machining. For machining, the billet would need to be in annealed form, therefore post-machining heat treatment for optimum properties would be necessary. This would increase design optimisation complexity and so, preferentially avoided.

Another prospective material was Titanium (Ti-6Al-4V), with a density approximately half that of steel, with higher strength and high corrosion resistance. However, machining is typically difficult, as is welding. Furthermore, the main hub disc is aluminium, presenting an increased galvanic corrosion potential compared to stainless steel and could lead to detrimental damage and therefore catastrophic failure, particularly if saline solutions were used.

As the design progressed, the option of a multi-component sample holder was investigated, allowing mass reduction and ensuring manufacturability within a reasonable cost. This led to the development of a CFRP tail section. This tail section comprised of two outer shells manufactured from CFRP, sandwiching a foam core. The foam core aided alignment during bonded assembly. The tail required an anchor point for fixing to the main sample holder body. Drilling or creating holes in CFRP is undesirable as this creates a stress concentration within the structure significantly weakening it, generally adhesive bonding is preferred. Therefore, the tail section required a fixation plate for

mounting, manufactured from 2mm stainless steel sheet. The fixation plate and the main body of the tail were then bonded together using a high-strength aerospace epoxy. Due to the following reasons, the tail section was assumed to be well bonded and so the separation of the two halves was considered an unlikely event and therefore was not simulated:

- The epoxy was a high strength aerospace epoxy
- Forces were lateral forces and so most of the bond lines would be loaded in shear, which adhesives operate best in
- All bond lines had a relatively high surface area, meaning if failure occurred, it would likely be progressive and slow, rather than immediate
- The CFRP had an epoxy matrix, meaning matrix and adhesive compatibility was high
- Majority of the forces acting on the tail section would be radial forces and so the bolts penetrating the foam core of the tail section would need to be deep for load transmission

Any of the materials listed could also be coated. Ideally, the sample holder manufacturer would also coat the sample holders and would be capable of advising on coating suitability for the intended application, reducing cost and lead times.

6.5.3.3 Methodology: Shape and Assembly

Figure E.1 can be seen in appendix E shows the design progression of the first manufactured form of the sample holder. Diagrams from the DNVGL guidelines indicate the sample would be manufactured with flanges. It was initially assumed these flanges could be used for fixation. Fixation across the rear section of the sample would be desireable, reducing the compressive stresses in the end of each sample caused by the centrifugal forces. Especially as these stresses would increase with speed. This would also reduce loading of the sample holder end piece and additionally any stresses from the end piece fixation. However, upon discussions with LM Windpower, it became

apparent that these flanges were not present and fixation would need to occur through other means, i.e clamping the sample between the end piece and the main body of the sample holder, which increased the design complexity significantly. Maintaining sample position during operation required the design of an additional component, termed the 'inner cover'. This component wouldn't be loaded and essentially acted to guide the sample. During operation, if the sample was kept in position, no lift would be generated and so aerodynamic drag would push the sample into the sample holder mitigating any load applied to this component.

As discussed in section 6.5.3.2, the tail section of the sample holder was initially solid, however due to centrifugal stresses, mass reductions were required. This led to the design modification discussed above whereby the tail became a hollow or semi-hollow structure (sandwich structure) manufactured from composite material (either GFRP or CFRP). FRPs typically have very high specific strengths, ideal for this application. Internal composite manufacture was also to manufacture and following mould manufacture, also quicker.

The main body of the sample holder was initially hollowed, however this added significant manufacturing complexity. Whilst reducing overall component mass, costs were too high and so this feature was discounted.

In earlier designs the enclosure diameter hadn't been confirmed, allowing the sample holder length to be briefly extended with a shroud component incorporated into the design. This was aimed at reducing drag. However, challenges with the manufacture of these components, as well as wall interactions due to the sample holder length, as well as enclosure size restraints restricted the implementation of this component. Each simulation setup for design versions V3-V9 is detailed below, in table 6.11.

For design versions V4-V8, the tail section featured a ridge, allowing a press-fit assembly and negating the need for bolted fixation to the main beam section of the sample holder. The end piece provided additional clamping for the tail section. For these simulations, the tail section was simulation as though bonded to this ridge and also acting through the end piece bolt holes.

Design versions V3-V8 featured a clamping fixation plate for the sample providing

Table 6.11: Simulation setup for finite element analysis on each of the different design configurations of the sample holder. Unless explicitly stated, all components in each of the scenarios simulated have the same material as the sample holder main body.

Scenario	V3	V4	V5	V6	V7	V8	V9
Mesh Type	Standard Mesh						
Element size	2.55823mm						
Tolerance	0.127911mm						
Mesh Quality	High						
Fixtures	4 connector bolt holes were fixed on their cylindrical face						
	Centrifugal (2100rpm)						
Loads	Remote load for the air resistance during operation was calculated as before in section 6.5.2.8. In all cases this was assumed to be constant and the same. These loads were distributed over the front faces of the sample holder that would be exposed to drag forces, acting perpendicular to the sample. Remote masses for the end piece was applied through the inner surface of its mounting holes. For design versions 4-8, The tail sections were mounted using the ridge in the main body of the sample holder and the end piece. For design versions 3 and 9, the tail section was instead mounted to the main body of the sample holder. For design versions 3-8 that featured the clamping plate fixation, the remote mass was applied to the front face of the sample holder, the inner fixation holes from the clamp, and the bolt holes used for the end piece fixation. For design version 9, the sample was just clamped in place using the end piece and so only the bolt holes for the end piece fixation were used.						
Materials							
Sample holder main body	Al-7075-T6	17-4PH or Ti-6Al-4V					Al-7075-T6
Tail	Al-7075-T6	Al-7075-T6	CFRP				CFRP, foam core and stainless steel fixation plate
Samples	Glass (For simulation), $\rho = 2460, E = 69GPa$						

an anchor point, using the flanges present in the DNVGl-RP-0171. However as discussed earlier the flanges were not present in the samples, likely due to manufacturing

complexities. This led to the sample clamping plate being removed from the design.

6.5.3.4 Results

Due to the extensive nature of the design optimisation study, the results have been compiled into table 6.12.

The design optimisation goals were to reduce peak stresses in the sample holder, whilst minimising their mass. As stated above, the concept of 3D printing was investigated, however concerns were raised about the tensile and fatigue strength of the 3D printed components, the required welding in order to fuse the two halves together and corrosion, led to these materials and design concepts being discounted. However, significant progress was made in reducing the sample holder mass from 1,295g to 767g (Table 6.12), resulting in a reduction of 41% and therefore, using equation 6.1, a centrifugal force reduction of 41%.

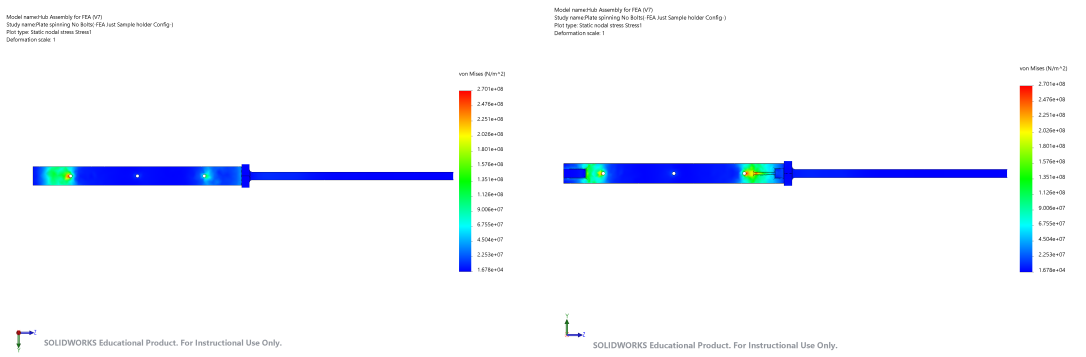

(a) (b)

Figure 6.13: Figures 6.13a and 6.13b show the front and back of the sample holder, respectively.

During the evolution of the sample holder, the maximum speed attainable (1300rpm) whilst still remaining within reasonable safety limits (1.9) (Table 6.12) was found to be significantly lower than those envisioned initially (2100rpm), even with the reduced mass. The initial sample holder speed was designed to be $150ms^{-1}$, however this had reduced to $100ms^{-1}$, which according to [35] is still approximately the maximum velocity of the majority of wind turbine blades in use today. This reduced mass and speed also means that the longevity of the hub disc would be significantly extended.

Table 6.12: Stresses inside foundation plate and bolts due to braking force. Masses stated in this table do not include the sample.

Version		V3	V4		V5		V6		V7		V8	V9
Material		Al-7075-T6	17-4PH	Ti-6Al-4V	17-4PH	Ti-6Al-4V	17-4PH	Ti-6Al-4V	17-4PH	Ti-6Al-4V	17-4PH	Ti-6Al-4V	Al-7075-T6
Stress (MPa)	Avg	16.4	47.2	33.9	31.1	24.3	44.0	29.0	19.4	13.1	35.1	23.2	19.1
	Max	539	1,732	1,395	326.9	384.5	603	406.4	841.1	622.8	995.2	666.2	270.1
	Min	0.0	0.0	0.0	0.1	0.1	0.0	0.0	0.0	0.0	0.0	0.0	0.0
	RMS	30.8	99.2	74.3	55.6	46.7	74.2	48.9	52.8	36.1	67.6	45.7	36.8
Safety Factor	Avg	50.1	997.8	1,163.0	269.8	262.2	629.2	701.9	1,205.0	1,244.0	735.0	805.5	367.3
	Max	46,190	418,400	550,300	10,010	11,230	150,300	165,100	31,760	35,700	73,650	100,600	30,090
	Min	0.3	0.7	0.6	3.9	2.2	2.1	2.0	1.5	1.3	1.3	1.2	1.9
	RMS	479.0	5,481.0	7,182.0	664.6	708.0	3,017.0	3,334.0	2,104.0	2,217.0	2,036.0	2,211.0	1,239.0
Mass (g)		1,295	1,253	837	1,097	650	1,604	938	1,353	795	1,350	793	767
ω (rpm)		2100	2100	2100	2100	2100	2100	2100	2100	2100	2100	2100	1300

However, especially with this reduced safety factor, fatigue damage monitoring would be required throughout the operation of this component.

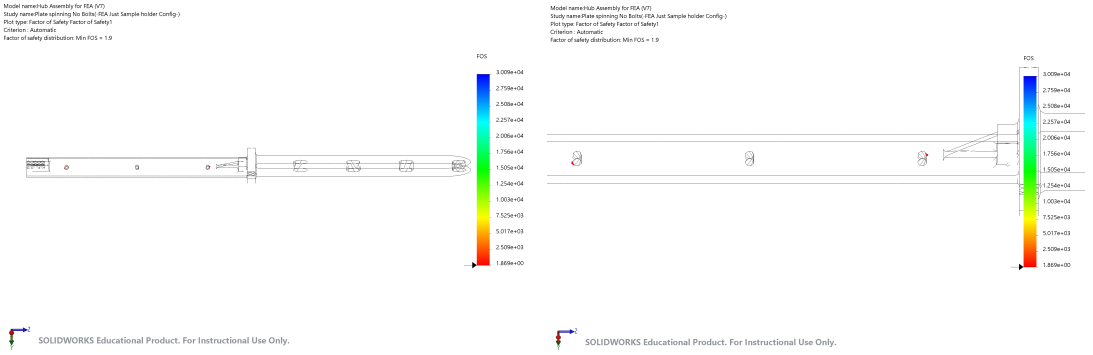

(a) (b)

Figure 6.14: Figures 6.14a and 6.14b show the minimum safety factors found in the V9 sample holder simulation.

Figure 6.13 shows the stress concentrating around the tail section fixation bolt holes, as expected. Generally, higher stresses in the sample holder were preferential over higher stresses in the main hub disc as the cost of manufacture was lower and a catastrophic failure of the main hub disc would be significantly worse that of the sample holder. Higher stresses were also found in the rib connecting long, thin fixation beam section to the main hub connection section of the sample holder, which again would be expected. The rib aimed to reduce loading in the fixation beam section, also reducing any deflection that could occur.

6.5.3.5 Discussion

6.5.3.6 Manufacture

The hub disc was jet cut from a 20mm plate of Al 7075-T7351. The detailing was then milled using a 5-axis CNC. The bolt holes that would allow the fixation of the electronics box were then hand-tapped. The disc was not coated with an additional coating, however, this could be considered at a later stage. It would likely be necessary before the use of any corrosive working fluids or any significant usage of the rig.

The sample holders, end pieces, dovetail counterweights and plate covers were CNC

milled from solid billets of Al 7075-T6. The sample holders and end pieces were subsequently hard anodised. The dovetail counterweights were then threaded. The electronics box panel was jet-cut from a sheet.

For the tail section, firstly the mould was manufactured for the carbon fibre sections, using the following methodology:

1. A negative of the tail sections was first milled into an EP700 High Temp Epoxy Tooling Board (EasyComposites)
2. The mould was then sanded smooth using 240-grit sandpaper
3. The mould was then polished using 600-grit sandpaper
4. A coat of S120 Advanced Board & Mould Sealer (EasyComposites) was applied and allowed to cure for 15 minutes
5. Steps 3 and 4 were then repeated four more times

For the tail section manufacture, the process was carried out using the following methodology:

1. Mould release was applied to the mould, five times, leaving 5 minutes to dry between successive coats
2. During step 1, sheets of carbon fibre were cut to size. To provide the necessary grading so that at the very tip of the tail each half would be flat, each successive layer had to be slightly smaller than the previous layer (estimated using Solidworks). To create the 2mm thickness, 9 layers of carbon fibre prepreg biaxial carbon fibre (XPREG XC130 210g 3K 2x2 Twill Prepreg Carbon (1250mm) 1m, EasyComposites) were cut. The middle (5th) layer orientated at +/- 45◦ and the rest of the layers orientated at 0/90◦, creating a symmetric layup
3. The layers were then layed up one after the other, carefully to avoid fraying and wrinkles
4. Once the layers were then applied, release film was then added over the top of the fabric

5. bleeder fabric was then added over the top

6. a bag was then applied over the whole mould

7. the bag was then pierced to allow a vacuum valve to be placed, which when attached created an airtight seal

8. the bag was then sealed using tacky tape and placed inside an autoclave at $120°C$ for several hours

9. after the component had finished its cycle and cooled the bag was then removed and the mould was cleaned with acetone

An alignment block was milled out of wood so that each of the tail halves could be bonded together maintaining alignment. The foam cores were milled from High-Density Polyurethane Foam (Easy Composites). The stainless steel fixation plates were then jet cut from 2mm thick 316 stainless steel sheet. The fixation plate then had 3 4.1mm holes drilled into it for the M4 fixation bolts that would attach it to the main sample holder. The foam cores were first coated with a thin layer of the epoxy adhesive and then cured at 40°C for approximately 2 hours. This reduced absorption of resin into the foam cores. Epoxy was then applied, first to the carbon fibre inner surfaces and after to the core. Release film was applied over the top of the tail section and the sub-assembly was then clamped to the alignment block and cured for at least 2 hours at 40°C and then subsequently at room temperature overnight. The fixation plates were first sanded with 120-grit sandpaper and then coated in epoxy. The foam cores were also then coated with another layer of epoxy on the bonding face and the two parts were then fixed together and cured for at least 2 hours at 40°C and subsequently at room temperature overnight.

The inner cover was 3D printed from the standard resin from a PolyJet 3D printer. As this component required a good fit to not generate lift and maintain the sample position so that it wouldn't be loaded, this component was manufactured and the fit was tested to ensure a very tight. This inner cover was then bonded to the main body of the sample holder using the same epoxy as mentioned above.

The sample holders were initially bolted to the hub disc, the plate covers to the hub disc, the end caps and tail sections to the main body of the sample holders; all using A4-80 stainless steel bolts of the correct size. Where possible nyloc nuts were used, in other situations, thread locking bolts were used. The hub disc was bolted to the Mercedes rear wheel hub using 10.8 steel bolts. At present the working fluid was intended to be water and so was deemed acceptable, however an effort was made to visually monitor all bolts in the test rig for signs of wear, damage, torque and corrosion through regular inspection.

6.6 Impact Safety and Enclosure

6.6.1 Enclosure and Frame

The enclosure can be separated into three main structural components, the lid, the enclosure walls and the cone (Figure 6.15). These components were made from 2 main materials, steel box section for the outer frame (See Appendix C) and stainless steel for panels that could come into contact with the working fluid. The interior was also lined with a white Pakcel foam layer dampening noise and impacts, improving corrosion resistance, providing better imaging capabilities and improving water tightness. An access door was incorporated into the design with a large viewing window, allowing characterisation, operational monitoring and easy access to the samples. Polycarbonate was selected as the window material, due to its impact properties and optical clarity [212].

Three main types of working fluid will be used during operation for investigating rain erosion; water, artificial seawater and artificial acid rain. This meant any component in direct contact or any components in indirect contact, i.e that may be splashed or in contact with vapour or aerosols must be corrosion-resistant to water at a minimum. In addition, tests with either of the other two fluids require either corrosion resistance or coatings that provide corrosion resistance. Therefore, the enclosure was coated with 2 coats of anti-corrosion primer. Polycarbonate is corrosion resistant to both working fluids [213], as are the marine grade 316 stainless steel panels and Pakcel lining [214].

Figure 6.15: Displayed here is the Full Enclosure, including the coned drainage system and lid, however in this diagram the door was omitted.

To capture wastewater, a cone-shaped sleeve was designed with drainage grating holes made of 8 sections, similar to the enclosure. The cone was water jet cut from 3mm stainless steel panels and bolted together with a set of joining plates. The sections were subsequently bent into shape and lined with the Pakcel foam (See Appendix C).

6.6.2 Impact Safety

The stainless steel panels provided a primary safety barrier during the rig operation, for users and the equipment in the vicinity. Further to this, as will be discussed in section L, access to the vicinity of the rig is restricted during operation, providing additional safety for the users. The most severe, but highly unlikely failure scenario would be if one of the sample holders broke off (at the outermost bolt hole) or a part of one and impacted the side wall or door at the highest tip speed used (190m/s). For conservative estimates, the mass of this projectile was approximated to weigh 889.5g,

including the sample. Simulation results showed penetration did not occur for 2mm stainless steel panels, however, high stresses were observed. Panels of 3mm stainless steel were therefore selected, with the Pakcel foam lining providing additional impact damping.

During the simulations, none of the available thicknesses of single pane polycarbonate (2-12mm) prevented full penetration of the sample holder. Therefore, as a minimum, a second pane of polycarbonate was selected with a separation of 25mm between the two panes, allowing the dissipation of kinetic energy from the impact with the first pane, prior to an impact with the second, through the significant deflection of the first pane and subsequent failure. Two configurations were simulated for this. one configuration with bolt holes to hold the panes in place and another without. The largest available thickness (12mm) was then tested. For the bolted simulation, Both panes failed. However, the no-bolt simulation passed, with full penetration through one pane, however stresses in the second were substantially lower. Failure of the bolt configuration is likely due to the notch sensitivity of polycarbonate [212]. The success of the configuration with no bolt holes and the 25mm separation could be explained by the separation allowing the first pane to deflect (up to 25mm), dissipating the initial kinetic energy of the impact, with the second pane then receiving significantly reduced kinetic energy. The door design was then adapted to incorporate this additional pane (Figure 6.16).

The door frame was made from stainless steel box section, which was welded together. The polycarbonate panes slotted into the frame and held in place using 2 3mm jet-cut 316 stainless steel sheet panel sections. These were then lined with the Pakcel foam, providing a tight fit, but also preventing the polycarbonate from being scratched. The panels were then bolted to the frame. A temporary locking mechanism was added by the workshop team, which comprised of a metal tab with a bolt hole welded to the door, allowing the door to be bolted to the steel enclosure, shutting it during operation. An electrical lock and cut-off switch were then included in the design and fitted to the outer frame. This switch was designed originally to provide safety and security during operation, with delay switches to prevent access to the interior of the rig during

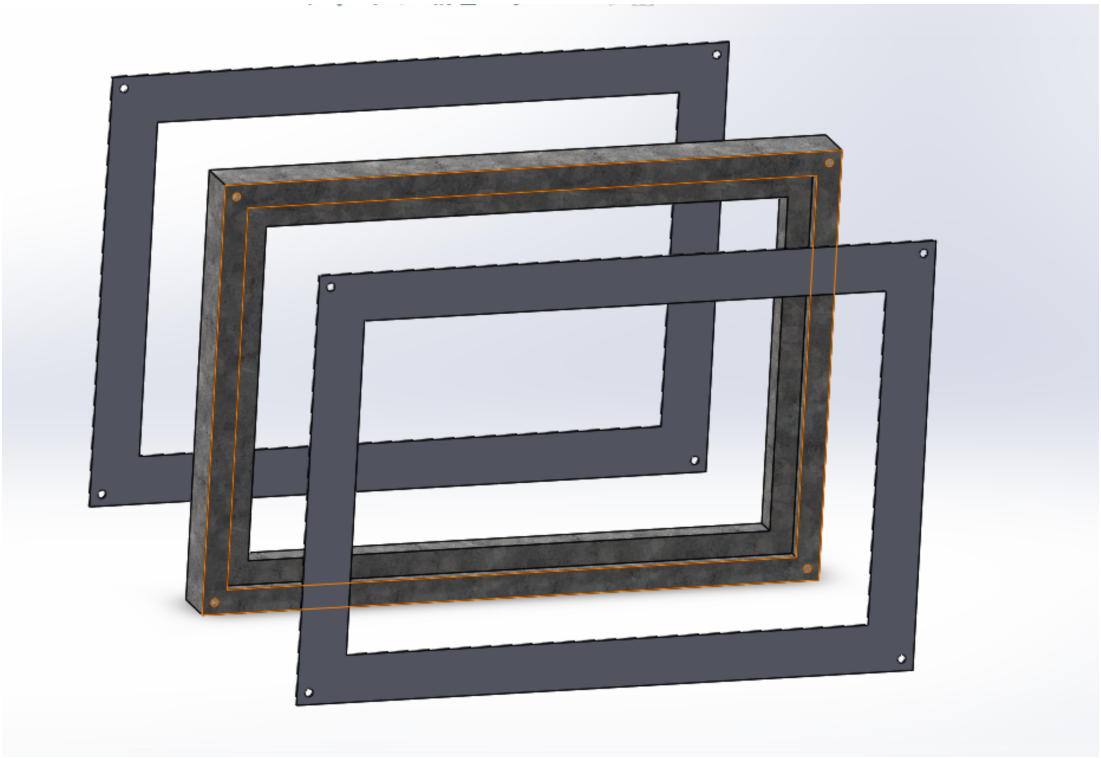

Figure 6.16: Displayed here is the door and viewing window, which comprises of 2 sections of 12mm thick polycarbonate, separated by 1" 316 stainless steel box section and sandwiched together using 3mm thick 316 stainless steel shell panels.

operation and for a given time period after power to the rig had been cut, ensuring the rig had stopped moving, prior to access.

6.6.3 The Motor Stand

The design for the motor stand was selected to be a triangular base pyramidal shape, which has much higher structural stiffness and a more stable base (against shear) than cube/ rectangular prism-shaped foundations. In addition, possessing a smaller physical footprint than a square base pyramid, using less material too. As detailed in section 6.8, a modal analysis was carried out on the motor stand, ensuring no resonant frequencies within the operational range of the rig prior to construction. The motor stand shape provided manufacturing and alignment challenges. Sections were cut from 50mm structural steel square box tube. 2 thick steel plates were jet cut from structural steel, one (20mm) to mount the motor and another (10mm) for mounting the main

bearing. The motor mounting plate, required milling an additional groove for the motor flange, with both plates requiring the drilling of holes mounting holes. Each of the frame sub component were aligned and welded together (Figure 6.17). Later the motor stand was modified to mount the brake caliper. Similarly to the enclosure in section 6.6.1, the motor stand was coated with 2 coats of anti-corrosion primer and with an additional coat of silver paint.

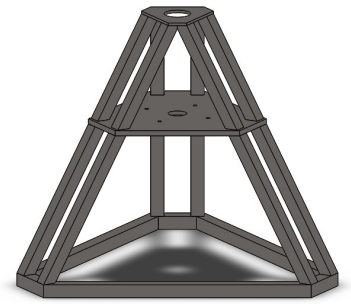

Figure 6.17: Displayed here is the CAD model for the motor stand assembly.

6.6.4 Foundation Fixation

For safe operation, the motor stand was mounted to the floor with sufficiently large bolts, for sustaining the braking forces required to stop the rig in the case of an emergency. Three 8.8 steel bolts with a size of M20 were selected and stresses were calculated in the plate and bolts.

6.6.4.1 Methodology

For the safety calculations, the rig is assumed to be operating at full speed (2100rpm) and the brake is then activated with the required stopping time of 1 second. The maximum driving torque of the motor is 24Nm, significantly lower than the braking torque applied (table 6.17) and so can be neglected. If we consider the friction forces

generated from the main bearing and brake pads, these will reduce the braking time and so, to be conservative are also neglected. Friction forces between the mounting plates and floor which are clamped by the bolts in question are also neglected. Bolts mounting the motor stand to the concrete floor were therefore loaded in a single shear format (Figure 6.19) using a chemical anchor.

Figures 6.18a and Figure 6.18b show the physical setup for assembly containing the rotating components and the anchor points, respectively.

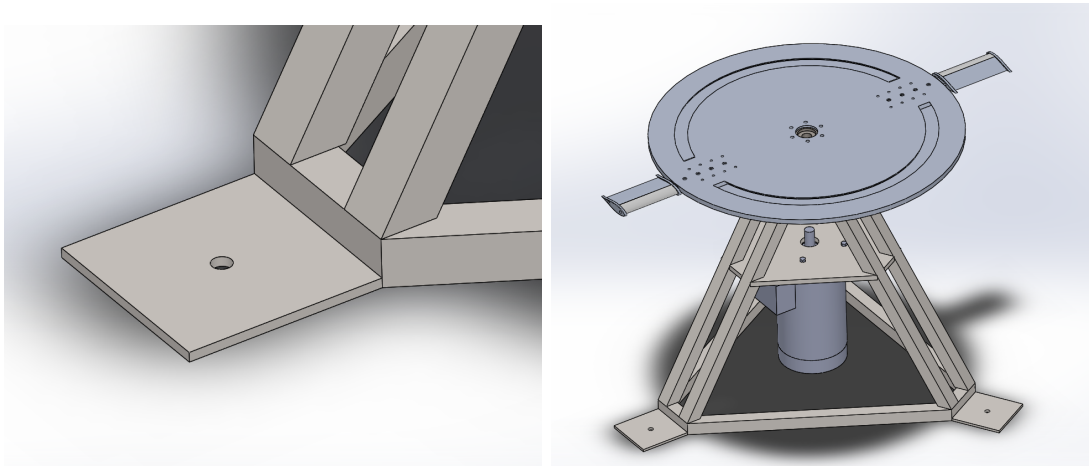

(a) (b)

Figure 6.18: Figures 6.18a and 6.18b show The motor stand, hub and motor setup and bolted ground fixation (M20), respectively.

Bolted joints loaded in this format cause three main stress areas to develop [18]:

- The bolts loaded in shear
- The bolt interface with the hole is compressed
- The plate is subject to shear loading due to the bolt-hole location

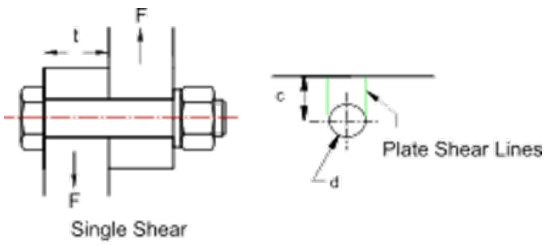

Figure 6.19: Diagram taken from RoyMech [18] showing shear loading conditions for bolts and plates where the bolts holes are close to the edge. t is the plate thickness, F is the force or load being applied, c is the distance from the centre of a given bolt hole to the edge of the plate and d is the diameter of the bolt hole.

The force, F, from braking could be calculated using the angular acceleration, α, $220 rad/s^2$.

$$\alpha = T/J \tag{6.5}$$

Where J is the mass moment of inertia (5.3) calculated using SolidWorks.

$$F = T/r \tag{6.6}$$

where r is the radial position of the bolt relative to the axis of rotation. In order to calculate the shear ($\sigma_{S,max}$), compressive ($\sigma_{C,max}$) and plate shear stresses ($\sigma_{P,S,max}$) the following calculations were performed[18]:

$$\sigma_{S,max} = 4F/\pi d^2 \tag{6.7}$$

$$\sigma_{C,max} = F/dt \tag{6.8}$$

$$\sigma_{Plate,S,max} = F/2ct \tag{6.9}$$

Table 6.13: Stresses inside foundation plate and bolts due to braking force.

Case	d(m)	c(m)	t(m)	r(m)	α ($rads^{-2}$)	T(Nm)	F(N)	$\sigma_{S,max}$	$\sigma_{C,max}$	$\sigma_{P,S,max}$
One bolt	0.02	0.04	0.01	0.69	220	1166	1689.9	5.4	8.4	0.8
Distributed						388.7	563.3	1.8	2.8	0.3

6.6.4.2 Results and Discussion

Based on these calculations, the likelihood of the foundation bolts becoming damaged or loose seems exceedingly unlikely. Bolt grade 8.8 should be sufficient to withstand any forces applied during operation or braking. However, care would need to be taken, monitoring and inspecting these bolts regularly, ensuring that they do not come loose or damaged.

6.7 Drivetrain

6.7.1 Motor

The motor was selected based on the requirement to achieve the desired maximum operational speed of 150m/s (Section 6.4.2) using an aerofoil profile as detailed in the DNVGL guidelines [72]. The selected profile is part of the 6 series NACA profiles, specifically developed for maximising laminar flow, and thus any drag produced is substantially lower than other airfoil types [215]. The aerofoil design was selected to be neutral, producing no lift. During operation, minimising lift was required, as lift would lead to axial forces being generated, loading the bearings unfavourably and would stress components in unforeseen ways. Furthermore, it would add no additional benefit. For drag estimation, a 2D CFD simulation was set up using ANSYS 17.1 Fluent. It was assumed that no objects were within range that would influence this result. Of course in practice, the enclosure walls, floor and ceiling would be close enough during operation to influence the results and there would be additional drag forces produced from interference drag generated from discontinuities in the structure of the sample holder and rotational assembly. However, modelling the complexities would have been computationally expensive and outside the scope of this project, so

conservative estimates were taken.

6.7.1.1 Methodology

As per the DNVGL-RP-0171 guidelines, the aerofoil profile NACA 63_4-021 was selected for the sample holder design. For the simulation a structured C mesh was designed and constructed, with the methodology stated in table 6.14.

Table 6.14: 2D CFD simulation of the aerofoil used for simulating the sample holder for calculating the drag coefficient during operation at 150m/s. Model coefficients are taken from the paper by Spalart and Allmaras [22]. The domain shape and each of the respective sizings can be seen in (Appendix D) and in table .

Mesh Type	Structured quadrilateral
Sizing Method	Edge sizing using Bias
Bias	50
Number of radial elements	150
Number of trailing edge elements	200
Sizing Method	Equal Spacing
Number of Inlet elements	20
Number of separation point to TE elements	80
Mesh Quality parameters	
Minimum orthogonality	9.09388e-01
Maximum skew	9.06117e-02
Maximum Aspect Ratio	6.96945e+01
Boundary Conditions	
Inlet velocity (m/s)	(150 0 0)
Outlet	Pressure farfield
Aerofoil	No slip
Turbulence Model	
Type	Spalart-Allmaras
cb1	0.1355
cb2	0.622
Cv1	7.1
Cw2	0.3
Cw3	2
Prandtl Number	0.667
Energy Prandtl Number	0.85
Wall Prandtl Number	0.85
Spalart-Allmaras Production	Vorticity-Based

Other turbulence models could have been used, however there were far greater sources of error, such as the interference drag produced by the sample holder slots inside the hub disc, drag produced by the bolts fixing the sample holder to the disc,

interaction between the rotating assembly and the the drainage system, or any of the other features inside the wider enclosure and the rotating assembly. Therefore the Spalart-Allmaras model was deemed sufficient[22]. The forces were then decomposed into x and y directional components and integrated over the surface of the aerofoil profile, producing the drag and lift forces, respectively.

6.7.1.2 Results

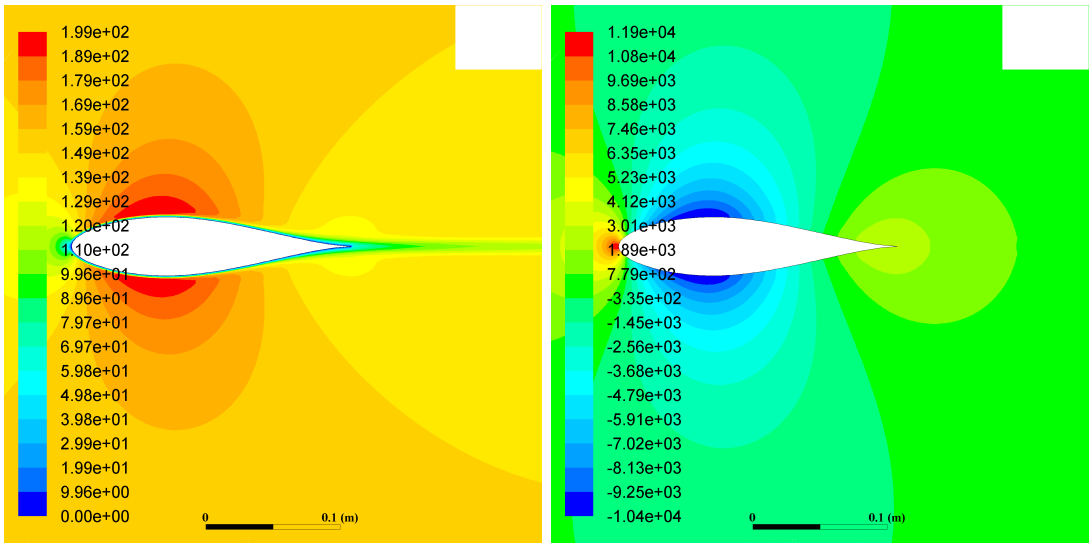

(a) (b)

Figure 6.20: The Velocity and pressure distribution around on the aerofoil during a flow rate of 150m/s.

As expected, the simulation shows a symmetrical profile for the velocity and pressure distribution (Figure 6.20). The drag coefficient was calculated as 0.00885. Relatively speaking this is quite low (0.025 for a 2-Element Aerofoil or 0.05 for a 4-Element Aerofoil) and is of the expected order of magnitude for a low drag aerofoil of this type [216, 217].

To account for the additional drag sources mentioned previously and additional friction and power train losses generated by the mechanical linkage, this drag coefficient was then rounded up to the nearest significant figure i.e to 0.01 and then multiplied by a factor of 10 to 0.1.

Table 6.15: Values taken for calculating the drag force on the rig.

Parameter	Value
$\boldsymbol{C_d}$	0.1
$\boldsymbol{L_{sh}}$	0.263
$\boldsymbol{R_{sh,s}}$	0.610
$\boldsymbol{R_{sh,m}}$	0.7415
$\boldsymbol{R_{sh,e}}$	0.873
$\mathbf{V}$	150
$\mathbf{t}$	0.028
$\boldsymbol{\rho}$	1.225
$\boldsymbol{N_{sh}}$	2

Using equation 6.4, the angular speed, ω was calculated to be: 202.3 rads/s. Using the angular speed and the equation for drag 6.3 the following equation for the total drag of the sample holders can be formulated:

$$F_D(x) = 1/2 N_{sh} \rho V^2 C_D(\omega^2) t x^3 \tag{6.10}$$

This equation can then be evaluated over the length of the sample holder (x) between $R_{sh,s}$ and $R_{sh,e}$, to give the total drag force:

$$F_D = \int_{R_{sh,s}}^{R_{sh,e}} 1/2 N_{sh} \rho V^2 C_D(\omega^2) t x^3 \, dx \tag{6.11}$$

However, as the power requirement is a function of torque, the drag torque must be calculated using:

$$T(x) = F_D x \tag{6.12}$$

$$T_D = \int_{R_{sh,s}}^{R_{sh,e}} 1/2 N_{sh} \rho V^2 C_D(\omega^2) t x^4 \, dx \tag{6.13}$$

The power requirement can then be calculated using equation 6.14

$$P = \omega * T \tag{6.14}$$

Electric motors typically come in 2-pole or 4-pole configurations, which operate at 3000rpm or 1500rpm respectively when operating at 50Hz, meaning that the power

requirement should be sufficient to meet the required torque at either selected speed. As calculated before, $\omega = 202.3 rad/s$ which equates to 1931rpm, therefore a 2-pole configuration was selected. To meet the 150m/s tip speed would mean:

$$P_min = (3000/\omega) * P \tag{6.15}$$

Finally, to account for any additional losses and ensure the rig would be capable of operation with eroded samples, this power requirement was doubled, giving a calculated power requirement of 7.4543e+03W or $7.5kW$. This doubling of the power requirement should be sufficient to account for any additional drag generated by the degraded leading edge profile, which for moderate erosion is approximately 100-200% increase and for severe erosion this can be much higher, up to 500% [37, 218]. If erosion progresses significantly and becomes severe at the tip, testing would need to stop as this could start to affect the structural integrity of the sample, especially as the outer end receives significantly higher centrifugal forces.

Using this specification a 3-phase 7.5kW Siemens electric motor was purchased with an appropriate inverter drive and rotary encoder from Fraser & MacDonald (Electric Motors) Ltd, (Glasgow).

6.7.2 Coupling, Drive Shaft and Main Bearing

The welding of the motor stand would be a manual process and so, angular and lateral misalignments were likely. To manage this, a shaft coupling that would permit relatively large deviations would be necessary, additionally vibration dampening was desirable. With this specification, a flexible tyre coupling was selected. This device couples two rotating shafts with a rubberised tyre. This tyre allows both in-plane and angular misalignments, whilst also dampening vibrations without generating excessive wear or forces that would damage components. Additional direct connections from the motor to the coupling and from the coupling to the main bearing (See Appendix B) were required. So, a set of upper and lower drive shafts were designed for turning using a lathe from hardened steel.

To mount the hub disc, a large main bearing was required, ensuring its smooth rotation and also reducing axial loading and wear on the motor and coupling. For this component, a rear wheel hub assembly from the Mercedes Sprinter van was selected. This provided 3 main benefits: Firstly, typically bearing designs for the commercial vehicle automotive sector are very rugged, with high safety factors, as well as loads produced in a van both axially and centrifugally being higher than those that would be observed in this case (As will be discussed in section 6.7.3); secondly, No significant additional machining or design work would be required for the implementation and thirdly, this component would be manufactured in large quantities reducing cost and providing excellent availability. The full assembly can be seen in 6.21.

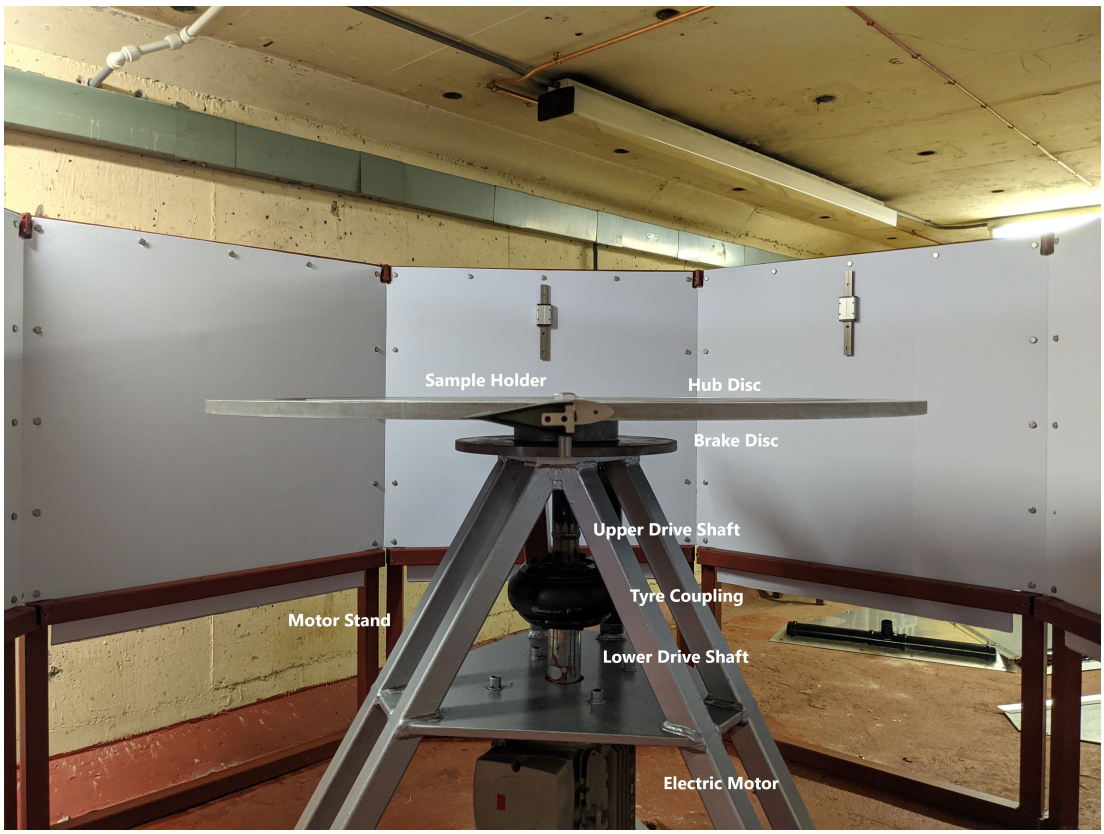

Figure 6.21: Displayed here are the Motor Stand, the Hub Disc, the Aerofoil Sample Holders, the Brake Disc, the Upper Drive Shaft, the Tyre Coupling, the Lower Drive Shaft and the Electric Motor, correctly assembled and configured.

6.7.3 Brake

The initial electric motor was purchased without a brake fitted. Therefore, a braking system was required for safe operation. Due to its wide availability, reduced costs (Due to mass production), reliability and high safety standards, and its ability to fit with the designed system with relative ease an automotive, hydraulic braking system was selected. The initial brake disc, caliper, caliper bracket and brake pads were purchased. Similarly to the van rear wheel hub, the vehicle model for this selected system was a Mercedes Benz Sprinter. After attempting to fit the components in place, it was found that the caliper could not grip the brake disc sufficiently. Several solutions were considered; firstly, whether a larger brake disc could be used; secondly, if a spacer could be added to the brake shaft; thirdly, if the brake could be fitted below the drive coupling; fourthly, if the motor stand could be modified to allow the caliper to fit closer to the shaft and finally, if a different brake system could be used. The various pros and cons of each design modification was considered (as outlined in the table below). Similarly to the rain erosion test rig design matrix 6.2, the brake disc design was assessed using the following equation:

$$S = W_{Cmpl} * Complexity + W_T * Ttime + W_{Cst} * Cost + W_R * Risk \tag{6.16}$$

Using the table above (Table 6.16), the most effective option available was using a larger brake disk. After extensive research, a large enough replacement brake disc was not available for purchase and so the disc needed to be designed and manufactured.

During operation, the rig has a lower required torque and kinetic energy to stop (Calculated using equation 6.17) compared to a typical Mercedes Benz Sprinter van per wheel 6.17. Therefore the currently selected system will provide sufficient deceleration without any additional modification. As is discussed elsewhere (Section 6.6.4) the mass moment of inertia of the rotational components is far lower than the value used here and in addition, the required brake disc is larger, creating a larger moment arm for the brake pads, thus reducing the required braking force compared to the Mercedes

Table 6.16: Binary Weighted Design Matrix. Values for Weightings ranged from 1-5 and referred to: Complexity of the designing, implementing and operating the system, Time taken to complete design and implementation (including lead times), Cost and Risk referred to how safe this type or braking system was and to potential irreversible alterations that could affect the ability to complete the project.

Option No.	Parameter	Complexity	Time	Cost	Risk	Total Score
	Weights	3	4	2	5	
1	Larger Brake Disc	2	2	1	1	21
2	Additional Spacer(s)	1	4	1	3	36
3	Brake Fitted Below Drive Coupling	4	4	1	1	35
4	Motor Stand Modification	5	5	2	5	64
5	Alternative braking system	4	4	4	5	61

Sprinter.

$$E_{K,Rotation} = 0.5J\omega_s^2 \tag{6.17}$$

Table 6.17: The mass moment of inertia stated here was for an early design configuration and conversation assumptions.

Parameter	Van	Rig
Mass (kg)	3500	-
Tangential speed (ms^{-1})	26.8	-
Rotational speed (RPM)	-	2100
Mass moment of inertia (kgm^2)	-	11.52
Linear momentum ($kgms^{-1}$)	93900	-
Brake midpoint radial position (m)	0.122	0.168
Total required braking torque to stop in 1 second (Nm)	2860 (average per wheel)	2530
Kinetic energy (kJ)	315 (average per wheel)	279
Required braking force (N)	13000	23500

6.7.3.1 Material

For the manufacture of the brake disc, materials needed to be compared. Brake discs are subjected to a complex set of mechanical and thermal stresses. They need to manage thermal fatigue and to absorb and dissipate heat as quickly as possible. For most automotive vehicles, grey cast iron (250 grade) is the most common. In the USA, cast iron with the addition of titanium ($>$ 200ppm) is sometimes used as it increases

the wear resistance of the component, however it also reduces the coefficient of friction. More recently, manufacturers have introduced high carbon, high conductivity grades. They are however weaker, meaning the brakes are often larger and heavier. These brakes owe their higher conductivity to their carbon content, which allows lower operational temperatures, increasing their longevity [219].

This also allows more flexibility in material selection as usage frequency of the brake will be significantly less than required for use inside a van and due to the reduced angular momentum, braking times are lower. This reduces thermal performance requirements in terms of thermal fatigue and conductivity. There are dimensional limitations, but no mass limits. The main design drivers here therefore are cost and availability, with thermal properties still considered to a lesser extent. For optimum thermal conductivity properties, cast iron with graphite flakes is preferred over graphite spheres [219]. Possible grades considered were:

- Grade 250
- Grade 200
- High Carbon Gray Iron
- Titanium Alloyed Gray Iron

Grade 250 was selected mainly due to price and availability, but to a lesser extent thermal properties. The overall brake design remained the same, except the diameter was larger and the groove, designed for dust removal wasn't included (Appendix F). The elimination of the groove was deemed acceptable due to its reduced usage compared to a van and the additional distance between the brake pad position and the inner embossed section. In addition, the centrifugal forces should extract the dust anyway. With the increased size of the new design compared to the original and the reduced useage, the brake will be expected to last for the life of the machine, with temperatures kept within thermal limits.

The brake was connected through a long copper tube to a foot pedal, allowing the brake to be operated remotely (Figure 6.22) from the control station. The copper tube

ran directly from the rig up to the control station above and was filled with automotive brake fluid. As will be discussed in section L, during operation, if the brake is required, power to the rig should be cut prior to using it. This is important as otherwise, the motor would be attempting to accelerate, whilst being physically restrained and so could damage the electric motor, power electronics or the control equipment.

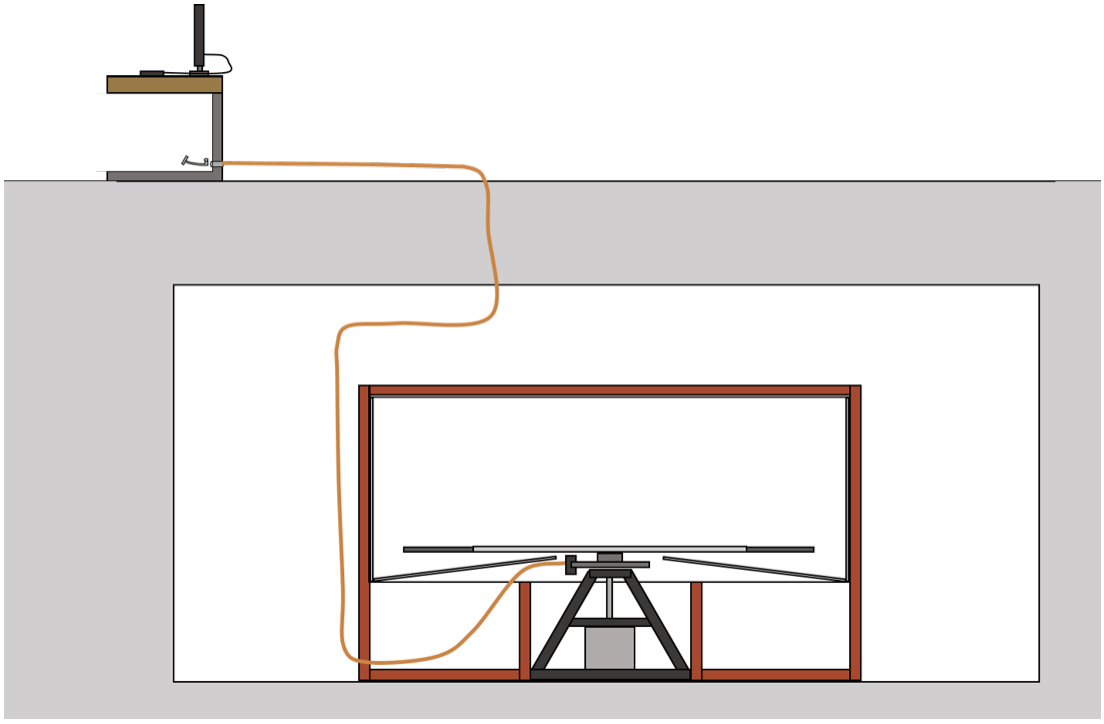

Figure 6.22: Full diagram of the brake system. The brake pedal is located at the control station, mounted onto the control station desk and is connected to the brake caliper, via copper tubing, and disc, mounted directly onto the test rig.

6.7.3.2 Braking Force and Master Cylinder

The braking force generated in the pedal is transferred to the master cylinder which applies pressure to the brake fluid, which is then transferred to the slave cylinder inside the hydraulic brake caliper. Therefore it is important to maintain a consistent ratio between the face area of the master cylinder(s) inside the brake pedal and the slave cylinder(s) located inside the brake caliper. Of course, when considering a vehicle with multiple wheels (which in some cases contain multiple cylinders inside each caliper),

the effective area must instead be considered (total combined area of all slave cylinders and master cylinders). In the case of the Mercedes Sprinter Van and most vehicles, the front brake is typically larger and requires a larger braking force, as during the braking process, due to the forward momentum of the vehicle and the suspension allowing the forward movement of the centre of mass the forward wheels receive a higher proportion of the load. In this case, the van front wheels have a dual cylinder disc brake caliper (48mm diameter piston) [220] and the rear wheels have a single cylinder disc brake (51mm diameter piston [221]). The OEM master cylinder has a diameter of 23.81mm [222] and is a tandem master cylinder, meaning it effectively has two cylinders. Most standard manual foot pedals provide a pedal ratio of 6:1 and so a pedal of the same ratio would be selected and used, therefore meaning there would be no influence [223]. The importance of selecting the right ratio influences the feel and ease of use when operating the brake petal. Relative to the effective slave cylinder area, if the master cylinder area is smaller, the required force applied to the brake foot pedal is lower to fully compress the master cylinder and the converse is also true. However if the master cylinder is too small, then the applied braking force may not be high enough to stop the rig, further, if the master cylinder is too big, then the required force may be too large and it may not be possible for the operator to fully compress the brake and stop the rig. As stated above, the kinetic energy of the rig is significantly lower than a Mercedes Sprinter van and so a lower ratio would still be sufficient to fully brake the rig, whilst also being easy enough for the operator to use. Bosch manufacture master cylinders for the Mercedes Sprinter van and so with this data, a typical master cylinder ratio was calculated. A suitable master cylinder was selected and its master cylinder ratio was calculated before purchasing to ensure suitability (Table 6.18). A handbrake master cylinder was selected instead of a foot brake cylinder, as they typically have 1 outlet port instead of two and sourcing an appropriately sized cylinder was easier.

The master cylinder selected has a ratio of 10.7 which when compared to 12.7 is similar. As mentioned above, the kinetic energy, required braking torque and force are lower than that of the Mercedes Sprinter van, meaning that a lower ratio should be acceptable (Table 6.17). In addition to the above calculations, the brake system

Table 6.18: Master and slave cylinder specifications and calculation results for the master cylinder ratio calculation for both the Mercedes sprinter and the rig setups.

Parameter	Mercedes Van		Rig
Master cylinder diameter (mm)	23.81		15.625
No of cylinders	2		1
Total master cylinder area (mm^2)	894		192
Cylinder	Front	Rear	-
Slave cylinder diameter(mm)	48	51	51
Number of cylinders per wheel	2	1	1
Number of Wheels	2	2	1
Slave cylinder area, per cylinder (mm^2)	2040	1810	1810
Total slave cylinder effective area (mm^2)	7240	4090	1810
Total slave cylinder area (mm^2)	11320		1810
Master cylinder ratio	12.7		10.7

was tested too (Section 6.10), to ensure it provided sufficient braking force required to stop the rig quickly. The master cylinder [224] and appropriate foot pedal [225] were purchased for the rig and installed at the control station.

6.8 Balancing System, Vibrations and Noise

6.8.1 Introduction

Vibrations inside the rig will only occur from moving components. The rig is comprised of 2 physically separate main sub-assemblies: the outer enclosure and the motor stand. As the two sub-assemblies were isolated from each other and the outer enclosure had no significant moving parts, only the motor stand underwent modal analysis. The outer enclosure was also directly fixed to the concrete ground of the test room inside the MAE workshop, which can be assumed to have infinite mass. Therefore, no vibrations would be transmitted between the two. Vibrations from the water hitting the enclosure panels contain insufficient energy to generate significant vibrations. The enclosure was also lined with white Pakcel foam which also damped vibrations.

The hub disc and the samples were attached to the motor stand via the rear wheel hub and which would likely absorb the majority of the little energy generated by droplet impact. Therefore this was not considered. Further to this, early failure of the van hub due to vibrations was not considered a likely possibility, due to the rigorous standards automotive components adhere to and the fact that they are designed to withstand

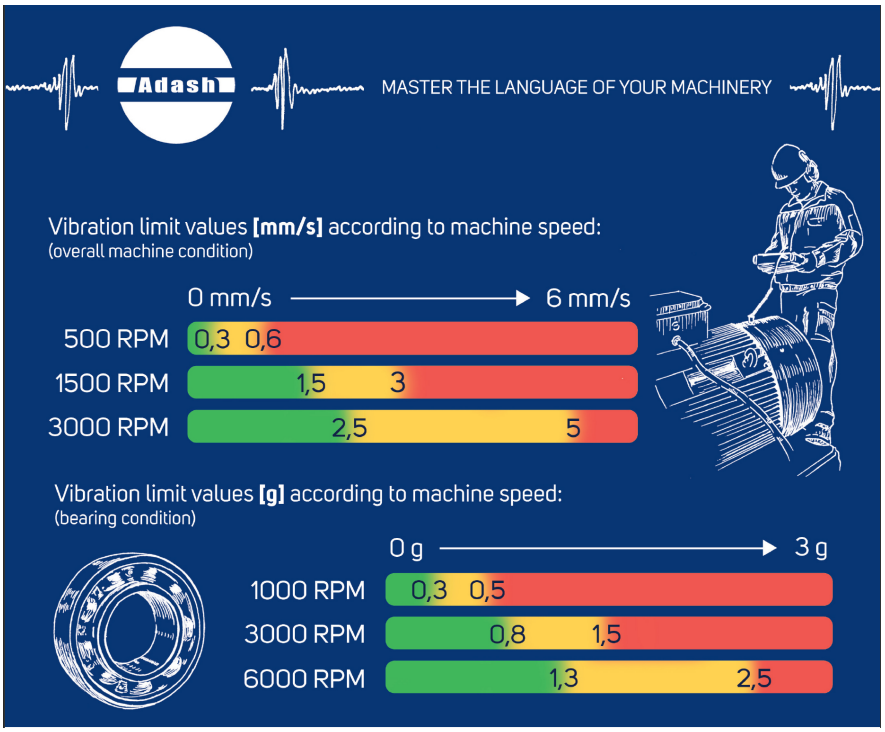

Figure 6.23: Quick guide for the Vibration limits for rotating machinery, taken directly from the Adash website [19].

offset axial loads that would cause vibration. In this case considering the aerofoil shape is neutral and so no further examination of this was considered necessary. An assembly of the motor stand was designed and a modal analysis was simulated using FEA, allowing the detection of resonant frequencies. As the rig would operate at constant speeds during operation with little dynamic loading (only during acceleration and deceleration, which would be quasi-static loading due to the slow acceleration). This is a typical operational safety approach applied to rotating machinery, including RET rigs in the past [133].

To limit component wear and reduce vibrations as much as possible, a balancing system was incorporated into the motor stand assembly. The design, incorporation and manufacture of the balancing system was followed up by testing and real-time condition monitoring of the rig to ensure safe operation using literature from the condition monitoring company Adash (Figure 6.23) [19].

6.8.2 Methodology

6.8.2.1 Modal Analysis

A finite element model of the motor stand was created from its CAD model on SolidWorks. The mesh resolution was set to fine. The electric motor mass was set using data from the Siemens data sheet, supplied with the motor. The masses and I_{ZZ} of both the cast iron van hub and the hub assembly were calculated using their respective CAD models. The motor stand material was set to mild steel. For more details see table 6.19.

Table 6.19: Simulation setup for modal analysis

Mesh Type	Standard Mesh
Maximum element size	21.9783 mm
Tolerance	1.09891 mm
Fixtures	Anchor bolt holes on cylindrical faces
	Electric motor with centre of mass located on rotational axis at 292.5mm from the ground (approx. centre of mass location). Mass = 57kg. IZZ =0.031 kgm2.
Remote loads	Hub and sample holder assembly with centre of mass located on rotational axis, 1060.72mm from ground (determined using SolidWorks). Mass = 63.77177kg. IZZ = 5.33231362kgm2.
	Cast iron hub component with centre of mass located on rotational axis, 999.84 mm from ground (determined using SolidWorks). Mass = 3kg. IZZ = 0.00452kgm2.
Materials:	
Motor Stand	Mild Steel

6.8.2.2 Balancing

To balance the motor stand sub-assembly there were three options that were considered:

- Drilling holes or removing material until the plate disc is balanced
- Buying off-the-shelf weights to balance the disc
- Manufacture custom weights with a bespoke method of holding them in place

Drilling holes into the disc was one possible method, however, if different sample holders or different samples were used then the disc would then need to be altered again which could be costly and time-consuming. This method also could introduce stress concentrations in areas where material had been removed, reducing the safety of the

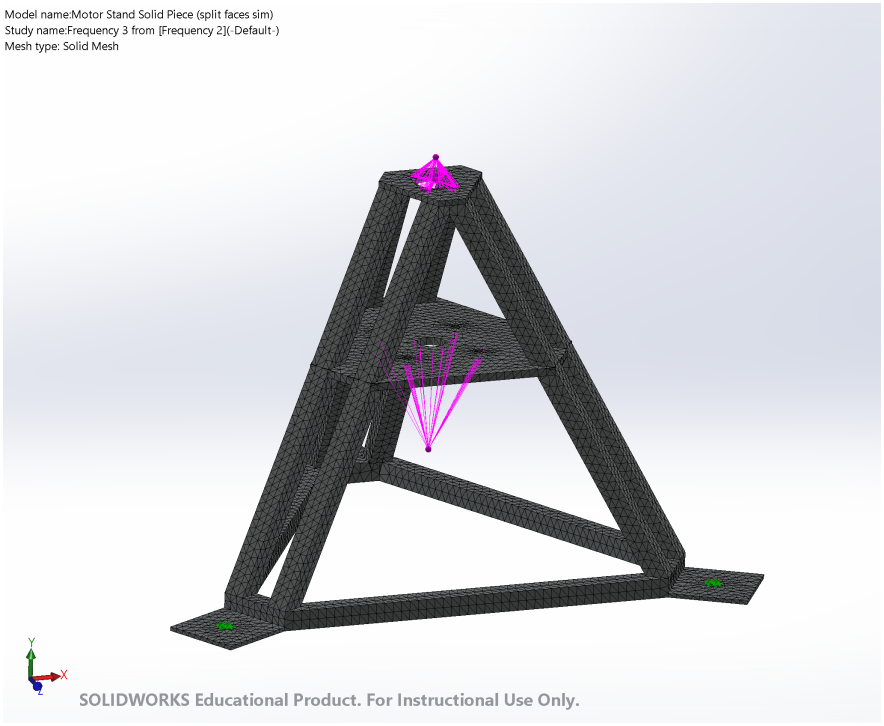

Figure 6.24: Mesh and setup for Modal analysis

rig. A further concern was that any alterations would be permanent and so could limit future use.

Purchasing off-the-shelf weights would be a fast simple solution, however a fixation system would need to be devised. Off-the-shelf weights Are also unlikely to be aerodynamic and so could create additional turbulence inside the rig which would deteriorate testing conditions.

Manufacturing custom weights would be the ideal scenario, with the ability to tailor their shape, allowing the reduction of additional turbulence or drag generated. Furthermore this design feature would allow their integration without damage the main disc. However this option could potentially costly, with long lead times.

Manufacturing custom weights was considered the best option with the advent of rapid prototyping companies, allowing a significantly reduced cost and lead time, even with Al 7075. Inspiration was taken from the balancing weights used on angle grinders. This follows the format of two or three balancing weights that are each split into two parts and slot into dovetail grooves. These are then fixed in place using grub

screws. A chamfer was designed into the balancing weight to reduce any additional drag introduced by them.

6.8.3 Results

6.8.3.1 Modal Analysis

Table 6.20: Resonant frequencies of the test rig.

Mode	Frequency($Rads^{-1}$)	Frequency(Hz)	Frequency(RPM)	Period (seconds)
1	278.37	44.304	2658.24	0.022571
2	280.81	44.692	2681.52	0.022375
3	350.3	55.752	3345.12	0.017937
4	397.95	63.336	3800.16	0.015789
5	464.93	73.996	4439.76	0.013514

As can be seen in table 6.19, the fundamental frequency of the motor stand is at least 400RPM outside of the maximum motor speed analysed. Including the motor coupling and shaft would add mass to the system, which would reduce the fundamental frequency. However, adding the shaft into the system would increase the stiffness of the system, which would likely mitigate this addition. Figure 6.25 shows the first five modal shapes. The modal shape with the highest amplitude is the fundamental frequency (Modal shape 1). As all of the modes were outside of the operational range of the rig, it is unlikely that resonance would cause a serious problem during operation. However, during operation vibrations would be monitored for any significant change in amplitude using the Reactec device and the accelerometers.

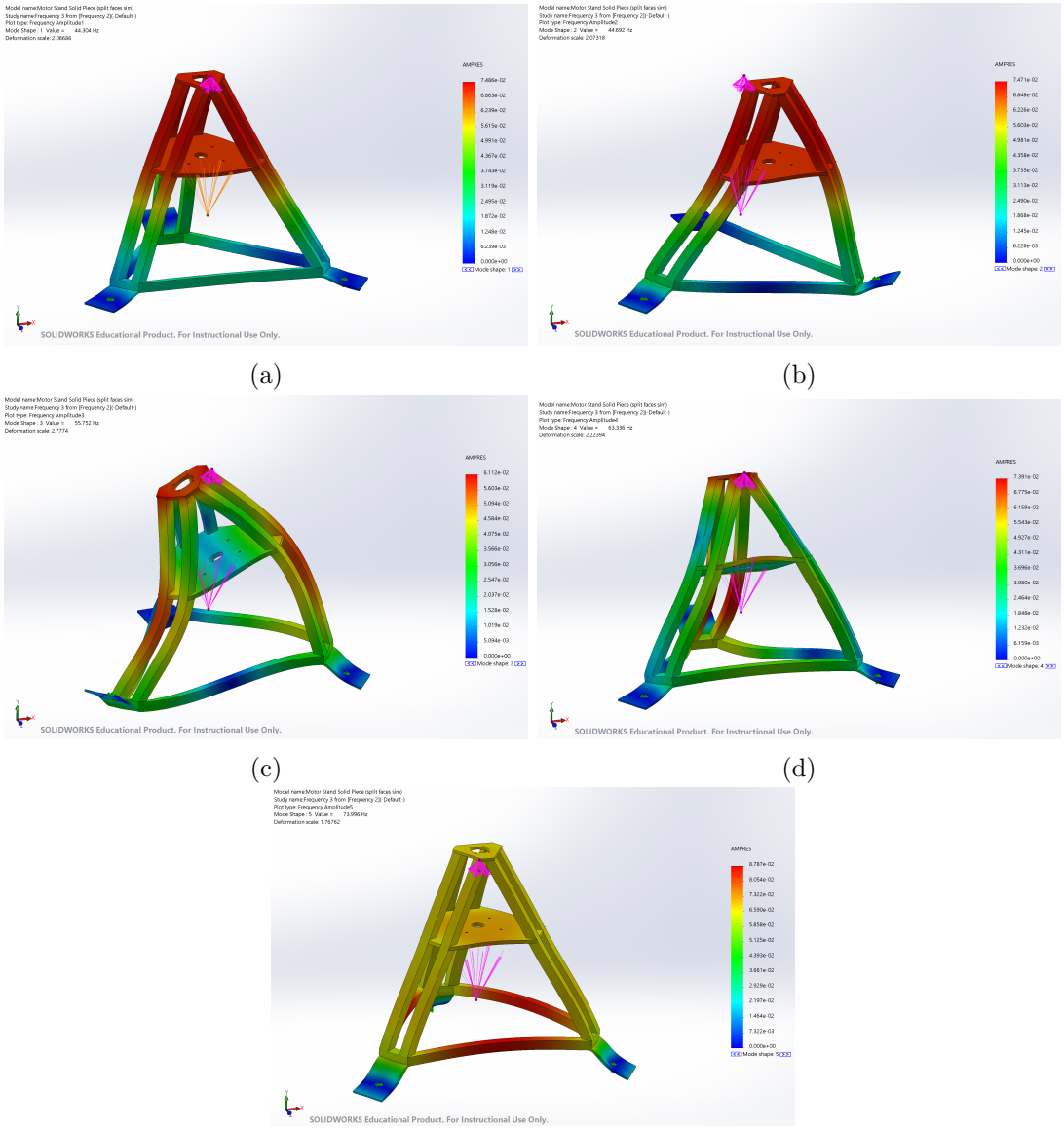

Figure 6.25: Modal shapes 1, 2, 3, 4 and 5 for motor stand, respectively

6.8.3.2 Balancing and Condition Monitoring

For both the balancing and condition monitoring, two Knowles BU23173 accelerometers were purchased and bonded to a small Neodymium magnet with epoxy, allowing its easy attachment and removal on a desired location. The accelerometers were connected to an NI DAQ device and a simple program for converting the signal into acceleration

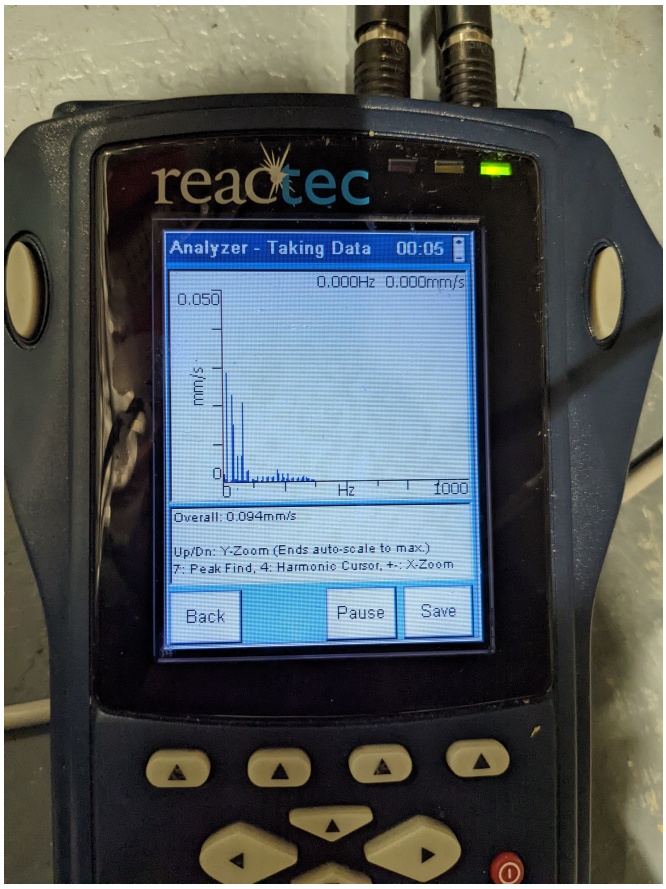

Figure 6.26: Reactec RT-440 being used to measure vibrational velocity during operation at 300rpm, in order to balance the rig.

and velocity was implemented, allowing the real-time monitoring of vibration parameters. A Fast Fourier Transform was also then calculated and monitored for monitoring resonant frequencies or harmonics during operation.

Attempts were made to balance the test rig, firstly using a Reactec RT440. This device employs up to two accelerometers and comes with a built-in balancing function (Figure 6.26). Secondly, using the data output from the Reactec RT440 accelerometer and the app developed by Adash spol. s r.o. (Czech Republic), the 'Balancer App' [226]. However, the vibrational velocity as measured by the accelerometer was too low for the machine to be balanced. It is likely that the vibrations measured were within the tolerances of the motor itself, which would make balancing not possible.

6.9 Electronics, Sensors and Rain System

6.9.1 Electronics

The rig is controlled and monitored from a control station as can be seen in figure 6.27. The control station features a CCTV system of 4 cameras, one mounted below the rig facing the brake and drive train, one facing the access stairs, that led from the access gate into the operations room, one facing the exterior of the rig and one inside the rig, facing the hub disc and the sample holders. This CCTV network allows continuous remote monitoring of the rig during operation allowing the users to see whether there are individuals inside the operations room and also allows the users to see remotely when hazards arise, such as a large water leak or damage to the rig due to a component failure. The control station features an emergency power button that allows the power to the rig to be cut at any point if required. The peristaltic pumps are controlled by setting the % current supplied to their motors. Calibration of the pumps will be outlined in section 6.10.

To use the TIA program from Siemens, the emergency power button must be released and the security gate closed. During operation, the desired speed (in rpm) is set inside the control interface and stopped inside the program. If for any reason the rig loses power, i.e the door is opened, the emergency power button is pressed or the security gate opened, the rig switches off and immediately begins to slow down. If for any reason the rig needs to be stopped, then the first required action is to stop the rig using the TIA interface. However, if the rig needs to be stopped quickly, then in addition the brake can be pressed. In the event of an emergency, the power should be cut first using the emergency stop button and then the brake should be pressed. For the purpose of safety, a security gate was fitted to the entrance to the operating area of the rig, with a warning sign stating that there was a dangerous machine operating in the area.

As with the electric motor, the power electronics and control units were supplied by Fraser & MacDonald (Electric Motors) Ltd. They included:

- Siemens Sinamics Control Unit CU250S-2 USS (6SL3246-0BA22-1BA0)

Figure 6.27: Displayed here is the control station. The red emergency power button can be seen on the right, the foot brake situated underneath the desk on the left, the CCTV screen above the central two computer monitors used to operate and monitor the rig and the peristaltic pump control units below the screen on the right-hand side.

- Siemens Sinamics Power Module PM240-2 (6SL3210-1PE21-8UL0)
- Siemens Output Reactor (6SL3202-0AE21-8CA0)
- Siemens Line Reactor (6SL3203-0CE21-8AA0)
- Siemens SINAMICS Intelligent Operator Panel (IOP-2) (6SL3255-0AA00-4JA2)

An electronics cabinet was purchased from RS online and modified, installing 2 vents and a cooling fan that would operate when power was supplied to the rig. The electronic components were mounted onto the cabinet back plate, allowing sufficient ventilation space between them (See Appendix G.1 for motor cabinet layout), as outlined in the G120C manual (Siemens [227]). The electric motor required 3-phase power and so this was installed by the University of Strathclyde Estates team. The build of the control cabinet was carried out by the Electronic and Electrical Engineering department, installing the cabinet and wiring the setup together. Additional cooling was also set up, with two large fans positioned below the cone ventilating the motor during operation.

For safety and security, a power switch was installed on the access gate, which was manually locked shut prior to each operation. Following this, there were a number of security features that were due to be implemented:

- A lit beacon will be installed, so that during operation an orange light would indicate that the rig was being used
- Two electrical locks (solenoid: Schmersal AZM150SK-02/02RT024 and relay: Siemens 3SK11211AB40) will be installed, replacing the manual lock on the gate. One would be installed on the door of the rig, which was currently locked using a bolt, and a further one on the access gate. So that during operation the door to the rig and the access gate would be locked and after operation and when powered down, would become unlocked.
- A timer relay (Siemens 3RP25051AW30) will be installed, which when power is cut from the rig, the electronic lock on the door would stay active for a period of time (to be decided), after which would unlock and allow access to the rig

Two 50W DC LED lights IP65 were selected and mounted above and below the rotational plane of the sample holders inside the test chamber. Both lights had a metal bracket allowing them to be offset from their mounting surface and orientated as desired. As neither lights were mounted on the floor of the rig and the test rig was not watertight, no flooding could occur, however splashing was expected. The lighting connectors were waterproof. DC lights were required for high speed imaging due to the flicker of AC lights at 100Hz, which make high speed imaging very challenging.

6.9.2 Sensors

As discussed in Chapters 5 and 3, coatings used for the protection against rain erosion are temperature and moisture sensitive and currently there is a lack of understanding of the effect of both rain temperature, air temperature, temperature gradients between the air and rain and humidity on the rain erosion process. Therefore during rain erosion testing, the temperature of the coating, and the temperature and humidity in the test chamber need to be monitored. Understanding the impact velocity is of significant importance to the rain erosion process, but also for the control loop of the electric motor in terms of safety and stability. Further, the ASTM [71] and DNVGL [72] guidelines make requirements for some of the following sensors during rain erosion testing. Therefore, the following sensors were selected:

- 1 x Submersible inlet water tank temperature sensor (Blue Maestro Tempo Disc™ Wireless Waterproof Temperature)
- 2 x Enclosure humidity, pressure, temperature and dew point sensor (Blue Maestro Tempo Disc™ Wireless 4 in 1 Sensor and Logger)
- 1 x Incremental encoder for rotational speed (Kuebler Sendix 5020 rotary encoder)
- 2 x Contact thermocouples attached to the inside of the samples (Omega SA2C-KI-1M-SMPW-CC)

The sample holders were designed, such that the thermocouples would be attached directly to the surface of the inside of the samples with a hole allowing wires to pass

next to the sample holders and into a set of pockets (one for each sample holder). Designed and manufactured using 3D printing, a set of covers for these pockets (electronics boxes) contained the electronics assembly which allowed the processing and transmission of data. The electronics assembly included: an Arduino MKR1010, a thermocouple amplifier, a switch and a Li-Po battery (See Appendix H.1 for layout). The Arduino MKR1010 uses WiFi to transmit the thermocouple data wirelessly from the rig during operation to the control station computer and can be recharged using the mini usb port when required. Additional accelerometers were also purchased for future experiments, attaching to the samples and allowing the sensing of acceleration data from droplet impacts, allowing the circuit to have multiple purposes, depending on the desired research objectives. The electronics box had a complex design, making CNC milling from a solid billet of material unfavourable and expensive. The box needed to be lightweight, with a specialised shape. 3D resin printing provided the necessary flexibility and quality and with a polypropylene-like material, provided the necessary inertness to saline and acidic conditions. Furthermore, the rubberised resin when screwed in place provided a reasonably good seal, with the thermocouple cable running out of a slot in the side. As the air inside the rig would be humid especially when using artificial seawater, corrosion of the electrical components would be a risk, and so this slot can be sealed using a liquid electrical tape coating.

6.9.3 Rain System (Artificial Rain Field)

The inlet tank is fed directly from a mains pipe with a connected overflow pipe. The inlet tank is connected to a set of 4 peristaltic pumps, whose flow rate is controlled from the control station by a set of current-controlling dials. The peristaltic pumps have outflow tubes that split, through Y connectors, enough times to feed 32 needles per octant, with each pump feeding 1 or two octants depending on the desired configuration. The running water 'rains' onto the cone-shaped assembly of stainless steel panels, with water running into a jet-cut grating. The wastewater is collected in gutters attached to the grating, which are connected to large yellow tubes that feed into the outlet tank, which intern is connected to a variable-speed pump (IMP pump NMT SAN SMART

25/80-180). The pump's operation is controlled via a float switch, which switches on when the outlet tank fills to a preset level of water. The inlet and outlet tanks are two 1000 Litre ICB tanks. The ICBs and tubing types were selected based on compatibility with dilute acids and artificial seawater (Figure 6.28).

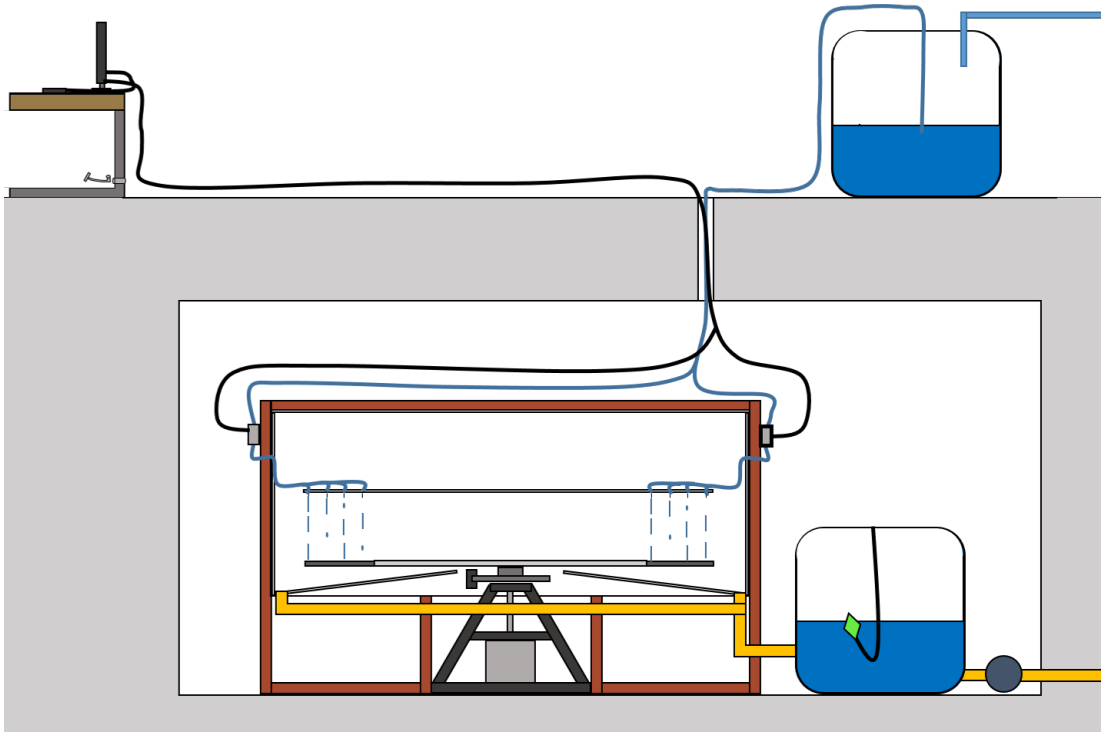

Figure 6.28: Diagram showing the full water system.

The artificial rain field was designed to allow easy adaption and replacement of components when needed. The hypodermic needles fit directly to Luer locks. Luer loc-to-barb fittings were purchased, with their outer diameter measured as 11mm. Following this a small panel was cut with 4 different sizes, 10.9mm, 11mm, 11.1mm and 11.2mm. Luer lock fittings were tested in each hole, with the tightest fit found as 11mm. The rainfield panels were then laser cut with 11mm holes, providing a push-fit for the luer locks. This made the system simple to use, replace and customise, as required.

Blunt hypodermic needles were selected for safety reasons and their wide ranges of needle sizes can produce a range of droplet sizes repeatably at a range of different rates.

This offers good flexibility within the design. Finnegan et al. discuss that during the design of the whirling arm rig at ETC, several options were investigated and that blunt hypodermic needles were the optimal selection for this role [75].

A helical needle configuration was chosen, which staggers the droplet production locations ensuring there were no hot spots. Repeated impacts in exactly the same location can cause significantly accelerated failure [75]. Previous rain erosion test rig designs have not considered this issue and evidence from particle tracking simulations suggests that there are preferential hot spots produced by them which may lead to accelerated failure [228]. Needle spacing was 56.18mm radially, with 8 columns and 4 rows, giving 32 needles per octant (Figure 6.29). The distances from the closest and farthest needles to the centre of rotation were 655.9mm and 875.0mm, respectively.

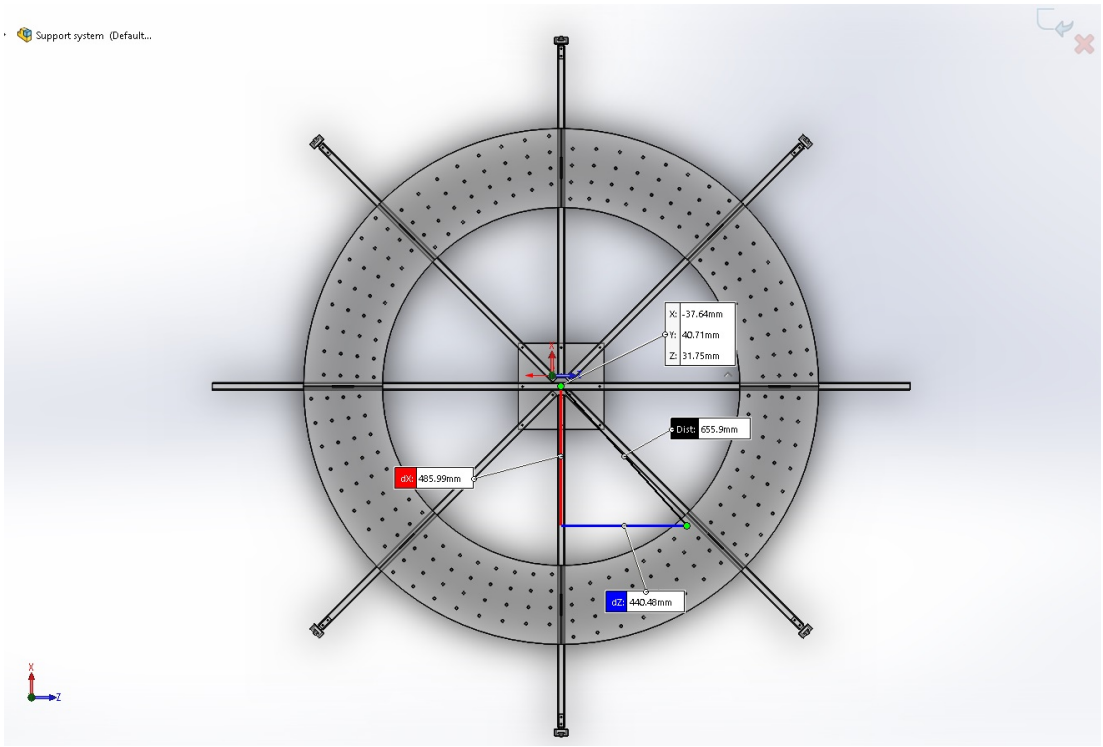

Figure 6.29: CAD drawing of the rain system from above, showing the helical needle configuration on each octant of the system as well as the U-channel frame.

The rain system was supported by an aluminium U-channel frame. The water tubes ran inside the U-channel sections and so kept away from rotating components. Each

octant had Luer fittings, allowing for disconnection simply and quickly. This allowed sections to be added, swapped or removed simply and safe needle exchange. The rain system was mounted on a set of 6 sliders with an adjustable friction force, allowing for it to be locked in place during operation. The height of the system could be adjusted using two linear actuators and a pulley system using an electrical switch.

In this section droplet size was investigated using a droplet shape tensiometer and additionally a high speed camera and the artificial rain system to characterise how the artificial rain system would operate in practice. Additionally, any influence of using a peristaltic pump on droplet shape and size instead could be outlined.

6.9.3.1 Methodology

Firstly, droplet sizes were investigated for 14 different needle sizes. For each needle size, droplets were produced and visualised using a DSA25 drop shape tensiometer (Kruss) at the University of Edinburgh. This creates droplets using a positive displacement pump to deliver a precise volume of liquid, which are then visualised optically. From a minimum of 3 droplets for each needle gauge, the mean droplet diameter was calculated.

Secondly, an octant of the rain system was attached to pump 2 and 6 different needle sizes were fitted. For each needle size investigated, all of the needles had to be replaced with that needle. this is because each needle size provides a different resistance to the flow and so if wider needles are fitted with thin needles then there is preferential flow through the wider needles. This creates two problems, firstly this makes degassing the needles challenging, but additionally, this makes quantifying the rain rate through each needle or needle set more challenging. Additionally, the minimum and maximum flow rates meant that in order to produce droplets, there had to be a sufficient number of outlets for the flow such that the needles could produce droplets rather than a jet. It was not possible to fully degas the rain system with G34 needles, so when running the rain system, the resistance caused by the presence of air was larger than the pressure from the silicone tubes around the fittings. In this case, the water took the path of least resistance and so instead flowed out of the fittings. The results are included as they provide some insight into how similar the droplet sizes are compared to the tensiometer,

but it is difficult to ascertain what the influence of increasing flow rate is. 4 different flow rates were attempted for all needle sizes, however, it was not possible to create droplets from G27 at higher flow rates than 30% power from pump 2. Experimental details can be seen in table 6.21. The rain rates produced in each experiment are double those calculated in table 6.24, as the volumetric flow rate used here is the same, however the rain area is half. Rain rates given in 6.21 are calculated using equation 6.22 and the coefficients stated in table 6.25.

Table 6.21: Droplet diameters for each of the respective needles tested, as measured by the tensiometer (University of Edinburgh).

Needle Gauge	Tensiometer	Pump Power Ratings/ **Calculated Rain Rates (mm/hr)**			
12	Yes	100/**21.4**	80/**16.8**	60/**12.3**	40/**7.7**
13	Yes				
14	Yes				
15	Yes				
16	Yes				
17	Yes	100/**21.4**	80/**16.8**	60/**12.3**	40/**7.7**
18	Yes				
20	Yes	60/**12.3**	50/**10**	40/**7.7**	30/**5.4**
22	Yes				
25	Yes	50/**10**	40/**7.7**	30/**5.4**	25/**4.3**
27	Yes	30/**5.4**	25/**4.3**		
30	Yes				
32	Yes				
34	Yes	50/**10**	40/**7.7**	30/**5.4**	

Images of the droplets were captured using a Chronos 1.4 Highspeed camera at a resolution of 1280 x 1024 pixels at a frame rate of 1000fps. In each of the images, directly behind the droplets, a section of matt white Pakcel foam was present to remove any features from the image. For scaling, a ruler was present each image, allowing distance travelled and the dimensions of each droplet to be calculated. A Python script was developed using the Canny edge detection algorithm [126] to extract the edges of each feature in each image. The positions of each needle were then manually found and the needle producing the clearest droplet shadow in experiment was selected. A bounding box was created, the beginning centroid of the droplet and the maximum dimension for each experiment were then estimated visually. The images were then iterated over removing all pixels at a greater distance than 2 times the maximum dimension from

the centroid. From the remaining pixels, an ellipse was fitted using an adaption of the python implementation by Christian [229] "Numerically Stable Direct Least Squares Fitting Of Ellipses" algorithm by Halir and Flusser [230], assuming a 0-degree rotation from the x-axis, the script was adapted. The equation for an ellipse is given by equation 6.18:

$$Ax^2 + Bxy + Cy^2 + Dx + Ey + f = 0 \tag{6.18}$$

A rotated ellipse satisfies the following equation:

$$tan(2\alpha) = B/(A - C) \tag{6.19}$$

Where alpha is the angle between the x-axis and the major ellipse axis. If we set $\alpha = 0$, B must also be 0, thus reducing equation 6.18 to equation 6.20:

$$Ax^2 + Cy^2 + Dx + Ey + f = 0 \tag{6.20}$$

The solution can then be calculated using the adapted method, providing horizontal and vertical diameters and the newly calculated centroid. Each calculated centroid was passed to the next time step and the process continued through all images for each experiment. This allowed tracking of the moving droplet through each image due to the low time step. The frames were filtered to ensure that velocity of the calculated centroid of the droplet was consistently increasing.

6.9.3.2 Results

For the edge detection results, it was not possible to clearly visualise droplets at power ratings of 40% and 50% for G25 Needles and for the G27 needles it was not possible to visualise any droplets at any of the power ratings tested. In addition to this, for power ratings of G25, it was not possible to clearly distinguish single droplets from the images as in each instance of droplet production, several droplets were produced and so these results were discounted.

Mean droplet widths and heights calculated are displayed in figures 6.30 and 6.31, respectively.

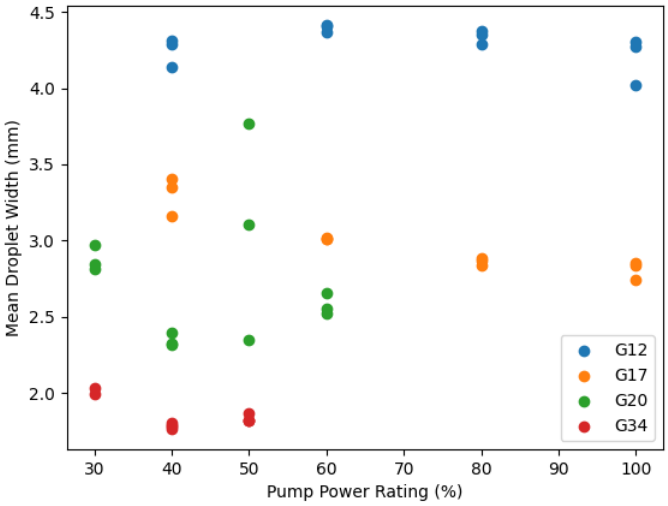

Figure 6.30: Mean droplet width values for a range of different pump flow rates.

Needles with higher gauge numbers produced smaller droplets than lower gauge numbers. At 50% power with G20 needles, the droplets produced had a large variation in droplet width (Figure 6.30), compared with other needle sizes and for one droplet, a very large mean droplet height at approximately 6mm (6.31).

Standard deviations in droplet height were particularly high for G17 and G20 droplets (Figure 6.32) and for G20 in droplet width (Figure 6.33).

In general, standard deviations in droplet width were lower than those observed in droplet height as can be seen in figures 6.33 and 6.32, respectively.

During the droplet imaging analysis, oscillations in droplet height and width were observed, which were 90 degrees out of phase of each other. It was visibly easier to observe this in images of larger droplets, with oscillations damping over time (Figure 6.34). The time period and frequency of the oscillations were in the order of $\sim 0.01-0.1$ seconds and 10-100Hz, respectively.

The results from the tensiometer can be seen in table 6.22.

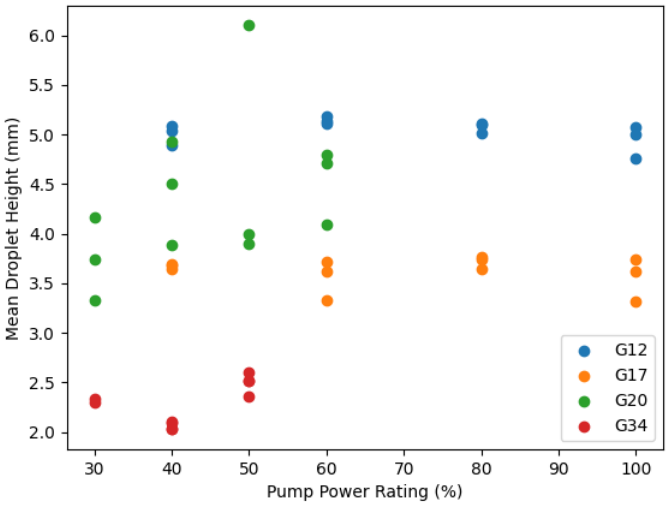

Figure 6.31: Mean droplet height values for a range of different pump flow rates.

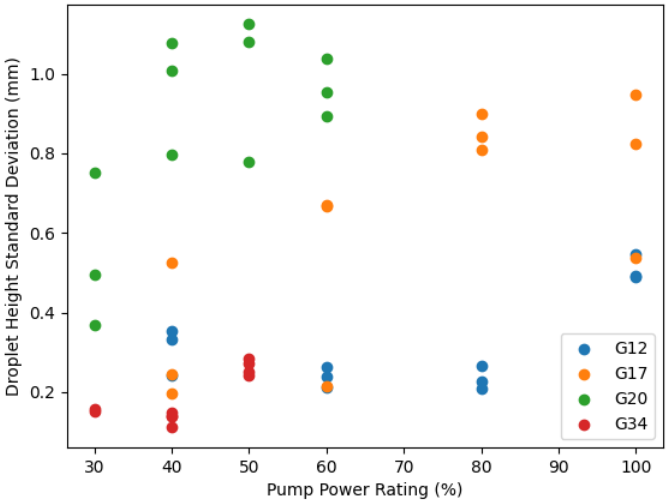

Figure 6.32: Standard deviation for droplet height values for a range of different pump flow rates.

6.9.3.3 Discussion

As mentioned above, smaller needles were challenging to work with, particularly for the generation of consistent droplet creation. One challenge was due to difficulties in degassing the system. It was observed that when setting up the experiment for the

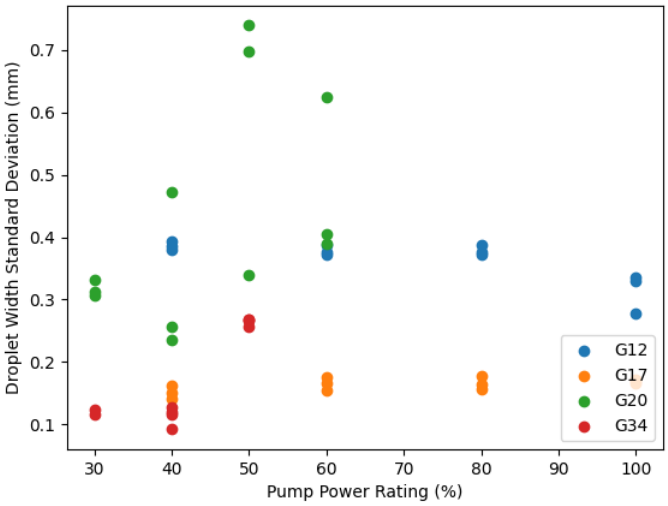

Figure 6.33: Standard deviation for droplet width values for a range of different pump flow rates.

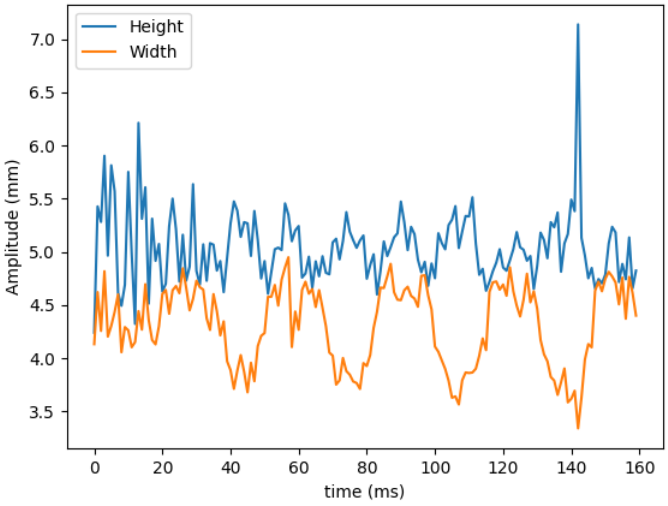

Figure 6.34: An example of the shape oscillations observed for droplets produced by the G12 needle.

34G needles, that some of the tubes for the needles were filled with air. Water was able to flow through the needles with tubes that had no air and were filled with water. In needles where their tubes had air, these instead did not produce droplets. This lead to uneven droplet production. Additionally, air was observed passing inwards through

these needles through the system. To combat this, Purging the air was attempted by using a higher flow rate, which worked with larger needles, however this caused leakage through connection points and did not remove the air from the needles. This is an inherent challenge with using a system with a large number of couplings. In addition, the process of attaching and detaching needles requires for it to be drained, which introduces air into the system.

These challenges could be mitigated through the use of solid manifolds for a given number of needles, which would reduce the number of connectors. Additionally, adding taps with luer fittings for the needles to attach to would improve the connection process, allowing the system to be filled before needle attachment.

Some needles produced additional small satellite droplets that were unintended which has been reported elsewhere and occurs as a consequence of the use of needles and due to the surface tension forces being released. These satellite droplets varied in size. This can be observed at 40%, 50% and 60% power for the G20 needles and 25% and 30% for the G25 needles. This was likely not observed in the G34 needles due to the challenges observed during the setup and testing with that needle size. These were not counted in the droplet size analysis (Figure 6.35). In general, these were only produced at higher power ratings, which indicates that the flow rate was too high for

Table 6.22: Equivalent droplet diameters for each of the respective needles tested, as measured by the tensiometer (University of Edinburgh).

Needle Gauge	Mean Volume (µL)	Equivalent Droplet Diameter (mm)
12	46.93	4.48
13	42.67	4.34
14	32.78	3.97
15	30.63	3.88
16	28.67	3.80
17	25.96	3.67
18	22.69	3.51
20	17.65	3.23
22	14.61	3.03
25	11.26	2.78
27	8.51	2.53
30	7.53	2.43
32	6.65	2.33
34	4.91	2.11

stable droplet production.

In particular, when producing droplets using the G25 needles, there was a large spread of droplet sizes, however using the script developed for the current process, it was not possible to assess the variation in droplet size of these smaller droplets. Additionally, large variations in droplet speed were observed for the satellite droplets, and there were instances of the satellite droplets and larger droplets occupying the same pixel, however it was not possible to confirm whether the droplets were impacting each other or whether they were in front or behind each other.

Droplets produced by the G20 needles in general produced results that varied significantly. There were significant differences in the results, which challenges their reliability as can be seen in the standard deviation. There are three possible reasons for these results:

- the droplet generation system was producing inconsistent results
- the edge detection algorithm had challenges in detecting the droplets
- there were artefacts inside the images which were detected and so created problems for the ellipse fitting.

Challenges with the droplet production system were observed for smaller needles, however upon inspection of the input data, no satellite droplets or moving erroneous droplets were produced by the rain system. In general the Canny edge detection algorithm is well documented to be noise tolerant and so is unlikely to be the cause [116, 126, 127]. It is likely, the issues arise with the post-processing of the data in identifying and capturing the droplet shape data correctly. For the G20 needles, there was a reasonable amount of additional noise generated within each image, which made capturing the droplet shape correctly challenging In some of the analysed results. This can be further seen by the relatively high standard deviations in figures 6.33 and 6.32 due to the presence of artefacts inside the image, in the form of reflective items, water splashes, satellite droplets and other highly contrasting features.

The droplet sizes calculated here are relatively consistent with the equivalent diameters captured by the tensiometer 6.23. However understanding how representative

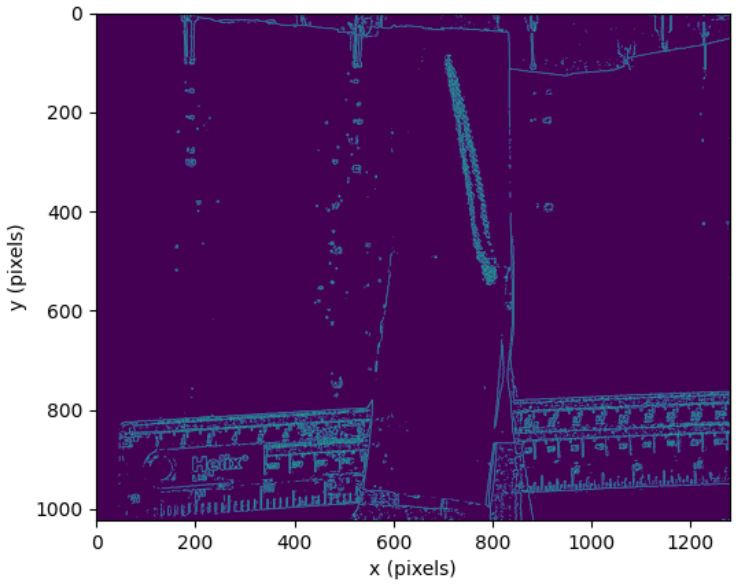

(a)

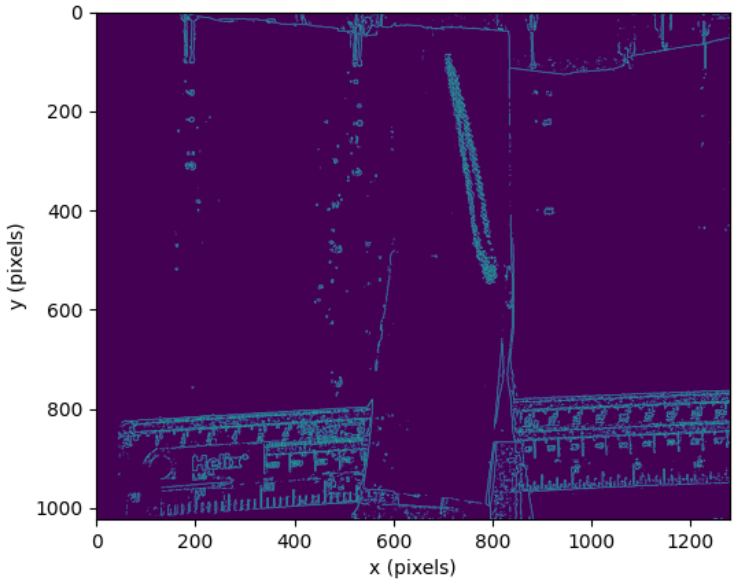

(b)

Figure 6.35: Figures 6.35a and 6.35b show the additional satellite droplets produced by G25 needles, with the pump set to 40% power.

the data presented here is a challenges as there was a limited amount of data. Further work is required to gather more data and confirm the results produced here.

Table 6.23: Comparison of the droplet dimensions calculated using the method here and using the tensiometer.

Needle Gauge	12	17	20	34
Tensiometer Equiv. Diameter (mm)	4.48	3.67	3.23	2.11
Calculated Width (mm)	4.70	3.13	2.72	1.85
% difference	+4.9%	-14.7%	-15.9	% - 12.5%
Calculated Height (mm)	5.50	3.87	4.34	2.29
% difference	+22.7%	+5.4%	+ 34.6%	8.5%

However as noted by Halir and Flusser, the fitted ellipse does estimate a smaller ellipse then is correct, however this is an inherent challenge with ellipse fitting and the algorithm provides a very fast and robust solution that does not require iteration. Additionally, the physical resolution of the camera used in the present setup was a limiting factor with approximately 6 pixels per mm. If it were possible to use a macro lens for this work, then a higher pixel resolution would have been possible.

A detailed explanation of the droplet detachment and physics that lead to the oscillations is provided by Raza et al. [231]. Essentially there are two main forces that are acting on the droplet during its formation on the needle end, gravity and surface tension [76]. When the gravitational forces are larger than the surface tension forces, the droplet elongates forming a neck, which as time progresses is broke, releasing this stored energy and producing a capillary wave on the surface of the droplet. The droplet proceeds to vertically contract and expand horizontally, then vice versa, oscillating between oblate and prolate spheroids. The oscillations decay with time, which is related to the viscosity of the liquid and the droplet size [231]. As the droplet falls through the air, increasing in velocity there is likely to dampen the oscillations due to the air resistance, although this requires further investigation.

The oscillation period as described in section 6.9.3.2, is much lower than the impact duration discussed by finnegan et al. [75] and Johansen [76]. It would therefore be reasonable to assume that the droplet shape can be assumed quasi-static during the impact process. However as the shape of the droplet is oscillating between prolate

and oblate, the spherical droplet shape assumption may not be valid for this case. It is important to note that as this investigation did not occur within an operating RET, it is not possible to know whether the droplet will experience these oscillations, especially considering the aerodynamic forces that control droplet impingement [75, 76]. Additionally, if the droplet is oscillating just after it is produced, this may affect droplet stability and lead to early breakup inside the RET. Further work is required to assess whether it is present during rain erosion testing. There is growing consensus that droplet shape within RET is non spherical and highly complex, highlighting the need for further research in this area [232, 233].

6.10 Testing and Calibration

For the safe and consistent operation of such a complex machine, the rig needed calibration, several risk assessments, safety protocols and operational tests. Details on motor calibration, risk assessments and safety protocols can be found in Appendices I and L.

6.10.1 Pump Calibration

The pumps used to feed the needles in the rain system required calibration prior to use. During the main setup of the rig, one of the adjacent octants to the door was removed, allowing better visualisation of the sample holder during operation using the high speed camera. This was due to be the typical test setup and would allow periodic remote visualisation using the high speed camera through the viewing window, without having to stop the test.

Each pump was connected to a single tube and was run at different current levels for a total time of 120s. The tube was held in place with a stand and flowed into a bucket located on top of a set of scales, measuring the mass of water for the given time period. Prior to beginning the timer, the water flowed into a waste bucket and was only collected after any transient fluctuations were no longer present. The minimum current that still produced a flow rate was found to be 22%. To calculate the rain rate, the area

over which the rain acts must first be calculated (A_{rain}). The sample was 250mm in length, the needle configuration was designed such that the droplet impacts would be sufficiently far from the sample edges, preventing edge effects from influencing results. An edge offset of approximately 12.5mm was initially selected, providing an exposed sample length of 225mm, although due to the helical pattern in reality the exposed length was 219.1mm, providing a border of 15.5mm. The area over which the rain acts was calculated as:

$$A_{rain} = \pi(r_{n,o} + d_b)^2 - \pi(r_{n,i} - d_b)^2 \tag{6.21}$$

Where $r_{n,f}$ is the radial position of the outer needle, $r_{n,i}$ is the radial position of the inner needle and d_b is the border offset, all of which is in m. Using equation 6.21 gives an area of $0.30m^2$ per quarter. The flow rates and therefore rain rates can be observed in table 6.24. Pump 4 is the pump located by the door meaning that it will only be operated with one octant, therefore care would need to be taken to adjust the flow rate accordingly during testing. The total flow rate during testing can be calculated as the summation of all other pumps at their selected flow rate. The flexibility of this system, allows multiple needle sizes to be used and multiple flow rates to be used, all of which are easily adjustable and modifiable.

There was found to be no significant difference between the pumps, with all pumps outputting the same flow rate to within 5-10% of each other. Plotted flow rate values can be seen in figure 6.36, with flow rates varying approximately linearly with supplied current. With all octants running at full flow rate in the default configuration, this gave a range of 5.5 -42.6mm/hr, although due to the modular nature of the test rig, lower rain rates could be used by using less than 4 pumps.

The equation for calculating the rain rate from supplied current is given by equation 6.22. Coefficients for each pump is given in table 6.25. coefficients were calculated using linear regression.

$$RR = a_{PRR} * I_{PRR} + b_{PRR} \tag{6.22}$$

Table 6.24: Pump flow rates as measured during the pump calibration tests.

Pump Number	Current %	mass (g)	flow rate (ml/s)	Rain rate (mm/hr)
1	100	1181.7	9.85	10.66
	80	941.1	7.84	8.49
	60	688.2	5.74	6.21
	40	410.7	3.42	3.70
	22	153.2	1.28	1.38
2	100	1167.7	9.73	10.53
	80	945.7	7.88	8.53
	60	694.5	5.78	6.26
	40	423.4	3.53	3.82
	22	191.6	1.60	1.73
3	100	1153.5	9.61	10.40
	80	912.5	7.60	8.23
	60	662.9	5.52	5.98
	40	403	3.36	3.63
	22	160.9	1.34	1.45
4	100	1222.2	10.19	11.02
	80	982.1	8.18	8.86
	60	728.1	6.07	6.57
	40	444.7	3.71	4.01
	22	196.9	1.64	1.78

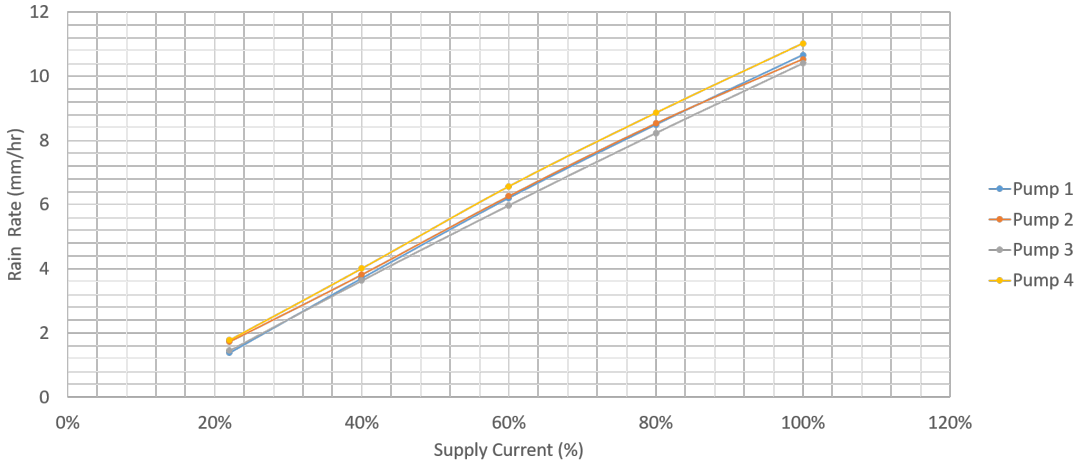

Figure 6.36: Pump flow rates, plotted as a function of supply current %.

Where a_{PRR} and b_{PRR} are calculated coefficients RR and I_{PRR} are the rain rate and the supplied current, respectively.

Table 6.25: Coefficients for equation 6.22, as calculated for each pump.

Pump Number	1	2	3	4
$\mathbf{a_P RR}$	0.1191	0.1138	0.1148	0.119
$\mathbf{b_P RR}$	-1.1034	-0.6988	-0.9932	-0.7384

6.10.2 Brake & Speed Tests

As initially mentioned in section 6.4.3, there were two sample holders designed for use in this test rig. Firstly, there was the low drag aerofoil sample holder, designed for use at high speeds and secondly, there was the flat sample holder, designed for the use of long, thin, flat samples by Dr. Kieran Pugh. This sample holder also allowed a three-point bend test to be applied to samples during testing. Due to the shape of this sample holder, testing at high speeds was not possible.

The total operational time of the test rig with both sample holders is listed in appendix J.

6.10.2.1 Leading Edge 1 and Brake Test

Start Time/Date: 11:30am 16/02/2022 **Attendees:** James Nash, Kieran Pugh, Drew Irvine **Speed:** 500rpm, 750rpm **Duration:** Approx. 30min, 15min

Description: This was the first time the operational speed had exceeded 300rpm. Vibrations were monitored using the accelerometer connected to the Reactec Device in parallel with the Knowles accelerometer connected to the National Instruments DAQ (monitored using LabView at the control station). The rig was monitored using the CCTV which showed no abnormalities during operation. Displacement was measured to be 1 micron using the Reactec device. The speed was then increased to 750rpm, at which point the rig became audible from the stairwell. The displacement reading on the Reactec increased to 2 microns and displaying no sharp spikes, thus indicating no significant resonant frequencies.

Following the completion of this test, the mechanical brake was tested, first by pushing the e-stop button, which was quickly followed by the foot pedal brake. The rig stopped spinning within 2 seconds. A subsequent visual inspection took place of the

hub, rotor, motor and interior of the test enclosure.

Observations:

- Bolts had not moved
- Elevated temperature inside the test chamber, likely due to brake test
- Slight smell and black dust, likely due to new brake disc and pads generated by brake test

Following the test, p1120 modified from 3000s to 2000s.

6.10.2.2 Leading Edge 2

Start Time/Date: 13:10pm 16/02/2022 **Attendees:** James Nash, Kieran Pugh, Drew Irvine **Speed:** 750rpm, 1000rpm, 1100rpm, 1200rpm **Duration:** Approx. 15min, 10min, 10min, 10min

Description: Post inspection, operation resumed by initially accelerating to 750rpm for 15 minutes. This was for safety and to ensure stability in the rig. The speed was then increased to 1000rpm. was a slight increase in sound. Displacement readings from the Reactec were 2.5 microns. After approximately 10min operation time the speed was subsequently increased again to 1100rpm and operated for a further 10min. Noise was more audible at this speed, however visuals from the CCTV and readouts from the accelerometers were steady. Following the consistent stability of the rig, the speed was further increased to 1200rpm for 10min. Displacement increased to 3 microns, which as can be seen from figure 6.23 is well within safe vibration limits for a rotating machine.

Following this successful test, the E-Stop was once again pressed with the brake subsequently tested at this higher speed. The brake stopped in approximately the same time as stated for the first test (2s). The rig was once again inspected.

Observations:

- Bolts had not moved
- Elevated temperature inside the test chamber

- Slight smell and black dust, although less than previously

The increased temperature, smell and dust were once again present, likely due to the brake test.

6.10.2.3 Leading Edge 3

Start Time/Date: 14:39pm 17/02/2022 **Attendees:** James Nash, Kieran Pugh, Drew Irvine, Iasonas Zekos, Chris Cameron **Speed:** 1200rpm, 1300rpm **Duration:** Approx. 60min, 5min

Description: Further to the previous experiments, the long-term stability of the rig needed to be characterised. Both accelerometers from the Reactec Device were attached, one directly on the motor and one on the main bearing. The motor was accelerated up to a speed of 1200rpm and held at this speed for 1h, accelerating in approximately 12min. Maximum displacements were measured at 2.7 microns and 1.4 microns on the bearing and motor, respectively. Peak velocity and acceleration were measured at 0.4mm/s and 0.3mm/s^2, respectively.

After 1h of operation, the speed was increased to 1300rpm, accelerating within 2 minutes. Accelerometers showed no significant change in readouts. However after 5 minutes a loud bang was heard, so power was cut immediately, through the e-stop and the mechanical brake applied. An inspected was carried out immediately. On first inspection, debris from the tail sections of the sample holder were found all over the rig, and leading edge samples were present, although in a more complete state. A more detailed inspection was carried out in the following week as detailed in 6.10.2.4.

6.10.2.4 Root Cause Analysis

Upon inspection there was a significant amount of debris inside the test chamber, as can be seen in Figure 6.37.

From the accident debris, one of the tail sections (T1) was almost completely intact, however one of them was found in fragments (T2) (Figure 6.38). It is likely that T2 had multiple impacts, with the first likely being an impact with the enclosure and at least one other with the sample or sample holder, as the amount of fragmentation implies a

(a) (b)

Figure 6.37: Figures 6.37a and 6.37a show some of the initial debris upon first inspection following the failure.

significant amount of energy that was released. This would also explain the loud bang heard by the operators during the experiment that caused the emergency procedure to be initiated.

T1 had less fragmentation, although both corners had material removed implying multiple impacts (Figure 6.39). However due to the relative completeness of this section, the amount of energy absorbed by these impacts was significantly less than those experienced by T2 and so was likely with the enclosure walls rather than either sample holders or samples.

Both samples were almost completely intact, however, from the damage to one of them (S1) it was deduced that it had likely been impacted whilst still attached.

(a)

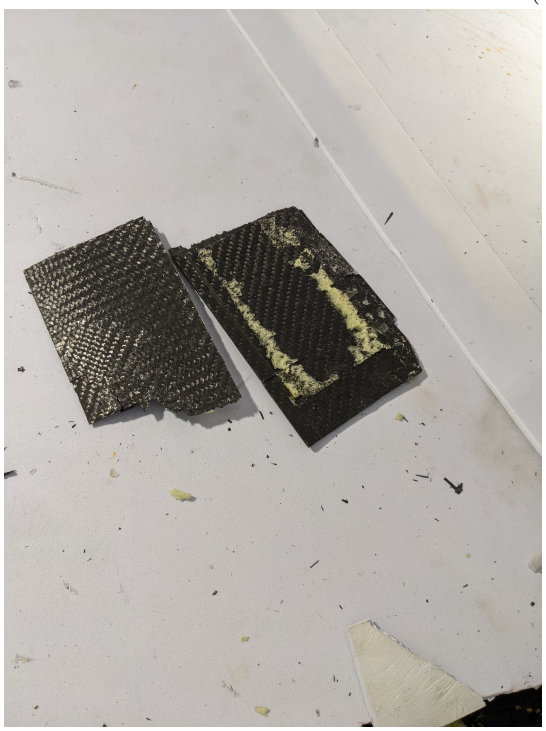

(b)

(c)

Figure 6.38: Figures 6.38a and 6.38b show The residual debris from T2. Figure 6.38c shows the impact damage observed on the enclosure walls.

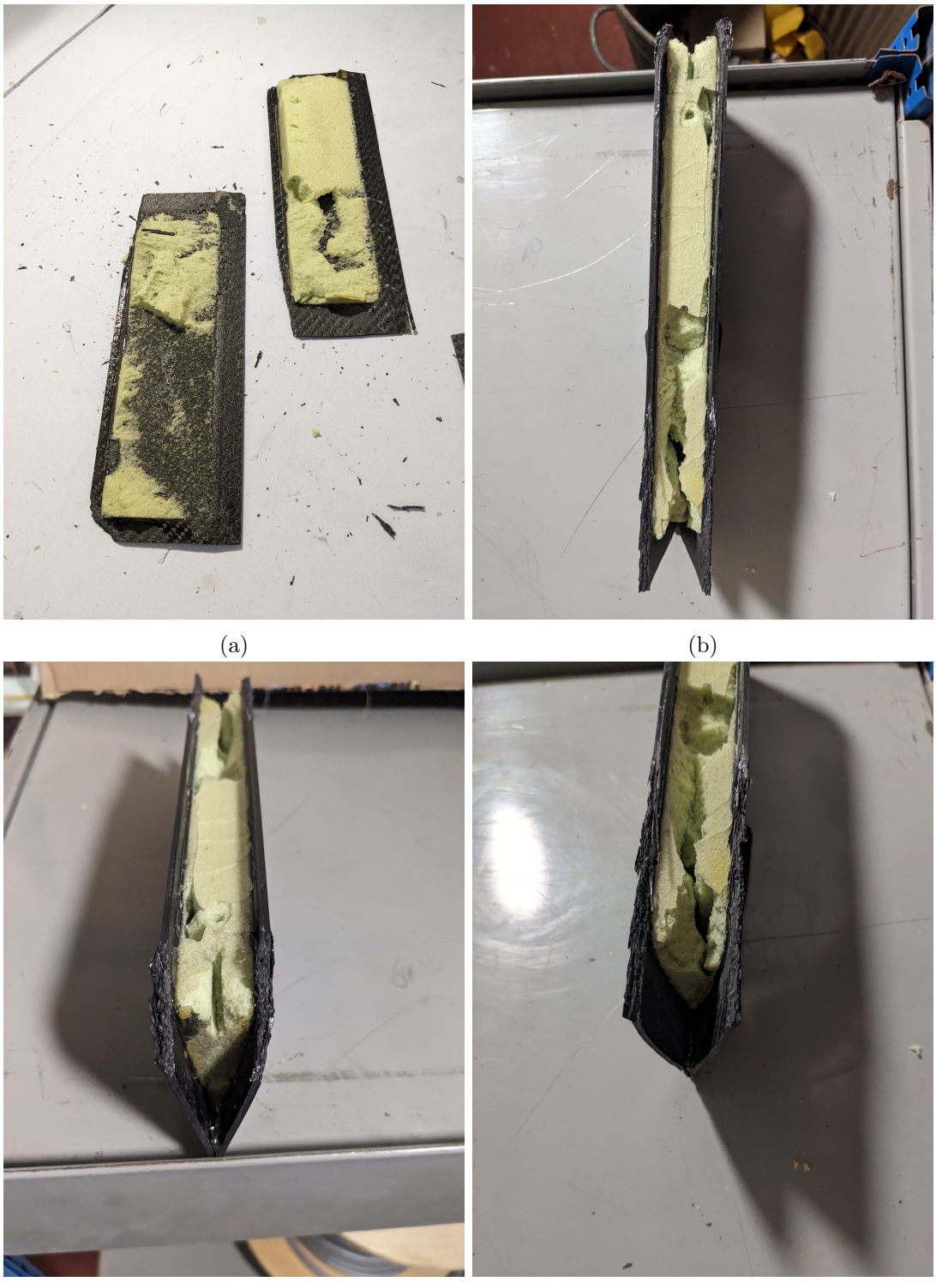

(a) (b)

(c) (d)

Figure 6.39: Figures 6.39a 6.39b, 6.39c and 6.39d show T1. Figures Figure 6.39b shows T1 reassembled emphasising how this tail section is nearly intact, excluding the fact that the two halves have debonded.

Given the fragmentation of T2, it was likely that this tail section had become detached from the sample holder and then due to the speed of rotation and the centrifugal forces, it had been flung outwards and whilst still in mid-air, S1 would have hit the T2, detaching it from the sample holder. This would explain the impact damage observed on S1.

Judging by the lack of obvious significant point damage to S2 (Figure 6.41), it is reasonable to suppose it hit the sides of the enclosure and not the sample holder or sample, with impact damage reduced by the foam. It's possible that this impact happened when the rig had begun to slow down after the e-stop was pressed and the brake applied.

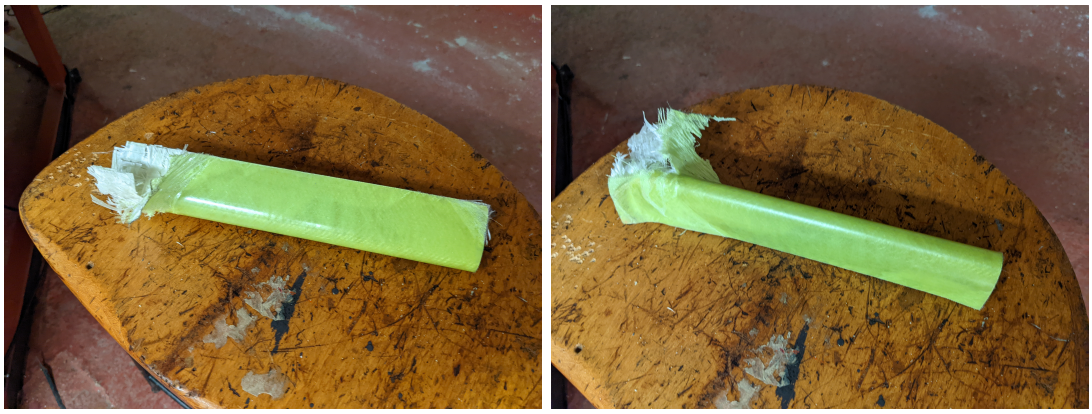

(a) (b)

Figure 6.40: Figures 6.40a and 6.40b show the impact damage to S1.

Whilst no significant impact point is visible, the sample is visibly deformed indicating that it had sustained some damage, likely due to the failure event. The end faces of the sample show some delamination, which could be due to buckling of the composite as a result of an impact with the chamber walls. The foam lining on the test chamber walls would distribute the point forces over more of the surface of the end of the sample, making the impact location less visible. If the impact occurred on the rear corner where the most deformation occurred it would help to explain the deformation observed.

Cracks or debonding typically follow the path of least resistance or least energy. On both sample holders the tail section fixation plates were still attached with their

respective screws. One of them had a smooth surface with no residual foam (Figures 6.42a and 6.42a) and the other had a roughened surface (Figures 6.42c and 6.42d).

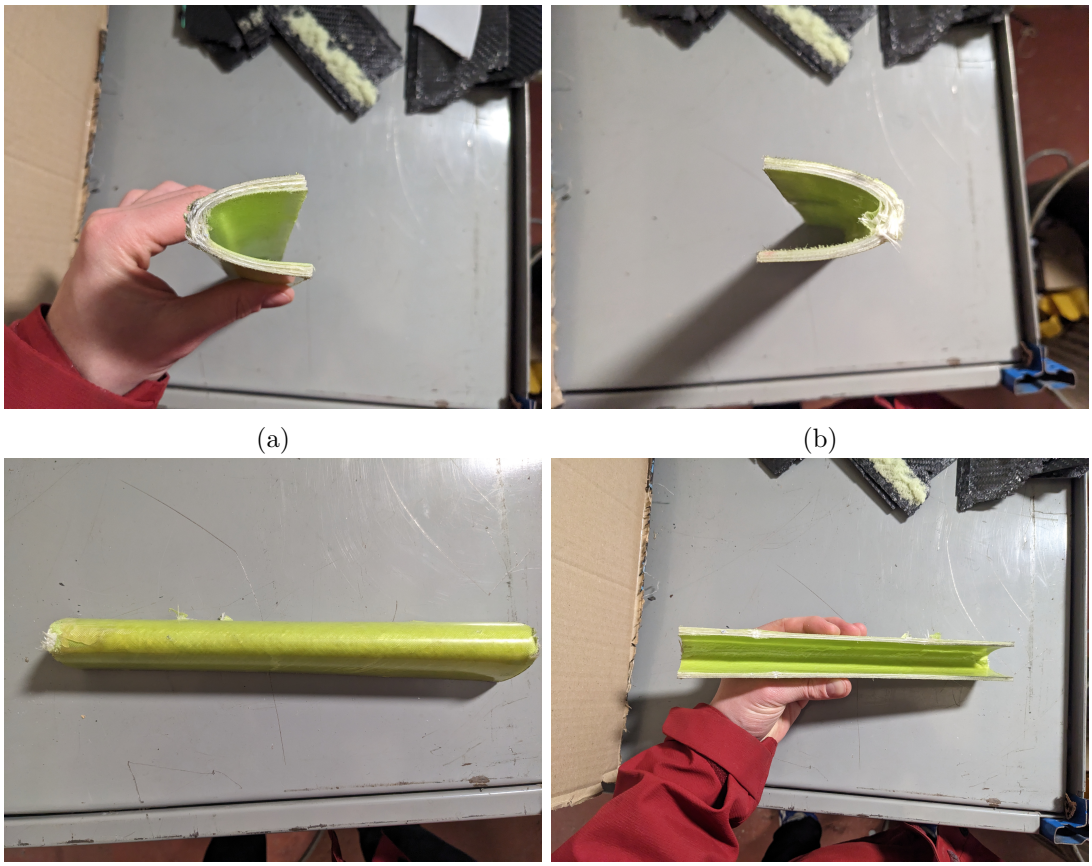

(a) (b)

(c) (d)

Figure 6.41: Figures 6.41a 6.41b show the ends of S2, with small impact marks visible. Figures 6.41c and 6.41d show the front of the sample, with deformation to the shape visible.

The smooth surface indicates poor adhesion and low surface energy and that the failure would have initiated inside the adhesive bond. A roughened surface indicates better adhesion, and potentially a cohesive failure from inside the foam material. Judging by the remains of the foam core of T1, which had a particularly smooth surface, it is likely that T1 came from the sample holder with the smooth surface and T2 came from the sample holder with the roughened surface.

The Sample Holder End Pieces had cracks initiating from their inner face. It is likely that when T1 became detached, it peeled away initiating at its innermost point and

peeled outwards, when this would have happened, this would have caused a moment about the end piece causing high stresses at the point of contact and therefore initiating this crack. It's likely when T2 became detached too a similar process happened. For the sample holder with the roughened fixation plate, the end piece had a crack initiating on the bottom, indicating that the tail section here peeled downwards, meaning it likely have hit the drainage panels, later ricocheting upwards into the path of the following sample holder. The sample holder with the smooth fixation plate had a crack present on the top of its respective end piece. The End Pieces and respective cracks can be seen in figure 6.43.

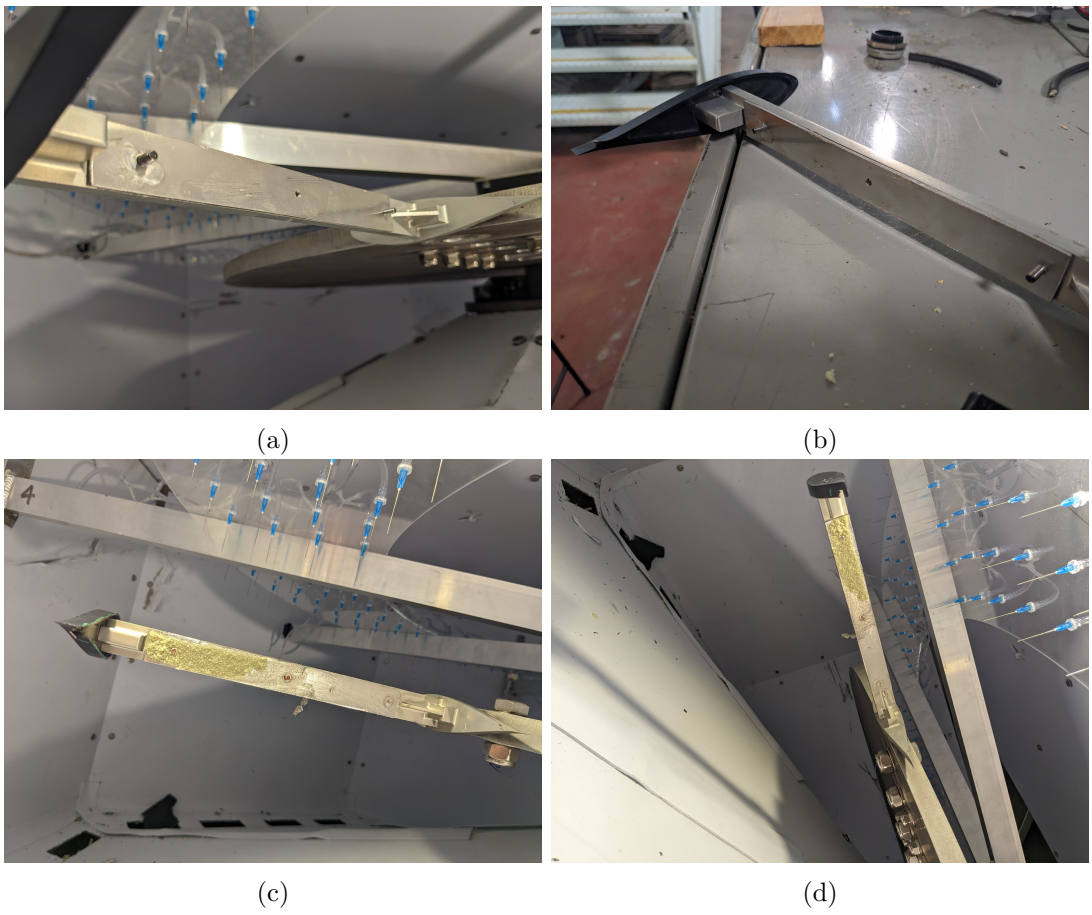

(a) (b)

(c) (d)

Figure 6.42: Figures 6.42a and 6.42b show the clean tail section fixation plate and Figures 6.42c and 6.42d show the Roughened tail section fixation plate.

Further to this the end pieces were bent about the airfoil thickness direction, which

was likely due to the moments generated by both the sample detaching and the tail sections detaching. This would have been due to how close the end piece bolts were together which meant that during operation the high centrifugal forces would have produced a large moment about the fixation hole closest to the front, which would have then caused this component to deform.

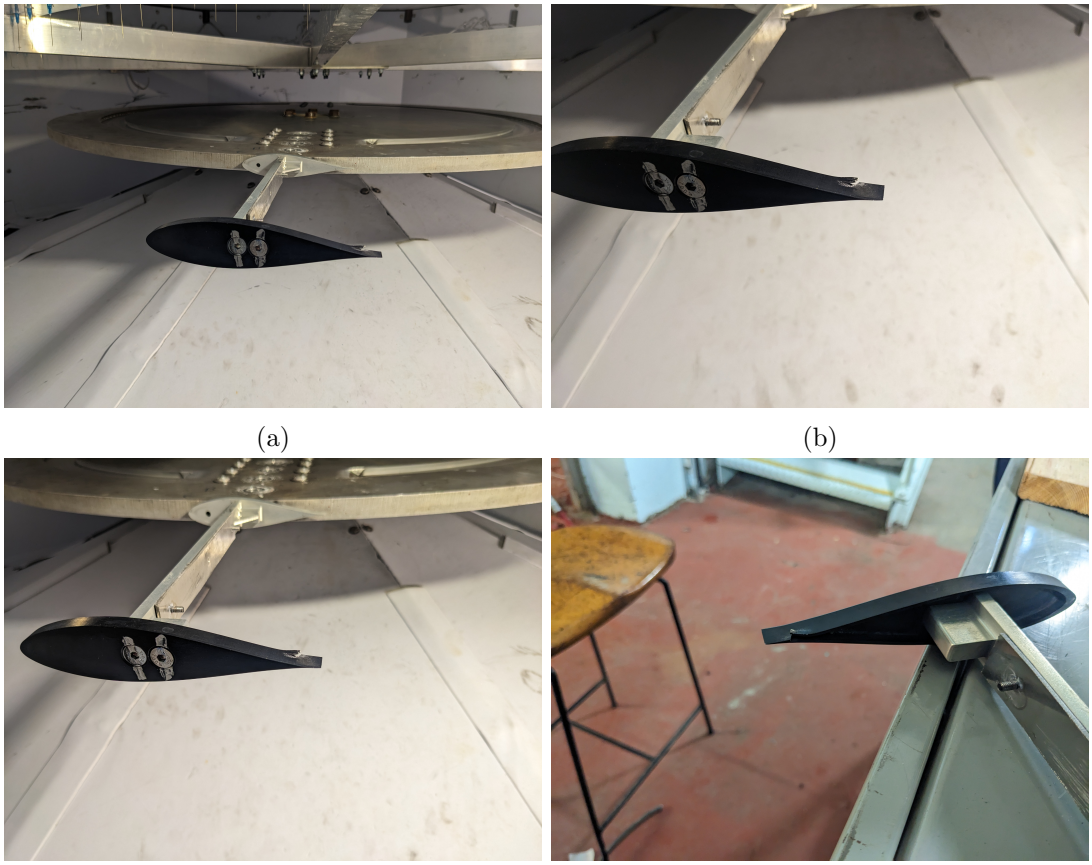

(a) (b)

(c) (d)

Figure 6.43: Figures 6.43a, 6.43b,6.43c and 6.43d show crack on both end pieces.

There was no visible damage to the main bearing, hub disc, main body of the sample holder, door, lid or enclosure walls (other than the one mentioned). Some residual black marks and dust was found inside the rig and on the sample holder, likely generated from impact of the carbon fibre with the enclosure walls. There was some minor damage to the needles and rain system, but nothing noteworthy. Further to this both the CCTV and lights were not damaged.

Following discussions with the Safety Officer and Workshop Manager concerning the incident and safety procedures, it was mutually agreed that the safety procedures were appropriate for safe the operation of the rig, providing safety and security for the equipment itself and the personnel operating it.

Whilst it was not possible to deduce the exact sequence of events that led to or caused this failure, the following conclusions can be made:

1. The enclosure design was robust enough to handle a component failure at 1300rpm without significant damage or risk to personnel operating it
2. The enclosure design provided sufficient safety for personnel operating it in the event of a component failure at 1300rpm
3. The application and use of foam likely reduced damage to the enclosure itself from the impact event
4. Safe operation of the rig must always occur with at least one person situated within full reach of the emergency stop switch and mechanical brake.

The following recommendations should also be carried out:

1. There were inconsistencies in the adhesive bonding of the tail sections to their respective fixation plates. Therefore the use of adhesives is a cause for concern and should be avoided
2. The modularity of the sample holder and the number of components were likely a contributor to its failure, therefore if possible the tail section should be integrated into the sample holder, which in turn should be one component, rather than an assembly.
3. The bolts on the End Piece component were located too close together and should be separated, reducing the moment about the bolts generated by the samples.
4. Fixation of the sample should be integrated as much as possible into the main body of the sample holder

5. Further more rigorous tests are required prior to the use of sample holders and their respective components prior to operation at high speeds.

6. Although not strictly necessary, it would be beneficial if the CCTV system could be used for recording tests, rather than just monitoring, particularly on higher speed tests.

7. Although not strictly necessary, it would be beneficial to record accelerometer data during tests, particularly on higher speed tests.

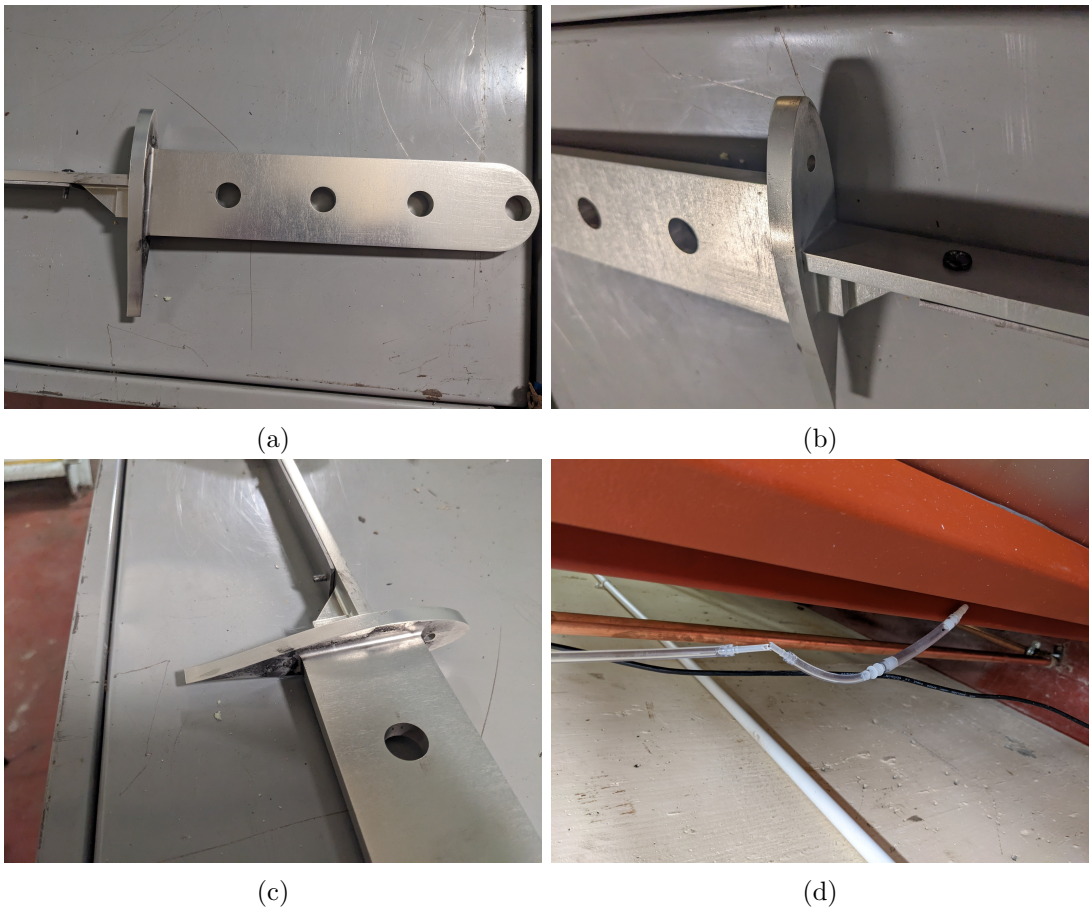

(a) (b)

(c) (d)

Figure 6.44: Figures 6.44a, 6.44a and6.44c show both sample holders and display the dust observed on the sample holders posts failure. Figure 6.44d shows some of the damage observed on the rain system.

6.10.2.5 Flat 1

Start Time/Date: 16:10pm 22/2/22 **Attendees:** James Nash, Kieran Pugh, Drew Irvine, Iasonas Zekos, Chris Cameron **Speed:** 250rpm, 500rpm **Duration:** Approx. 10min, 10min

Description: Following the failure of the Leading Edge sample holders, the test rig lid was removed and cleaned, removing any debris found inside. Broken needles and rain system tubes were replaced. New sample holders of a different design were installed for a different type of lower speed testing (3-point bending moment). The rig was inspected thoroughly and all procedures, as outlined in section L for the first startup were followed. The rain system was also tested. The following tests were then carried out: 250rpm for 10 min, which was then increased to 500rpm for 10 min more. The rig was then stopped using the TIA software and the e-stop was then pressed. As with all previous tests, all accelerometers displayed minimal vibrations. Following this operation, the rig was inspected once again.

Following this startup test procedure, the rig was then operated under rain erosion testing conditions using flat samples for a series of tests that will not be discussed here.

6.11 Version 2

6.11.1 Redesign: New Sample Holder Design

The new sample holder was designed that would prevent the ejection of the tail section, through integrating the tail section into the sample holder main body. This was made possible due to advancements in on-demand manufacturing, more specifically with a newly available material (Al 7050) with the added benefit of an increased fatigue strength. It was also possible as the manufacturer (Hubs, formerly 3DHubs) had expanded their manufacturing capabilities, allowing for more complex designs. These were still more expensive than the previous, however, still less than traditional CNC manufacturers. This design feature additionally mitigated the use of adhesive bonding, whilst maintaining a similar overall weight. The new component underwent various

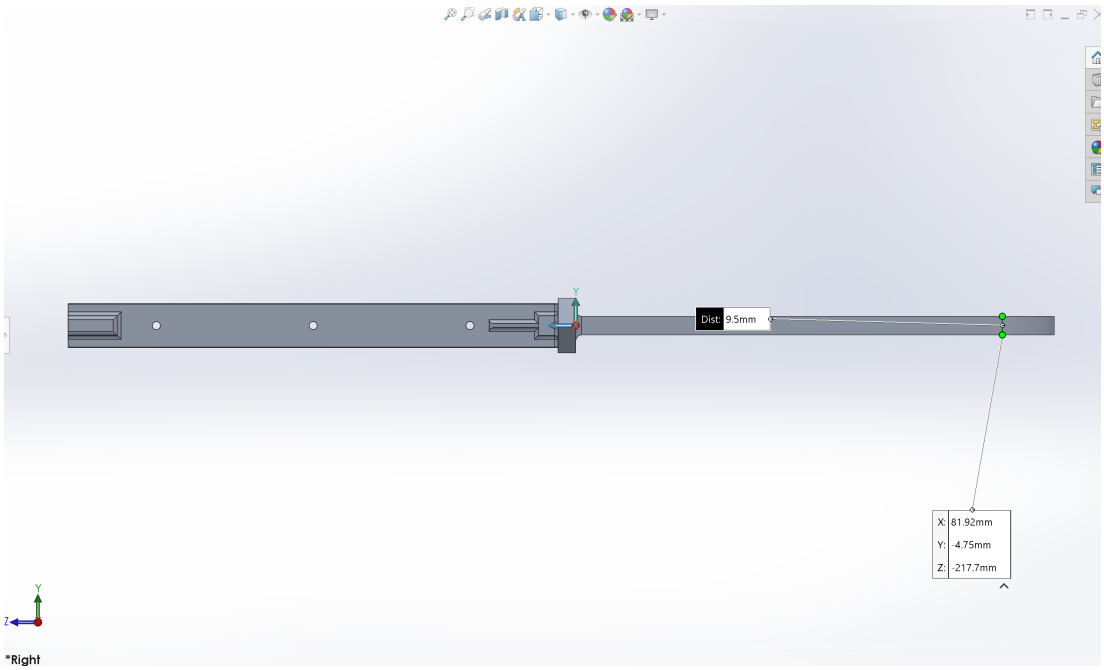

Figure 6.45: The original sample holder designed and manufactured for the rig.

iterations in order to minimise peak stresses and its mass, whilst ensuring manufacturability and acceptable costs. Similarly to the version 1 sample holder, the design optimisation was carried out using FEA on SolidWorks (Section 6.5.3).

6.11.2 Hub-Sample Holder Bolted Connection

Following disassembly, of the hub and sample holder connection, wear marks were noticed from where the washers had been positioned. Due to safety concerns, a different mounting mechanism that did not cause wear was required for the sample holder connection to be used. Furthermore, the bolts needed to be loaded in shear. A design error was noticed, where the initial assembly was not able to clamp the sample holder in place as it was physically restricted by the offset for the cover plate (10mm), with the sample holder thickness falling short (9.5mm) (Figure 6.45), leaving an approximate gap of 0.5mm.

Loading the bolts initially in tension, when combined with the shear stress generated from the centrifugal forces from the sample holder would also lead to cyclic loading at high combined stresses leading to fatigue in the bolts, particularly if using high speeds

inside the test rig. Therefore, if it is possible to simply load the bolts in shear, as opposed to the combined tension and shear (instead using them as pins, rather than bolts) then fatigue stresses in the bolts would be lower. In addition, loading the bolts or pins in pure shear would make higher safety factors possible too.

A castellated nut or castle nut, is a nut, with a set of 6 notches cut into one of its sides. They allow a bolted connection to be locked in place, preventing the separation of a bolted connection, even if there is considerable vibration. The nut is combined with a standard bolt that has a small hole drilled into it radially and a locking pin that passes through one of the castellation, which restricts the movement of the nut. The locking pin is typically either a cotter pin or an R-pin. Because of the mechanical interlock between the pin and the nut, they allow for a significantly lower torque bolted connection.

Castellated nuts were selected to replace the bolted connection, using disposable cotter pins to lock them in place. For safety reasons these cotter pins were disposable, as they would need to be bent into shape each time the connection is assembled and disassembled, weakening them.

6.11.3 Design Optimisation

Similarly to the version 1 design optimisation process (Section 6.5.3), the results were extensive. Therefore to be concise, again statistical stress values will be reported here. Although, the final design iteration and its respective results will be discussed below in more detail. In contrast to Sample Holder Version 1, the results will be expanded to include the End Piece simulations. Initial simulations were carried out, firstly on the sample holder by itself. Secondly, if satisfactory, it was then followed by a simulation just on the End Piece with the sample. Thirdly, manufacturability was assessed online by multiple rapid prototyping manufacturers. Finally, if the previous three previous steps were all successful, a simulation on the combined setup, providing a comprehensive simulation set, including bolt failure was carried out. Again, minimising the total mass of the sample holder was an optimisation goal in combination with minimising peak operational stresses. The aim of achieving 2100rpm again, was a secondary objective,

whilst maintaining the constraint of a minimum safety factor > 2.

6.11.4 Methodology

The first goal (V10) was to integrate the tail section into the sample holder as well as providing an integrated sample positioning feature (replacing the inner cover). This required creating a hollow pocket along the length of the sample holder. The mass of a solid tail section would have been too high, leading to problems elsewhere and so was not possible. From V11 onwards, the fixation points for the end piece were separated as much as possible. It was found that the initial stresses on this component were particularly high (likely contributing to the bending observed in section 6.10.2.4) and this simple design modification greatly reduced stresses. This was then followed by a slimming down of the sample holder, reducing excess mass where possible as well as the stresses experienced on the hub disc. Further to this, a pocket was opened up on the airfoil thickness plate, improving manufacturability and reduced overall cost. Some other minor changes included changing fillet radii and wall thicknesses specifically for manufacturing. The design evolution can be seen in appendix Efigure E.2. Setup parameters for the simulations are stated in table 6.26.

Table 6.26: Simulation setup for finite element analysis on each of the different design configurations of the sample holder version 2.

Scenario	V10	V11	V12	V13	V14	V15
Mesh Type	Standard Mesh					
Element size	2.55823mm					
Tolerance	0.127911mm					
Mesh Quality	High					
Fixtures	4 connector bolt holes were fixed on their cylindrical face					
	Centrifugal (2100rpm)					
	Remote masses for the end piece and sample were applied through the inner surface of its mounting holes.					
Materials						
Sample holder Main Body and End Piece	Al-7050					
Samples	Glass (For simulation), $\rho = 2460, E = 69GPa$					

Table 6.27: Design optimisation results for sample holder version 2. SH refers to the sample holder and EP refers to the End Piece.

Case	V10	V11	V12	V13	V14	V15
Sample Holder Peak Stress (MPa)	214	179	149	284	149	147
End Piece Peak Stress (MPa)	Failed	130	130	130	130	190
manufacturable	-	No	No	No	No	Yes
Full Simulation Peak Stress (MPa) (SH, EP)	-	-	-	-	-	175, 139
Mass, excluding sample (g)	1133	1163	916	997	911	928.95
Simulation speed (rpm)				2100		

6.11.5 Results

Simulation results were not reported where either the end piece or sample holder failed during simulations. The design optimisation process was able to achieve all primary and secondary objectives stated above. Results for the process can be seen in table 6.27.

6.11.6 In-Depth Analysis Sample Holder Version 2: Methodology

FEA simulations were set up for the selected design for the new version 2 aerofoil sample holder and the sample holder end piece using SolidWorks Simulation in the various configurations as outlined in table 6.28.

The mesh and simulation setup for the first simulation can be seen in figure 6.46. In Appendix K, it is possible to see the area onto which the centrifugal force from the sample is acting. During the root cause analysis (Section 6.10.2.4), one of the damaged areas noticed was this region on the end piece and so the distance between the fixation bolt holes was increased.

In Appendix K, the full component setup and mesh simulated can be viewed. For this simulation, the sample was simulated however, the stiffness was assumed to be that of glass and as it was not of interest, the stress values on the sample are not considered here.

Table 6.28: Simulation setup for finite element analysis on sample holders for a range of conditions. Yield strengths for the aerofoil sample holder and end piece components 450MPa were taken directly from the manufacturer's website (Hubs, formerly 3D Hubs).

Scenario	Aerofoil Sample Holder	Sample Holder End Piece	Full Sample Holder and sample
Mesh Type	Standard Mesh		
Maximum element size	3.600mm	1.279mm	2mm
Minimum element size	0.1800mm	0.0640mm	0.1800mm
Contact type	-		No Penetration, bolted connection between end piece and rotator carrier arm, bonded between sample and end piece [a]
Fixtures	4 connector bolt holes were fixed on their cylindrical face	2 Counter sunk faces (see figure 8)	4 connector bolt holes were fixed on their cylindrical face
Loads	Centrifugal 2100rpm		
	Remote load for the air resistance during operation were calculated as before in section 6.5.2.8. These loads were distributed over the front faces of the sample and sample holder that would be exposed to drag forces. Acting perpendicular to the sample.	Remote mass acting through contact area on inner surface	Remote load for the air resistance during operation were calculated as before in section 6.5.2.8. These loads were distributed over the front faces of the sample and sample holder that would be exposed to drag forces. Acting perpendicular to the sample.
	Remote mass from sample and end piece acting through cylindrical faces on the end of the sample holder where bolts are attached.	-	
Materials			
Component	Al 7050 (yield strength = 450MPa, fatigue strength = 240MPa @5x10^8 Cycles)		
Samples	Glass (For simulation), $\rho = 2460, E = 69GPa$		
Bolts	-		Alloy Steel Bolts (Default) with 5Nm torque applied M6 x 35mm. Yield strength 600MPa

[a] It is important to note here that using the bolted connection feature will lead to higher stresses reported in the model within the vicinity of 1 diameter of the bolt holes.

6.11.7 Results: Aerofoil Sample Holder

In figure 6.47a, the locations with higher stresses are either locations with sharp geometry changes, stress concentrating features or regions where the moment of the sample is

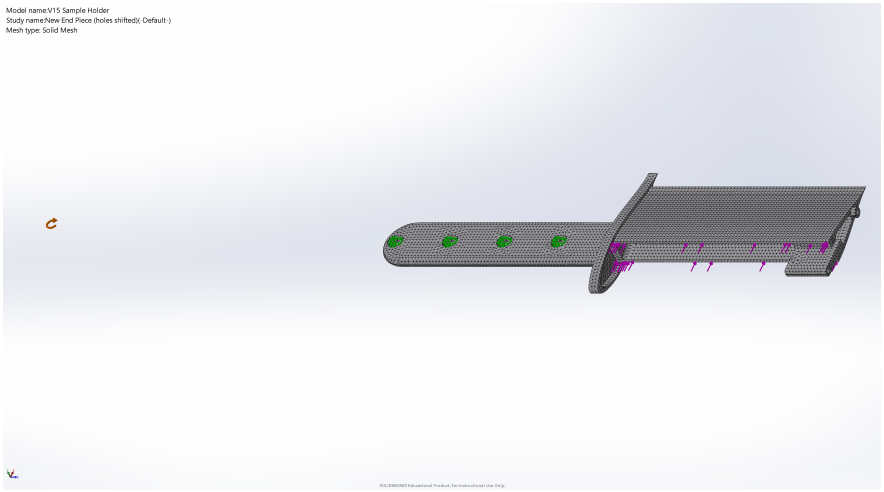

Figure 6.46: Full setup for the Aerofoil Sample Holder simulation, showing Mesh, fixtures and loads.

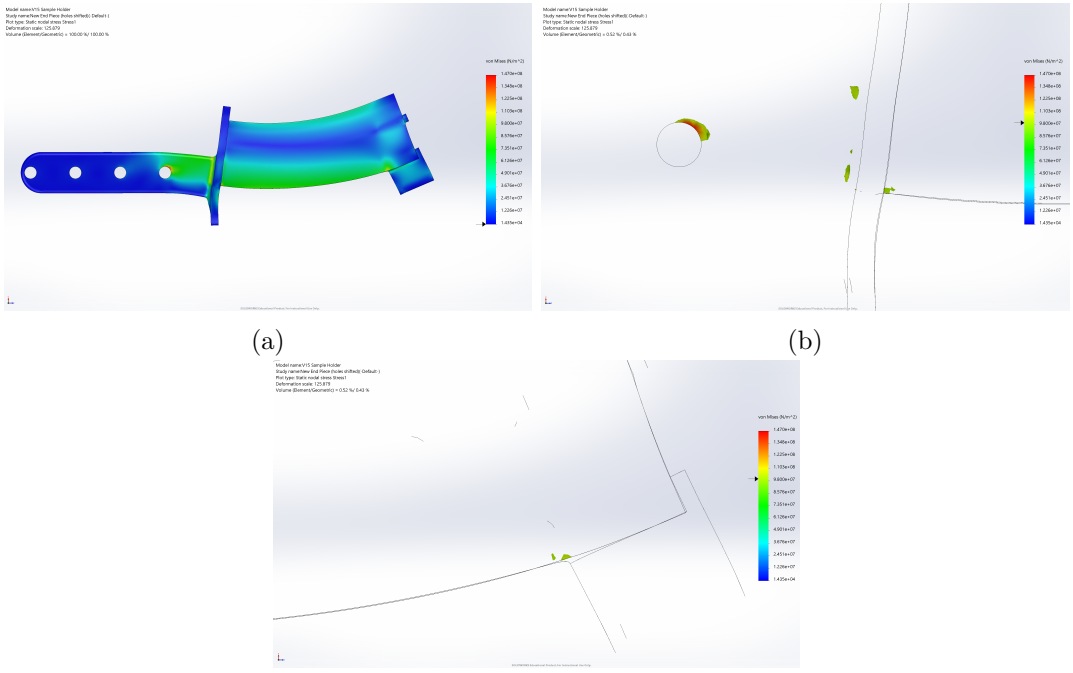

(a) (b)

(c)

Figure 6.47: Figure 6.47a shows a stress map of the top of the aerofoil sample holder whilst rotating at 2100 rpm. Figures 6.47b and 6.47c show peak stress hotspots on the sample holder ($>$ 100MPa).

acting about the sample holder. The majority of stresses simulated are below 100MPa and the highest stresses experienced are located around the bolt hole closest to the

Table 6.29: Stress data and safety factors for the new Aerofoil Sample Holder simulation.

Aerofoil Sample Holder	Stress (MPa)			Failure Mode Safety Factor	
	Avg	Max	Min	Yield/ Failure	Fatigue
Value	24	147	0.014	2.6	1.6

middle of the sample holder at 147MPa 6.29.

6.11.8 Results: Sample Holder End Piece

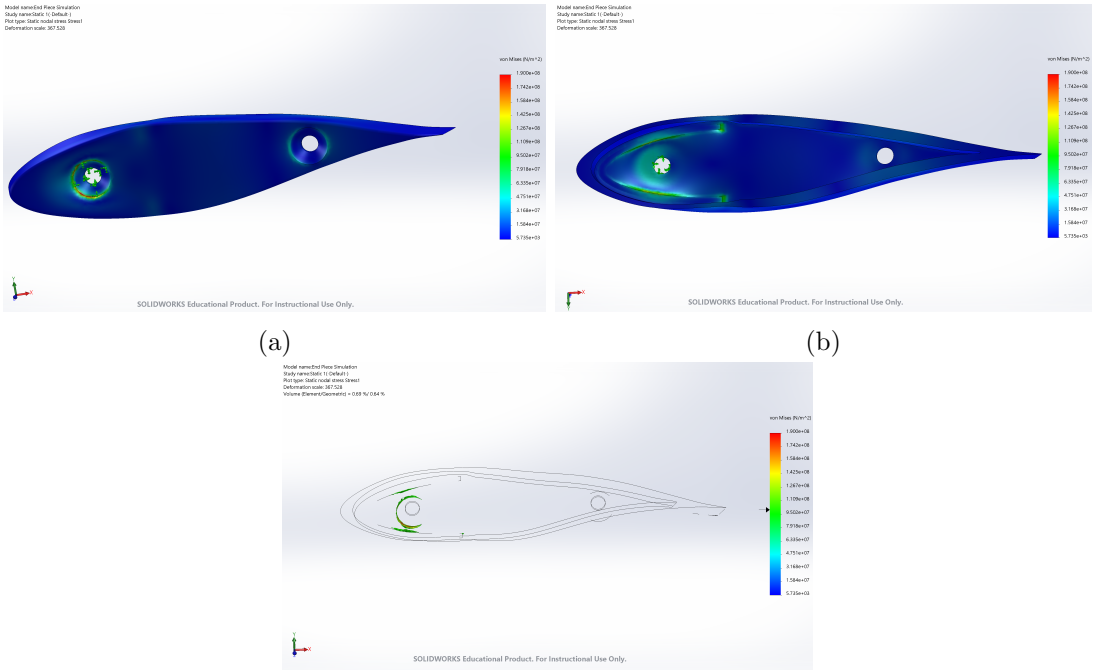

(a) (b)

(c)

Figure 6.48: Figures 6.48a and 6.48b stress maps of both the outside and inside of the component whilst rotating at 2100 rpm, respectively. Figure 6.48c shows the peak stress hotspots on the the sample holder end piece ($> 100MPa$).

Stresses on the end piece can be seen here, with peak stresses focused around the geometry changes whereby the bolts will clamp the end pieces to the main body of the sample holder. Stresses are also increased in the region where the sample loads the end piece during operation, which would be expected. As the bolt holes were sufficiently separated the moment generated by the sample, does not generate excessive stress in

the end piece with peak stresses of 190MPa (Table 6.30)

Table 6.30: Stress data and safety factors for the new Sample Holder End Piece simulation.

Sample Holder End Piece	Stress (MPa)			Failure Mode Safety Factor	
	Avg	Max	Min	Yield/ Failure	Fatigue
Value	9.5	190	0.006	2.4	1.3

6.11.9 Results: Full Sample Holder and Sample

In the full sample holder simulation, stresses differ from the previous two simulations in this section, with stresses that are higher in the main sample holder body and lower in the end piece. However, the stresses are of the same magnitude. This occurs because the way that the components are being loaded is fundamentally different and because there is direct interaction between the two bodies during this rotational loading as well as including the bolted connection. More specifically, as the bolts modelled have an elastic modulus (rather than being infinitely stiff), the bodies deform during the simulation and this deformation causes the loading pattern to change. The actual sample was also included in the simulation meaning the interaction between these two bodies was also present. This allows the stresses on the end piece to reduce from 190 (Table 6.30) to 139 (Table 6.31), whilst the average stress increases from 9.5MPa to 11MPa. Similarly, this change in loading behaviour leads to an increase in the peak for the main sample holder body leading, from 147MPa (Table 6.29) to 175 (Table 6.31) as well as the increases in average stress from 24MPa to 28MPa. This can also be seen by the stress hotspots increasing in size. Whilst these stresses are increasing in magnitude, they still give a reasonable safety factor to tensile failure for the sample holder of 2.6. However, the safety factor for fatigue failure is lower than desired (1.3) and so signs of fatigue would need to be monitored closely. Bolt safety factors were also lower than desired at 1.4 for the front bolt, however, for the rear bolt these were sufficient.

Table 6.31: Stress data and safety factors for the new Full Sample Holder simulation, including bolt safety factors.

Full Sample Holder	Stress (MPa)			Failure Mode Safety Factor	
	Avg	Max	Min	Yield/ Failure	Fatigue
Sample Holder	28	175	0.006	2.6	1.3
End Piece	11	139	0.023	3.2	1.7
Front Bolt		-		1.4	-
Rear Bolt		-		2.3	-

6.11.10 Discussion

The results for the aerofoil sample holder, show that immediate failure from single instances of use is unlikely. However, with the lower safety factors, care would need to be taken when operating the rig using these sample holders for extended periods of time as fatigue of the sample holder is possible, however still unlikely. Signs of fatigue would need to be monitored regularly in the locations highlighted here. If fatigue were to occur, the most likely locations are those indicated.

The forward bolt connection has a higher risk of failure than the rear, which is likely due to the tensile loading caused by the moment from the sample and so would need to be regularly checked during operation The bolt strength is typically 600MPa for A4-80 bolts and according to research conducted by BUMAX an A4-80 Bolt should be able to withstand 10 million cycles at a 400MPa +/-50 [234]. This again would indicate that the bolts would fail due to fatigue rather than immediate failure and so provided that these were changed regularly, should not be an issue.

High stresses in the initial simulations of the End Piece component here indicate a design flaw that, fortunately, was found and addressed. The additional more comprehensive simulation sets outlined here should provide more confidence in the new design and allow the mistakes that led to the failure observed in section 6.10.2.4 to not be repeated again.

6.11.11 Manufacture

The design optimisation process outlined here led to satisfactory results from FEA simulations, helping to significantly reduce observed stresses inside the components,

without significantly increasing the overall mass of the system. Fortunately, access to on-demand prototyping greatly reduced costs and allowed the manufacture of the new sample holders, from more suitable materials whilst maintaining within the required budget.

Further research into the use of hard anodisation techniques for 7000 series alloys led to the discovery by the author that it can significantly reduce the fatigue life on these alloys [235, 236]. As this would have been detrimental to the use of these new sample holders. Further conversations with the manufacturer (Hubs, Formerly 3D Hubs [237]), who were also unaware of this led to removal of the anodised coating from the design.

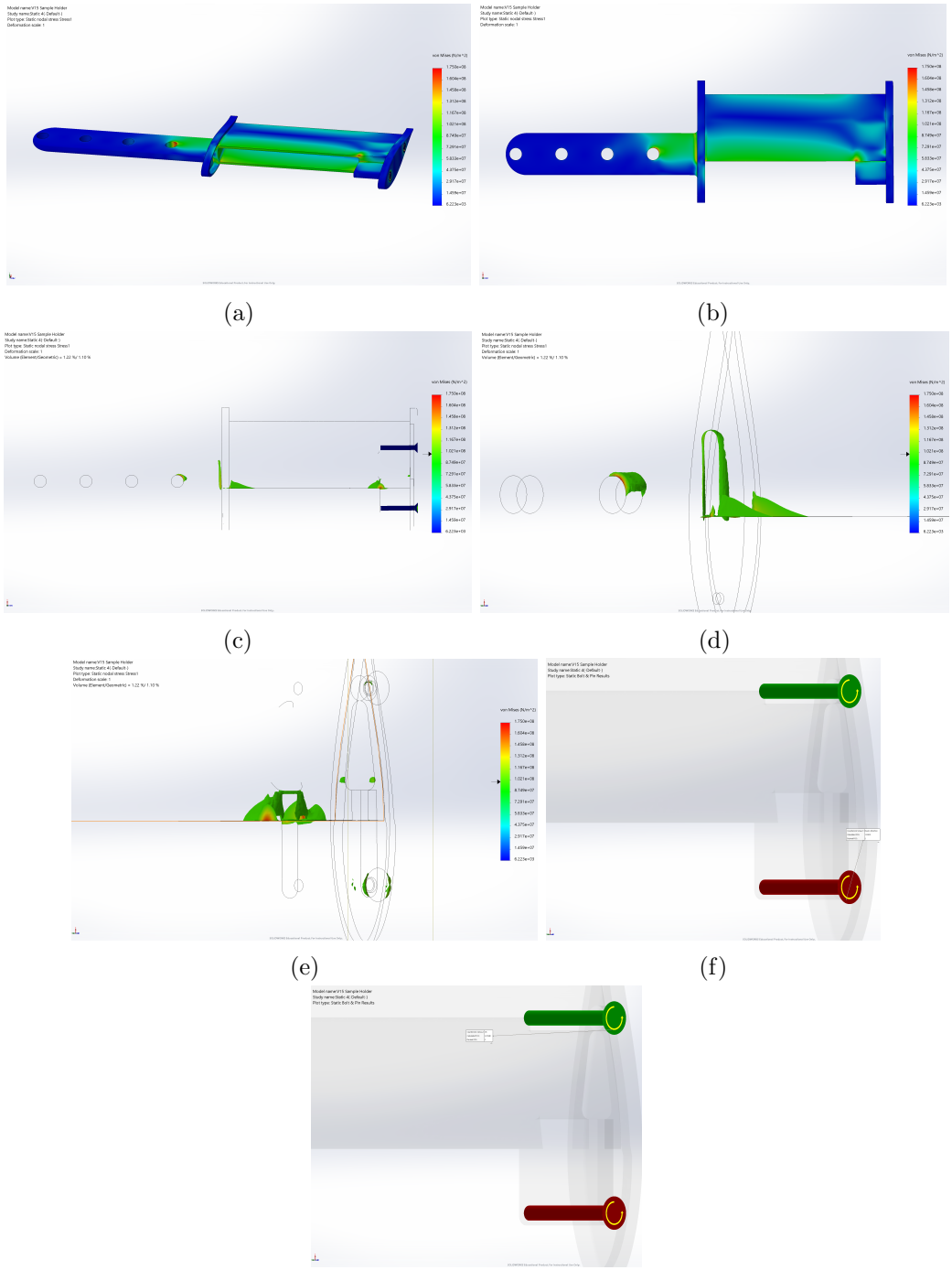

Figure 6.49: Figures 6.49a and 6.49b show stress maps of for the full simulation of the sample holder, end piece, sample and bolts. Figures 6.49c, 6.49d and 6.49e show peak hot spots (> 100MPa) on the main sample holder and end piece. Figures 6.49f and 6.49g show the bolt safety factors present during operation.

6.12 Discussion

In addition to the incident (Section 6.10.2.4), the rotary encoder became damaged, requiring replacement, as this helps to ensure operational loads and conditions are well characterised.

Without the availability of publicly available designs or access to rain erosion test facilities that have regular availability and are reasonably priced. Access to rain erosion data for research is greatly restricted. Currently the drive within industry is to produce a product that can resist rain erosion, however without time spent investing in understanding the fundamental causes and characterising the associated parameters, developing a solution to this problem is increasingly challenging.

The aim of this chapter was to develop a modular low-cost whirling arm rain erosion test rig, with the capabilities of modifying parameters that have not been explored properly or even in some cases not investigated at all. Current rain erosion research uses material model damage models such as the Springer model [11], which do not appropriately represent viscoelastic materials. In particular their time dependent and environmental dependent material properties and how sensitive these materials are to conditions experienced in real wind farms.

Here, the design, manufacture, testing and calibration of a rain erosion test rig has been discussed in detail, with the authors providing a framework for others to build upon in the future. Here it has been shown to be possible to carry out this process using a reasonably low-cost and widely accessible methodology. It has not been possible to disclose the exact cost spent during the design and manufacturing process, however with the help of the Mechanical Engineering workshop and the Electrical Engineering department, most of the labour costs were kept within the University, which significantly reduced costs. However, much of the cost associated with these machines lies in technical development.

The design development of the facility was significantly accelerated through access to the DNVGL-RP-0171 standard [72]. In addition, Research from Herring et al. [228] investigating rain erosion test rig aerodynamics indicates that the aerodynamic design

of similar RET facilities produce favourable and consistent droplet impact patterns supporting the design produced here.

The majority of the components used for the manufacture of the rain erosion test rig were off-the-shelf components making the manufacture of another test rig using the framework and designs certainly viable for others who wish to develop such devices. The use of widely available components aids in reducing repair complexity, time and costs. With access to rapid prototyping companies such as Hubs [237], access to complex manufacturing processes at greatly reduced costs was instrumental in the development of this test rig. Particularly with access to new and improved materials and manufacturing processes.

Whilst the designs here have been largely successful, there was a significant failure, highlighting the dangers of such machines and rotating machine design. On this note, the authors accept no liability for the use of the research carried out here and/or test rigs constructed from it in any situation. However with research and innovation, accidents can happen and failures are likely, making safe procedure and design fail-safes, critical to the development of complex projects such as the one discussed here.

In addition to the safety features discussed, the rain erosion test rig was operated inside an underground room with thick concrete walls and ceiling (1ft thick minimum). If an accident had occurred power could be cut remotely and if it was possible for any projectile to leave the test chamber or outer enclosure, the operators would have been safe at all times, protected by this concrete 'bunker'.

Purchasing an electric motor with an inbuilt brake could have reduced the work required to manufacture the rig, however having a decoupled mechanical system provided additional design redundancies.

Initial size restrictions, reduced the overall diameter of the rig, meaning that the rotational speed was higher than desired. Authors looking to emulate this design or others like it should seek to increase its diameter. This would allow the operation of lower speeds, which improves operational safety. In addition, it also reduces centrifugal stresses inside the sample, which may potentially (depending on the test speed) influence results.

It was not possible to test the second iteration of the leading edge sample holders and subsequent testing of these sample holders is necessary to ensure safe operation. Further to this the hub disc and new sample holders require some form of coating to prevent corrosion, which was not discussed here in significant detail. More broadly, any individual looking to coat components should be wary of any coating techniques and do sufficient research to ensure that they do not compromise the mechanical performance of the respective component. As such it is not possible to recommend a suitable coating here. To prevent corrosion, the bolts securing the hub disc to the van hub should be exchanged for high strength corrosion resistant bolts to increase the longevity of the rain erosion test rig.

Upon inspection later inspections of the rig tanks, biofouling was noticed inside the ICB tanks, which was one challenge not considered by the author or other team members involved in the design. This largely occurred due to the reduced usage of the rig, following the incident discussed in section 6.10.2.4. Completely emptying the ICB inlet and outlet tanks was not possible, with residual water persistently remaining. Further steps should be taken to develop a tipping system for emptying the tanks or drying the interior when extended periods of disuse occur.

6.12.1 Final Rig Design specification

Within this thesis, parameters relevant to the rain erosion process have been identified. Methods to monitor or control these identified parameters have been implemented into the design to allow their influence to be characterised. See Table 6.32 for the full rig specification.

The main objective of designing and building the test rig was to improve the capabilities of the Tribos research group at the university, producing a test facility able to investigate parameters with little previous research. This primarily focused on parameters identified in previous chapters 3, 5 and 4.

Droplet diameter, needle configuration and impact rate were identified as key parameters without clear links between them and the damage process. The incorporation of a modularised rain system with easily changeable needles and rain system segments

Table 6.32

Parameter	Value Range	Monitored, Controlled or Both
Sample Shape	Aerofoil	Controlled
Rotational Radius (Centre of Sample)	0.74m	Controlled
Sample Length	250mm	Controlled
Gauge Length	200mm	Controlled
Number of Test Samples	2	Controlled
Droplet Diameter Range	2.11 – 4.48mm	Both
Impact Angle	90°	Controlled
Number of Needles	32 - 224 w/ visualisation, 256 w/o visualisation (8 removable panels of 32)	Controlled
Needle Configuration	Helical	Controlled
Needle Height	15-33cm	Controlled
Rain Rate	5.5 - 42.6mm	Controlled
Working Fluid	Water (Current), Salt Water and Acid Rain (Future)	Controlled
Test Chamber Temperature	Ambient	Monitored
Test Chamber Humidity	Ambient	Monitored
Test Chamber Pressure	Ambient	Monitored
Sample Temperatures	Ambient	Monitored
Impact Visualisation	Highspeed Camera	Both
Impact Speed	$< 150m/s$	Both
Main Bearing Vibrational Acceleration		Monitored
Motor Vibrational Acceleration		Monitored

make controlling these parameters simple and easily testable. The pumps were tested and calibrated to ensure consistent precipitation amounts. In addition, droplet size and shape is easily monitored through the viewing window in the door and accompanying high-speed camera as is impact location and density. In addition, the newly designed helical pattern reduces the chance of hot spots produced in previous RET rig designs.

The droplet imaging study highlighted some of the challenges associated with droplet production systems and in addition showed that the system produced good agreement with the size characterisation investigated by the tensiometer. Droplet shape oscillations were observed from the production of droplets using this rain system. Droplet shape is a parameter that influences the stress distribution in the coating itself and so the changing shape of the droplet may lead to differences in rain erosion performance.

Polymeric LEPs are sensitive to humidity and temperature which can change their properties. In addition, there has been little research into rain erosion whilst monitoring or controlling temperature. According to the DNVGL RP [72], monitoring several temperature parameters as well as humidity and pressure should occur. However, there is little public research investigating how temperature or humidity change the damage process. These parameters were selected during the design phase of the rig and thus were included for monitoring during rig operation.

Current materials typically used for rain erosion protection are susceptible to chemical attack, highlighting the need for the investigation of alternative rain chemistries. Both experimental lab testing and in-the-field research [12, 105] indicate damage progression develops differently in the presence of alternative compositions. The testing facility developed here utilises materials with resistance to rain chemistry changes and although it was not possible to complete all necessary requirements for ensuring chemical resistance to both salt water and light acid, the facility has been designed in such a way that completing this task is of relative ease.

This combined with the Strathclyde Tribos research group ageing capabilities, the research into subsurface defect quantification outlined in Chapter 4 and Tribos' hail erosion rig allows research into the effect of ageing, the effect of subsurface defects and the combined effect of hail and rain on the erosion process. Further to this, with the

modularity offered by these designs, the modification of components and parameters is far easier than those of commercial rigs, through the use of off-the-shelf components.

6.13 Conclusion

The research discussed in this chapter outlines the framework for developing a whirling arm type rain erosion test rig. The complexities and challenges have been outlined with various methods of addressing them. It should be stated that the framework discussed here is in no way exhaustive and does not cover every possible challenge encountered or potential failure mode, but instead provides a reasonable basis to build upon and develop. It is hoped that the framework and conceptual design here can help increase access to rain erosion test facilities and test data at the University of Strathclyde and in the wider research community.

Chapter 7

Discussion

Rain erosion of wind turbine blades is a pressing issue for the wind industry and with offshore expansion is only likely to worsen. Currently, OEMs and coating developers are mostly using laboratory testing and RET experiments to develop coatings for protection against rain erosion. The overall aim is to mitigate the structural damage and aerodynamic losses caused by the rain erosion phenomenon.

This thesis aimed to understand the current coating characterisation and rain erosion testing methodologies for leading-edge erosion. These were outlined as follows:

1. The appropriate practice for the characterisation of coating properties. Specifically, the influence of material and physical properties as well as providing a more representative characterisation of viscoelastic materials, such as those used for rain erosion protection.

2. Finding appropriate methods for detecting the presence of defects within coatings typically used for rain erosion protection. More specifically, finding a cost-effective approach, fast enough and versatile so that its application could be more widespread.

3. Using mathematical models and meteorological data to characterise realistic weather conditions that a wind turbine would experience during its lifetime. The goal here was to provide key insights into how realistic current rain erosion testing practice

actually is and whether there are parameters that are numerous in nature, yet hadn't been investigated.

4. The development of a framework for the design and manufacture of a rain erosion test rig, which would allow the testing of key parameters identified that are not normally tested for. This design would feature modularity, tuneability and the use of widely available off-the-shelf components. This would allow its construction, repair and maintenance to be fast and cost-effective and its application flexible. Furthermore, it would provide a clear framework for the development of new rigs.

Understanding the relevant coating parameters is key to the development of new ones. Currently, the industry standard material damage model is the Springer model [11]. Challenges around its implementation for viscoelastic materials is driving the testing of rain erosion materials in the search of new material models. Identified in this thesis are several parameters (particularly relating to viscoelastic materials) that have been identified as important by various authors and the key to understanding the influence of one particular parameter relies on the standardised reporting of all other parameters thought to influence the result. Failure to do so reduces the clarity of the problem and makes it challenging for authors to compile databases and build appropriate material models.

Finding suitable methods for the characterisation of the subsurface of a coated composite panel is key to the progression of rain erosion understanding more generally. Currently, it is thought the presence of subsurface defects inside rain erosion protection coatings is behind some of the inconsistencies in test results. However, the true influence is known. X-ray CT is one possible method for inspecting rain erosion coupons, however, this process is expensive, cumbersome and only typically able to scan a small region, limiting its application. Provided in this thesis is the first qualitative analysis of the subsurface of a coated composite panel using three different NDT methods. In the research presented here, ultrasound has shown to be a promising method for the characterisation of subsurface voids as small as 100 microns in diameter as well as other defects that were discussed inside rain erosion coatings, with its versatile use and

significantly reduced cost compared to X-ray CT.

The characterisation of realistic conditions that lead to rain erosion in the field is a key pillar of solving this issue. Current testing standards require the testing of rain erosion materials in conditions that are not typically observed in nature. Moreover, the influence of accelerated testing is currently unknown and there is little research into the effect of specific parameters such as intensity, droplet diameter, temperature, humidity and chemical composition on the rain erosion process. Results here provide a characterisation of the current meteorological conditions that exist on the island of Ireland, which helps to display how realistic current testing standards are. The influence of environmental parameters such as temperature and humidity are known to influence the mechanical performance of viscoelastic materials. In addition to this, to the author's knowledge, the results displayed here are the first attempt to geospatially map the rain erosion potential around the island of Ireland using number of impacts and kinetic energy, indicating areas more susceptible to rain erosion.

Rain erosion testing methods are typically very expensive and there is a challenge around access to data. Whirling arm rain erosion test rigs currently produce the most reliable data and so are the industry gold standard. To the author's knowledge, there are no publicly available designs and the development of such rigs is costly and complex, requiring a team of highly specialised individuals. In this thesis, the framework for the development of such a rig has been outlined, with the ability to monitor and record key parameters that have not been tested before. In addition, droplets produced from an array of different needle sizes using the designed rain system, has been carried out, characterising shape parameters from droplets produced using high speed footage. Further to this, lessons learnt from the development and subsequent component failure emphasise the need for the highest level of safety for such a complex and dangerous device. With the modularity of this device and the incorporated sensors, it is hoped that the inconsistencies reported elsewhere can be investigated in more detail to understand the root cause.

Chapter 8

Future Work

This thesis has sought to address some of the main challenges concerning the rain erosion topic, with the specific objective of enhancing rain erosion testing methodology. Inconsistencies during testing are a challenge and a better understanding of various parameters that influence the rain erosion process, in reality, is key to the development of new coatings to mitigate damage. This thesis is aimed at providing future researchers with the appropriate knowledge and tools to investigate the phenomenon further.

The thesis has contributed to the knowledge space around rain erosion, however, there are several key areas of development that would progress solutions further. The most important development currently is creating a damage model for viscoelastic materials is essential for the lifetime estimation of different LEPs, furthermore, it would allow the prediction of optimal coatings without the need to test every formulation. The current damage model (the Springer model) is insufficient, as it doesn't capture the time-dependent viscoelastic properties of materials used for rain erosion protection. Requirements for this are the standardised reporting of material properties; standardising rain erosion test conditions, including the reporting of temperature, humidity and water composition, as well as exposure to UV, ozone or additional chemicals and finally, a characterisation of the surface and subsurface of any coating or coating system. Failure to do this can lead to erroneous conclusions being drawn and incorrect models developed.

Understanding the cohesive strength of a material (Fracture toughness) and the

adhesive strength (interlaminar/interfacial toughness) and developing an appropriate testing method for assessing how these parameters influence the rain erosion process has had little investigation. Further to this, understanding these parameters in more detail will likely explain how they influence damage progression.

In addition to the influence of mechanical properties, further work characterising the influence of droplet diameter, different testing regimes and therefore rain cycles, rain intensity, temperature (sample, test chamber and water temperature), humidity, salt water, acid rain, UV and the combined influence of other projectile impacts such as hail stones or sand on rain erosion testing is further required. The DNVGL guidelines only require the monitoring of temperature, droplet diameter, rain intensity. As outlined here, low temperatures, rain intensities and droplet diameters are common, as are high humidities and exposure to chemicals. None of which are standard testing practice and the influence of these different parameters and synergy between them has received comparatively little attention.

Defects are a well-known problem in the manufacturing sectors and currently, there are no guidelines or understanding as to what concentration or size of defect is relevant to the rain erosion process. There is also a lack of clear testing methodology for the detection of relevant defects inside the coating or interface. Outlined in this thesis are a number of NDT methods that can detect various types of defects, however, progress is required to understand which defects are actually relevant to the rain erosion process. Ultrasound has shown promise in detecting defects, however as shown by other authors, thermography is another method able to detect defects in sites where erosion initiated. Rain erosion testing research is required into understanding the influence of defects such as voids on the rain erosion process, which should be combined with the NDT methods used here. This would allow the understanding of firstly, where failure initiated, secondly, the defect size relevant to rain erosion and thirdly, which NDT method, if any, was suitable for detecting such a defect.

In addition to characterising and understanding the influence of these parameters, further work is needed to correctly characterise their relative occurrence. Work should be done to expand the research here on modelling rain erosion geospatially. The relative

simplicity of linear regression has its benefits, however it lacks the ability to appropriately characterise site-specific conditions correctly. The use of radar technology and numerical weather prediction models to characterise historic site data and the use of SCADA data would greatly enhance rain erosion modelling predictions, additional work needs to be carried out on developing ways to integrate their data, with sufficiently high resolution that high intensity rain events can be correctly characterised. In addition, there is a need to find a more representative droplet size distribution model than the 'Best' model as well as convert 10m surface wind speeds to hub height.

Research has indicated a link between rain chemistry and early rain erosion failure and the rain chemistry analysis conducted here is an initial insight into relevant chemicals likely deposited onto a wind turbine blade surface. Further work is required to test the influence of salt and acid on the rain erosion process. Whilst it was not possible to characterise other chemical depositions, some research has indicated an influence. Therefore a more holistic approach to chemical influence on the rain erosion process is required, with the results here providing a basis. Furthermore, chemical deposition models such as the EMEP model would allow the modelling of any chemicals of interest to be traced and areas of concern highlighted. In addition to the influence on the rain erosion process the rain chemistry data listed here will influence some of the other corrosion prone components made from steel or aluminium and so will have wider implications.

The research discussed here outlined one scenario whereby defects were detected and so the applicability of the results here is limited. Further work is required to apply the NDT methods utilised here to other materials and coating system combinations. Repair work is another scenario with significantly less understanding and characterising repair quality is a necessary subsequent step, defect quantification in repair work requires attention. If coatings applied in lab conditions experience coating failure due to the presence of defects, it is significantly more likely that more defects are present in the field. To the author's knowledge, there is no data concerning the relative occurrence of LEP defects in real wind turbine blades or in LEP repair work and additional data-gathering campaigns are required.

In addition to the improvements required for rain erosion testing, access to modular and tuneable rain erosion testing rigs is required. Outlined in this thesis is the framework for developing a rain erosion test rig with the capabilities to test the parameters discussed in this thesis. It is hoped that the development of this test rig will allow data to be published on the parameters outlined here using the recommendations made in this thesis.

During the development of the rain erosion test rig, the lack of published research outlining the influence of test rig design decisions highlights a critical area in understanding this problem. As research has consistently shown [71, 72, 74–76, 106], rain erosion test results are highly dependent on the testing setup used to derive them. Furthermore, it is widely accepted that in modern LEPs, failure is largely defect driven which presents an increasing problem in the lack of characterisation work carried out on rain erosion test rigs. The work by Mackie [133] and Frost Jensen-Johansen [76] are important early steps in providing a deeper understanding of rain erosion testing characterisation. Further work is needed in quantifying LEP failure drivers, whether this is due to the test setup, environmental, application or material-based.

Chapter 9

Conclusion

Throughout this thesis, rain erosion has been discussed in some detail. As has been outlined, this topic is complex and even considering that it has been a topic of research and study for 100 years, there are still many research questions to answer. In this thesis, the main focus has been on enhancing the current rain erosion testing methodology, with the goal of improving the current reporting and understanding of relevant rain erosion testing parameters.

Traditionally, the lack of consistent reporting of mechanical and superficial properties of leading edge protection systems has hindered the rain erosion research community for some time. In this thesis, an enhanced mechanical testing protocol has been outlined with the aim of providing other researchers with the correct data to develop more representative material damage models. The hope of which, to develop lifetime prediction models that can actually be used in practice.

Moreover, a coherent understanding of the appropriate weather conditions found in the field has been lacking for some time. This brings into question the applicability of historic rain erosion testing results and requires the investigation of these parameters to develop appropriate material response and degradation models. In this thesis, weather data has been analysed and the results reported, providing a key understanding of an area with previously little insight.

There is currently little understanding of the role of defects in the rain erosion process as well as their abundance. Moreover, there is a lack of clear guidance for

applicable non-destructive testing methods for this type of coating/substrate formulation. In this thesis, ultrasound testing methods have shown real promise and present an opportunity to characterise these parameters in more detail.

The design, manufacture and testing of a rain erosion test rig have been developed. The research into developing a machine of this type has been discussed in some detail and the methodology provided gives guidance for others to build upon. The rig constructed allows the testing and monitoring of the parameters outlined in the other thesis chapters, which are either not typically reported or modified, with the potential to properly characterise their influence on the rain erosion process.

The methodology outlined here provides academia and industry with the tools necessary to advance the current understanding in the field. It is hoped that the results outlined here will advance the current understanding of the rain erosion phenomenon.

Bibliography

[1] Leon Mishnaevsky Jr, Kim Branner, Helga Nørgaard Petersen, Justine Beauson, Malcolm McGugan, and Bent F Sørensen. Materials for wind turbine blades: An overview. *Materials*, 10(11):1285, 2017.

[2] M Rosemeier and M Bätge. A concept study of a carbon spar cap design for a 80m wind turbine blade. In *Journal of Physics: Conference Series*, volume 524, page 012039. IOP Publishing, 2014.

[3] Bent F Sørensen, Erik Joergensen, Christian P Debel, FM Jensen, HM Jensen, T Jacobsen, and KM Halling. Improved design of large wind turbine blade of fibre composites based on studies of scale effects (phase 1)-summary report. 2004.

[4] TD Ashwill, A Ogilvie, and J Paquette. Blade reliability collaborative: Collection of defect, damage and repair data. *Sandia National Laboratories, Albuquerque, NM, SAND2013-3197*, 2013.

[5] Kadhirvel Boopathi, Leon Mishnaevsky Jr, Bose Sumantraa, S Anthonyraj Premkumar, Krishnaraj Thamodharan, and Kannan Balaraman. Failure mechanisms of wind turbine blades in india: Climatic, regional, and seasonal variability. *Wind Energy*, 25(5):968–979, 2022.

[6] FJ Heymann. High-speed impact between a liquid drop and a solid surface. *Journal of Applied Physics*, 40(13):5113–5122, 1969.

[7] HM Slot, ERM Gelinck, C Rentrop, and Emile Van Der Heide. Leading edge

erosion of coated wind turbine blades: Review of coating life models. *Renewable Energy*, 80:837–848, 2015.

[8] A. O'Carroll, M. Hardiman, E. F. Tobin, and T. M. Young. Correlation of the rain erosion performance of polymers to mechanical and surface properties measured using nanoindentation. *Wear*, 412:38–48, 2018.

[9] A. G. Evans, M. E. Gulden, G. E. Eggum, and M. Rosenblatt. Impact damage in brittle materials in the plastic response regime. Technical report, ROCKWELL INTERNATIONAL THOUSAND OAKS CALIF SCIENCE CENTER, 1976.

[10] M. H. Keegan, D. H. Nash, and M. M. Stack. On erosion issues associated with the leading edge of wind turbine blades. *Journal of Physics D: Applied Physics*, 46(38):383001, 2013.

[11] G. S. Springer. *Erosion by Liquid Impact*. A Halsted Press book. Scripta Publishing Company, 1976. URL `https://books.google.co.uk/books?id=2J-sAAAAIAAJ`.

[12] Hamish Law and Vasileios Koutsos. Leading edge erosion of wind turbines: Effect of solid airborne particles and rain on operational wind farms. *Wind Energy*, 23 (10):1955–1965, 2020.

[13] Copyright met éirann. source: www.met.ie. data presented here has been modified, as described in this article. this data is published under a creative commons attribution 4.0 international (cc by 4.0). https://creativecommons.org/licenses/by/4.0/. met Éireann does not accept any liability whatsoever for any error or omission in the data, their availability, or for any loss or damage arising from their use., .

[14] François Beauducel. Readhgt: Import/download nasa srtm data files (.hgt) (https://www.mathworks.com/matlabcentral/fileexchange/36379-readhgt-import-download-nasa-srtm-data-files-hgt), 2021.

[15] MATLAB. *version 9.7.0.1190202 (R2019b)*. The MathWorks Inc., Natick, Massachusetts, 2019.

[16] DL Fitzgerald. Estimation of point rainfall frequencies. Technical report, Met Éireann, 2007.

[17] Frederick Letson, Rebecca J Barthelmie, and Sara C Pryor. Radar-derived precipitation climatology for wind turbine blade leading edge erosion. *Wind Energy Science*, 5(1):331–347, 2020.

[18] Roymech. n.d. Bolted joint design - roymech.

[19] Adash spol. s r.o. Adash vibration limit values quick guide. .

[20] RA Pethrick. Non-destructive evaluation (nde) of composites: dielectric techniques for testing partially or non-conducting composite materials. In *Non-Destructive Evaluation (NDE) of Polymer Matrix Composites*, pages 116–135. Elsevier, 2013.

[21] Tom Benson. Shape Effects on Drag, 2021. URL `https://www.grc.nasa.gov/www/k-12/rocket/shaped.html`.

[22] Philippe Spalart and Steven Allmaras. A one-equation turbulence model for aerodynamic flows. In *30th aerospace sciences meeting and exhibit*, page 439, 1992.

[23] Laurel Klafehn. Vanuatu: The Word's First Group of Climate Change Refugee, December 2016. URL `https://borgenproject.org/climate-change-refugee/`.

[24] Heavy rain causes floods and travel chaos across UK. *BBC News*, January 2023. URL `https://www.bbc.com/news/uk-64253800`.

[25] Tom Balmforth. Freak cold in Texas has scientists discussing whether climate change is to blame. *Reuters*, February 2021. URL `https://www.reuters.com/article/us-global-weather-polar-vortex-idUSKBN2AH2O7`.

[26] Energy The Department for Business and Industrial Strategy. Electricity generation costs 2020. 2020.

[27] Aubrey Allegretti and Helena Horton. Sunak set to end ban on new onshore windfarms in face of Tory rebellion. *The Guardian*, December 2022. ISSN 0261-3077. URL https://www.theguardian.com/environment/2022/dec/06/sunak-set-end-ban-new-onshore-windfarms-england-tory-rebellion.

[28] James Carroll, Alasdair McDonald, and David McMillan. Failure rate, repair time and unscheduled O&M cost analysis of offshore wind turbines: Reliability and maintenance of offshore wind turbines. *Wind Energy*, 19(6):1107–1119, June 2016. ISSN 10954244. doi: 10.1002/we.1887. URL https://onlinelibrary.wiley.com/doi/10.1002/we.1887.

[29] Brian Ray Resor, David Charles Maniaci, Jonathan Charles Berg, and Phillip William Richards. Effects of increasing tip velocity on wind turbine rotor design. Technical Report SAND2014-3136, Sandia National Lab. (SNL-NM), Albuquerque, NM (United States), May 2014. URL https://www.osti.gov/biblio/1177045.

[30] G Kiely. Climate change in ireland from precipitation and streamflow observations. *Advances in water resources*, 23(2):141–151, 1999.

[31] Mahmood M Shokrieh and Roham Rafiee. Simulation of fatigue failure in a full composite wind turbine blade. *Composite structures*, 74(3):332–342, 2006.

[32] Wiesław Ostachowicz, Malcolm McGugan, Jens-Uwe Schröder-Hinrichs, and Marcin Luczak. *MARE-WINT: new materials and reliability in offshore wind turbine technology*. Springer Nature, 2016.

[33] DNV/GL Standard. Rotor blades for wind turbines, dnvgl-st-0376, 2015.

[34] Marta Menéndez. A winning collaboration behind the recyclableblade. *Siemens Gamesa*, 2021.

[35] Mark Hugh Keegan, David Nash, and Margaret Stack. *Wind Turbine Blade Leading Edge Erosion: An investigation of rain droplet and hailstone impact induced damage mechanisms.* PhD thesis, University of Strathclyde, 2014.

[36] B Kjærside Storm. Surface protection and coatings for wind turbine rotor blades. In *Advances in Wind Turbine Blade Design and Materials*, pages 387–412. Elsevier, 2013.

[37] Agrim Sareen, Chinmay A Sapre, and Michael S Selig. Effects of leading edge erosion on wind turbine blade performance. *Wind Energy*, 17(10):1531–1542, 2014.

[38] Ece Sagol, Marcelo Reggio, and Adrian Ilinca. Issues concerning roughness on wind turbine blades. *Renewable and sustainable energy Reviews*, 23:514–525, 2013.

[39] Antonio Herrera Sierra and Eduardo García Pérez. Wind farm owner's view on rotor blades—from o&m to design requirements. In *International Conference on Wind Turbine Rotor*, 2013.

[40] Hatziargyriou N. Hancock M., Jenkins N. Lightning protection of wind turbines. *Joule III*, 1997.

[41] Richard Kithil. Case study of lightning damage to wind turbine blade. *National Lighting Safety Institute (NLSI)*, 2008.

[42] Addcomposites. How to identify the defects and damage in composites materials and structures? 2022.

[43] Søren Fæster, Nicolai Frost-Jensen Johansen, Leon Mishnaevsky Jr, Yukihiro Kusano, Jakob Ilsted Bech, and Martin Bonde Madsen. Rain erosion of wind turbine blades and the effect of air bubbles in the coatings. *Wind Energy*, 24(10): 1071–1082, 2021.

[44] Lennart Mischnaewski III and Leon Mishnaevsky Jr. Structural repair of wind turbine blades: Computational model for the evaluation of the effect of adhesive properties. *Wind Energy*, 24(4):402–408, 2021.

[45] Leon Mishnaevsky Jr. Repair of wind turbine blades: Review of methods and related computational mechanics problems. *Renewable energy*, 140:828–839, 2019.

[46] J. Chen and S. J. Bull. Approaches to investigate delamination and interfacial toughness in coated systems: an overview. *Journal of Physics D: Applied Physics*, 44(3):034001, 2010.

[47] Á. Pomázi and A. Toldy. Multifunctional gelcoats for fiber reinforced composites. *Coatings*, 9(3):173, 2019.

[48] Leon Mishnaevsky. Root causes and mechanisms of failure of wind turbine blades: Overview. *Materials*, 15(9):2959, 2022.

[49] Leon Mishnaevsky Jr, Nicolai Frost-Jensen Johansen, Anthony Fraisse, Søren Fæster, Thomas Jensen, and Brian Bendixen. Technologies of wind turbine blade repair: Practical comparison. *Energies*, 15(5):1767, 2022.

[50] S Stephenson. Wind blade repair: planning, safety, flexibility. *Composites World*, pages 1–13, 2011.

[51] W. Han, J. Kim, and B. Kim. Effects of contamination and erosion at the leading edge of blade tip airfoils on the annual energy production of wind turbines. *Renewable Energy*, 115:817 – 823, 2018. ISSN 0960-1481. doi: https://doi.org/10.1016/j.renene.2017.09.002. URL `http://www.sciencedirect.com/science/article/pii/S0960148117308649`.

[52] A. Sareen, C. A. Sapre, and M. S. Selig. Effects of leading edge erosion on wind turbine blade performance. *Wind Energy*, 17(10):1531–1542, 2014. doi: 10.1002/we.1649. URL `https://onlinelibrary.wiley.com/doi/abs/10.1002/we.1649`.

[53] S. Zhang, K. Dam-Johansen, S. Nørkjær, P. L. Bernad, and S. Kiil. Erosion of wind turbine blade coatings – design and analysis of jet-based laboratory equipment for performance evaluation. *Progress in Organic Coatings*, 78:103 – 115, 2015. ISSN 0300-9440. doi: https://doi.org/10.1016/j.porgcoat.2014.09.016. URL `http://www.sciencedirect.com/science/article/pii/S0300944014003269`.

[54] Omid Gohardani. Impact of erosion testing aspects on current and future flight conditions. *Progress in Aerospace Sciences*, 47(4):280–303, 2011.

[55] M Grundwürmer, O Nuyken, M Meyer, J Wehr, and N Schupp. Sol–gel derived erosion protection coatings against damage caused by liquid impact. *Wear*, 263 (1-6):318–329, 2007.

[56] Mark Hugh Keegan, David Nash, and Margaret Stack. Modelling rain drop impact on offshore wind turbine blades. *ASME Turbo Expo 2012*, pages Article–GT, 2012.

[57] Shizhong Zhang, Kim Dam-Johansen, Sten Nørkjær, Pablo L Bernad Jr, and Søren Kiil. Erosion of wind turbine blade coatings–design and analysis of jet-based laboratory equipment for performance evaluation. *Progress in Organic Coatings*, 78:103–115, 2015.

[58] N Fujisawa, S Takano, K Fujisawa, and T Yamagata. Experiments on liquid droplet impingement erosion on a rough surface. *Wear*, 398:158–164, 2018.

[59] Akshay Koodly Ravishankara, Huseyin Özdemir, and Edwin van der Weide. Analysis of leading edge erosion effects on turbulent flow over airfoils. *Renewable energy*, 172:765–779, 2021.

[60] Polytech. How to protect wind turbine rotor blades from leading edge erosion? *White Paper*, 2023.

[61] Javier Contreras López, Athanasios Kolios, Lin Wang, and Manuel Chiachio. A wind turbine blade leading edge rain erosion computational framework. *Renewable Energy*, 203:131–141, 2023.

[62] Xiaohang Wang, Zhenbo Tang, Na Yan, and Guojun Zhu. Effect of different types of erosion on the aerodynamic performance of wind turbine airfoils. *Sustainability*, 14(19):12344, 2022.

[63] Yanan Zhang, Francesco Avallone, and Simon Watson. Leading edge erosion detection for a wind turbine blade using far-field aerodynamic noise. *Applied Acoustics*, 207:109365, 2023.

[64] Mingwei Ge, De Tian, and Ying Deng. Reynolds number effect on the optimization of a wind turbine blade for maximum aerodynamic efficiency. *Journal of Energy Engineering*, 142(1):04014056, 2016.

[65] Jakob Ilsted Bech, Charlotte Bay Hasager, and Christian Bak. Extending the life of wind turbine blade leading edges by reducing the tip speed during extreme precipitation events. *Wind Energy Science*, 3(2):729–748, 2018.

[66] Anna-Maria Tilg, Charlotte Bay Hasager, Hans-Jürgen Kirtzel, and Poul Hummelshøj. Brief communication: Nowcasting of precipitation for leading-edge-erosion-safe mode. *Wind Energy Science*, 5(3):977–981, 2020.

[67] JE Field, CR Seward, CS Pickles, EJ Coad, and M Watt. Studies of rain erosion mechanisms in a range of ir transmitting ceramics-including coated samples. Technical report, CAMBRIDGE UNIV (UNITED KINGDOM) CAVENDISH LAB, 1994.

[68] F. J. Heymann. Erosion by liquids. *Machine Design*, 10:118–124, 1970.

[69] Michael Papadakis, See-Cheuk Wong, Arief Rachman, Kuohsing E Hung, Giao T Vu, and Colin S Bidwell. Large and small droplet impingement data on airfoils and two simulated ice shapes. Technical report, 2007.

[70] Sang Lee and Eric Loth. Simulation of icing on a cascade of stator blades. *Journal of Propulsion and Power*, 24(6):1309–1316, 2008.

[71] ASTM. *Standard Test Method for Liquid Impingement Erosion Using Rotating Apparatus*. G73-10. 2017. URL `http://www.astm.org/cgi-bin/resolver.cgi?G73`.

[72] DNVGL. DNVGL-RP-0171: Testing of rotor blade erosion protection systems. *Recommended Practice*, 2018.

[73] DNVGL. DNVGL-CP-0424: Coatings for protection of FRP structures with heavy rain erosion loads. *Class Programme*, 2016.

[74] DNVGL. DNVGL-RP-0573: Evaluation of erosion and delamination for leading edge protection systems of rotor blades. *Recommended Practice*, 2020.

[75] William Finnegan Jakob Ilsted Bech, Charlotte Bay Hasager, Kirsten Dyer Edmond Tobin, Nicolai Frost-Jensen Johansen, Ioannis Katsivalis, Fernando Sánchez López, Ian Hamerton, Heiko Blattert, Lena Sühling, Nicolas Quievy Julie Teuwen, Ole Bang, Christian Rosenberg Petersen, Søren Fæster, and Trevor Young. Review on available technologies for laboratory erosion testing. *Wind Task 46*, 2022.

[76] Nicolai Frost-Jensen Johansen. *Test Methods for Evaluating Rain Erosion Performance of Wind Turbine Blade Leading Edge Protection Systems*. PhD thesis, 2020.

[77] K Pugh, JW Nash, G Reaburn, and MM Stack. On analytical tools for assessing the raindrop erosion of wind turbine blades. *Renewable and Sustainable Energy Reviews*, 137:110611, 2020.

[78] D. Eisenberg, S. Laustsen, and J. Stege. Wind turbine blade coating leading edge rain erosion model: Development and validation. *Wind Energy*, 21(10):942–951, 2018.

[79] CM Preece. Erosion: Treatise on materials science and technology, vol. 16, 1979.

[80] WF Adler. The mechanisms of liquid impact. treatise on materials science and technology, 1979.

[81] H. M. Slot, R. M. IJzerman, M. le Feber, K. Nord-Varhaug, and E. van der Heide. Rain erosion resistance of injection moulded and compression moulded polybutylene terephthalate pbt. *Wear*, 414:234–242, 2018.

[82] E. Cortés, F. Sánchez, A. O'Carroll, B. Madramany, M. Hardiman, and T. Young. On the material characterisation of wind turbine blade coatings: the effect of interphase coating–laminate adhesion on rain erosion performance. *Materials*, 10 (10):1146, 2017.

[83] M. K. Lee, W. W. Kim, C. K. Rhee, and W. J. Lee. Liquid impact erosion mechanism and theoretical impact stress analysis in tin-coated steam turbine blade materials. *Metallurgical and Materials Transactions A*, 30(4):961–968, 1999.

[84] M. Sankarasubramanian, M. Torabizadeh, Z. A. Putnam, J. C. Moosbrugger, M. Y. Huang, and S. Krishnan. Enhanced elastomer toughness and fracture properties imparted by chemically reactive flat nanoparticles. *Polymer Testing*, page 105932, 2019.

[85] B. N. J. Persson and E. A. Brener. Crack propagation in viscoelastic solids. *Physical Review E*, 71(3):036123, 2005.

[86] A. Tcharkhtchi, S. Farzaneh, S. Abdallah-Elhirtsi, B. Esmaeillou, F. Nony, and A. Baron. Thermal aging effect on mechanical properties of polyurethane. *International Journal of Polymer Analysis and Characterization*, 19(7):571–584, 2014.

[87] S. Zhang, K. Dam-Johansen, P. L. Bernad, and S. Kiil. Rain erosion of wind turbine blade coatings using discrete water jets: Effects of water cushioning, substrate geometry, impact distance, and coating properties. *Wear*, 328:140–148, 2015.

[88] ISO. Pd iso/ts 19392-1:2018 paints and varnishes — coating systems for wind-turbine rotor blades. part 1: Minimum requirements and weathering. 2018.

[89] E. A. Valaker, S. Armada, and S. Wilson. Droplet erosion protection coatings for offshore wind turbine blades. *Energy Procedia*, 80:263–275, 2015.

[90] E. F. Tobin and T. M. Young. Analysis of incubation period versus surface topographical parameters in liquid droplet erosion tests. *Materials Performance and Characterization*, 6(2):144–164, 2017.

[91] Anthony O'Carroll. Correlation of mechanical properties to rain erosion resistance of polymeric materials. 2018.

[92] Frank J Heymann. Conclusions from the astm interlaboratory test program with liquid impact erosion facilities. *elsi*, pages 20_1–20_10, 1979.

[93] M. C. Shaw and G. J. DeSalvo. The role of elasticity in hardness testing. *Metallography, Microstructure, and Analysis*, 1(6):310–317, 2012.

[94] H. Busch, G. Hoff, G. Langbein, G. Taylor, D. C. Jenkins, M. A. Taunton, A. A. Fyall, R. F. Jones, and T. W. Harper. Rain erosion properties of materials. *Philosophical Transactions for the Royal Society of London. Series A, Mathematical and Physical Sciences*, pages 168–181, 1966.

[95] S. Zhang, S. Kiil, K. Dam-Johansen, and P. L. Bernad Jr. *Accelerated rain erosion of wind turbine blade coatings*. Danmarks Tekniske Universitet (DTU), 2014.

[96] G. Pechlivanoglou, S. Fuehr, C. N. Nayeri, and C. O. Paschereit. The effect of distributed roughness on the power performance of wind turbines. In *ASME Turbo Expo 2010: Power for Land, Sea, and Air*, pages 845–855. American Society of Mechanical Engineers, 2010.

[97] Leon Mishnaevsky Jr, Charlotte Bay Hasager, Christian Bak, Anna-Maria Tilg, Jakob I Bech, Saeed Doagou Rad, and Søren Fæster. Leading edge erosion of wind turbine blades: Understanding, prevention and protection. *Renewable Energy*, 169:953–969, 2021.

[98] BVG Assosiates. 10 years of whitelee windfarm. 2018.

[99] Mott MacDonald. Costs of low-carbon generation technologies. *Committee on Climate Change, London*, 2011.

[100] P. Lammel, L. D. Rafailovic, M. Kolb, K. Pohl, A. H. Whitehead, G. Grundmeier, and B. Gollas. Analysis of rain erosion resistance of electroplated nickel–tungsten alloy coatings. *Surface and Coatings Technology*, 206(8-9):2545–2551, 2012.

[101] A. Davis, Y. H. Yeong, A. Steele, E. Loth, and I. S. Bayer. Nanocomposite coating superhydrophobicity recovery after prolonged high-impact simulated rain. *Rsc Advances*, 4(88):47222–47226, 2014.

[102] F. P. Bowden and J. H. Brunton. The deformation of solids by liquid impact at supersonic speeds. *Proceedings of the Royal Society of London. Series A. Mathematical and Physical Sciences*, 263(1315):433–450, 1961.

[103] C. Siddons, C. Macleod, L. Yang, and M. M. Stack. An experimental approach to analysing rain droplet impingement on wind turbine blade materials. *EWEA 2015 Annual Event*, 2015.

[104] J. "Foldyna, J. Klich, P. Hlaváček, M. Zeleňák, and J." Ščučka. Erosion of metals by pulsating water jet. *Tehnički vjesnik*, 19(2):381–386, 2012.

[105] K. Pugh, G. Rasool, and M. M. Stack. Some thoughts on mapping tribological issues of wind turbine blades due to effects of onshore and offshore raindrop erosion. *Journal of Bio-and Tribo-Corrosion*, 4(3):50, 2018.

[106] E. F. Tobin, T. M. Young, D. Raps, and O. Rohr. Comparison of liquid impingement results from whirling arm and water-jet rain erosion test facilities. *Wear*, 271(9-10):2625–2631, 2011.

[107] E. F. Tobin, T. M. Young, and D. Raps. Evaluation and correlation of inter-laboratory results from a rain erosion test campaign. In *Proceedings of 28th International Congress of the Aeronautical Sciences*, 2012.

[108] E. F. Tobin, O. Rohr, D. Raps, W. Willemse, P. Norman, and T. M. Young. Surface topography parameters as a correlation factor for liquid droplet erosion test facilities. *Wear*, 328:318–328, 2015.

[109] A. Selmi. Void effect on carbon fiber epoxy composites. In *Second International Conference on Emerging Trends in Engineering and Technology (ICETET), London, May*, pages 30–31, 2014.

[110] L. Di Landro, A. Montalto, P. Bettini, S. Guerra, F. Montagnoli, and M. Rigamonti. Detection of voids in carbon/epoxy laminates and their influence on mechanical properties. *Polymers and Polymer Composites*, 25(5):371–380, 2017.

[111] K. B. Katnam, A. J. Comer, D. Roy, L. F. M. Da Silva, and T. M. Young. Composite repair in wind turbine blades: an overview. *The Journal of Adhesion*, 91(1-2):113–139, 2015.

[112] M Haag. Advances in leading edge protection of wind turbine blades. *Proceedings of the EWEA*, 2013.

[113] Friederike Jensen, Elie Abi Aoun, Oliver Focke, Andreas Krenz, Christian Tornow, Mareike Schlag, Catherine Lester, Axel Herrmann, Bernd Mayer, Michael Sorg, and Andreas Fischer. Investigation of the Causes of Premature Rain Erosion Evolution in Rotor Blade-like GFRP Structures by Means of CT, XRM, and Active Thermography. *Applied Sciences*, 12(22):11307, January 2022. ISSN 2076-3417. doi: 10.3390/app122211307. URL `https://www.mdpi.com/2076-3417/12/22/11307`. Number: 22 Publisher: Multidisciplinary Digital Publishing Institute.

[114] David Nash, Grant Leishman, Cameron Mackie, Kirsten Dyer, and Liu Yang. A Staged Approach to Erosion Analysis of Wind Turbine Blade Coatings. *Coatings*, 11(6):681, June 2021. ISSN 2079-6412. doi: 10.3390/coatings11060681. URL `https://www.mdpi.com/2079-6412/11/6/681`. Number: 6 Publisher: Multidisciplinary Digital Publishing Institute.

[115] Leon Mishnaevsky Jr, Søren Fæster, Lars P. Mikkelsen, Yukihiro Kusano, and Jakob Ilsted Bech. Micromechanisms of leading edge erosion of wind turbine blades: X-ray tomography analysis and computational studies. *Wind Energy*, 23(3):547–562, 2020. ISSN 1099-1824. doi: 10.1002/we.2441.

URL https://onlinelibrary.wiley.com/doi/abs/10.1002/we.2441. _eprint: https://onlinelibrary.wiley.com/doi/pdf/10.1002/we.2441.

[116] Friederike Jensen, Marina Terlau, Michael Sorg, and Andreas Fischer. Active Thermography for the Detection of Sub-Surface Defects on a Curved and Coated GFRP-Structure. *Applied Sciences*, 11(20):9545, January 2021. ISSN 2076-3417. doi: 10.3390/app11209545. URL https://www.mdpi.com/2076-3417/11/20/9545. Number: 20 Publisher: Multidisciplinary Digital Publishing Institute.

[117] Collaboration for NDT Education. Wavelength & defect detection. *NDT Resource Center*, 2001.

[118] J. F. Vandenrijt, F. Languy, C. Thizy, and M. Georges. Laser ultrasound flexible system for non-contact inspection of medium size and complex shaped composite structures made of carbon fiber reinforced polymer. In *Multidisciplinary Digital Publishing Institute Proceedings*, volume 2, page 455, 2018.

[119] O. Focke, M. Kalms, C. V. Kopylow, and W. Jueptner. Ndt of free formed cfrp composites with laser ultrasonic. In *12th Asia Pacific Conference on NDT*, 2006.

[120] R. Halmshaw. Non-destructive testing. second edition. *Edward Arnold, Mill Rd, Dunton Green, Sevenoaks, Kent TN 13 2 YA, UK, 1991. 323*, 1991.

[121] B. Ehrhart, B. Valeske, and C. Bockenheimer. Non-destructive evaluation (nde) of aerospace composites: methods for testing adhesively bonded composites. In *Non-destructive evaluation (NDE) of polymer matrix composites*, pages 220–237. Elsevier, 2013.

[122] B Stakenborghs. Evisivescan microwave scanning ndt. *NPL Project VITCEA*, 2015.

[123] M Gower, M Lodeiro, A Aktas, and R Shaw. Validated inspection techniques for composites in energy applications. *NPL Project VITCEA*, 2015.

[124] NPL. Microwave ndt for composites explained. *NPL E-Training Course*, 2019.

[125] NP Avdelidis and T-H Gan. Non-destructive evaluation (nde) of composites: Infrared (ir) thermography of wind turbine blades. In *Non-Destructive Evaluation (NDE) of Polymer Matrix Composites*, pages 634–650e. Elsevier, 2013.

[126] John Canny. A computational approach to edge detection. *IEEE Transactions on pattern analysis and machine intelligence*, (6):679–698, 1986.

[127] John A Tsanakas, Dimitrios Chrysostomou, Pantelis N Botsaris, and Antonios Gasteratos. Fault diagnosis of photovoltaic modules through image processing and canny edge detection on field thermographic measurements. *International journal of sustainable energy*, 34(6):351–372, 2015.

[128] Xiru Zheng, Seongmin Kim, and Chan Woo Park. Enhancement of thermal conductivity of carbon fiber-reinforced polymer composite with copper and boron nitride particles. *Composites Part A: Applied Science and Manufacturing*, 121:449–456, June 2019. ISSN 1359-835X. doi: 10.1016/j.compositesa.2019.03.030. URL `https://www.sciencedirect.com/science/article/pii/S1359835X19301095`.

[129] Bhyrav Mutnuri. Thermal conductivity characterization of composite materials. Master's thesis, West Virginia University Libraries, May 2006. URL `https://researchrepository.wvu.edu/etd/1715`.

[130] Eunbi Lee, Chi Hyeong Cho, Sae Hoon Hwang, Min-Geun Kim, Jeong Woo Han, Hanmin Lee, and Jun Hyup Lee. Improving the Vertical Thermal Conductivity of Carbon Fiber-Reinforced Epoxy Composites by Forming Layer-by-Layer Contact of Inorganic Crystals. *Materials*, 12(19):3092, September 2019. ISSN 1996-1944. doi: 10.3390/ma12193092. URL `https://www.ncbi.nlm.nih.gov/pmc/articles/PMC6804115/`.

[131] Shiren Wang and Jingjing Qiu. Enhancing thermal conductivity of glass fiber/polymer composites through carbon nanotubes incorporation. *Composites Part B: Engineering*, 41(7):533–536, October 2010. ISSN 1359-8368. doi:

10.1016/j.compositesb.2010.07.002. URL https://www.sciencedirect.com/science/article/pii/S1359836810001071.

[132] N. Tanaka, D. Aoyagi, R. Sasamoto, Y. Izawa, and K. Nishijima. Difference of Discharge Phenomena under GFRP and CFRP Insulation Barrier with Steep Impulse Voltage. In *2018 IEEE Conference on Electrical Insulation and Dielectric Phenomena (CEIDP)*, pages 566–569, October 2018. doi: 10.1109/CEIDP.2018.8544753. ISSN: 2576-2397.

[133] Cameron Mackie. Establishing the optimal conditions for rotating arm erosion testing, materials characterisation and computational modelling of wind turbine blade rain erosion. 2020.

[134] James WK Nash, Iasonas Zekos, and Margaret M Stack. Mapping of meteorological observations over the island of ireland to enhance the understanding and prediction of rain erosion in wind turbine blades. *Energies*, 14(15):4555, 2021.

[135] Hamish Macdonald, David Infield, David H Nash, and Margaret M Stack. Mapping hail meteorological observations for prediction of erosion in wind turbines. *Wind Energy*, 19(4):777–784, 2016.

[136] JR Macdonald and MM Stack. Some thoughts on modelling hail impact on surfaces. *Journal of Bio-and Tribo-Corrosion*, 7(2):1–7, 2021.

[137] Hamish Macdonald, David Nash, and Margaret M Stack. Repeated impact of simulated hail ice on glass fibre composite materials. *Wear*, 432:102926, 2019.

[138] Iham F Zidane, Greg Swadener, Xianghong Ma, Mohamed F Shehadeh, Mahmoud H Salem, and Khalid M Saqr. Performance of a wind turbine blade in sandstorms using a cfd-bem based neural network. *Journal of Renewable and Sustainable Energy*, 12(5):053310, 2020.

[139] Mike Godfrey, Oliver Siederer, Jurgita Zekonyte, Ismail Barbaros, and Robert Wood. The effect of temperature on the erosion of polyurethane coatings for wind turbine leading edge protection. *Wear*, page 203720, 2021.

[140] GuangYou Liu, HaiTang Cen, Qin Zeng, WenLiang Tian, and Ling Li. Erosion mechanism and simulation analysis of wind turbine blade coating. In *2019 4th International Conference on Mechanical, Control and Computer Engineering (ICMCCE)*, pages 1036–10364. IEEE, 2019.

[141] Giovanni Fiore and Michael S Selig. Simulation of damage for wind turbine blades due to airborne particles. *Wind Engineering*, 39(4):399–418, 2015.

[142] N Dalili, Afsaneh Edrisy, and Rupp Carriveau. A review of surface engineering issues critical to wind turbine performance. *Renewable and Sustainable energy reviews*, 13(2):428–438, 2009.

[143] Karen Wood. Blade repair: Closing the maintenance gap. *Composites Technology*, 9(2), 2011.

[144] H Ashrafizadeh, P Mertiny, and A McDonald. Evaluation of the effect of temperature on mechanical properties and wear resistance of polyurethane elastomers. *Wear*, 368:26–38, 2016.

[145] Luis Bartolomé and Julie Teuwen. Prospective challenges in the experimentation of the rain erosion on the leading edge of wind turbine blades. *Wind Energy*, 22 (1):140–151, 2019.

[146] James G Speight. *Chapter 14 - Monomers, Polymers, and Plastics. Handbook of industrial hydrocarbon processes (2nd Edition)*. Gulf Professional Publishing, 2019.

[147] Ajay Padsalgikar. *Plastics in medical devices for cardiovascular applications*. William Andrew, 2017.

[148] R Bruce Prime. Dynamic mechanical analysis of thermosetting materials. 2005.

[149] A Boubakri, K Elleuch, N Guermazi, and HF Ayedi. Investigations on hygrothermal aging of thermoplastic polyurethane material. *Materials & Design*, 30(10): 3958–3965, 2009.

[150] Xiong F Yang, J Li, SG Croll, DE Tallman, and GP Bierwagen. Degradation of low gloss polyurethane aircraft coatings under uv and prohesion alternating exposures. *Polymer Degradation and Stability*, 80(1):51–58, 2003.

[151] Oliver Frank. Material wear and erosion at the surface of plastics caused by weathering. *Die Angewandte Makromolekulare Chemie: Applied Macromolecular Chemistry and Physics*, 176(1):43–53, 1990.

[152] Sabina Alessi, Giuseppe Pitarresi, and Giuseppe Spadaro. Effect of hydrothermal ageing on the thermal and delamination fracture behaviour of cfrp composites. *Composites Part B: Engineering*, 67:145–153, 2014.

[153] ZA Oğuz, A Erkliğ, and ÖY Bozkurt. Effects of hydrothermal seawater aging on the mechanical properties and water absorption of glass/aramid/epoxy hybrid composites. *International Polymer Processing*, 36(1):79–93, 2021.

[154] Kieran Pugh, Ghulam Rasool, and Margaret M Stack. Some thoughts on mapping tribological issues of wind turbine blades due to effects of onshore and offshore raindrop erosion. *Journal of Bio-and Tribo-Corrosion*, 4(3):50, 2018.

[155] Kieran Pugh and Margaret M Stack. Rain erosion maps for wind turbines based on geographical locations: a case study in ireland and britain. *Journal of Bio-and Tribo-Corrosion*, 2020.

[156] Ghulam Rasool, Anna C Middleton, and Margaret M Stack. Mapping raindrop erosion of gfrp composite wind turbine blade materials: Perspectives on degradation effects in offshore and acid rain environmental conditions. *Journal of Tribology*, 142(6), 2020.

[157] B Beltman, G Rouwenhorst, A Whilde, and M Ten Cate. Chemical composition of rain in western ireland. *The Irish Naturalists' Journal*, 24(7):267–274, 1993.

[158] Sean O'Hogain, Anna Reid, Liam McCarton, Jenny Pender, and Niamh McNtyre. Water savings and rainwater harvesting–pilot project in ireland. In *Proceedings of*

the European Water and Wastewater Management (EWWM) Conference. Technological University Dublin, 2007. ISBN 1-903958-24-5.

[159] J Aherne and EP Farrell. Deposition of sulphur, nitrogen and acidity in precipitation over ireland: chemistry, spatial distribution and long-term trends. *Atmospheric Environment*, 36(8):1379–1389, 2002.

[160] Svetlana Tsyro, Wenche Aas, Joana Soares, Mikhail Sofiev, H Berge, and GJAC Spindler. Modelling of sea salt concentrations over europe: key uncertainties and comparison with observations. *Atmospheric Chemistry and Physics*, 11(20): 10367–10388, 2011.

[161] David Simpson, Anna Benedictow, Halldis Berge, Robert Bergström, Lisa D Emberson, Hilde Fagerli, Chris R Flechard, Garry D Hayman, Michael Gauss, Jan Eiof Jonson, et al. The emep msc-w chemical transport model-technical description. 2012.

[162] Selena Georgiou, Nicolas Gaussiat, Huw Lewis, and Selena Georgiou. Dynamic modelling of the orographic enhancement of precipitation in the uk. In *Proceedings of the 6th European Conference on Radar in Meteorology and Hydrology, Sibiu, Romania*, 2010.

[163] AC Best. The size distribution of raindrops. *Quarterly Journal of the Royal Meteorological Society*, 76(327):16–36, 1950.

[164] Jonathan G Fairman Jr, David M Schultz, Daniel J Kirshbaum, Suzanne L Gray, and Andrew I Barrett. A radar-based rainfall climatology of great britain and ireland. *Weather*, 70(5):153–158, 2015.

[165] Jonathan G Fairman Jr, David M Schultz, Daniel J Kirshbaum, Suzanne L Gray, and Andrew I Barrett. Climatology of size, shape, and intensity of precipitation features over great britain and ireland. *Journal of Hydrometeorology*, 18(6):1595–1615, 2017.

[166] Met Office. NWP-UKV: Operational Numerical Weather Prediction (NWP) output from the UK Met Office UK Atmospheric High Resolution Unified Model (UM). *http://catalogue.ceda.ac.uk/uuid/78f23c539d304591b137cf986b69a525*, 24th August 2022, 2019.

[167] Dan Soto, Aurélie Borel De Larivière, Xavier Boutillon, Christophe Clanet, and David Quéré. The force of impacting rain. *Soft Matter*, 10:4929–4934, 2014. doi: 10.1039/C4SM00513A. URL `http://dx.doi.org/10.1039/C4SM00513A`.

[168] M. Angulo-Martínez, S. Beguería, and J. Kyselý. Use of disdrometer data to evaluate the relationship of rainfall kinetic energy and intensity (ke-i). *Science of The Total Environment*, 568:83–94, 2016. ISSN 0048-9697. doi: https://doi.org/10.1016/j.scitotenv.2016.05.223. URL `https://www.sciencedirect.com/science/article/pii/S0048969716311627`.

[169] MatWeb. Overview of materials for epoxy cure resin, . `http://www.matweb.com/search/datasheet.aspx?matguid=956da5edc80f4c62a72c15ca2b923494{Accessed:14-Jan-2021}`.

[170] MatWeb. Overview of materials for polyester (thermoset) - rigid, . `http://www.matweb.com/search/datasheet.aspx?matguid=1d92ed366503454ba49b8a44099f90de{Accessed:14-Jan-2021}`.

[171] Robbie Herring, Kirsten Dyer, Paul Howkins, and Carwyn Ward. Characterisation of the offshore precipitation environment to help combat leading edge erosion of wind turbine blades. *Wind Energy Science*, 5(4):1399–1409, 2020.

[172] Merhala Thurai, Viswanathan Bringi, Patrick N Gatlin, Walter A Petersen, and Matthew T Wingo. Measurements and modeling of the full rain drop size distribution. *Atmosphere*, 10(1):39, 2019.

[173] B Amirzadeh, A Louhghalam, M Raessi, and M Tootkaboni. A computational framework for the analysis of rain-induced erosion in wind turbine blades, part i: Stochastic rain texture model and drop impact simulations. *Journal of Wind Engineering and Industrial Aerodynamics*, 163:33–43, 2017.

[174] W Hu, X Wang, W Chen, Y Wang, Z Liu, J Tan, SC Pryor, and RJ Barthelmie. A computational model of wind turbine blade erosion induced by raindrop impact. In *Journal of Physics: Conference Series*, volume 1452, page 012048. IOP Publishing, 2020.

[175] Amrit S Verma, Saullo GP Castro, Zhiyu Jiang, Weifei Hu, and Julie JE Teuwen. Leading edge erosion of wind turbine blades: Effects of blade surface curvature on rain droplet impingement kinematics. In *Journal of Physics: Conference Series*, volume 1618, page 052003. IOP Publishing, 2020.

[176] Kjetil Tørseth, Wenche Aas, Knut Breivik, Ann Mari Fjæraa, Markus Fiebig, Anne-Gunn Hjellbrekke, C Lund Myhre, Sverre Solberg, and Karl Espen Yttri. Introduction to the european monitoring and evaluation programme (emep) and observed atmospheric composition change during 1972–2009. *Atmospheric Chemistry and Physics*, 12(12):5447–5481, 2012.

[177] D. Martin and C. O'Dowd. *Ireland's Atmospheric Composition and Climate Change Network.* Climate Change. Irish Environmental Protection Agency, 2020. ISBN 978-1-84095-962-8. URL `\url{https://www.epa.ie/pubs/reports/research/climate/research357.html[lastaccessed18thFebruary2021]}`.

[178] Environmental protection agency (epa), ireland. epa data can be downloaded directly via envision using the data download option, or can be downloaded using the epa database download section of the geoportal. data that is produced directly by the epa is free for use under the conditions of under the conditions of creative commons attribution license 4.0.

[179] Department for environment, food and rural affairs (defra). © crown 2021 copyright defra via uk-air.defra.gov.uk, licenced under the open government licence (ogl).

[180] Robert L Wilby, Simon Noone, Conor Murphy, Tom Matthews, Shaun Harrigan, and Ciaran Broderick. An evaluation of persistent meteorological drought using

a homogeneous island of ireland precipitation network. *International Journal of Climatology*, 36(8):2854–2865, 2016.

[181] Rowan Fealy and Gerald Mills. Deriving lamb weather types suited to regional climate studies: A case study on the synoptic origins of precipitation over ireland. *International Journal of Climatology*, 38(8):3439–3448, 2018.

[182] Global wind atlas 3.0, a free, web based application developed, owned and operated by the technical university of denmark (dtu). the global wind atlas 3.0 is released in partnership with the world bank group, utilizing data provided by vortex, using funding provided by the energy sector management assistance program (esmap). for additional information: https://globalwindatlas.info, .

[183] C Hasager, F Vejen, JI Bech, WR Skrzypiński, A-M Tilg, and M Nielsen. Assessment of the rain and wind climate with focus on wind turbine blade leading edge erosion rate and expected lifetime in danish seas. *Renewable Energy*, 149: 91–102, 2020.

[184] Jamie Ledingham, David Archer, Elizabeth Lewis, Hayley Fowler, and Chris Kilsby. Contrasting seasonality of storm rainfall and flood runoff in the uk and some implications for rainfall-runoff methods of flood estimation. *Hydrology Research*, 50(5):1309–1323, 2019.

[185] Graham Sinden. Characteristics of the uk wind resource: Long-term patterns and relationship to electricity demand. *Energy policy*, 35(1):112–127, 2007.

[186] RW Baker, SN Walker, and JE Wade. Annual and seasonal variations in mean wind speed and wind turbine energy production. *Solar Energy*, 45(5):285–289, 1990.

[187] Met eirann. climate of ireland (accessed: 21/01/2021) (https://www.met.ie/climate/climate-of-ireland), .

[188] Charlotte Hasager, Jakob Ilsted Bech, Yukihiro Kusano, Mikael Sjöholm, Torben Mikkelsen, Christian Bak, Witold Skrzypinski, Søren Fæster, Anna-Maria Tilg

DTU, Flemming Vejen DMI, et al. Rain and erosion on turbine blades. In *Science meets industry Bergen*, 2018.

[189] Met eirann. rainfall climate of ireland (accessed: 21/01/2021) (https://www.met.ie/climate/what-we-measure/rainfall), .

[190] Wind logger. how does cold weather affect wind speed? https://www.windlogger.com/blogs/news/how-does-cold-weather-affect-wind-speed. 2019. .

[191] Danqing Huang, Peiwen Yan, Xiucheng Xiao, Jian Zhu, Xiaowen Tang, Anning Huang, and Jing Cheng. The tri-pole relation among daily mean temperature, atmospheric moisture and precipitation intensity over china. *Global and Planetary Change*, 179:1–9, 2019.

[192] Haider Ali and Vimal Mishra. Contributions of dynamic and thermodynamic scaling in subdaily precipitation extremes in india. *Geophysical Research Letters*, 45(5):2352–2361, 2018.

[193] John D Valiantzas. Simplified versions for the penman evaporation equation using routine weather data. *Journal of Hydrology*, 331(3-4):690–702, 2006.

[194] Peter Brimblecombe. Temporal humidity variations in the heritage climate of south east england. *Heritage Science*, 1(1):3, 2013.

[195] M Still, H Venzke, F Durst, and A Melling. Influence of humidity on the convective heat transfer from small cylinders. *Experiments in fluids*, 24(2):141–150, 1998.

[196] Katarzyna Kluska, Katarzyna Piotrowicz, and Idalia Kasprzyk. The impact of rainfall on the diurnal patterns of atmospheric pollen concentrations. *Agricultural and Forest Meteorology*, 291:108042, 2020.

[197] Rasa Zalakeviciute, Jesús López-Villada, and Yves Rybarczyk. Contrasted effects of relative humidity and precipitation on urban pm2. 5 pollution in high elevation urban areas. *Sustainability*, 10(6):2064, 2018.

[198] Janae Csavina, Jason Field, Omar Félix, Alba Y Corral-Avitia, A Eduardo Sáez, and Eric A Betterton. Effect of wind speed and relative humidity on atmospheric dust concentrations in semi-arid climates. *Science of the Total Environment*, 487: 82–90, 2014.

[199] Olive G Engel. Mechanism of rain erosion. *Wright Air Development Centre, USA. Report*, (53-192):1–54, 1953.

[200] William F. Adler. Particulate impact damage predictions. *Wear*, 186-187: 35–44, 1995. ISSN 0043-1648. doi: https://doi.org/10.1016/0043-1648(95)07177-6. URL https://www.sciencedirect.com/science/article/pii/0043164895071776. 8th International Conference on Erosion by Liquid and Solid Impact.

[201] William F Adler. Rain impact retrospective and vision for the future. *Wear*, 233-235:25–38, 1999. ISSN 0043-1648. doi: https://doi.org/10.1016/S0043-1648(99)00191-X. URL https://www.sciencedirect.com/science/article/pii/S004316489900191X.

[202] Saeed Doagou-Rad and Leon Mishnaevsky Jr. Rain erosion of wind turbine blades: computational analysis of parameters controlling the surface degradation. *Meccanica*, 55(4):725–743, 2020.

[203] Søren Fæster, Yukihiro Kusano, and Jakob Ilsted Bech. *Characterization report of selected RET and SPIFT samples characterized by electron microscopy and X-ray tomography.* Number 763 in DTU Wind Energy I. DTU Wind Energy, Denmark, 2018.

[204] Anthony Fraisse, Jakob Ilsted Bech, Kaj Kvisgaard Borum, Vladimir Fedorov, Nicolai Frost-Jensen Johansen, Malcolm McGugan, Leon Mishnaevsky, and Yukihiro Kusano. *Development of Single Point Impact Fatigue Tester (SPIFT).* Number 751 in DTU Wind Energy I. DTU Wind Energy, Denmark, 2018.

[205] Mac Gaunaa, NN Sørensen, N Frost-Jensen Johansen, Anders Smærup Olsen, C Bak, and RB Andersen. Investigation of droplet path in a rain erosion tester.

In *Journal of Physics: Conference Series*, volume 1037, page 062030. IOP Publishing, 2018.

[206] Smiths Metal Centres Limited. 7000 series aluminium.

[207] Sandmeyer Steel Company. Stainless steel plate.

[208] Penta Precision Engineering Ltd. Stainless steel 17-4 ph machining a guide to 17-4 ph cnc machined parts: Properties, applications and design considerations.

[209] Paul Ahrens. What is Bolt Preload?, December 2018. URL `https://www.albanycountyfasteners.com/blog/what-is-bolt-preload/`.

[210] P. Lecomte, B. Paluch, and M. Brieu. Free edge effects study in laminated composites using Digital Image Correlation: effect of material and geometrical singularities. *EPJ Web of Conferences*, 6:20011, 2010. ISSN 2100-014X. doi: 10.1051/epjconf/20100620011. URL `http://www.epj-conferences.org/10.1051/epjconf/20100620011`.

[211] Victor Giurgiutiu. Chapter 5 - Damage and Failure of Aerospace Composites. In Victor Giurgiutiu, editor, *Structural Health Monitoring of Aerospace Composites*, pages 125–175. Academic Press, Oxford, January 2016. ISBN 978-0-12-409605-9. doi: 10.1016/B978-0-12-409605-9.00005-2. URL `https://www.sciencedirect.com/science/article/pii/B9780124096059000052`.

[212] British Plastics Federation. Polycarbonate (PC). URL `https://www.bpf.co.uk/plastipedia/polymers/Polycarbonate.aspx`.

[213] British Plastics Federation. Polycarbonate (PC), 2015. URL `https://www.bpf.co.uk/plastipedia/polymers/Polycarbonate.aspx`.

[214] PU foams | Adhesive Backed Materials Ltd. URL `https://www.abmuk.net/foam`.

[215] Brian J. Cantwell. The naca airfoil series. 2013.

[216] A Filipone. Aerodynamic database: Drag coefficients. *https://aerodyn.org/tables/#stream*, 2005.

[217] Airfoil Tools. NACA 63-015A AIRFOIL (n63015a-il), 2023. URL http://airfoiltools.com/airfoil/details?airfoil=n63015a-il.

[218] Woobeom Han, Jonghwa Kim, and Bumsuk Kim. Effects of contamination and erosion at the leading edge of blade tip airfoils on the annual energy production of wind turbines. *Renewable energy*, 115:817–823, 2018.

[219] G Cueva, A Sinatora, WL Guesser, and AP Tschiptschin. Wear resistance of cast irons used in brake disc rotors. *Wear*, 255(7-12):1256–1260, 2003.

[220] Brake Caliper - Front Left. URL https://www.gsfcarparts.com/za003683.

[221] Mercedes Benz Sprinter NK Brake Caliper Rear Right NK2133236 | Online Automotive. URL https://www.onlineautomotive.co.uk/car-parts/Mercedes-Benz/Sprinter/2.1L/Diesel/NK/Brakes/Brake-calipers/NK2133236/1/574?gclid=CjwKCAiA5Y6eBhAbEiwA_2ZWIfcnbyA8-sRx24jV3sHVUj7SvbUklzTtLbl3Gt3evUX0KuvMSRXiBhoCQZYQAvD_BwE.

[222] BOSCH F 026 003 484 BRAKE MASTER CYLINDER without brake fluid reservoir , EAN 4047024282285 online. URL https://www.euspares.co.uk/parts/bosch/1207047.

[223] Master Power Brakes Team. Calculating the right brake pedal ratio. 2015.

[224] Wilwood GS Compact Integral Reservoir Master Cylinder - 0.625 (5/8) Inch Bore, . URL https://www.ebay.co.uk/itm/142205172764.

[225] Wilwood Floor Mount Clutch / Brake Pedal Box Assembly 6:1 Ratio 340-13833, . URL https://www.ebay.co.uk/itm/231934314538.

[226] Adash spol. s r.o. Balancer app. .

[227] Siemens. Operating instructions sinamics sinamics g120c low voltage converter chassis units with frame sizes aa ... f. *SiemensDrives*, Edition 11/2016, 2016. URL https://inverterdrive.com/file/Siemens-G120C-Operating-Instructions.

[228] Robbie Herring, Kirsten Dyer, Alasdair MacLeod, and Carwyn Ward. Computational fluid dynamics methodology for characterisation of leading edge erosion in whirling arm test rigs. In *Journal of Physics: Conference Series*, volume 1222, page 012011. IOP Publishing, 2019.

[229] Christian. Direct linear least squares fitting of an ellipse. August 2021. URL `https://scipython.com/blog/direct-linear-least-squares-fitting-of-an-ellipse/`.

[230] Radim Halır and Jan Flusser. Numerically stable direct least squares fitting of ellipses. In *Proc. 6th International Conference in Central Europe on Computer Graphics and Visualization. WSCG*, volume 98, pages 125–132. Citeseer, 1998.

[231] MA Raza, J Van Swigchem, HP Jansen, Henricus JW Zandvliet, Bene Poelsema, and Ernst S Kooij. Droplet impact on hydrophobic surfaces with hierarchical roughness. *Surface Topography: Metrology and Properties*, 2(3):035002, 2014.

[232] Nils Barfknecht and Dominic von Terzi. On the significance of rain droplet slowdown and deformation for leading-edge rain erosion. *Wind Energy Science Discussions*, 2023:1–42, 2023.

[233] Suthyvann Sor Mendi. *Theoretical model for droplet deformation and trajectory in continously accelerating flows*. PhD thesis, Espacio, 2017.

[234] BUMAX. Bumax 88/bumax 109 datasheet (1.0).

[235] Michel Chaussumier, Catherine Mabru, Rémy Chieragatti, and Majid Shahzad. Fatigue life model for 7050 chromic anodized aluminium alloy. *Procedia Engineering*, 66:300–312, 2013.

[236] Majid Shahzad, Michel Chaussumier, Rémy Chieragatti, Catherine Mabru, and Farhad Rezai-Aria. Surface characterization and influence of anodizing process on fatigue life of al 7050 alloy. *Materials & Design*, 32(6):3328–3335, 2011.

[237] 3D HUBS B.V. Hubs — on-demand manufacturing: Quotes in seconds, parts in days.

Appendices

Appendix A

Initial Design

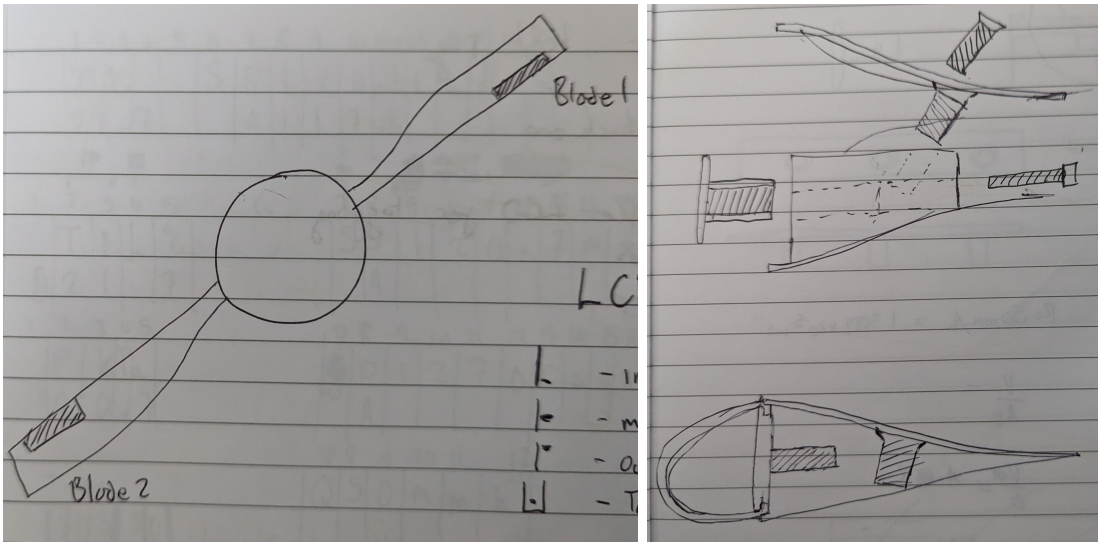

(a) (b)

Figure A.1: Figures A.1a and A.1b are both early design concepts for the rain erosion test rig.

Appendix B

Mercedes Van Wheel Hub

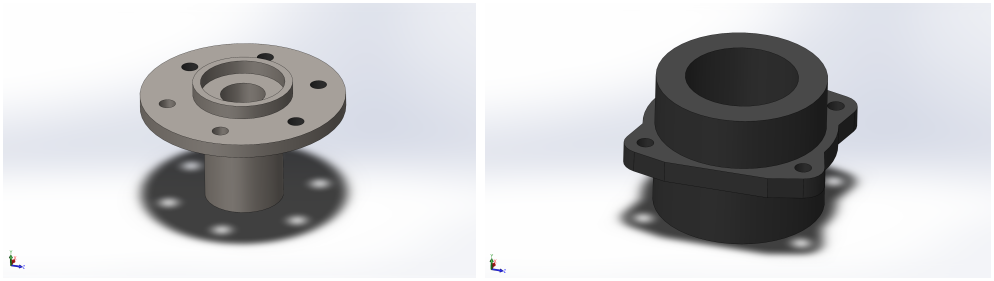

(a) (b)

Figure B.1: Both CAD models of the two halves of the Mercedes rear wheel hub

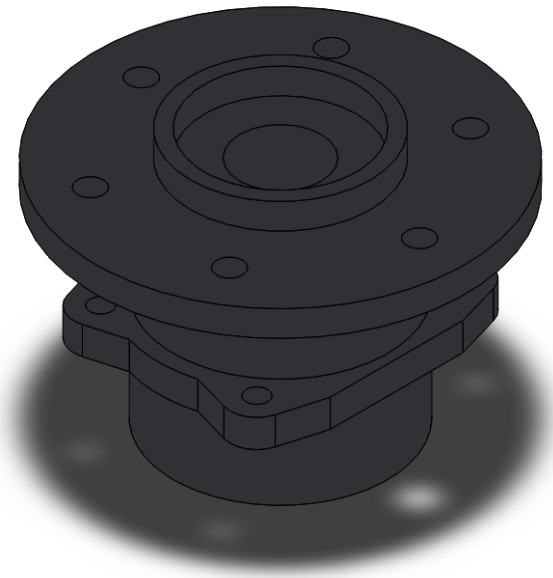

Figure B.2: CAD model of the main bearing, reproduced from metrology work carried out in-house.

Appendix C

Outer Enclosure Assembly

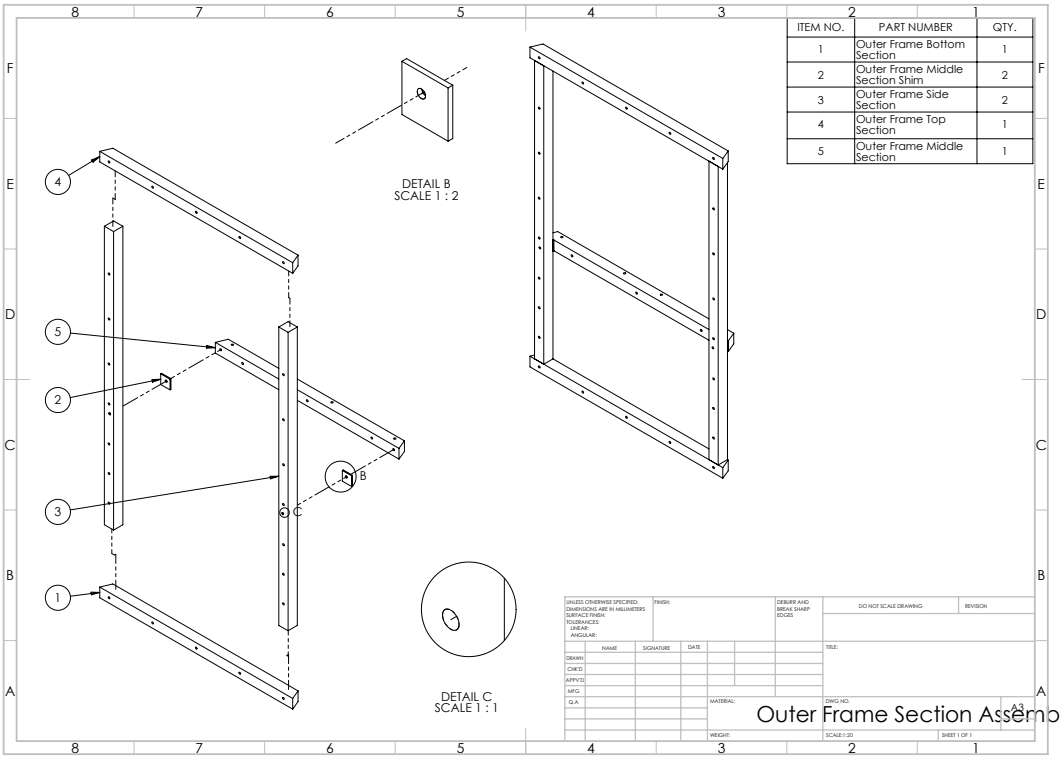

Figure C.1: Displayed here is one of the outer frame sections from the enclosure. There were 3 separate variants of the outer frame sections; one which allowed the installation of the door and viewing with, this section (which was a generic section with no significant features) and the final which allowed the attachment of the lid sections.

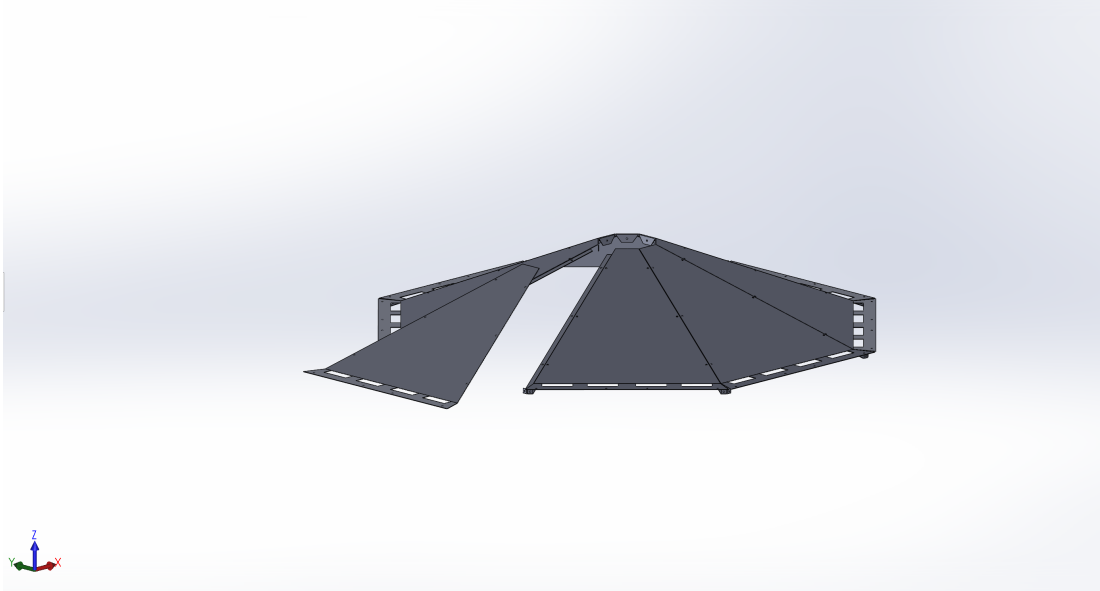

Figure C.2: Cone-shaped drainage panels.

Appendix D

Power Requirement CFD Simulation Mesh

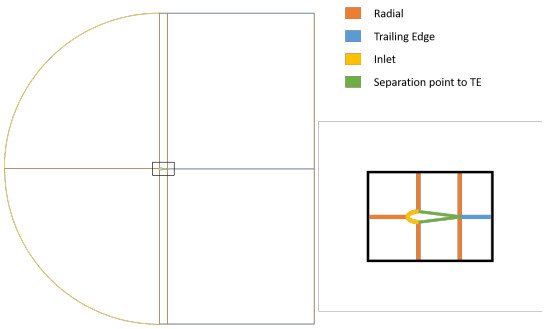

Figure D.1: Displayed here is the domain used for the 2D CFD simulation of the aerofoil. Each of the different colours represents a different bias and number of elements for the edges with their respective colours. The chord length (the horizontal distance of the Separation point to Trailing Edge) of the aerofoil was 0.1m. The domain height (2 x Radial) was 4m and the Trailing edge length was 2m

Appendix E

Sample Holder Design Optimisation Evolution

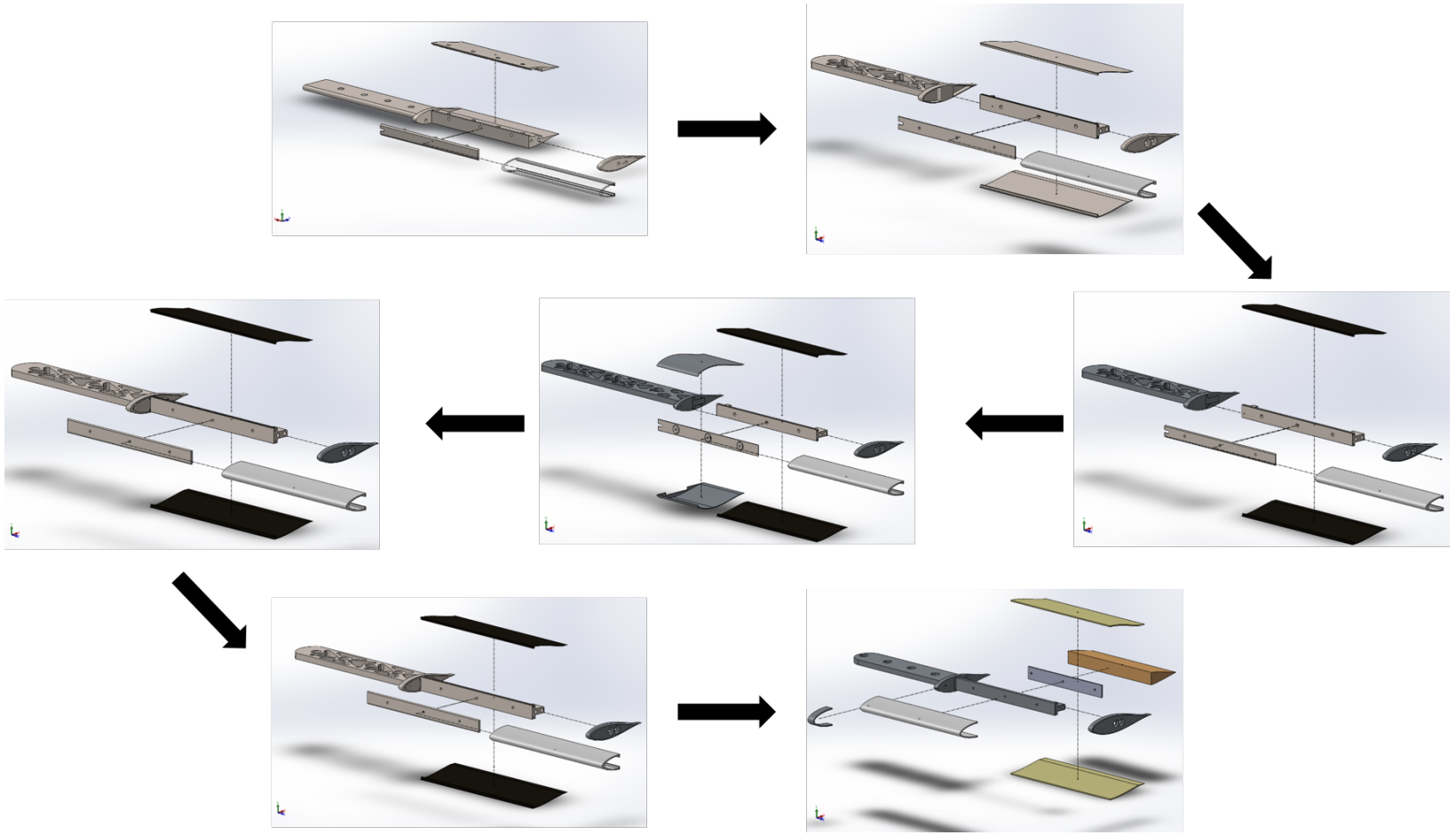

Figure E.1: Here the design evolution of the first manufactured version of the sample holder can be visualised.

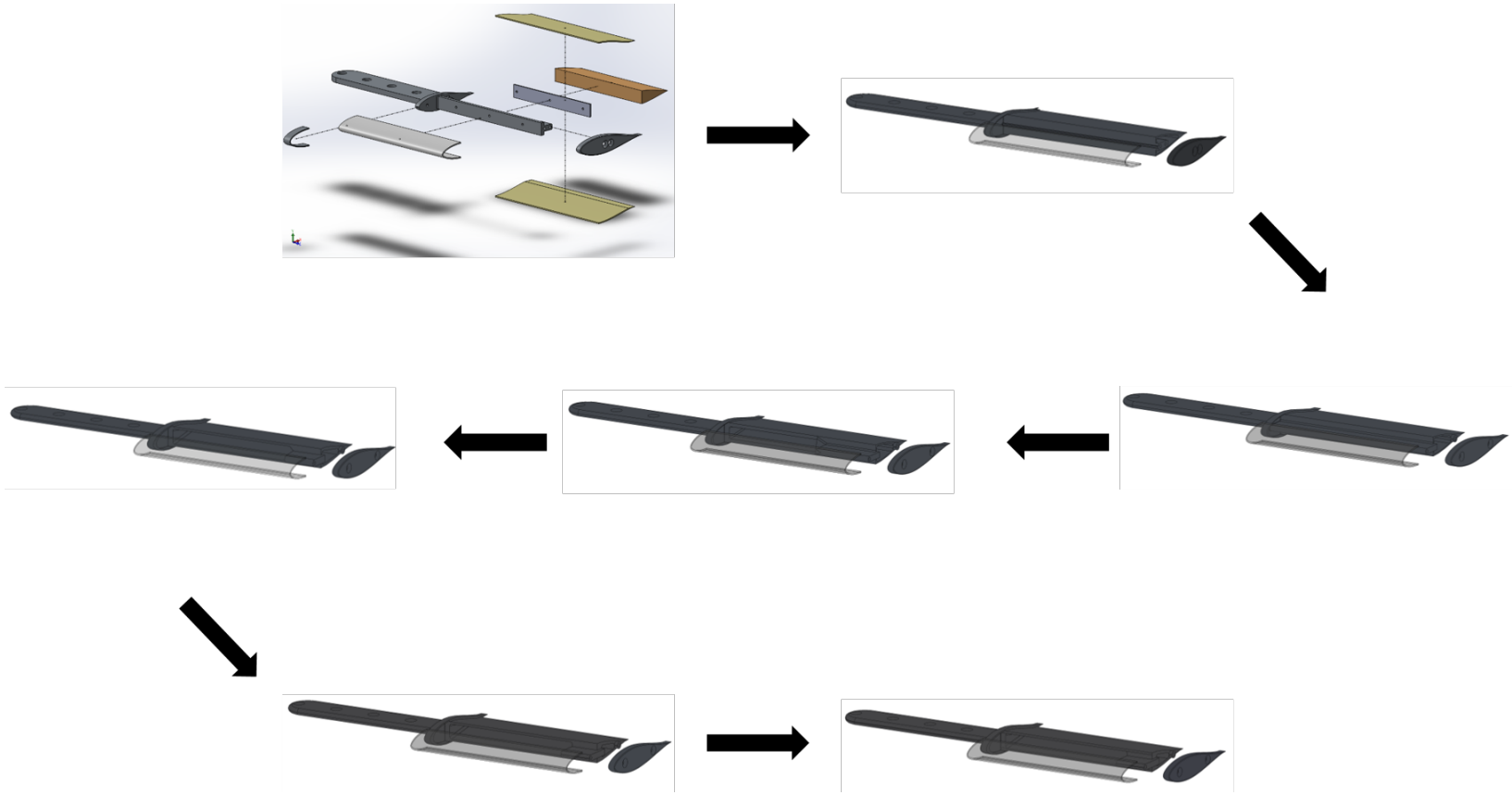

Figure E.2: Here the design evolution of the second version of the sample holder can be visualised.

Appendix F

Mercedes Brake Disc

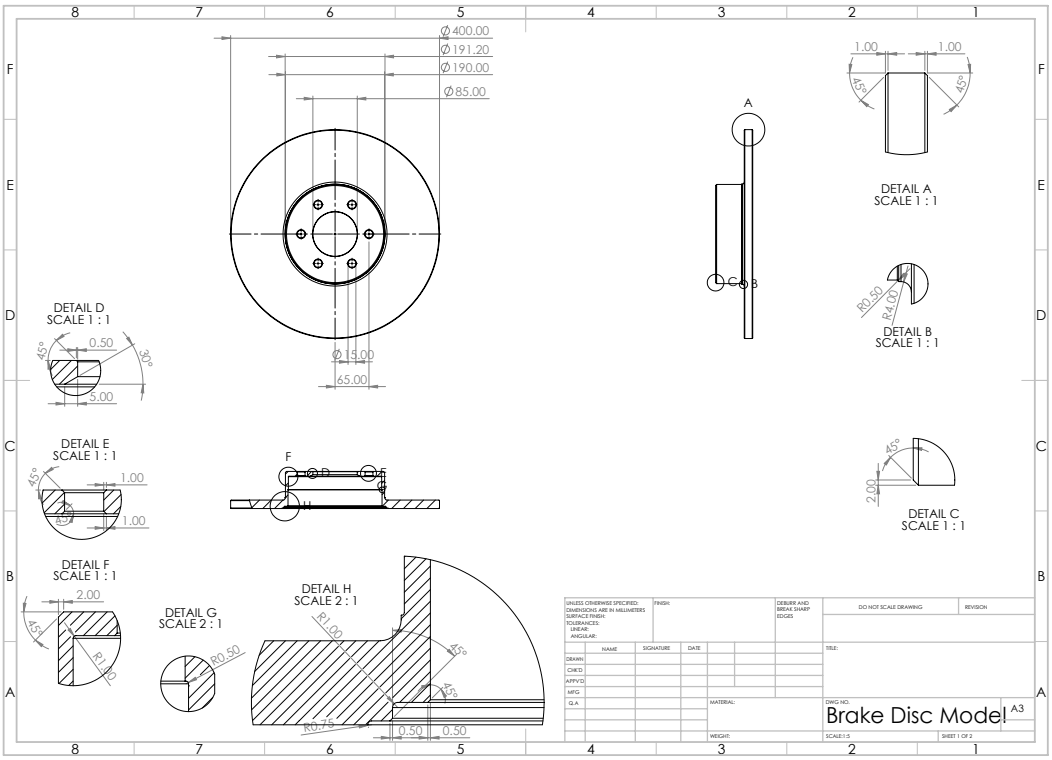

Figure F.1: Engineering drawing of the cast iron brake disc.

Appendix G

Electronics Cabinet Layout for the Electric Motor

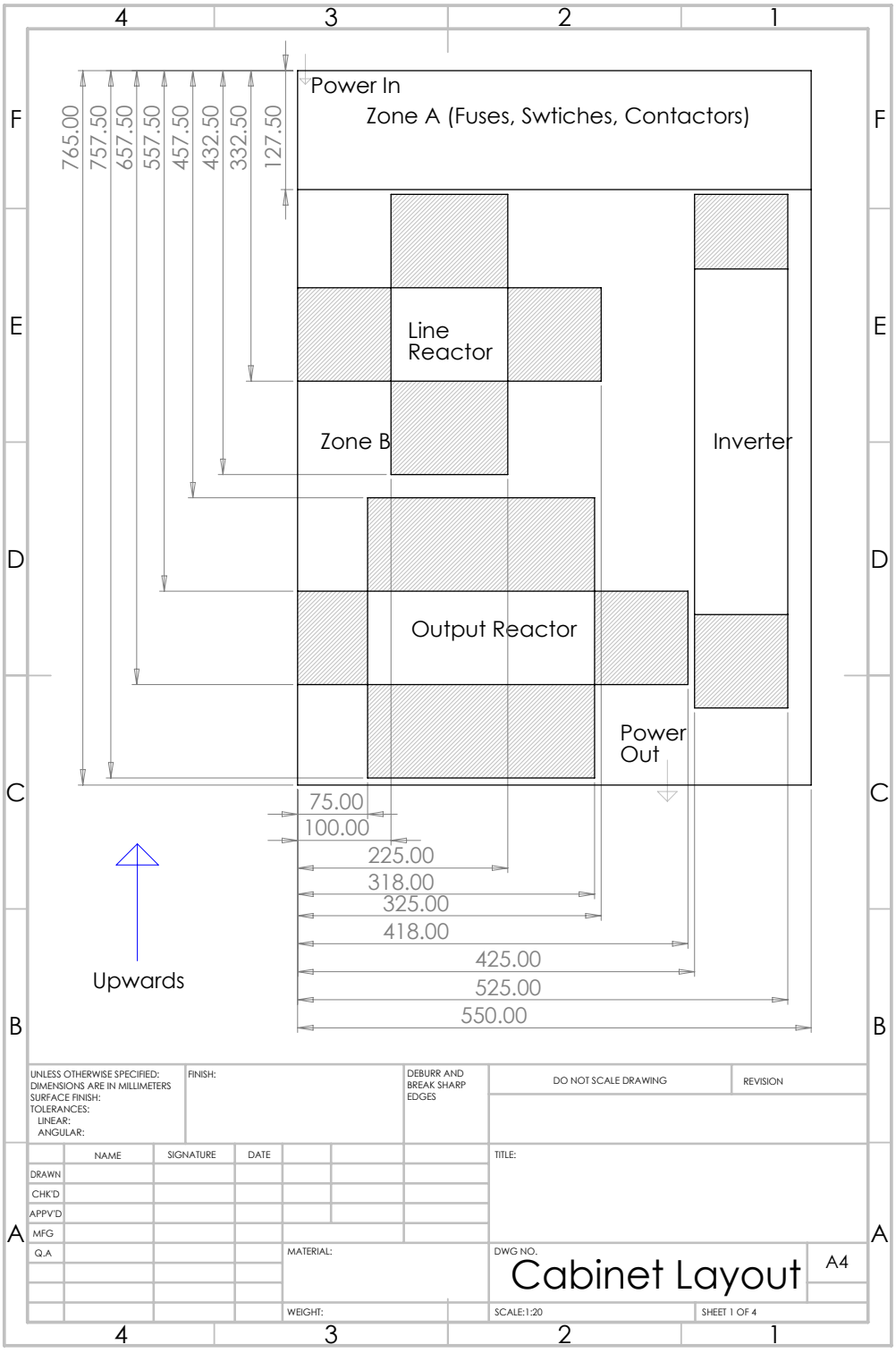

Figure G.1: An engineering drawing of the back plate for the motor cabinet purchased from RS Online. The shaded sections around each of the components indicate ventilation zones for each of the components.

Appendix H

Electronics Box Layout for onboard sensors

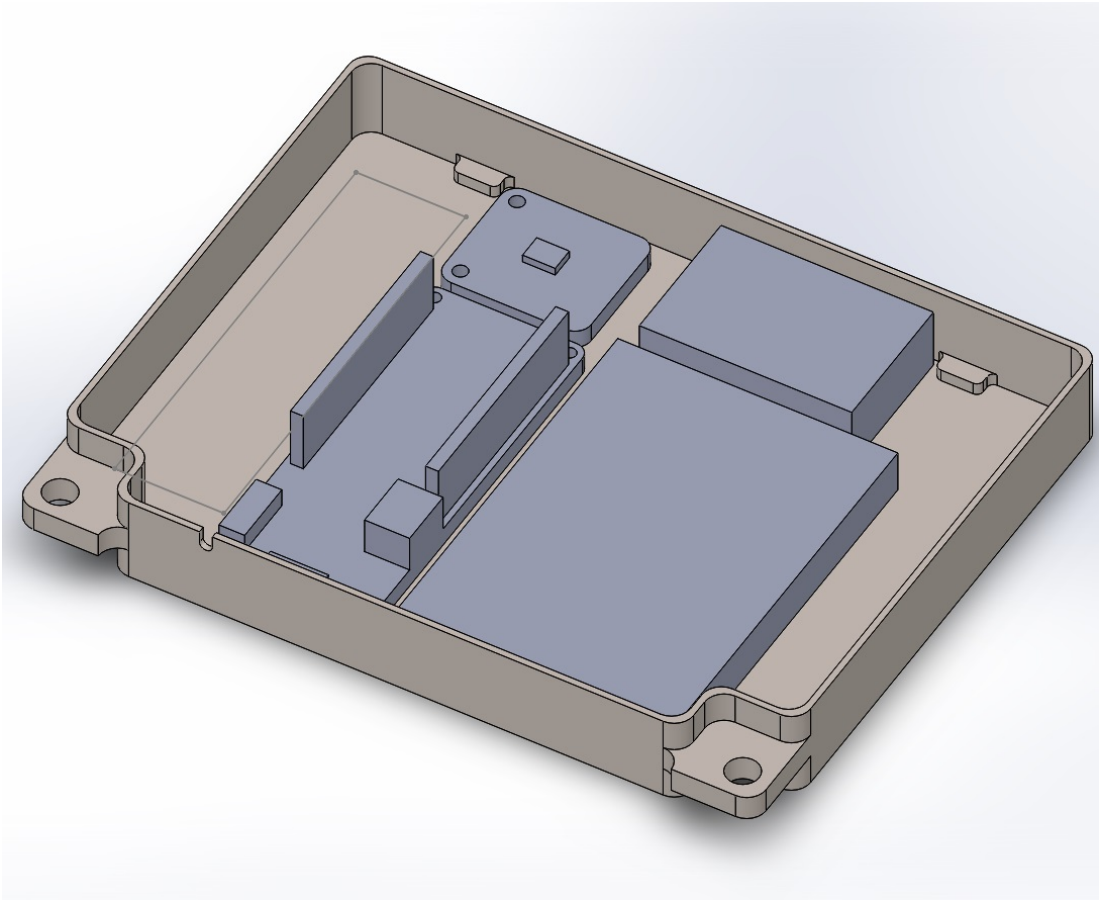

Figure H.1: CAD model of the electronics box, showing the battery, thermocouple amplifier, switch and MKR1010

Appendix I

Motor Configuration

The TIA Startdrive application is a sophisticated control software used to set up the configuration to control the inverter drive and electric motor. The Startdrive software can then be used to input the desired operational speed, as well as configuring any safety systems that will be integrated and any sensors required for the desired motor control. Initially the drive was configured using the TIA wizard using the following process and speeds of < 300rpm were tested. In the case of the inverter requiring a reset or is connected to a new computer, the following protocol is required:

1. Download and open Startdrive V17 from the Siemens website (newer versions may be available, however the device has not been tested with this)
2. Create a new project, with a desired name
3. Connect to the inverter via either the USB/mini usb cable, 9 pin cable or ethernet cable
4. After connecting, go to the online/ diagnostics section and click on the accessible devices. Then select the appropriate interface (i.e S7SUB for usb)
5. Search for the device
6. It should appear in the available drives section and hit show
7. Under the online access section the drive should appear

8. Double click commissioning and open the commissioning wizard

Due to stability issues, it was the drive operated inconsistently and stopped frequently without obvious reason or warning. After discussions, the supplier stated that in practice electric motors have stability issues at very low speeds ($< 10\%$) and in practice this could be as high as 20%. Following discussions with the supplier, Siemens were contacted directly and the motor was commissioned with the help of one of their engineers, Mr. Phil Hicks. Further to the initial advice, the cause of the stability issues was deduced as being that the motor was providing the incorrect torque and when the motor did not accelerate fast enough (due to the increased mass from the rotor components) the machine rose a fault and the drive stopped working. Care was taken to modify the ramp-up time to 3000s providing enough time for the drive to startup and reach equilibrium. with the settings displayed in table I.1.

Table I.1: Siemens advised setting p1462 = 0 to improve drive operation. Mass moment of inertia of plate and samples was $\sim 5.32 kgm^2$. The time to reach the maximum speed is p1120. After initial commissioning, p1120 can be reduced for a faster acceleration. Any changes should be incremental with care taken to monitor for motor faults. It should be stated here explicitly that any individual aiming to purchase and install an electric motor should do so with a qualified electrician and that the author here accepts no liability for the design, manufacture and testing of a rain erosion testing or any assembly or sub-assembly stated in this document.

Drive Setup Wizard Settings	
Application Class	Dynamic Drive Control
Defaults of the setpoints/command sources	[12] Standard I/O with analog setpoint
Drive setting	
Standard:	[0] IEC-Motor (50Hz, SI units)
Drive unit line supply Voltage:	415V
Drive Options	
	No breaking resistor
Drive filter type motor side	[1] Motor reactor
Inductance	0.54mH
Motor	
Motor type	[10] 1LE1 induction motor (not a code number)
Motor connection type	Delta
p305[0] Rated motor current	$13.10 A_{rms}$
p307[0] Rated motor power	7.5kW
p311[0] Rated motor speed	2950rpm
p304[0] Rated motor voltage	$400 V_{rms}$
p310[0] Rated motor frequency	50Hz
p335[0] Motor cooling type	[0] Natural ventilation
Temperature sensor	[1] PTC alarm & timer
Motor holding break	
Motor holding brake configuration	[0] No motor holding brake available
Current limit	$18.50 A_{rms}$ (Leave as Calculated, should be approx. this value)
Minimum speed	0rpm
Maximum speed	3000rpm
p1120 Ramp-function generator ramp-up time	3000s
OFF1 ramp-down time	10s
OFF3 (quick stop) ramp-down time	0s
Drive functions	
Technological application (standard drive control)	[1] Speed-dependent load (parabolic characteristic)
Motor identification	[2] Identifying motor data (at standstill)
rated speed	2950rpm
Encoders	
	Encoder 1 as motor encoder (If running with encoder speed control)
Encoder interface	[1] terminal interface
Encoder configuration	Select standard encoder from list:
Encoder type	3001
Manual Settings Changes	
p342	271.7058
p340	[4] calculation of controller parameters

Appendix J

Test Record for Rain erosion test rig

Table J.1: Test times for the rain erosion test rig. Duration times stated here just refer to the time spent at the stated speed and do not include the approximate 15 minutes to speed up and slow down.

Sample Holder Type	Date	Test Speed (rpm)	Duration (minutes)	Test Type	Rain system (Y/N)
Leading Edge	16/2/22	500	30	Calibration	N
	16/2/22	750	15	Calibration	N
	16/2/22	750	15	Calibration	N
	16/2/22	1000	10	Calibration	N
	16/2/22	1100	10	Calibration	N
	16/2/22	1200	10	Calibration	N
	17/2/22	1200	60	Calibration	N
	17/2/22	1300	5	Calibration	N
	Total Testing Time (inc. startup/shutdown): 155 minutes (275 minutes)				
Flat (3 point bend)	22/2/22	500	30	Calibration	N
	23/2/22	500	0	Calibration	N
	23/2/22	750	30	Calibration	N
	23/2/22	1000	15	Calibration	N
	23/2/22	955	15	Calibration	N
	23/2/22	955	15	Calibration	N
	1/3/22	717	60	Erosion	Y
	1/3/22	717	60	Erosion	Y
	2/3/22	717	60	Erosion	Y
	2/3/22	717	60	Erosion	Y
	2/3/22	717	60	Erosion	Y
	3/3/22	717	60	Erosion	Y
	3/3/22	836	51	Erosion	Y
	3/3/22	836	51	Erosion	Y
	3/3/22	836	51	Erosion	Y
	3/3/22	836	51	Erosion	Y
	4/3/22	836	51	Erosion	Y
	4/3/22	836	51	Erosion	Y
	4/3/22	955	45	Erosion	Y
	4/3/22	955	45	Erosion	Y
	4/3/22	955	45	Erosion	Y
	4/3/22	955	45	Erosion	Y
	7/3/22	955	45	Erosion	Y
	7/3/22	955	45	Erosion	Y
	7/3/22	955	45	Erosion	Y
	7/3/22	717	60	Erosion	Y
	7/3/22	717	60	Erosion	Y
	7/3/22	836	51	Erosion	Y
	7/3/22	836	51	Erosion	Y
	8/3/22	955	45	Erosion	Y
	8/3/22	836	51	Erosion	Y
	Total Testing Time (inc. startup/shutdown): 1414 minutes (1879 minutes)				
Total Testing Time, w/ Rain System: 1299 minutes					
Total Testing Time, Both Sample Holders: 1569 minutes (2154 minutes)					

Appendix K

FEA Meshes for the Second Design Optimisation of the Sample Holder

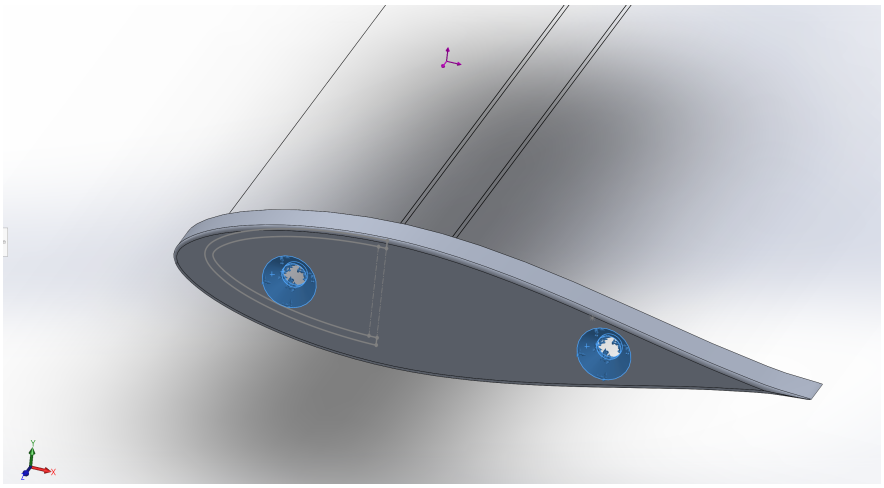

Figure K.1: Here it is possible to the fixture points for the end piece. It is also possible to see marked in the image, the area onto which the leading edge profiled sample is acting upon.

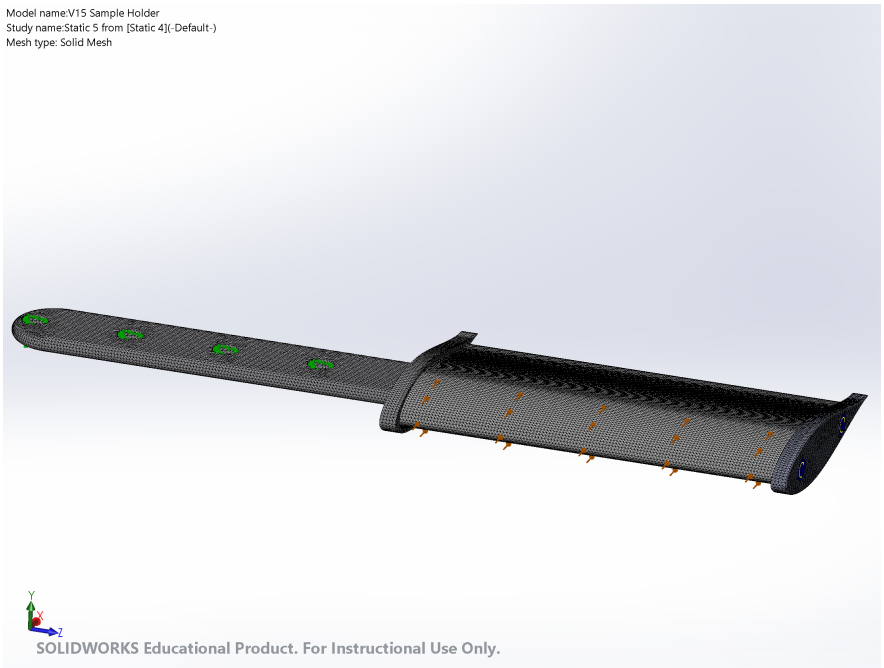

Figure K.2: Here it is possible to the fixture points for the end piece. It is also possible to see marked in the image, the area onto which the leading edge profiled sample is acting upon.

Appendix L

Risk Assessments and Safety Protocols

The operation of the rig and safety protocols were discussed with the workshop manager and safety coordinator for the department. For the safe operation of a complex and potentially hazardous machine like this, strict operational procedures were required. For the initial startup and calibration, a safe system of work was required. Together with the Mechanical & Aerospace Department safety team and the workshop manager (Drew Irvine), an initial startup procedure was devised. This procedure allowed a range of operating speeds to be progressively tested, whilst carefully monitoring vibrations, bolts, component wear and the overall structural integrity of the machine. The first startup Safe System Of Work (SSOW) was devised as follows:

1. Ensure power off.
2. Ensure Rain system is off using controllers on desk.
3. Ensure CCTV cameras on.
4. Turn internal rig lights on.
5. Empty the drainage tank downstairs using drainage pump, if required.
6. Fill the inlet tank upstairs using fitted tap.

7. Attach sample holders (see separate operations).

8. Check bolt torques (see Bolt torques PDF).

9. Lock rig door using bolt and ratchet or security interlock, if fitted.

10. Place both accelerometers onto motor frame (One for use with Labview and one for use with the Reactec vibrational analysis device). If possible attach them to the main bearing for maximum sensitivity.

11. Complete visual sweep of the operations area to look for safety hazards and obstructions to the rigs operation; this includes visual inspection of: inside the rig, inside the water tank, under the rig, behind the shelves and the room parallel to the rig. This also include looking for personnel, to ensure that there is no human presence in the vicinity of the rig prior to and during operation.

12. Turn on the power switch for the rig, located on the wall.

13. Leave the operations area, ensuring there are no personnel in the area.

14. Lock the access gate at the top of the stairs, securing the downstairs area and restricting access to any personnel.

15. Conduct a final check on all CCTV cameras for personnel and hazards.

16. Release emergency power button and turn on the motor using the TIA software on the computer at the control station.

17. Ensure that both Labview and the Reactec vibrational monitoring device are correctly setup and ready to monitor signals from the accelerometers.

18. Ramp speed to 300rpm.

19. Operate the rig for at least 5 minutes, monitoring the speed on the TIA software and vibrations signals and FFT generated using both devices.

20. Turn off the motor using the TIA program, waiting until the rig has completely stopped moving using the CCTV.

21. Cut power to the rig using the emergency power button.
22. Unlock the gate at the top of the stairs.
23. Proceed downstairs and turn off the power.
24. Check Bolt torques, ensuring they match original torques.
25. If there are no large amplitudes on the FFT and amplitudes were within range as according to 6.23 repeat steps 18-24 for speeds up to the maximum design test speed, but for step 18, increasing this value by increments of 100RPM.
26. Unlock the rig door by using ratchet or security interlock.
27. Remove samples.

Aside from the first startup SSOW, a daily use SSOW was also devised. This SSOW is quite similar to the first startup SSOW, however there were some key differences. This SSOW was meant for daily use and experimental work, meaning the rain system would be operated at the same time. Secondly, the rig would not be incrementally increased in speed as previously described. Instead, the rig would be slowly accelerated to the desired speed and thirdly, the rig would be run for much longer periods of time. This daily use SSOW was outlined as follows:

1. Ensure power off.
2. Ensure Rain system is off using controllers on desk.
3. Ensure CCTV cameras on.
4. Turn internal rig lights on.
5. Empty the drainage tank downstairs using drainage pump, if required.
6. Fill the inlet tank upstairs using fitted tap.
7. Attach sample holders (see separate operations).
8. Configure rain system, if necessary.

9. Run rain system ensuring that none of the rain needles have bubbles inside and that they are all free flowing and then switch off.

10. Lock rig door using bolt and ratchet or security interlock, if fitted.

11. Place both accelerometers onto motor frame (One for use with Labview and one for use with the Reactec vibrational analysis device). If possible attach them to the main bearing for maximum sensitivity.

12. Complete visual sweep of the operations area to look for safety hazards and obstructions to the rigs operation; this includes visual inspection of: inside the rig, inside the water tank, under the rig, behind the shelves and the room parallel to the rig. This also include looking for personnel, to ensure that there is no human presence in the vicinity of the rig prior to and during operation.

13. Turn on the power switch for the rig, located on the wall.

14. Leave the operations area, ensuring there are no personnel in the area.

15. Lock the access gate at the top of the stairs, securing the downstairs area and restricting access to any personnel.

16. Conduct a final check on all CCTV cameras for personnel and hazards.

17. Release emergency power button and turn on the motor using the TIA software on the computer at the control station.

18. Ensure that both Labview and the Reactec vibrational monitoring device are correctly setup and ready to monitor signals from the accelerometers.

19. Ramp speed to desired test speed.

20. When rig is at desired test speed, turn on rain system and run test for desired length, monitoring the speed on the TIA software and vibrations signals and FFT generated using both devices.

21. Turn off the motor using the TIA program, waiting until the rig has completely stopped moving using the CCTV.

22. Cut power to the rig using the emergency power button.

23. Unlock the gate at the top of the stairs.

24. Proceed downstairs and turn off the power.

25. Unlock the rig door by using ratchet or security interlock.

26. Remove samples.

Following these discussions some additional safety recommendations were made:

- A test log for different speeds tested, with a bolt torque checklist for each speed
- Bolts positions to be marked with a white line, allowing bolt positions to be easily inspected
- The artificial rain field contained needles which presented a hazard. Therefore a first aid kit was required on site during testing
- Needles needed to be changed and disposed of safety if either students or staff are punctured
- In the case of an electrical fire, a CO2 fire extinguisher is required on site
- In the case of spills, a spill action plan was required and subsequently, a wet-vac was purchased
- A periodic inspection check list was required for all high risk components
- The operational area contains dust and so, this may trigger the fire alarm, Care must be taken to cover the fire alarm during testing to prevent triggering
- Testing requires the presence of at least one individual to be present at all times during testing and for there to be another person, responsible to check on that person at all times when testing is taking place

In addition to these recommendations, the observation was made that noise could be an issue. Although, it was only advised to monitor this. Following the recommendations, all bolts were marked with a white line and a weekly checklist was devised L.1.

Table L.1: Weekly checklist for the rain erosion test rig.

Item	Inspected by	Date	Time
Full test of the emergency stop including brake			
Empty both water tanks completely			
Mechanical test of interlock			
Check test log of rig for total operational time. (Approximately every 100 hours of testing, conduct inspection of drive train components, sample holders and hub disc, inspecting for cracks)			
Check torque on tyre coupling bolts and update white marker, if necessary			
Check for rain erosion of the sample holder			
Check for signs of corrosion inside the rig			

All items raised in the weekly checklist points above must be adhered to before operation was allowed. If any fault was found or any item on the checklist found not to have been signed off then the rig was stopped from operating.

In addition, if in doubt consultation was required with the Departmental DSC Dr. Fiona Sillars, Laboratory Manager Chris Cameron, Workshop Supervisor Drew Irvine or Deputy Workshop Supervisor Alastair Kerr for advice.

Bolts were purchased from ACCU Ltd. Prior to installation, ACCU were consulted for technical guidance when determining the required torque for each of the bolted connections. ACCU Ltd. advised on the following torques for each bolted connection and the respective material combination is stated in table L.2.

Table L.2: Bolt torques as recommended by ACCU Ltd in email correspondence.

Bolt Location	Bolt Type	Nut Type	Washer Type	Bolt Size	Bolt Torque (NM)
Sample holder connection (Al 7075) to main disc (Al 7075)	A4-80 Stainless Steel Hexagonal	Nyloc nut	Flat	M16	160
Plate cover to main disc	A4-80 Stainless Steel Cap Screw	Nyloc Flange nut	None	M10	40
Main disc to main bearing hub	10.9 Steel Hexagonal	-	Spring	M14	210